Connecting the Dots

Nanoparticles, Nanostructured Surfaces, and Wetting

G.H. ten Brink

Connecting the DOTS

Nanoparticles, Nanostructured Surfaces, and Wetting

Connecting the Dots

Nanoparticles, Nanostructured Surfaces, and Wetting

PhD thesis

to obtain the degree of PhD at the
University of Groningen
on the authority of the
Rector Magnificus Prof. C. Wijmenga
and in accordance with
the decision by the College of Deans.

This thesis will be defended in public on

Tuesday 13 September 2022 at 16.15 hours

by

Gerrit Hendrik ten Brink

born on 25 March 1967
in Assen, the Netherlands

Supervisors
Prof. G. Palasantzas
Prof. B.J. Kooi

Assessment committee
Prof. M.A. Loi
Prof. K.U. Loos
Prof. H.J.W. Zandvliet

In dedication to my beloved parents, my two beautiful daughters, and most off all, my loving wife (and for her patience during the last five years) and last but not least, in memory off all my loved ones who went too soon.

Gerrit Hendrik (Gert) ten Brink

Contents

CONNECTING THE DOTS

Nanoparticles, Nanostructured Surfaces, and Wetting

Gerrit Hendrik ten Brink
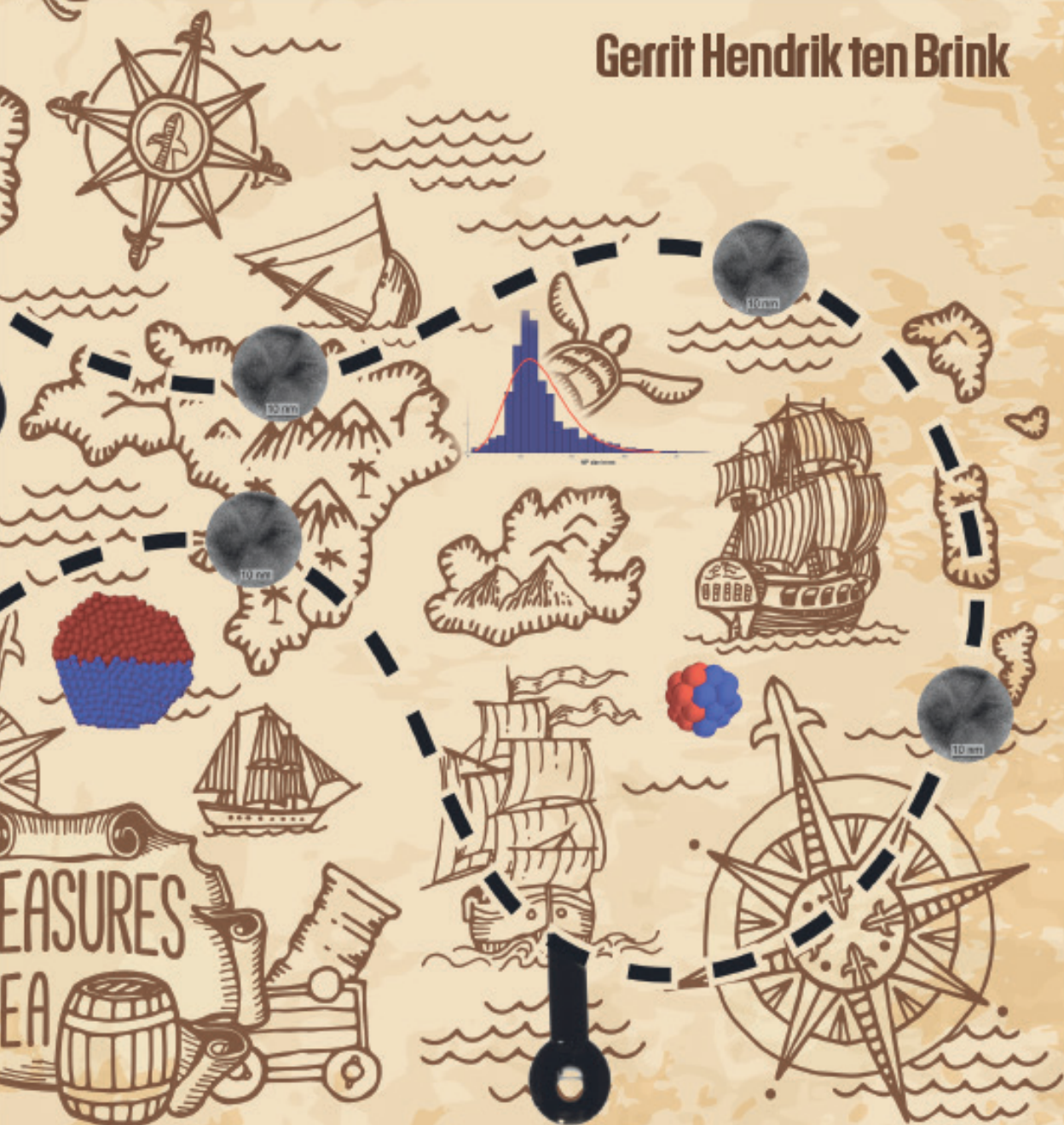
Chapter 1

**Introduction:
Nanoparticles, nanostructured surfaces,
and wetting**

1.1   Introduction

Nanoscience and nanotechnology are among the most visible and growing research areas in materials science. Nano-structured materials (NSMs) include atomic clusters, filamentary structures including tubes and wires, layered (lamellar) structures, and bulk nanostructured materials[1,2]. At least one dimension is less than 100 nm, more typically less than 50 nm. Nanoparticles are entities between single atoms and bulk materials generally showing behavior distinguishing them from the other two. In many cases, the properties of such nanoscale materials can be very different from the ones of the same substance in bulk. Materials built up from NSMs can display novel behavior, which manifests itself when the size of the building blocks is smaller than the critical length scale of a particular property[3–6].
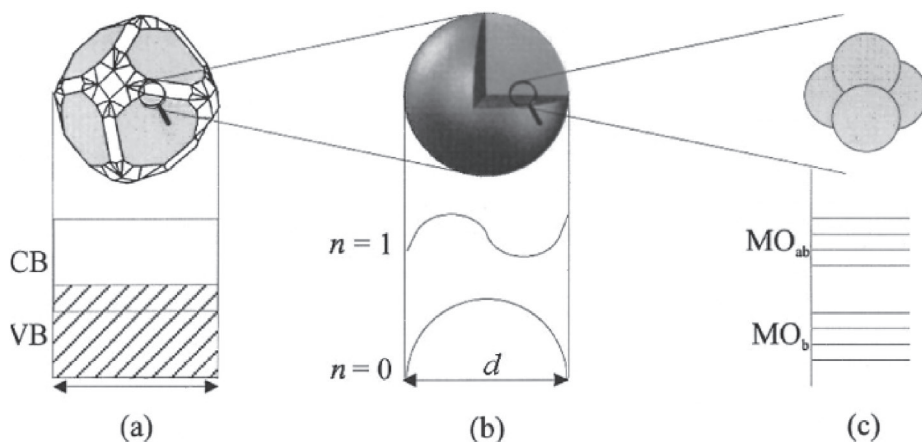
Figure 1-1 Illustration of the transition of a bulk metal via a nanocluster to a molecule[3]

The metallic band structure in Fig 1-1(a) turns to a discrete electronic energy level in Fig. 1-1(b), where the particle diameter corresponds with the de Broglie wavelength. In Fig 1-1(c), bonding and antibonding molecular orbitals are shown, occupied by electrons localized in bonds[3].

Another reason for the novel behavior of nanomaterials is the very high specific surface-to-volume ratio, leading to increased surface reactivity. The large interface area plays a significant role in the assembled nanophase forms. The surface-to-volume ratio in nanoparticles significantly affects the properties of the nanoparticles. To make it more specific, consider a sphere of radius r: The surface area of the sphere will be $4\pi r^2$, and the volume of the sphere equals $4/3(\pi r^3)$. Therefore, the surface area to the volume ratio will be $3/r$. It clearly shows that the surface area to volume ratio increases with the decrease in the sphere's radius. As the particle size decreases,

a more significant portion of the atoms is at the surface. A particle with a diameter of 3 nm has ~50% of its atoms on its surface. At 10 nm, ~15% of its atoms are on the surface, and at 30 nm, the particle has ~5% of its atoms on its surface. Therefore, nanoparticles have a much greater surface area per unit volume than larger particles. This attribute makes nanoparticles more chemically reactive. Hence, as growth and a catalytic chemical reaction occur at surfaces, nano-structuring will significantly impact product development[7–10]. In addition, to refer to a different field, the most diminutive dimensions in the semiconductor industry have already been reduced to the nanoscale regime (<100 nm), with a further decrease to 10 nm or less in the next 15 years (Semiconductors Roadmap, http://public.itrs.net) Therefore the ability to control surface features on this length scale is essential in future nanotechnology developments.

1.2   Why (a Ph.D. thesis) about Nano, the challenges and opportunities

Why study nano-sized materials? From 1996 till 1998, The International Technology Research Institute, World Technology Evaluation Center (WTEC), supported a panel study of research and development status and trends in nanoparticles, nanostructured materials, and nano-devices. The three related scientific/technological advances have made it a coherent area of research. These are:

1. New and improved synthesis methods that allow control of the size and manipulation of the nanoscale "building blocks."
2. New and improved characterization tools for study at the nanoscale (e.g., spatial resolution, chemical sensitivity)
3. Achieve a better understanding of the relationships between nanostructure and material properties and how these can be engineered.

The present work aims to demonstrate that these three developments can be jointly employed to achieve progress in nanoscience and nanotechnology.

(1) The new and improved synthesis method used in the present work is a home-modified nanoparticle source based on a commercially available Mantis Nanogen-50© unit that initially did not work well but was modified (in particular by the present author) to be one of the better-quality sources in the world.

(2) The characterization tools to reveal structural details include state-of-the-art scanning and transmission electron microscopy (SEM, TEM, and STEM).

(3) The better understanding of the relationships between nanostructure and material properties focused here on a better understanding of the wetting behavior of nanoparticles decorated surfaces.

The present thesis is also a condensate of the author's many years of keeping the associated equipment up and running and training many users to use the facilities properly. Instead of repeatedly explaining many details to new users, there is now the possibility of referring to the relevant parts in the present thesis.

1.3   Why nanoparticles in particular?

Taken from a famous lecturer "There's Plenty of Room at the Bottom" Feynman in 1959 stated that *"Atoms on a small scale behave like nothing on a large scale, for they satisfy the laws of quantum mechanics. So, as we go down and fiddle around with the atoms down there, we are working with different laws, and we can expect to do different things."*

Although nanoparticles (NPs) are entities between single atoms and bulk material, they are generally still largely affected by quantum mechanics. Therefore, it makes a lot of sense to study NPs and their properties as a function of their size for fundamental and technological reasons. NPs may offer ways to make new kinds of materials altogether because:

1. they show properties that differ from the bulk material;
2. they can show unique properties not found in bulk materials;
3. they can show size-dependent behavior allowing tuning of properties optimized for specific applications.

Three main reasons **can be put forward to explain** the unique/unusual behavior of NPs:

1. High **surface to volume** ratio. Like already mentioned above, the fraction of atoms at the surface of NPs is significant compared to atoms in the bulk and can be tuned by the NP size. Most (chemical) reactions take place at the interface. There NPs with a size close to 1 nm play an important role in catalysis.
2. NPs show **quantum confinement** and quantized states that can be tuned by the NP size: called quantum dots. For instance, the bandgap and optical properties of semiconducting. quantum dots are governed by quantum confinement.
3. Size compares to **characteristic length scales** and interacts with these length scales. For instance, when an NP has a size very similar to one of the magnetic domain wall widths in the bulk material, the coercivity typically reaches a maximum.
4. *Therefore, there's Plenty of Room at the Bottom regarding research where NPs are involved.*

1.4   Why focus on wetting of nanostructured surfaces

Surface wetting has been studied extensively because it is a fascinating topic for humankind that can be experienced abundantly in nature (e.g., on many different plants' leaves) and has large implications for technology. To mention a few relevant technological examples: self-cleaning, anti-icing, antifogging (of windows), surface adhesion, stiction (e.g., in microelectromechanical systems), and capillarity phenomena (e.g., in micro/nano fluidic systems). All wetting research is indebted to the seminal work performed by T Young in 1805, who showed the relationship between the contact angle (CA) θ, the surface tension of the liquid σ_{lg}, the interfacial tension σ_{sl} between the liquid and solid, and the surface free energy σ_{sg} of the solid. Although in this famous manuscript, this formula is not mentioned at all. Unfortunately, this Young's equation only holds for flat surfaces but breaks down for rough surfaces. The wetting research performed by Wentzel and Cassie-Baxter explained the influence of roughness on wetting. The massive variety of rough surfaces that can occur naturally or can be produced artificially in combination with the richness in surface and interface interactions between the different phases involved has introduced a complexity to wetting research that is still not properly understood. In some (limiting) cases, the so-called Wenzel and Cassie-Baxter models can explain the influence of roughness on wetting. However, many cases exist where these models do not agree with the observations. Therefore, more in-depth wetting research is required to arrive at a more comprehensive understanding of the wetting of real actual surfaces showing its roughness.

The lotus leaf effect is arguably the most famous case, where wetting is strongly controlled by roughness. The exceptionally low roll-off angle and the associated self-cleaning of the lotus leaf has been attributed to a hierarchical surface roughness, with roughness at both micrometer length scales (laterally and in height) and nanometer length scales. Successful efforts have mimicked the lotus leaf's behavior by artificially reproducing such hierarchical surface roughness. Still, producing such roughness artificially generally comes at a considerable price, particularly when using top-down techniques like lithography. The combination of nanoscale resolution with macroscopic length scales (e.g., a 12-inch wafer) that have to be patterned works well for rather expensive products like computer chips, but not for just roughening a surface for wetting purposes. Bottom-up approaches, like direct deposition of material on a surface, are therefore more attractive. Thin-film deposition can operate in a regime introducing roughness that increases when more material is deposited. However, starting with deposition from the atomic scale is not so efficient when roughness is not required at that scale. Starting with nanoscale clusters is, in this sense, clearly more efficient. The desired nanoscale roughness is achieved when these NPs stay distinct and intact after deposition. Then upon continued deposition of these nanoclusters, they form a porous network/aggregate that also shows additional roughness on/at longer length scales.

The requirement to stay distinct and with its shape preserved after deposition was the starting point of the present thesis work. A nanoparticle deposition source is used to create (starting from an as smooth as possible surfaces) rough surfaces and then study the wetting behavior, e.g., as a function of deposition time (coverage of the surface by nanoparticles), nanoparticle size, and nanoparticle chemistry (as illustrated in Fig. 1-2).
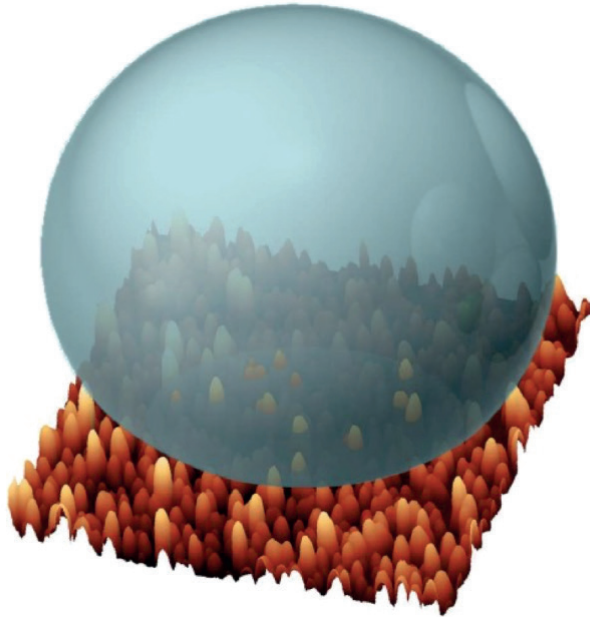
Figure 1-2 Artist impressing of a water droplet resting on an NPs covered surface.

1.5   Outline of this thesis

This thesis is divided into three main sections. The first section (chapters 2, 3, 4, and 5) is about making and characterizing nanoparticles containing of single or multiple elements.

The second part of this thesis shows some intriguing wetting properties of nanostructured materials made from nanoparticles (chapters 6, 7, and 8).

The third section and final chapters (9-12) of this thesis contain the summaries in Dutch and English, followed by the acknowledgments and a list of the papers published based on this thesis work. And last but not least, some final words about the author.

Below is a list of chapter titles:

Chapter 1   *Nanoparticles, nanostructured surfaces, and wetting*
Chapter 2   *How to make nanoparticles, e.g., The Mantis nanocluster source*
Chapter 3   *How to characterize nanoparticles and wetting properties*
Chapter 4   *Copper nanoparticle formation in a reducing gas environment*
Chapter 5   *Tuning structural motifs and alloying of bulk immiscible Mo–Cu bimetallic nanoparticles by gas-phase synthesis*
Chapter 6   *Roughness controlled superhydrophobicity on a single nanometer length scale with metal nanoparticles*
Chapter 7   *Control surface wetting with amorphous-to-crystalline phase transitions of GST nanoparticles decorating surfaces.*
Chapter 8   *Wetting of surfaces decorated by gas-phase synthesized silver nanoparticles: Effects of Ag adatoms, nanoparticle aging, and surface mobility*
Chapter 9   *Contains the Summary in English and Samenvatting in Dutch*
Chapter 10 Acknowledgements en Dankwoord
Chapter 11 A list of publications
Chapter 12 About the author

When a chapter has been published in a peer-reviewed journal, it is mentioned on the first page of the chapter. The reader can find a complete list of publications in chapter 11.

1.6   References

[1]   C.C. Koch, in *Encyclopedia of Materials: Science and Technology (Second Edition)*, edited by Editors-in-Chief: K. H. Jürgen Buschow, Robert W. Cahn, Merton C. Flemings, Bernard Ilschner (print), Edward J. Kramer, Subhash Mahajan, and Patrick Veyssière (updates) (Elsevier, Oxford, 2001), pp. 5901–5905.

[2]   G. Palasantzas, S.A. Koch, T. Vystavel, and J.Th.M. De Hosson, Journal of Alloys and Compounds **449**, 237 (2008).

[3]   G. Schmid, M. Bäumle, M. Geerkens, I. Heim, C. Osemann, and T. Sawitowski, Chem. Soc. Rev. **28**, 179 (1999).

[4]   S. Ramezani, *NANOPARTICLES, from Theory to Application (Gunter Schmid)*

[5]   R. Hippler, S.R. Bhattacharyya, and B.M. Smirnov, in *Introduction to Complex Plasmas*, edited by M. Bonitz, N. Horing, and P. Ludwig (Springer Berlin Heidelberg, Berlin, Heidelberg, 2010), pp. 299–314.

[6]   In *Introduction to Nanoscience and Nanotechnology* (John Wiley & Sons, Ltd, 2010), pp. 1–10.

[7]   G. Schmid, M. Bäumle, M. Geerkens, I. Heim, C. Osemann, and T. Sawitowski, Chemical Society Reviews **28**, 179 (1999).

[8]   B. Chen, G.H. ten Brink, G. Palasantzas, and B.J. Kooi, Scientific Reports **6**, srep39546 (2016).

[9]   Z. Liu, T. Zhou, L. Li, Y. Zuo, C. He, C. Li, C. Xue, B. Cheng, and Q. Wang, Applied Physics Letters **103**, 082101 (2013).

[10]   Y. Jia, C. Sun, S. Shen, J. Zou, S.S. Mao, and X. Yao, Renewable and Sustainable Energy Reviews **44**, 289 (2015).

[11]   A.S. Edelstein and R.C. Cammaratra, editors, *Nanomaterials: Synthesis, Properties, and Applications, Second Edition*, 2nd ed. (Taylor & Francis, 1998).

[13]   P. Jensen, Reviews of Modern Physics **71**, 1695 (1999).

[14]   http://scienceus.org/wtec/

[15]   http://www.zyvex.com/nanotech/feynman.html,https://en.wikipedia.org/w/index.php?title=There%27s_Plenty_of_Room_at_the_Bottom&oldid=991599406
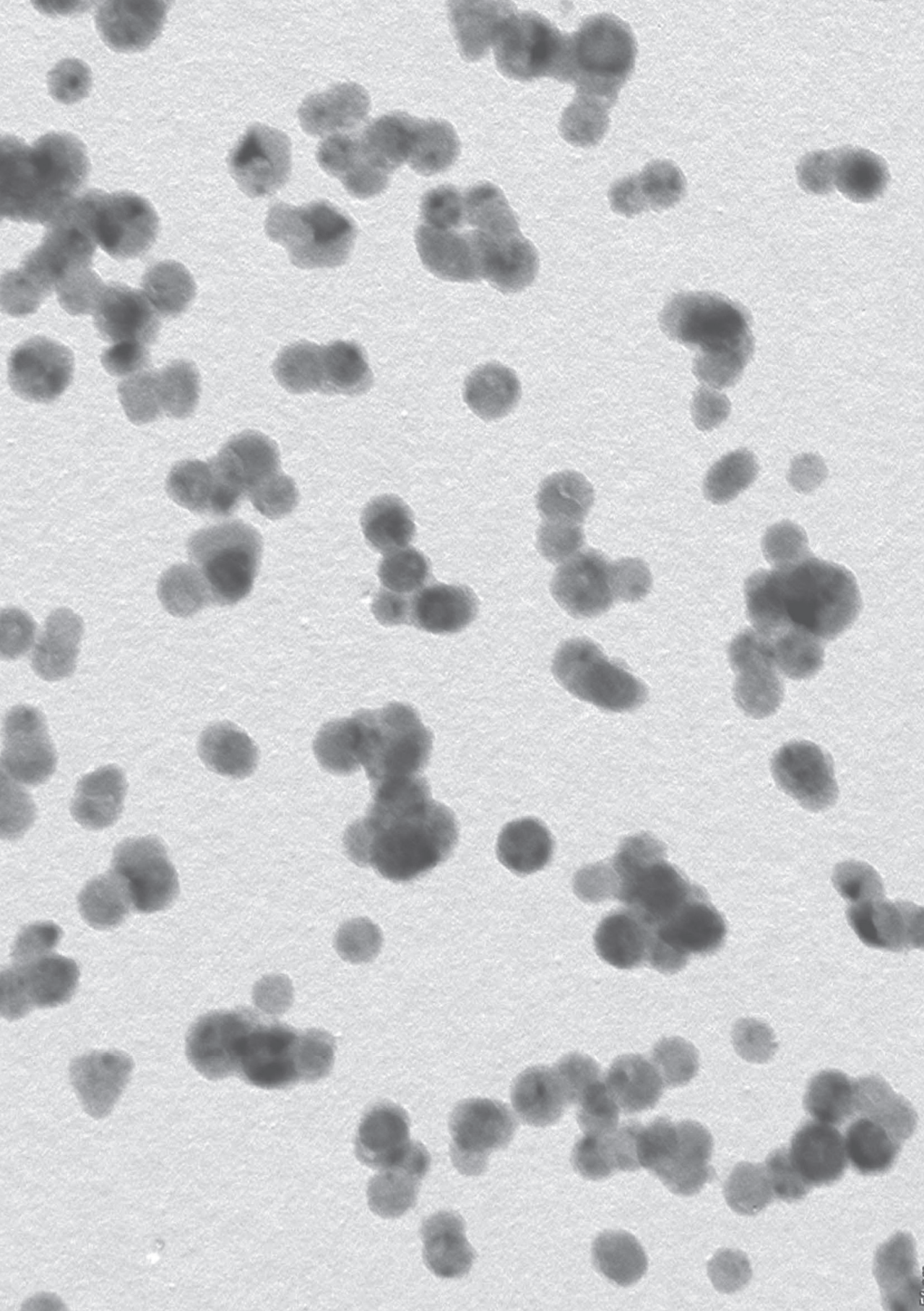
Chapter 2
**How to make nanoparticles:
Mantis nano-cluster source**

2.1   Synthesis of nano-scale materials

Nano-scale materials (NSMs) are of interest from fundamental science and the technological application point of view because of their physical, chemical, electronic, and magnetic properties. They can show properties that differ from the ones of the higher dimensional (bulk-like) counterparts. Furthermore, based on their dimension, NSMs can be divided into 0D, 1D, 2D, and 3D NSMs. Over the last ten years, many physical and chemical techniques have been developed to synthesize and fabricate 0D, 1D, 2D, and 3D NSMs with controlled size, shape, dimensionality, and structure.

2.2   Nanoparticle growth

In general, the current view is that the growth of nanoparticles can be divided into three stages: (1) nucleation, (2) coagulation, and (3) accretion of atoms and ions (also termed surface growth). The growth stages are depicted in Figure 2-1. Nucleation and growth of atoms occur when nuclei are formed via three-body collisions and subsequent growth through the attachment of single atoms. This so-called accretation of atoms and ions continues until the nuclei become stable (e.g. when the seeds consists of about 7 atoms) At this stage the internal degrees of freedom are high enough to dissipate the heat release during the condensation process, allowing further growth of the NPs. For more extensive explanations, one can read for example the many books written by Boris M. Smirnov for example: Cluster Processes in Gases and Plasmas, WILEY-VCH, ISBN 978-3-527-40943-3.
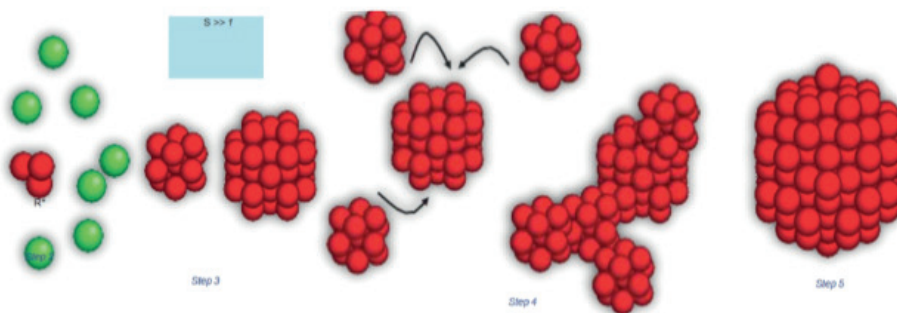
Figure 2-1 Schematic view of the nucleation and growth process.[11]

2

2.3   Chemical methods

An extensive review of the many different chemical methods to produce nanoscale materials is beyond the scope of this thesis. For reference a few books to read are:

- C. N. R. Rao, A. Muller, A. K. Cheetham (Eds.), The Chemistry of Nanomaterials Synthesis, Properties and Applications 2003, ISBN 3-527-30686-2
- Nanoparticles From Theory to Application Edited by Gunter Schmid ISBN 3-527-30507-6
- Jeevanandam, J., Barhoum, A., Chan, Y. S., Dufresne, A. & Danquah, M. K. Review on nanoparticles and nanostructured materials: history, sources, toxicity, and regulations. Beilstein J. Nanotechnol. 9, 1050–1074 (2018).

2.4   Physical methods

Gas-phase synthesis is an example of a (relatively new) physical vapor method to produce NSMs. More specifically, NPs are made from a bottom-up approach. The related scientific community is still small compared with the wet chemistry community, and industrial applications are still nonexistent. The technology has reached a degree of maturity that foresees fast growth in the coming years. As the fabrication process with gas aggregation sources is an out-of-thermodynamic equilibrium process, it is possible to fabricate structures that cannot be obtained by other means.[11]

Below is a list of the most common physical techniques to produce nano clusters:

- Evaporation technique
- Sputtering technique
- Hot and cold plasma
- Spray pyrolysis
- Inert gas phase condensation technique
- Pulsed laser ablation
- Sonochemical reduction
- Attrification
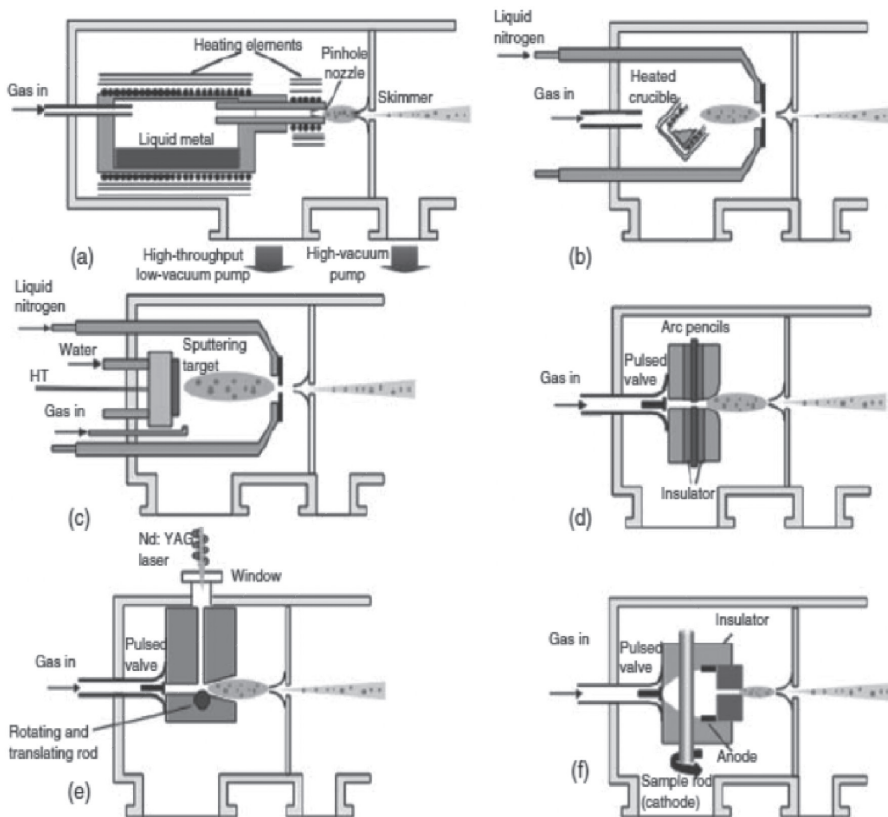
Figure 2-2 Basic layout and schematics of different physical vapor techniques using rare gases to produce supersaturated vapors. (a) Seeded supersonic nozzle source, (b) thermal gas aggregation source, (c) sputter gas aggregation source, (d) pulsed-arc cluster ion source, (e) laser ablation source, and (f) pulsed microplasma cluster source.[13]

2.5   A physical method: the Mantis nanocluster source

Nowadays, the Inert Gas Condensation (IGC) with Magnetron sputtering is a well-known sputtering technique. More than 30 years ago, in the 90s, Prof Haberland placed a "specially modified" magnetron sputter head able to operate at high-pressure conditions" inside the vessel. The cluster source has a small exit aperture, thus creating a higher pressure than normal for magnetron sputtering, yet it still operates without arcing.[11] The cluster source produced a conical beam of (mainly negatively charged copper) nanoclusters in the first instance. The original aim was to accelerate this small beam of copper nanoclusters ($\approx$15 nm), where up to 80% of the NCs are negatively charged, with an electrical field towards a substrate to fill deep holes made via lithography techniques in microelectronics industry.

The accelerated negative charged copper nanoparticles then create a well adhering thin copper film or fill up vials used as runners in a pattered semiconductor wafer. Since the commercialization of this concept, a few companies are supplying turn-key commercially available cluster sources/units, and the Mantis Nanogen50™ (see figures 2-3, 2-5, 2-10 and 2-11) being one of them. Other manufacturers for similar setups are;

- Von Issendorf; https://cluster.physik.uni-freiburg.de/
- The Oxford NC200; https://oaresearch.co.uk/
- HVM Plasma; https://www.hvm.cz/?id=en00
- Nikalyte; http://www.nikalyte.com/nl50

Figure 2-4 Russian Sputnik 1 (1957).

Figure 2-3 Mantis Nanogen 50™ image taken from the brochure published in 2010.

The whole setup is a UHV compatible vacuum system, with at the heart/core the Mantis cluster source

Figure 2-5 The Mantis NanoGen50™ image taken from the brochure published in 2010.

2.6   How magnetron sputtering works

The idea of producing small metal particles was first mentioned in a seminal paper by Granqvist and Buhrman[2,] and Prof. Haberland from the Freiburg University was the first to place a magnetron sputter head inside a closed confinement with a small aperture to produce a nanocluster-source in the 1990s[3–5]. Nanoparticle deposition based on Inert Gas Condensation (IGC), i.e. gas-phase aggregation, operates as follows: a noble gas is introduced inside an aggregation zone. Between the cathode the target material, for example a copper sputtering target (e.g. purchased from Alfa Aesar, 2.0-inch diameter x 0.125 inch thick, purity 99.999% metals basis), is placed on top of a strong magnet. This magnetron is enclosed with an open cylindrical anode (in the original design). The cathode is connected to a TDK-Lambda Genesys Gen 600-1.3 programmable DC power supply with a range up to 600 V and 1.3 A. During deposition the power is controlled by a built-in voltage and current limiter. The magnetron sputtering starts by supplying one or more gasses into the system from behind the magnetron head. The plasma starts by applying a potential between anode and cathode. Note: anode=target material, cathode=outer ring, or sputter head and the discharge voltage is material dependent. The accelerating argon ions initiate the plasma and generate secondary electrons which are trapped by the magnetic field. The plasma is sustained by feeding argon gas from behind the magnetron head and by maintaining the voltage between the target disk, which acts as a cathode, and the anode. The anode sits on top of the copper cooling block. The noble gas (Argon, or Xeon) plasma breaks off singular atoms of the target material, forming a vapor from the target material.

A cylindrical magnetic field, from a very strong magnet is used to trap the electrons. Charge production and surface erosion are maximal in the region where the magnetic field is parallel to the surface, as indicated by the two inserts in Figure 2-6. The gas will have three functions throughout the system: first sputtering, then cooling the target material vapor, and finally transporting the formed nano clusters. The deposition rate is measured with a home-built quartz crystal microbalance (QCM) placed slightly off the center of the conical cluster beam. The Argon (sometimes combined with Helium) gas is introduced in two different regions, (1) around the source, and (2) it is blown directly into the region where sputtering is maximal. The intensity and mass distribution of clusters can be optimized by playing with these two gas flows. The sputter head has to be water-cooled. The metal vapor is then transported away from the magnetron head into the aggregation volume, which is confined and cooled by the local high-pressure argon gas. The wall of the cluster source is water-cooled. The vapor reaches super-saturation by rapid cooling due to many collisions with the Argon atoms and the gas expansion from the vacuum. The formed copper NPs are transported by the Argon flow and accelerated by the pressure difference between the cluster source and the sample chamber. (Roughly a factor of 1.000 till 10.000 in

pressure difference) This differential pressure gives the NPs cluster beam a speed comparable to the speed of sound (340 m/s) until they are deposited onto the sample. Although the speed of the NPs may seem fast, it is still in the soft-landing regime. Upon impact with the substrate, the NPs do not deform. More recent research was performed by other groups, who placed a cluster source inside dedicated x-ray beams-lines and sophisticated optics. It revealed that the growth of the NPs takes place more directly inside the plasma, only a few millimeters above the target region end lesser in the aggregation chamber[12].These observations are opposite to the view of Haberland and Smirnov, who attribute further growth of NPs in the cluster due to the secondary plasma region inside the cluster source. According to these recent findings, NPs are found to be captured preferentially within a region circumscribed by the magnetron plasma ring. The NPs grow to 90 nm in this capture zone, whereas smaller ones sized 10–20 nm may escape and constitute an NPs beam. Time-resolved discharge measurements indicate that the electrostatic force acting on the charged NPs may be largely responsible for their capturing near the magnetron.[12] So, the story continues about the working mechanism of the Nanocluster source since it is not fully understood.

2.7 The magnetron head

The original Mantis gas head was designed with an open cylinder anode as seen in Figure 2-7 (as it assumed to have lesser turbulence than the oxford NC200 type source). It is converted (in-house) into a ring-shaped gas head with a variable bore diameter and measures to (re)produce an exact anode-cathode distance as seen in Figure 2-8
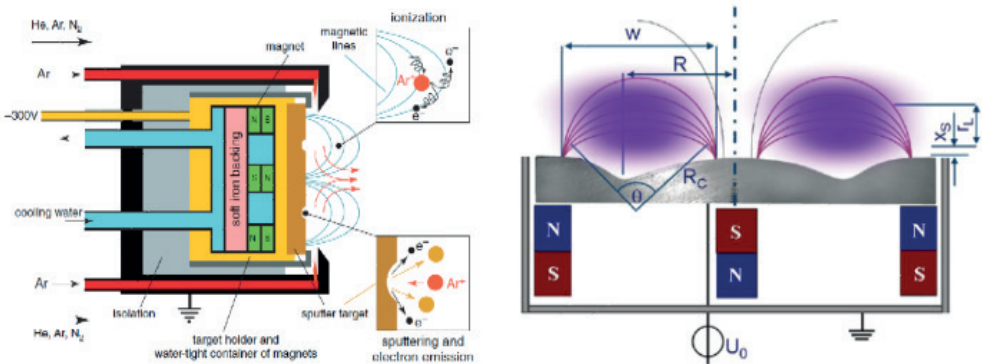
Figure 2-6 The magnetron sputter head in more detail.
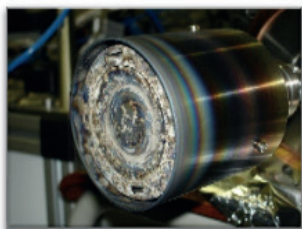
Figure 2-7 Original open cylindrical sputter head.

Figure 2-8 In-house modified sputter head.

Figure 2-9 Exchangable appertures as developed in-house.
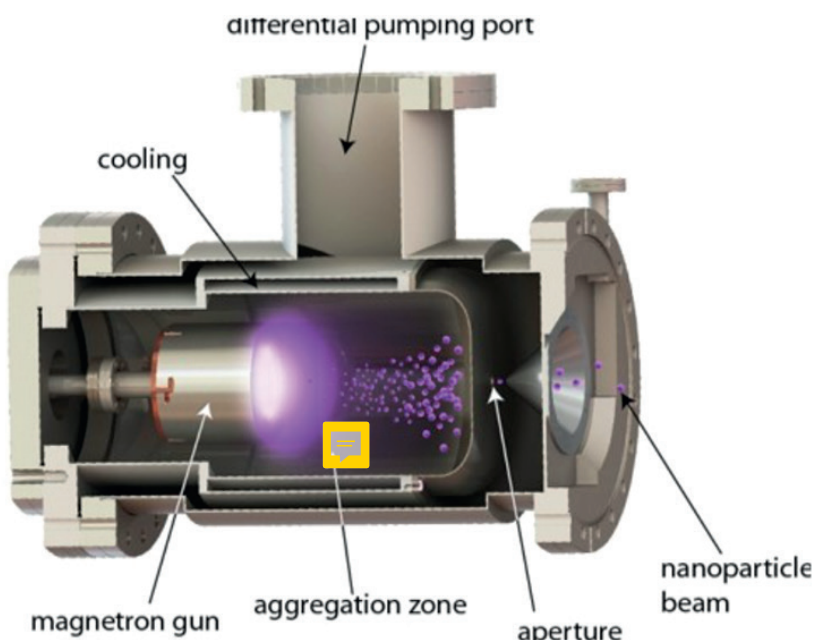
Figure 2-10 A cross-sectional view of the cluster source.

2.8 The NMI Mantis cluster source setup

The setup in Groningen, see Fig. 2-11, consists of two main components: the cluster source and the sample chamber. Two Leybold turbomolecular pumps have a capacity of 300 lt/s each. They are both connected to a backing pump; which in the current setup is a single scroll pump from Edwards XDS 10i. The system is a UHV oil-free vacuum setup. After bake-out, the system reaches a final vacuum of 5.10-9 mbar in the sample chamber and 5.10-7 mbar in the cluster

source. The system's core is the cluster source, as shown in Figure 2-5 and 2-10. It consists of a few components: a water-cooled magnetron head, a double gas inlet system controlled by 2 MKS mass flow meters, Penning pressure readings inside the aggregation chamber and the substrate chamber, and water cooling for the magnetron head and aggregation chamber wall.
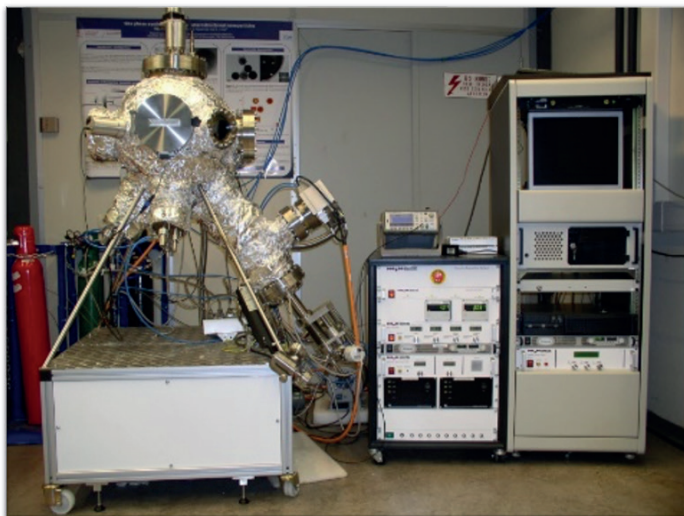
Figure 2-11 The Nanogen50© cluster source setup:

- 2x300L Oerlikon turbo pumps backed by one Edwards XDS-10i scroll pump
- All interconnects, and flanges are UHV components (ConFlat®)
- The pressures before operating are typical
- Main chamber 5.10-8 bar
- Aggregation chamber 5.10-6 mbar
- The whole setup is oil-free (mandatory)
- The gas is introduced via 3 2KS MFC 0-100 SCCM 1 MKS 200SCCM
- 6x10L gas cylinders 2xAr 5.0 and 6.0, He 5.0, CH4 6.0, H2 6.0, N2
- Per choice, a trace amount of spike gas; CH4, H2 via leak valve control
- In-house modified gas head
- In-house made exchangeable apertures as seen in Figure 2-9
- Mass filtering option (at the expense of yield loss and only based on ionized NPs)
- The system is LabVIEW controllable
- Home-built QCM (mass-based detection) to check deposition rate.

2.9   The quartz crystal microbalance

To check for the deposition rates of the cluster source, a simple crystal microbalance (QCM) monitor for sputtering application was made. It has been "homemade" constructed from few simple components. A QCM can work as a mass sensor, and a quantitative relation is given on how an oscillating crystal can measure this precise and accurate small mass chance. For small masses, this relation is proportional to the shift in the resonant frequency of the QCM as given by the Sauerbrey equation (2.1).

The homemade oscillator circuit is connected with a 12-digit frequency counter (Agilent 53220A). Most commercially operated QCM systems operate at 5 MHz, and they are less sensitive than the 10 MHz crystal we use, so we have to prepare our own crystal.
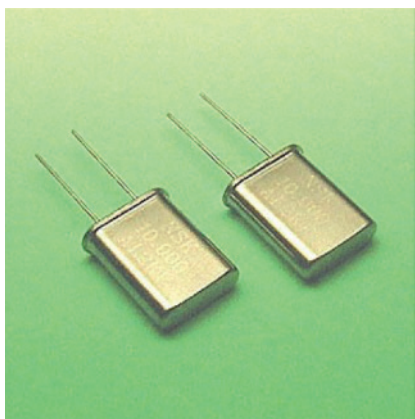
Figure 2-12 Commercially available 10 MHz oscillators with metal cap.
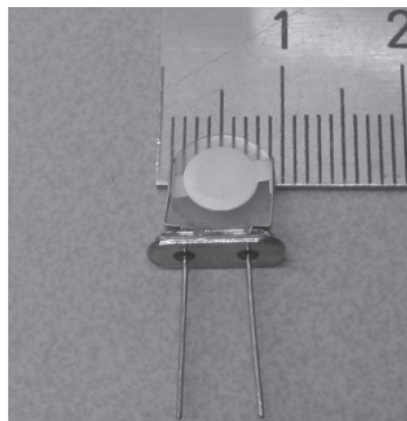
Figure 2-13 Uncapped Commercially available 10 MHz oscillator with the AT-cut quartz visible.

When a mass is deposited on the sensitive surface area of the QCM, the resonant frequency deceases. This sensitive area is the circular metallic electrode at the center of the crystal. This frequency drop/relation is given quantitatively by the Sauerbrey equation:

$$\Delta m = -C \, \Delta f \quad \textbf{(2.1)}$$

Δm is the areal density of the deposited mass, Δf the frequency shift, and C the constant of proportionality. The negative sign indicates that the resonance frequency drops when mass is deposited on the QCM. The expression for the constant of proportionality is given by:

$$C = \frac{N.\rho_q}{f_0^2} \quad \textbf{(2.2)}$$

Where N is the frequency constant of the specific crystal cut, ρ_q the density of quartz and f_0 the fundamental resonant frequency of the specific QCM.

Numerical values for the density and frequency constants for AT and BT-cut crystals are:

$$N_{AT} = 1.67 \cdot 10^3 \, Hz\, m$$
$$N_{BT} = 2.5 \cdot 10^3 \, Hz\, m$$
$$\rho_q = 2.65 \cdot 10^3 \, kg\, m^{-3}$$

In table 2-1, the numerical values for the proportionality constant C for different frequencies is listed. The C-constant is for AT-cut crystals since they are most frequently used in quartz resonators:

f0 (MHz)	C (ng cm^{-2} Hz^{-1})
4.00	27.7
6.00	12.3
8.00	6.91
10.00	4.43

Table 2-1: Values of C for AT-cut crystals

These commercially available crystals have a frequency stability better than 1 Hz; the deposition with nanopartiQles can therefore be monitored with reasonable resolution. Suppose the resonant frequency of a 10 MHz Quartz crystal is monitored with 0.01 Hz accuracy; it is even possible to measure the adsorption of much less than a monolayer of hydrogen[10]. Hence the need for the "somewhat expensive" 12-digit frequency counter.

2.10   Oscillator circuit

The oscillator circuit in Figure 2-14 drives the QCM at its resonant frequency. It oscillates at 10MHz. This circuit is built from available designs in the literature under the name "Clapp oscillator circuit," as is shown below.
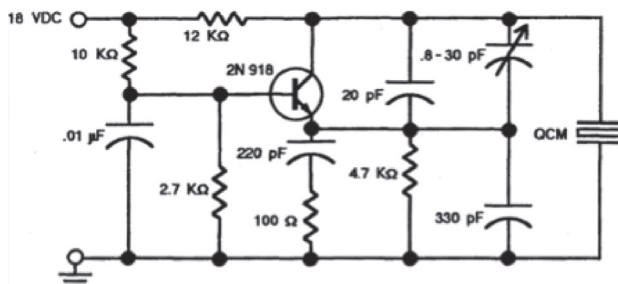
Figure 2-14 Clapp oscillator circuit diagram.

This circuit contains one transistor which functions as a switching device on the QCM. Therefore, crystals with different resonant frequencies can be driven by this circuit. The output is measured over the 100 Ohm resistor, which gives a sinusoidal signal with a peak-to-peak amplitude somewhere between 0.1 V and 1 V.
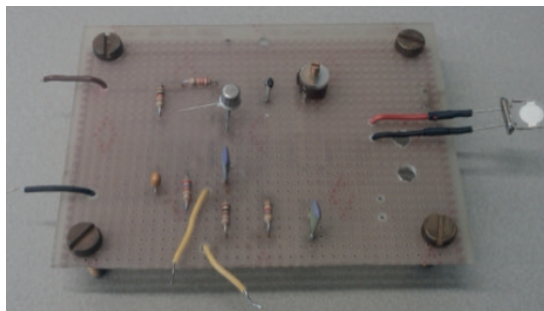
Figure 2-15 Clapp oscillator circuit.

The PCB board is made in-house using commercial electronic components. Then the components were soldered on a circuit board. The components are arranged identically to the circuit diagram of Figure 2-14.

2.11 The TEM sample exchanger/revolver head

The possibility to make multiple samples under identical conditions or to easily change deposition conditions without breaking vacuum or using a load lock is shown in Figure 2-16. In the current setup, 10 TEM samples (2 rows of 5 samples), like carbon coated copper grids or silicon nitride windows, can be inserted as substrates for deposition, which speeds up the process to find the right operating window.
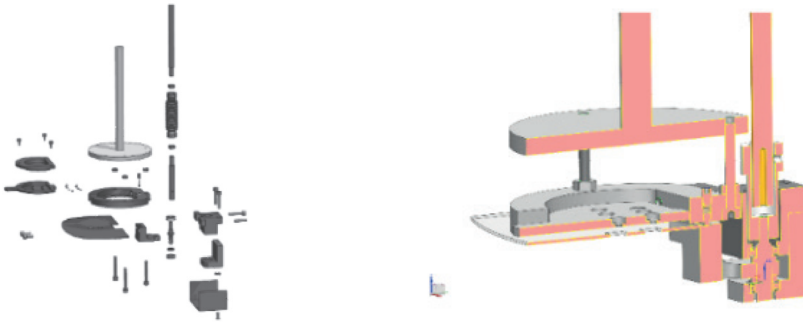
Figure 2-16 The TEM sample exchanger/revolver head (drawings Siemens NX©).

2.12 NPs systems produced with the Mantis cluster source

Magnetron sputtering is a suitable method for a wide range of materials. According to the OXFORD NC200 advertisement brochure (dated 2010), magnetron sputtering can make NPs from the following elements denoted in black in Figure 2-17.

Figure 2-17 Materials suitable to be used for magnetron sputtering are depicted in black according to the Oxford NC200 brochure from 2010.

Currently, the Mantis 50 setup at the NMI group in Groningen is equipped with a DC power source most suited to produce metallic and semiconducting NPs. For non-conducting material, an RF source is required (but not available). The wide range of materials from which NPs have been produced with this setup are shown in Table 2-2 below, i.e. by depicting representative TEM images.

2.13 References

[1] http://www.mantisdeposition.com

[2] C.G. Granqvist and R.A. Buhrman, J. Appl. Phys. **47**, 2200 (2009).

[3] H. Haberland, J. Vac. Sci. Technol. Vac. Surf. Films **10**, 3266 (1992).

[4] H. Haberland, Z. Insepov, M. Karrais, M. Mall, M. Moseler, and Y. Thurner, Mater. Sci. Eng. B **19**, 31 (1993).

[5] H. Haberland, M. Mall, M. Moseler, Y. Qiang, T. Reiners, and Y. Thurner, J. Vac. Sci. Technol. Vac. Surf. Films **12**, 2925 (1994).

[6] S. Schiller, U. Heisig, and K. Goedicke, Thin Solid Films **40**, 327 (1977).

[7] E. Mansfield, A. Kar, T.P. Quinn, and S.A. Hooker, Anal. Chem. **82**, 9977 (2010).

[8] G. Sauerbrey, Z. Fur Phys. **155**, 206 (1959).

[9] H. Haberland, in *Gas-Phase Synthesis of Nanoparticles*, edited by Y. Huttel (Wiley-VCH Verlag GmbH & Co. KGaA, 2017), pp. 1–21.

[10] Kasemo B and Tornquist E 1980 Physical Review Letters 44, 1555

[11] Dr. Yves Huttel, Gas-Phase Synthesis of Nanoparticles. Wiley-VCH.
ISBN: 978-3-527-34060-6

[12] J. Kousal, A. Shelemin, M. Schwartzkopf, O. Polonskyi, J. Hanuš, P. Solař, M. Vaidulych, D. Nikitin, P. Pleskunov, Z. Krtouš, T. Strunskus, F. Faupel, S.V. Roth, H. Biederman, and A. Choukourov, Nanoscale 10, 18275 (2018).

[13.] C. Binns, Chapter 3 Production of Nanoparticles on Supports Using Gas-Phase deposition and MBE, Handbook of Metal Physics, Elsevier, Volume 5, 2008, Pages 49-71.

Copper NPs

Copper/Zinc NPs

Iron NPs

Iron/Cobalt NPs

Mg NPs

MgNi NPs

MgTi NPs

MgCu NPs

Germanium NPs

Cu/Mo NPs

GST(225) NPs

MgTiPd NPs

Carbon NPs

Mo NPs

W NPs

Ag NPs
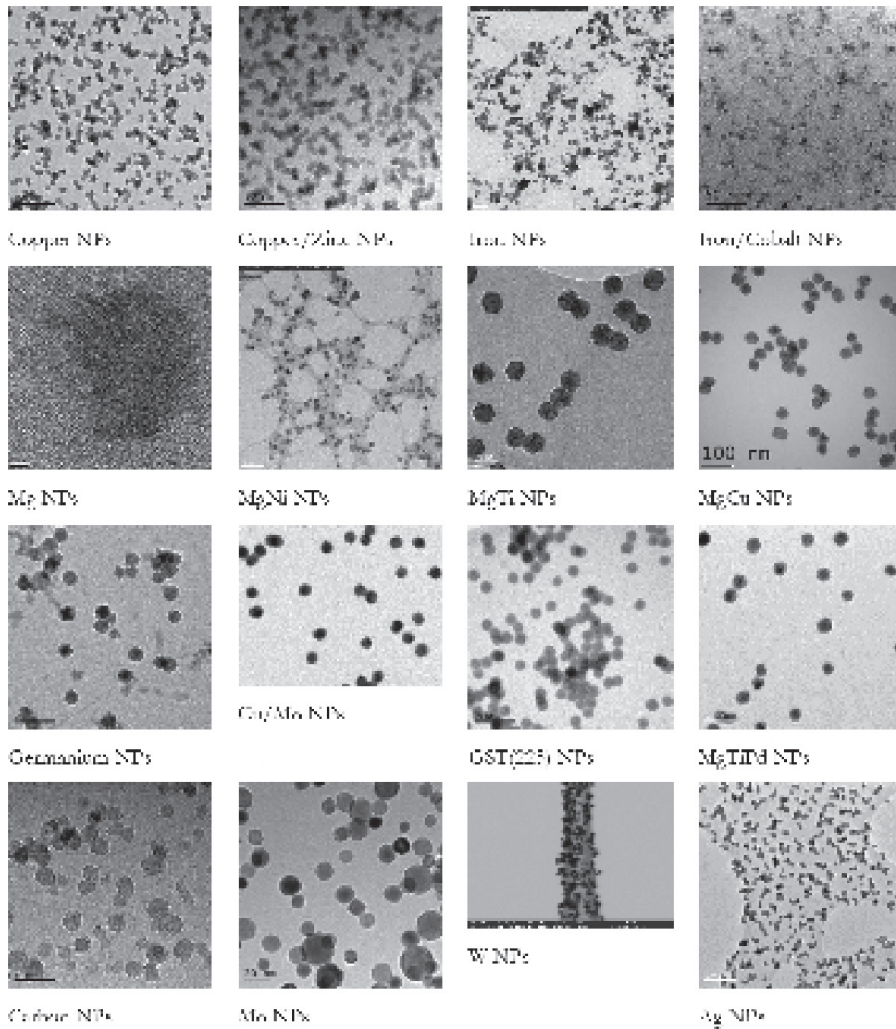
Table 2-2 TEM micrographs of some NPs systems that have been produced with the Mantis nanocluster source since it has been in operation from 2010 till present.
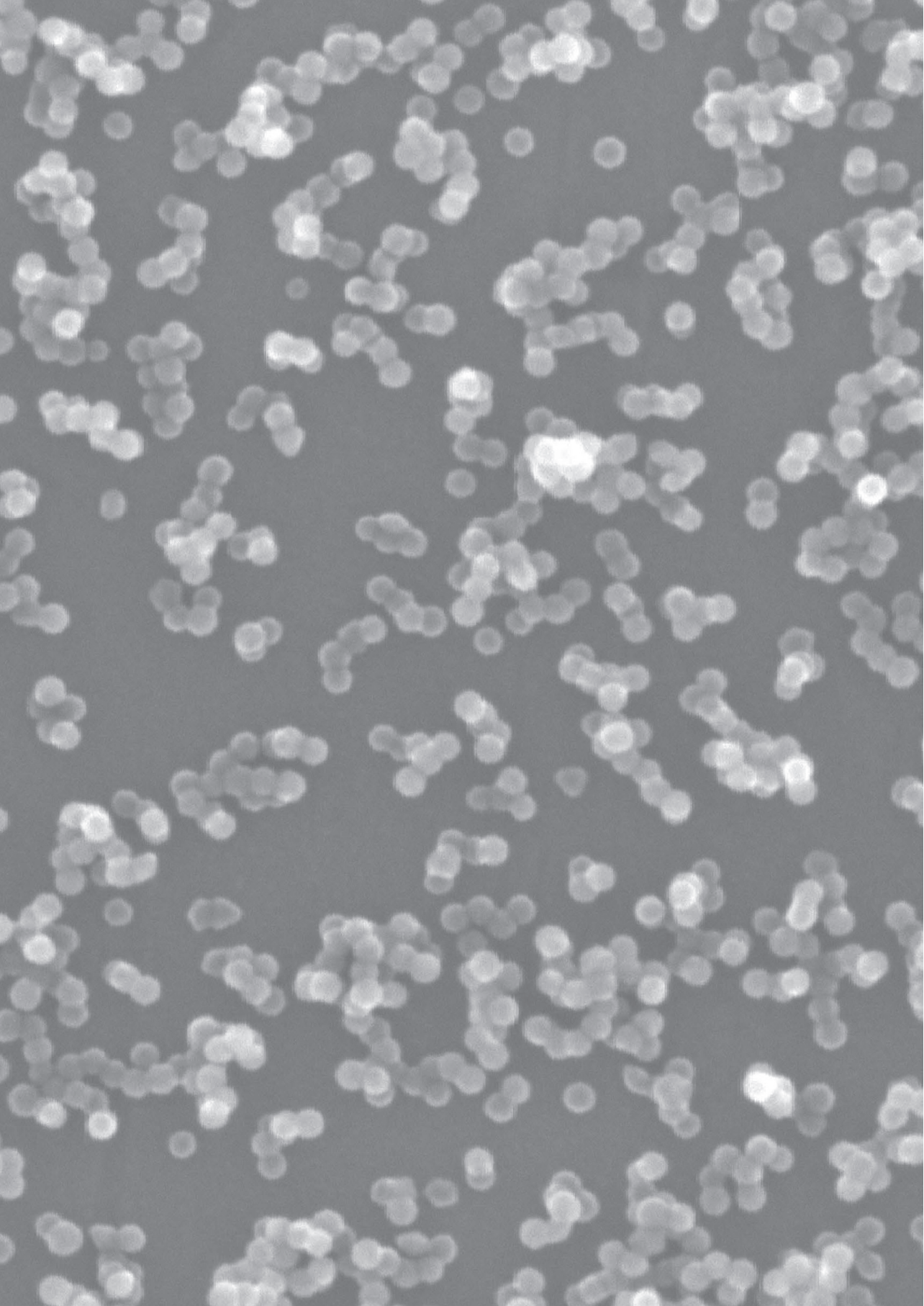
Chapter 3
How to characterize nanoparticles and surface wetting properties

3.1 Introduction

This chapter summarizes the experimental methods and techniques used to characterize the gas phase synthesized nanoparticles and nano-structured materials made from them. Being as small as a nanometer means they cannot be seen anymore with the naked eye, and one needs a microscope to observe them[1,2].

The word microscope stems from the Ancient Greek: μικρός, mikrós, "small" and σκοπεῖν, skopeîn, "to look" or "see"[3] "With a microscope, you often see the surface of things. It magnifies them but does not show you reality. It makes things seem higher and wider. But do not suppose you see things in themselves."Feng-Shen Yin-Te (1771 – 1810)[4].

Nanoparticles are entities in-between single atoms and bulk material and are smaller, in at least one direction, less than 50nm (<50.10^{-9} meter). It makes it necessary to use some form of magnification to see or characterize them, but with a few exceptions. It is not needed for the wetting properties (chapters 6 and 7, and 8), which links the macroscopic behavior to nanoscale size properties. The same holds for Plasmonic phenomena, which can be analyzed without a microscope. Otherwise, the main techniques to achieve the needed magnification are Atomic Force, Optical, Scanning, and Transmission Electron Microscopy. They are explained in more detail in the next sections.

3.2 Optical microscopy

A modern (visible) light microscope (often abbreviated to LM) has a maximum magnification of about 1200x and enables the eye to resolve objects separated by about 0.3 mm. The resolution of the human eye is ≈ 0.1 mm. The apparent resolution of the eye for a magnified object is: R ≈ 0.1 mm/ Magnification, see Table 3-1.

Magnification	Resolvable distance
100x	1 μm (10,000 Å)
1,000x	0. 1 μm (1,000 Å)
10,000x	0,01 μm (100 Å)
1,000,000x	0.0001 μm (1Å)

Table 3-1 Magnification and the corresponding resolvable distances

3.3 Magnifying an object

As seen in Figure 3-1, the tin lens formula, the magnifying of an object is achieved by placing a lens in between the object and the viewing point, the eye in this instance.

$$\frac{1}{f} = \frac{1}{d0} + \frac{1}{d1}; \; \boldsymbol{Magnification} = \frac{d1}{d0} \quad \textbf{(3.1)}$$
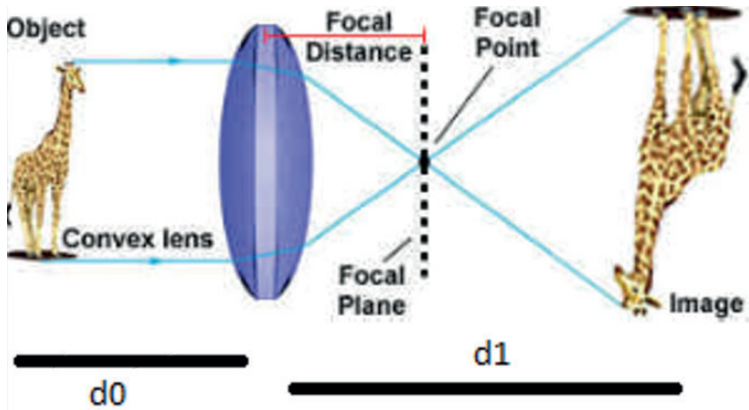
Figure 3-1 The simple/single-lens projection.

3.4 The difference between magnification and resolution.

Magnification is the apparent enlargement of an object, whereas resolution is the capability of distinguishing the individual parts of an object.
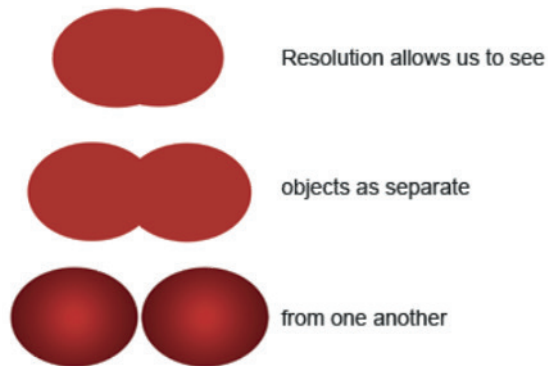
Figure 3-2 The meaning of resolution.

From equation 3.1, the magnification can go to infinity with ease. Many scientists and inventors tried to achieve higher magnifications and more resolution, soon to realized that the microscope's resolving power is limited by the quality of the lenses and the wavelength of the light used for illumination. It was impossible to resolve points in the object closer to a few hundred nanometers with visible light. It was the Dutch Antoni van Leeuwenhoek[5] (1632–1723) who made the single-lens microscope famous, having an average magnification in the order of 100 times.

Figure 3-3(a) Replica of one of the 550 light microscopes made by Antony van Leeuwenhoek.
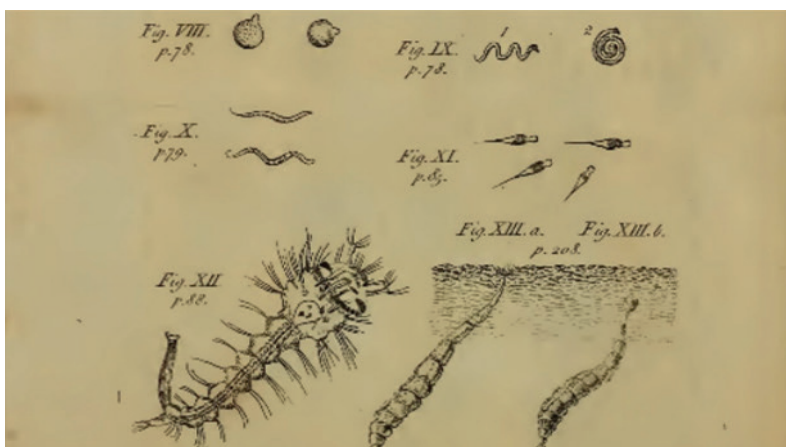
Figure 3-3(b) Drawings of artifacts imaged by the light microscopes made by Antony van Leeuwenhoek.

In a way, there is a lot of resemblance in how all the different microscopes operate, as can be seen in the following diagram (source wikipedia[2])
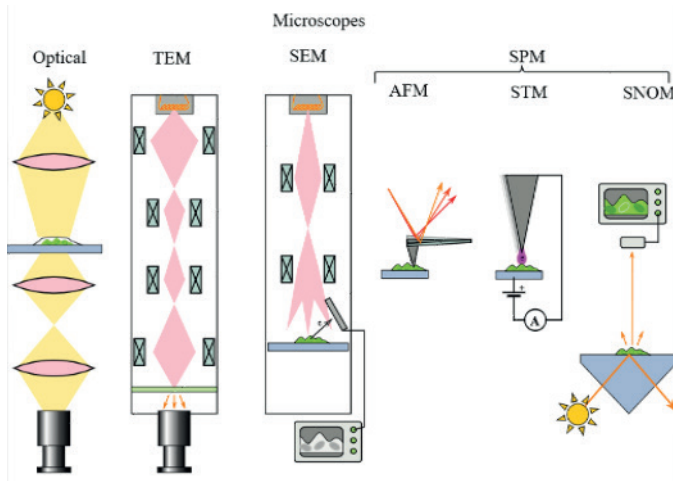
Figure 3-4 Schematics of the beam path in the different microscope's Light microscope, TEM, SEM, and SPM.

The used light source and the way of the optical path make up the name of the technique and the resulting image and image quality.
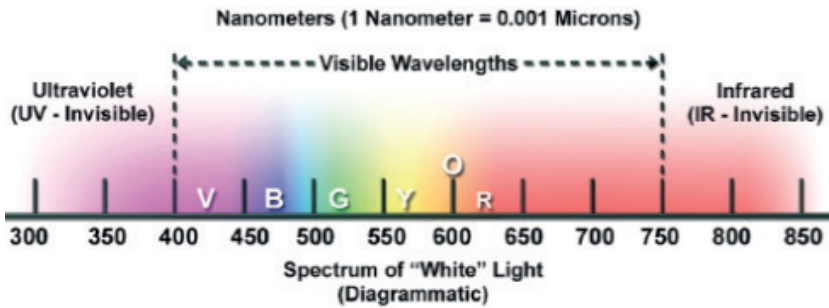
Figure 3-5 The photons from sunlight and the tungsten lightbulb have a visible range from 400 nm to 750 nm that can still be detected with the normal eye.

The maximum achievable resolution r (the so-called Raileigh criterion according to Abbe) is:

$$r = \frac{\lambda}{2\,NA} \quad (3.2)$$

In this equation,

λ = the wavelength,

NA. is the numerical aperture

the numerical aperture (N.A.) = n sin(μ)

n is the index of refraction of the material.

Sin(μ) is the sine of half the opening angle as determined by the aperture of the objective lens or this lens itself.In practice, the smallest object illuminated with white light and still visible with the naked eye and enlarged with a good microscope is ≈ 1200X times.
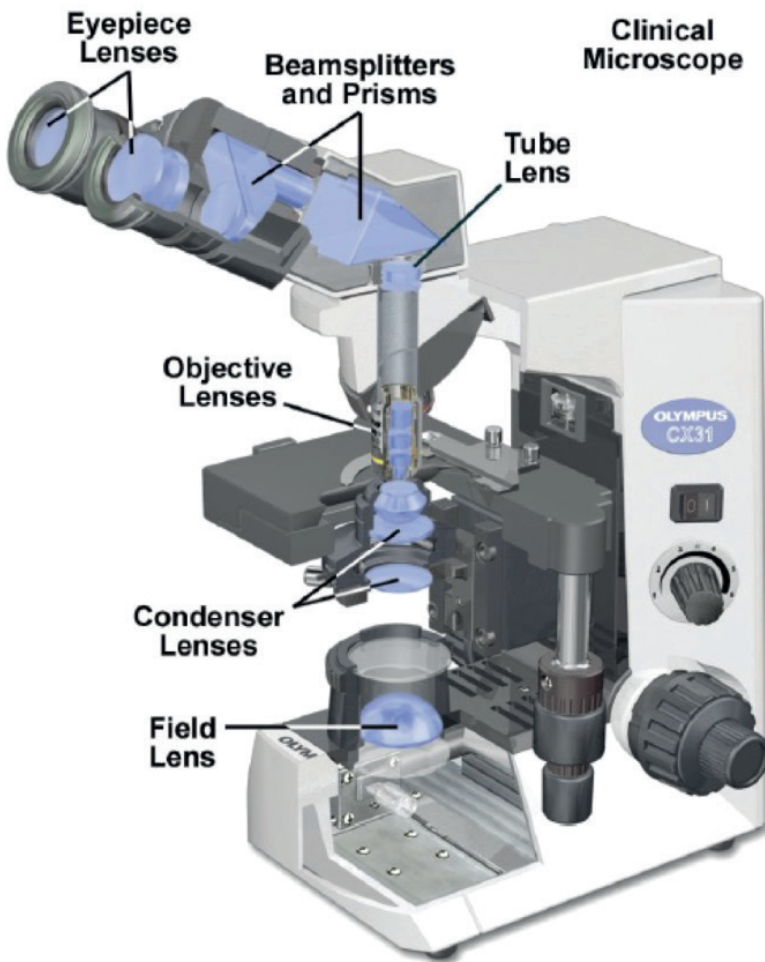
Figure 3-6 Schematics of a modern Light microscope.

However, even an excellent visible light microscope is nowhere near as good enough to see nanosized NPs. Imaging nanosized features require a smaller wavelength, which can be achieved using an accelerated electron beam that behaves like a wave. Yet electrons cannot be seen with the human eye. An electron-detector is needed for electrons to be made visible in SEM and TEM. In the past this was a phosphor screen or phosphor coating where electrons are converted into 'green' photons.

It was Broglie who suggested that particles can exhibit wave properties. The wavelength λ of electrons (Broglie equation [6]) and its energy relates as:

$$\lambda = h/p \quad \textbf{(3.3)}$$

where λ is the wavelength, h is Planck's constant, p is momentum, which is the classical sense it the product of the mass (m) of a particle and its velocity (v). However, note that the electrons can be accelerated (in TEM) to such high speeds that we must account for relativistic effects which can be readily included in the formula for momentum p:

$$p = mv / \sqrt{1 - \left(\frac{v}{c}\right)^2}$$

where c is the speed of light (in vacuum).

3.5 Resolution and wavelength

When a wave passes through an aperture,(or lens) the wave is diffracted by the edges of the aperture (or lens). The (even) perfectly shaped lens will be limited in its resolving power by it's diffraction limit as expressed by Eq. (3.2). This is why a high-quality optical lens is referred to as a diffraction-limited lens. The amount of diffraction is a function of the size of the aperture (or lens) and the wavelength of the light, with larger apertures or shorter wavelengths permitting better resolution (Eq. (3.2)).

The wavelength of an electron in a TEM is, for an accelerting voltage of the order of 200 kV, only a few picometers (1 pm = 10^{-12} m), more than 100.000 times shorter than the wavelength of visible light (400-700 nm). Still, and unfortunately, the magnetic lenses used in electron microscopes do not approach diffraction-limited performance. Therefore electron microscopes have for a long time, till the introduction of aberration correctors, not been able to take full advantage of the shorter wavelength of the electron. Ultimately, the resolving power of an electron microscope is determined by a combination of beam voltage, aperture size, lens aberrations, mechanical vibrations, and, particularly important, sample quality.

Energy kV	Wavelength nm
30	$6.98.10^{-3}$
100	$3.70.10^{-3}$
300	$1.968. 10^{-3}$

Table 3-2 Energy of the electrons in kV and the corresponding wavelength in nm

3.6   SEM/S(T)EM

To "see" electrons, one needs an electron microscope. It is not completely clear who first proposed the principle of scanning the surface of a specimen with a finely focused electron beam to produce an image of the surface. The first published description appeared in 1935 in a paper by the German physicist Dr.Max Knoll[7].(who was the co-worker of Prof. Ernst Ruska, who is known as the inventor of the TEM a few years earlier, where actually Max Knoll did most of the construction.)

Although another German physicist Dr. Manfred von Ardenne performed some experiments with what could be called a scanning electron microscope (usually abbreviated to SEM) in 1937.

It was in 1942 that three Americans, D. Zworykin, Dr.Hillier and Dr.Snijder first described a true SEM with a resolving power of 50 nm and a magnification of 8000x. Nowadays SEM's can have a resolving power of 1 nm and can magnify over 1.000 000x. Figure 3-14 compares light microscopy (using transmitted or reflected light) with TEM and SEM.

A combination of the principles used in both TEM and SEM, usually referred to as scanning transmission electron microscopy (STEM), was first described in 1938 by Dr Manfred von Ardenne. It is not known what the resolving power of this instrument was.

The first commercial instrument in which the techniques were combined was a Philips EM200 equipped with a STEM unit developed by Dr. Ong of Philips Electronic Instruments in the U.S.A. (1969). At that time, the resolving power was 25 nm and the magnification was 100.000x. Modern TEMs equipped with a STEM facility can resolve better than 1 nm at magnifications of up to 2 million times. After the introduction of aberration correctors (and high brightness electron sources) the resolving power even entered the sub-Angstrom regime.
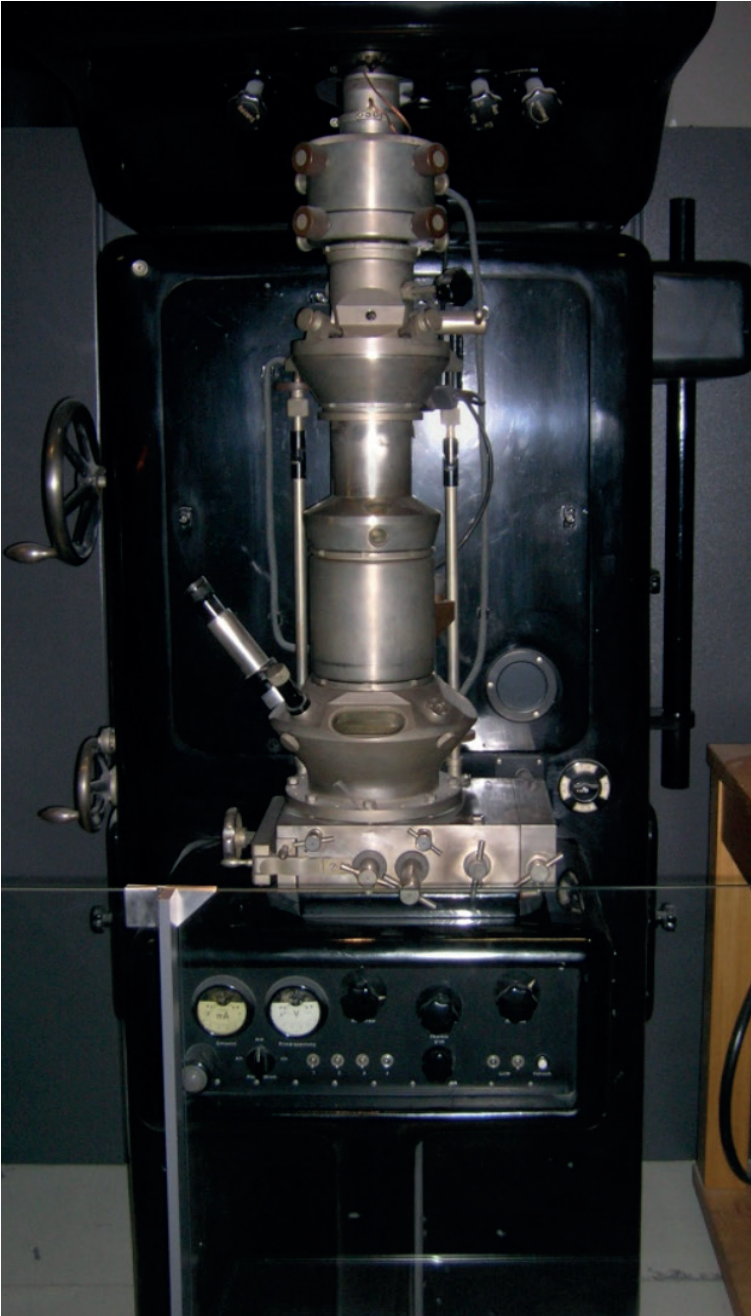
Figure 3-7 First electron microscope with resolving power higher than that of a light microscope Ernst Ruska, Berlin 1933. Replica by Ernst Ruska, 1980.
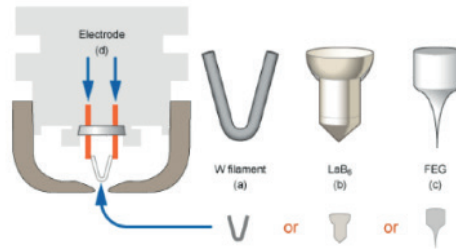
Figure 3-8 The source of electrons, including the Wehnelt cap with three different types of electron guns (source wikipedia).

Figure 3-9 Thermo Fisher (Fei) NovaNanosem 650.
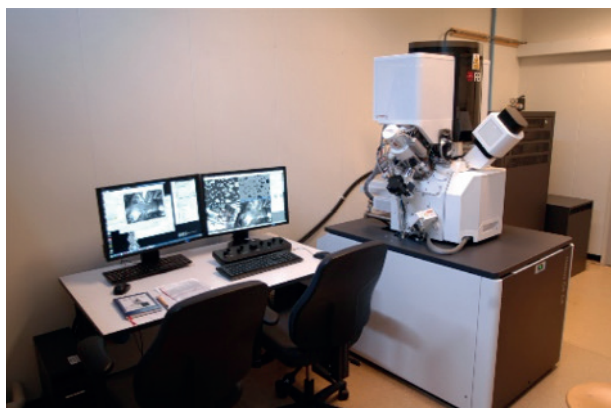
Figure 3-10 Thermo Fisher (Fei) Helios G4 CX.

3.7 Contrast mechanisms in S(T)EM

Electrons interact with matter. An atom consists of a nucleus (with protons and neutrons) surrounded by several orbiting electrons. For neutral atoms, the number of electrons is equal to the number of protons in the nucleus and is known as the atomic number of the atom (see periodic table by Dmitri Mendeleev). The incoming electrons in a beam can interact with the nucleus and be backscattered with virtually the same energy. Or they can interact with the orbiting electrons of sample atoms in a variety of ways, giving up some of their energy in the process. Each type of interaction potentially constitutes a signal that carries information about the sample. For instance, the most frequent interaction is the ejection of an electron from the atom with relatively low energy, a few eV. If this occurs near the sample surface, the liberated electron may escape and can be detected as a *secondary electrons*. Other signals include characteristic X-rays, cathodoluminescence, absorbed current and more, each carrying a specific type of information, see Figures 3-11 and 3-12.
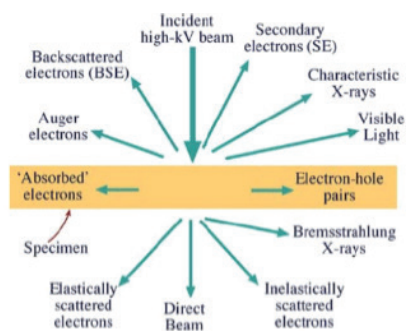
Figure 3-11 Electron specimen interactions (thin sample < 40nm).
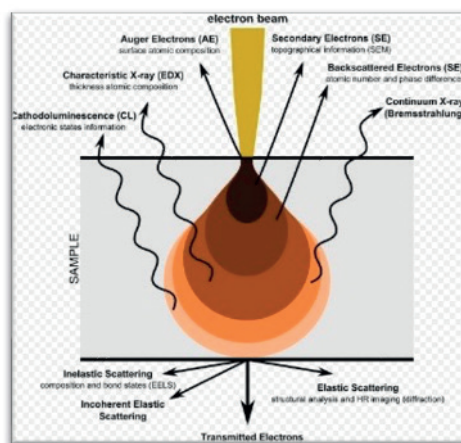
Figure 3-12 Electron specimen interactions in bulk material (>3 μm).

The most important differences and similarities between a TEM and SEM are:

- Rather than the broad static beam used in TEM, the SEM beam is focused into a fine probe and scanned line by line over the sample surface in a rectangular raster pattern.
- The accelerating voltages in a SEM are much lower than in TEM because it is no longer necessary to penetrate through the specimen. On the contrary, at low voltages there is more surface sensitivity and also charging of the sample can be reduced in SEM.

- In a SEM, the energy of the electrons ranges from 50 to 30000 Volts, whereas in TEMs it is tradionally in the range 100 – 400 kV. However, with aberration correctors it is now also extending down to even 30 or 20 kV.
- Sample preparation for SEM specimens is a lot easier because the samples do not need to be thin (electron transparent) which greatly simplifies specimen preparation. It is helpful for SEM if the sample is conductive.
- The interactions between the primary electrons and sample atoms are similar for TEM and SEM, but certain interactions can be more or less dominant depending on sample thickness and accelerating voltage.
- Secondary electrons are also present in TEM, but are mostly not detected, whereas are the dominant signal in SEM.
- Backscattered electrons (BSE) also constitute a dominant signal in SEM, but are irrelevant for TEM.
- In both techniques (SEM & TEM) the specimen emits X-rays.
- Electrons are absorbed by the specimen in SEM and this effect should be negligible in a good TEM specimen.
- Both TEM and SEM specimens sometimes emit photons of visible light (cathodoluminescence).
- If the sample is very thin, the SEM may be operated in STEM mode with a detector located below the sample to collect the transmitted electrons.

All these phenomena are interrelated, and all of them depend to some extent on the topography, the atomic number and the chemical state of the specimen. The most commonly imaged signals in SEM are thus SE and BSE. In special cases, the sample can be analyzed in low vacuum mode. In this mode there is no need to coat non-conducting samples. This imaging mode uses special detectors named HELIX and LVD which are available in the FEI Nova NanoSEM 650

The detected SEs; because of their very low energies, can escape the sample to be detected only if they originate very close to the sample surface. This gives SE images high spatial resolution and strong topographic contrast. The BSE imaged signal is used for its strong atomic number contrast and the characteristic X-rays are used in the SEM for elemental mappings and microanalysis.

3.8   TEM/(S)TEM

The transmission electron microscope can be compared with a slide projector (Fig. 3-13)
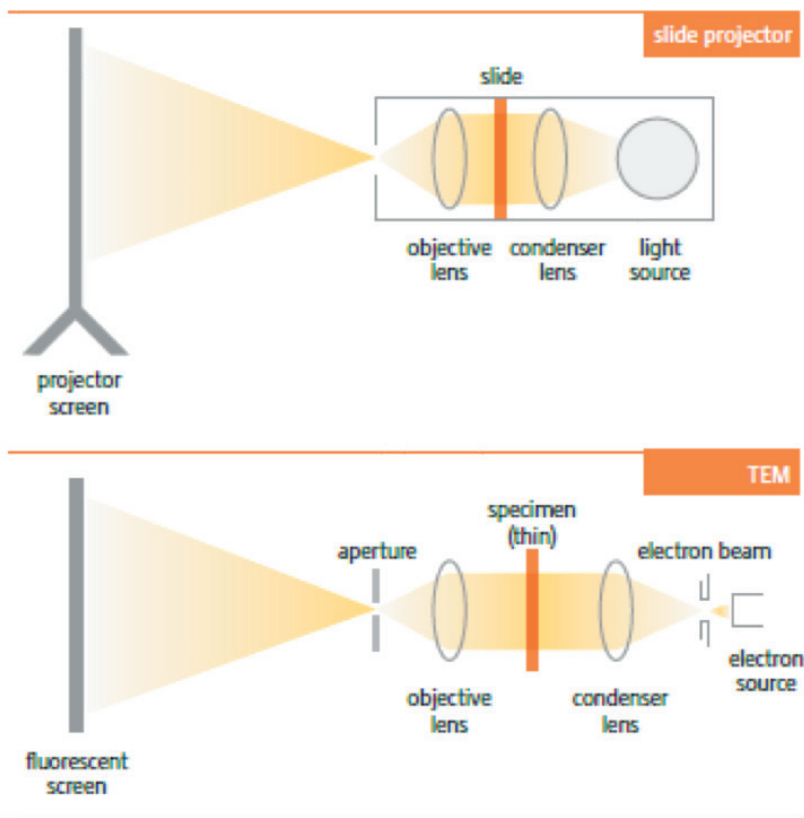
Figure 3-13 The beam path in a slide projector compared to the beam path in the TEM.

In the slide projector, the light is made into a parallel beam by the condenser lens, this passes through the slide (sample/object) and is then focused as an enlarged image onto the screen by the objective lens. In the electron microscope, the light source is replaced by an electron source (e.g. tungsten or LaB6 filament heated in vacuum), electromagnetic lenses replace the glass lenses and the projection screen is replaced by a fluorescent screen which emits light when struck by electrons. The whole trajectory from source to screen is under vacuum and the specimen (object) has to be very thin to allow the electrons to penetrate it. The first EM microscope used two magnetic lenses, and three years later, a third lens was added and demonstrated a resolution of 100 nm, three times as good as that of a light microscope optimized after a few hundred years of development.

light microscope

objective lens
light beam
specimen
light source

TEM

electron source
first condenser lens
second condenser lens
condenser aperture
objective condenser lens
objective aperture
minicondenser lens
specimen (thin)
selected area aperture
objective imaging lens
diffraction lens
intermediate lens
first projector lens
second projector lens
projection chamber
fluorescent screen

SEM

electron source
anode
gun align coils
lens 1
lens 2
electron beam
scan & stig coils
lens 3
collector system
secondary electrons
electron beam impact area
specimen (thick)
vacuum
turbo/diff pump
roughing line

FIB

Ga+ LMI source
suppresser
extractor
lens 1
octopole alignment
blanking plates
blanking aperture
scan & stig octopoles
lens 2
continuous dinode detector
secondary electrons or ions
ion beam impact area
specimen (thick)
turbo/diff pump
roughing line

Figure 3-14 Schematics of the common types of microscopes.

Figure 3-15 Ernst Ruska at the University of Berlin watching (on the left)), while Max Knoll (on the right) did most of the construction.

Figure 3-16 NMI JEOL 2010 LaB6 (S)TEM.

Figure 3-17 ZIAM/CogniGron Thermo Fisher (FEI) ThemisZ FEG (S)TEM.

Figure 3-18 ZIAM/CogniGron Thermo Fisher (FEI) ThemisZ FEG (S)TEM.

3.9   Contrast mechanisms in TEM

The image contrast mechanisms in the TEM are (way) more complicated than those in the SEM because of the wave character of the plane wave interacting with the specimen. Contrast can arise from position-to-position differences in the thickness or density ("mass-thickness contrast"), atomic number Z contrast (atomic number), crystal structure or orientation ("crystallographic contrast" or "diffraction contrast"), the slight quantum-mechanical phase shifts those individual atoms produce in electrons that pass through them ("phase contrast"), the energy lost by electrons on passing through the sample ("EELS spectrum imaging") and more. Each mechanism shows a different kind of information, depending not only on the contrast mechanism but on how the microscope is used, the settings of lenses, apertures, and detectors. Therefore, a TEM is capable of returning an variety of nanometer- and atomic-resolution information, in ideal cases revealing not only where all the atoms are, but also what kinds of atoms they are and how they are bonded to each other. For an extensive explanation of the various contrast mechanism in the TEM I would advise further reading the seminal bookwork of David B. Williams and C. Barry Carter[8]. A Textbook for Materials Science. One way to overcome the wave character in TEM mode is to switch to STEM mode and detect electrons scattered to high angles (the so-called high angle annular dark field, HAADF mode) provided this option is available. The recently installed Thermo Fisher (FEI) ThemisZ is now of the best microscope of its time making the image interpretations a lot easier. Besides a resolution down to about 50 pm !!, the HAADF detector makes the images interpretation as easy as BSE modes in the SEM (a small side-note, the HR-STEM images of the Ag NPs in chapter 8 were the first images recorded with this new state of the art microscope)

3.10   EDX in SEM and (S)TEM

EDX analysis stands for Energy Dispersive X-ray analysis. It is sometimes referred to also as EDS or EDAX analysis. It is a technique used to identify the elemental composition of the specimen or an area of interest. The EDX analysis system works as an integrated feature of an SEM, and cannot operate on its own without the latter. During EDX Analysis, the specimen is bombarded with an electron beam inside the SEM. The bombarding electrons collide with the specimen atoms' own electrons, knocking some of them off/out of orbit. This position vacated by an ejected inner shell electron is filled by a higher-energy electron from an outer shell. In doing so, it releases its excess energy by emitting an X-ray photon
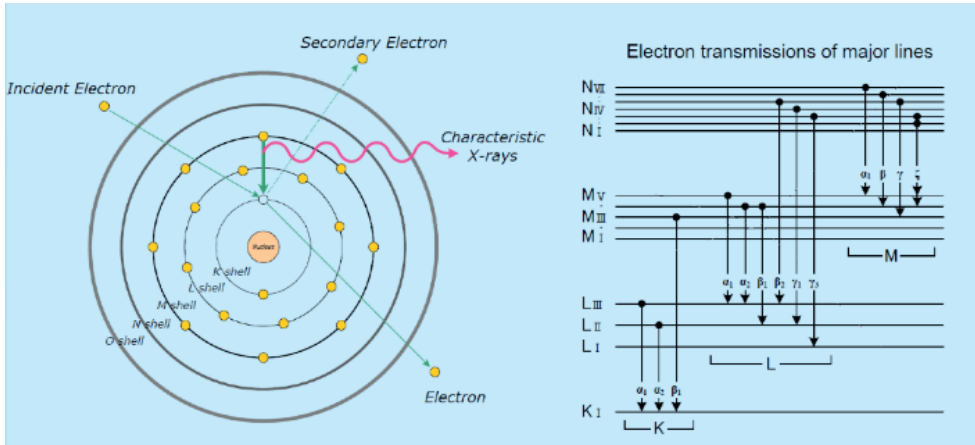
Figure 3-19 Characteristic X-rays.

The amount of energy released by the transferring electron depends on which shell it is transferring from and which shell it is transferring to. Furthermore, the atom of every element releases X-rays with unique amounts of energy during the transferring process. Thus, by measuring the amounts of energy present in the X-rays being released by a specimen during electron beam bombardment, the atom's identity from which the X-ray was emitted can be matched.

The output of an EDX analysis is an EDX spectrum (as shown in figure 3-21 on the left). The EDX spectrum is just a plot of how frequently an X-ray is received for each energy level. An EDX spectrum normally displays peaks corresponding to the energy levels for which the most X-rays had been received. Each of these peaks are unique to an atom, and therefore corresponds to a single element. The higher the intensity of a peak in a spectrum, the more concentrated the element is in the specimen.
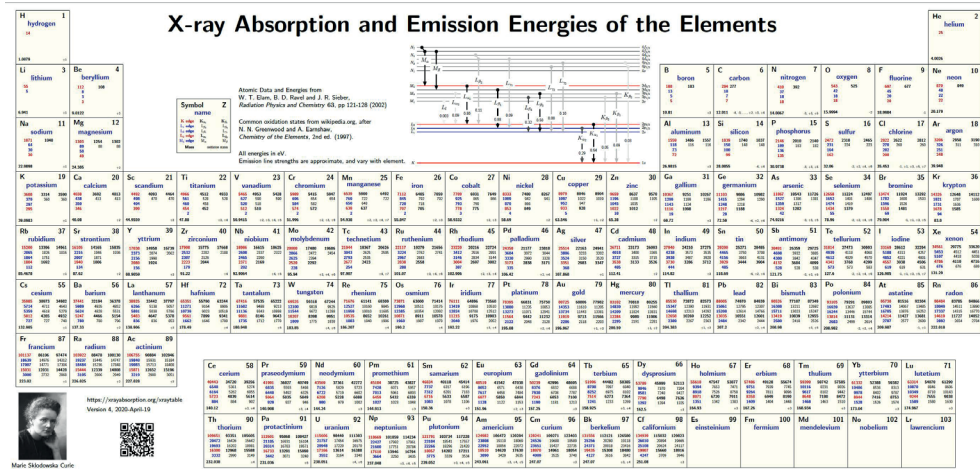
Figure 3-20 Dmitri Mendeleev periodic table with all the EDX energies from all the possible shell transitions.

An EDX spectrum plot not only identifies the element corresponding to each of its peaks, but the type of X-ray to which it corresponds as well. For example, a peak corresponding to the amount of energy possessed by X-rays emitted by an electron in the L-shell going down to the K-shell is identified as a K-Alpha peak. The peak corresponding to X-rays emitted by M-shell electrons going to the K-shell is identified as a K-Beta peak.
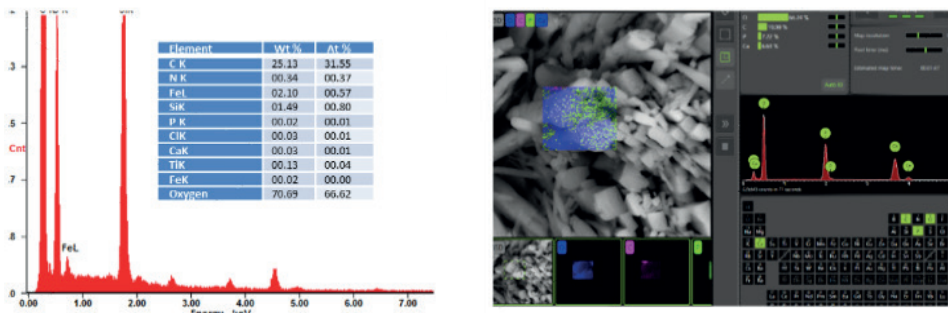
Figure 3-21 EDX spectrum and mapping outputs from different SEM/S(T)EM/EDX systems.

3.11 Atomic Force Microscopy

Whereas the TEM and STEM technique was found not to be suited as the application in the study of surfaces. The AFM definitely has. Since the introduction of the Nobel Prize-winning scanning tunneling microscope (STM) and then the invention of the atomic force microscopy (AFM) from the landmark publication by G. Binnig, C.F. Quate, and Ch. Gerber, the field of scanning probe microscopy has exploded.[9]
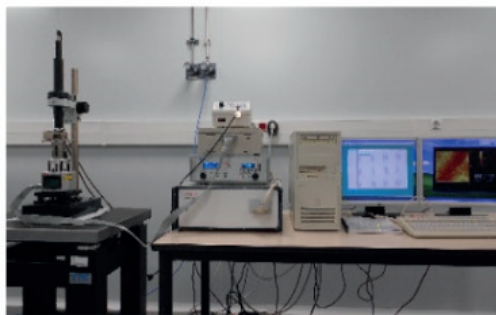
Figure 3-22 NMI AFM setup.
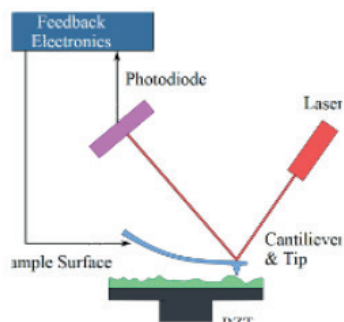
Figure 3-23 Schematic AFM presentation.

Topography imaging alone does not always provide the answers that researchers need and the surface topology often does not correlate to the material properties. For these reasons, advanced imaging modes have been developed to provide quantitative data on a variety of surfaces. Now, many material properties can be determined with AFM techniques, including friction, electrical forces, capacitance, magnetic forces, conductivity, viscoelasticity, surface potential, and resistance [REF!].

3.12 What about contact angles

The contact angle (also referred to as a wetting angle) is a measure of the ability of a liquid to wet the surface of a solid. The shape that a drop takes on a surface depends on the surface tension of the fluid and the nature of the surface. Therefore, a contact angle refers to a method of calculating surface free energy by evaluating the interface of a liquid and a solid surface. The angle formed between the surface and the line tangent to the edge of the drop of the water is called the contact angle. A contact angle[10] is thus giving us an indication of how well (or how poorly) a liquid will spread over a surface. A contact angle can be large or small, depending on the physical properties of the materials being investigated. Figure 3-24 shows three different droplets on a surface. The left-most droplet has a large contact angle, as it does not spread over the solid surface. The right-

most droplet has a low contact angle, as it has spread well. This spreading is known as 'wetting', and a droplet either 'wets' or 'dewets' when deposited on a surface.

Figure 3-24 A varying contact angle.[10]

Figure 3-26 shows a 2D cross-section of a droplet on a solid surface. Locate the point at which the droplet outline intersects the solid surface. The angle between the droplet outline and the solid surface is the contact angle.
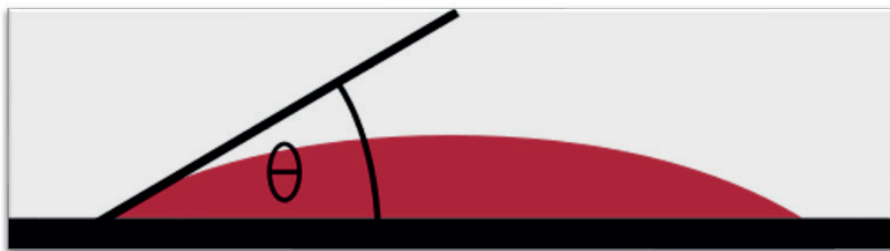
Figure 3-25 A contact angle.[10]

3.13   Surface tension

The surface tension of a droplet is determined by the interactions between its constituent atoms and/or molecules. The molecules in a droplet of liquid are shown in Figure 3-26. In the bulk of the droplet, intermolecular forces act upon a molecule from all sides equally. However, at the surface of the droplet, there is an absence of liquid molecules on the external side.
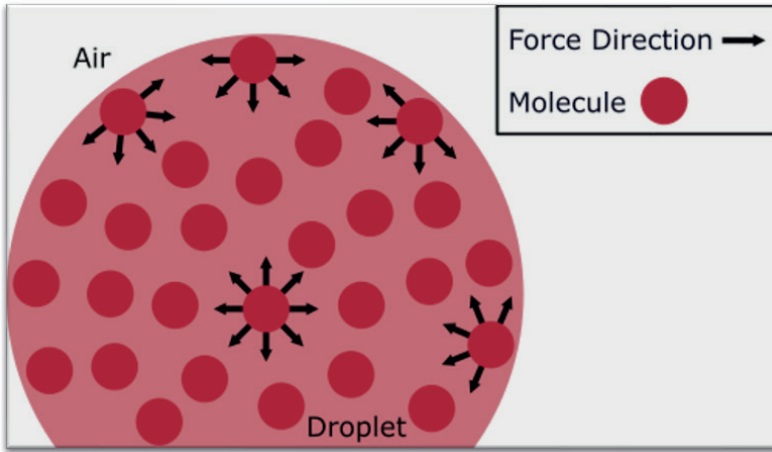
Figure 3-26 Surface tension of a droplet.[10]

The molecules at the surface are more strongly bound to each other than the molecules in the bulk, as they are not being pulled from all sides. This means that it is more difficult for an object to penetrate the surface than it is for an object to move within the bulk once submerged.

3.14 Balanced forces

There are three boundaries to consider when a droplet is in contact with a solid surface: the solid-liquid, the liquid-gas,(usually air, but in contact with liquid it can better be called vapor) and the solid-vapor. The three boundaries meet at the so-called TriplePoint (although it is actually a contact line, see Figure 3.27 left). Figure 3.27 shows a force diagram at the tiple point. The three arrows represent the forces exerted by the surface tensions at three interfaces: liquid-solid, liquid-vapor, and solid-vapor.
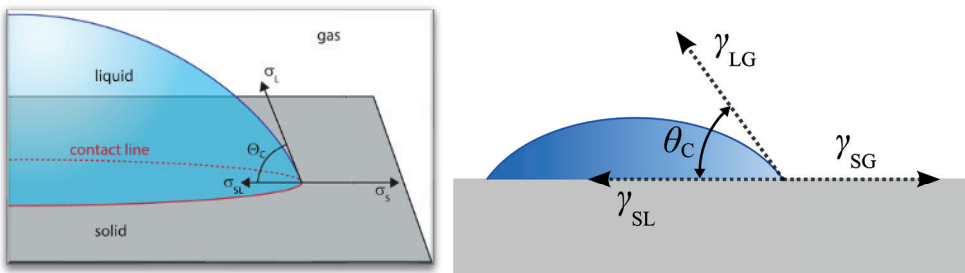
Figure 3-27 Contact angle forces.

Each force is pulling away from the equilibrium point, so if the droplet is in equilibrium, then the forces are balanced and can be described by the following Equation:[11,12]

$$\gamma_{sv} = \gamma_{ls} + \gamma_{lv} \cos\theta \quad \text{(3.1)}$$

Where $\cos\theta$ gives the x-component of the liquid-vapor surface tension, this can be re-arranged to give the well know Young equation:[11,12]

$$\cos\theta = \frac{\gamma_{sv} - \gamma_{ls}}{\gamma_{lv}} \quad \text{(3.2)}$$

This Young equation provides some useful information:

If $\gamma_{sv} < \gamma_{ls}$, then $\cos\theta$ will be negative, and θ is, therefore, < 90 (and the water droplet wets the surface). This can occur with a high surface-energy solid (such as a metal), or a low surface-tension liquid.

If $\gamma_{sv} > \gamma_{ls}$, $\cos\theta$ is positive, and θ is > 90 (and the water droplet dewets the surface). This can occur with a low surface-energy solid, or a high surface-tension liquid;(such as water).

One more step is needed to equate surface energy density (units J/m²) with surface tension (units N/m):

$$\text{Surface Energy Density} = \frac{Energy}{Area} = \frac{J}{m^2}$$

$$\text{Energy = Force x Distance} = Nm \quad \text{(3.3)}$$

$$\text{Surface Energy Density} = \frac{Nm}{m^2} = \frac{N}{m}$$
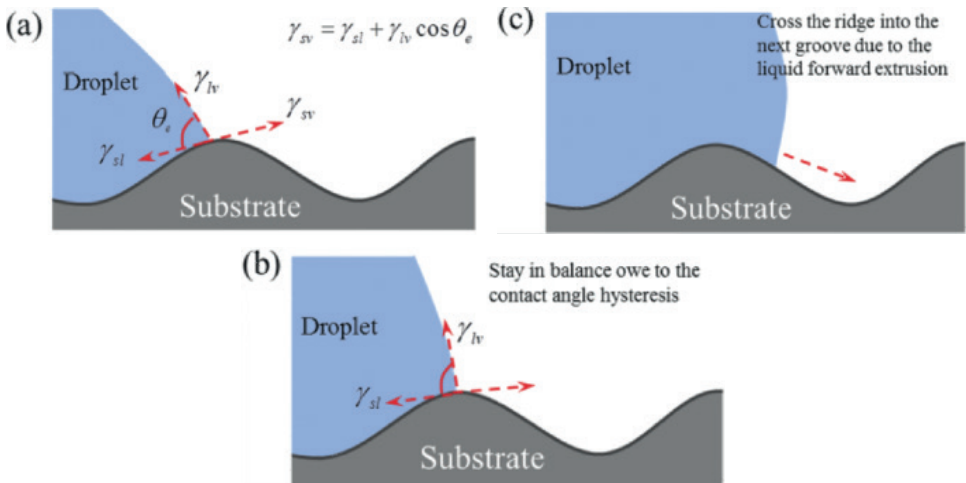
Figure 3-28 Droplet propagation in the lateral direction on sinusoidal surface.

Fig 3-28 is a schematic diagram of forces acting on a water droplet propagating in the lateral direction on a sinusoidal surface. In image (a), the water triple line stops at the front of the ridge. In image (b) the contact line stays still while the contact angle increases due to CA hysteresis. In the last image(c), the water/liquid crosses the ridge into the next groove.

3.15   Wetting measurements "DataPhysics OCA20™"

The OCA Optical contact angle measuring and contour analysis systems are made by https://www.dataphysics-instruments.com/DataPhysics.

In specific the OCA 20 system was used in comibination with the SCA 20 software.:
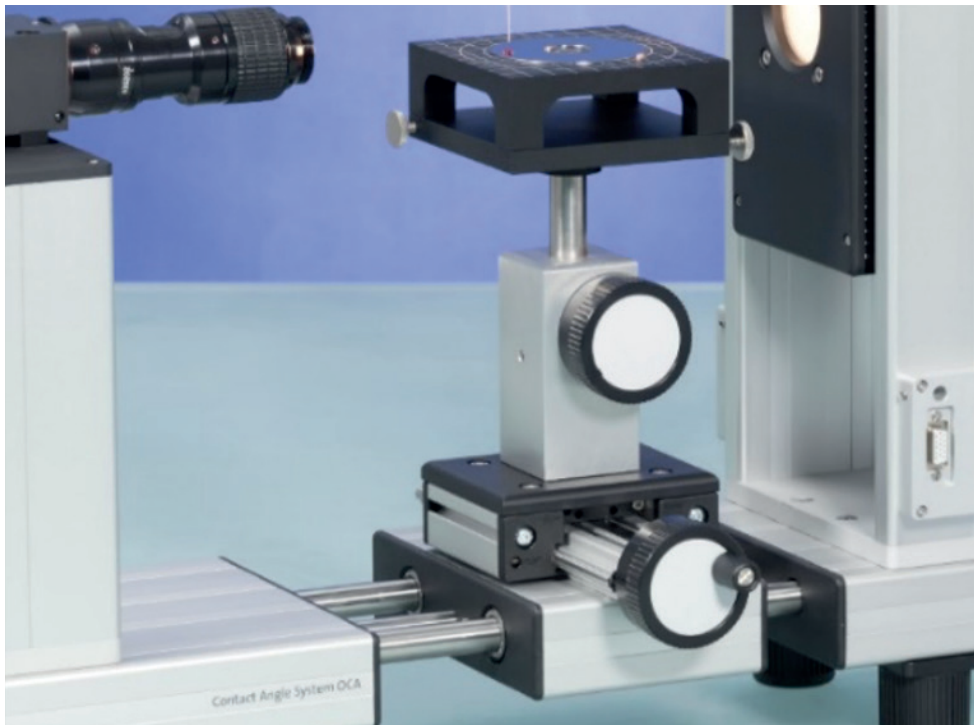
Figure 3-29 DataPhysics OCA20™ system.

The optical contact angle (OCA) measuring and contour analysis systems of the OCA20 is a high precision optical measuring device for the measurement of interfacial parameters and phenomena.
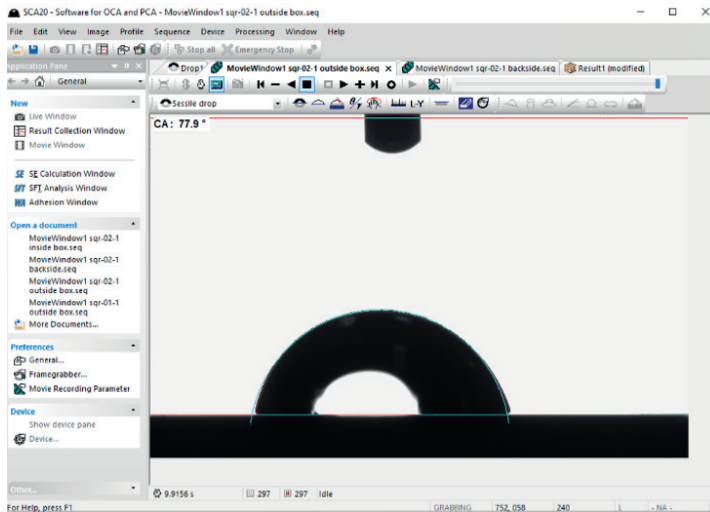
Figure 3-30 DataPhysics SCA20™ and SCA21™ software interface.

The OCA20 system is supplied with the SCA 20 Software which is divided into a few available modules:

- SCA automation dialogue with visual drop positioning.
- Automation dialogue with visual drop positioning.
- The SCA 20 module is the base software module that enables the measurement of contact angles.
- Measurement and presentation of the static contact angle on plane, convex and concave surfaces according to the sessile drop and the captive drop method.
- It uses automatic baseline detection on flat and curved surfaces.
- The needle-in-drop method measures dynamic contact angles (advancing and receding angles, contact angle hysteresis).
- The tilting method SCA 21.

3.16 Surface energy

With the SCA 21 software module, the surface energy of solids can be determined by measuring multiple contact angles with different liquids (Zisman plot). The main features are: the determination of the surface energy of solids as well as of its components (e.g., dispersive, polar, and hydrogen bond parts, acid and base portions) according to nine different theories of calculation and representation of wetting envelopes and work of adhesion/contact angle diagram.

3.17   References

1   M.W. Davidson and M. Abramowitz, in *Encycl. Imaging Sci. Technol.* (American Cancer Society, 2002).

2   Wikipedia (2021).https://en.wikipedia.org/wiki/Microscope

3   Wikipedia (2019).https://en.wikipedia.org/wiki/Microscope

4   Biol. Electron Microsc. https://www.biologicalelectronmicroscopy.com/

5   Wikipedia (2021).https://en.wikipedia.org/wiki/Antonie_van_Leeuwenhoek

6   Wikipedia (2017).https://en.wikipedia.org/wiki/Louis_de_Broglie

7   Wikipedia (2021).https://en.wikipedia.org/wiki/Max_Knoll

8   D.B. Williams and C.B. Carter, in *Transm. Electron Microsc. Textb. Mater. Sci.*, edited by D.B. Williams and C.B. Carter (Springer US, Boston, MA, 1996), pp. 349–366.

9   G. Binnig, C.F. Quate, and Ch. Gerber, Phys. Rev. Lett. **56**, 930 (1986).

10 Ossila,https://www.ossila.com/pages/contact-angle-theory-measurement?_pos=2&_sid=8f478e510&_ss=r#What-is-a-contact-angle

11 (2019).

12 T. Young, Philos. Trans. R. Soc. Lond. **95**, 65 (1805).

3
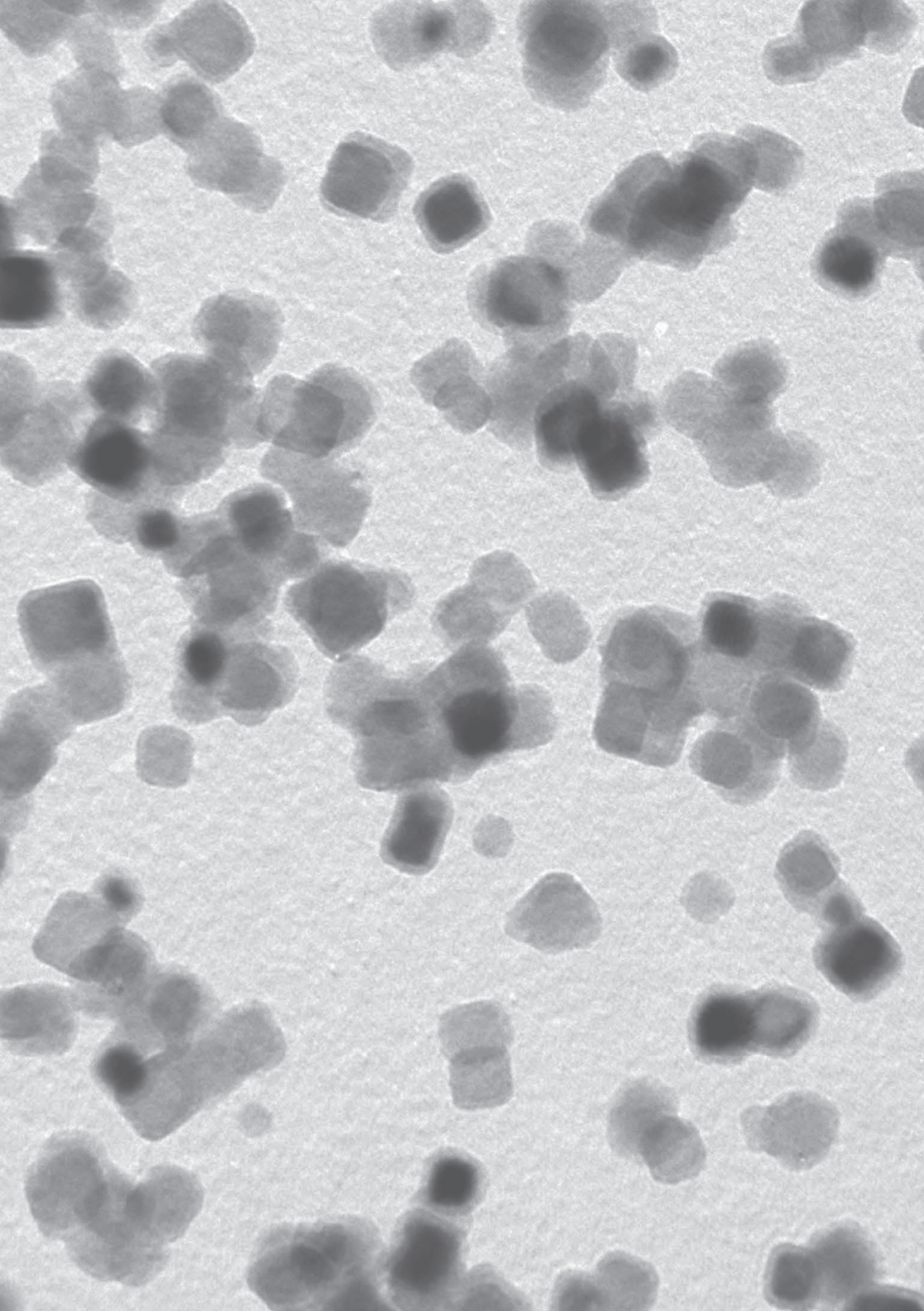
Chapter 4
Copper nanoparticle formation in a reducing gas environment

4.1   Abstract

Although copper nanoparticles are used as model nanomaterial because of their small nucleation barrier, their oxidization sensitivity hampers production of fully metallic nanoparticles with controlled size and shape. Nevertheless, we demonstrate here synthesis of copper nanoparticles, via high pressure magnetron sputtering, having highly tunable sizes and shapes over a size range spanning two orders of magnitude. This is achieved by exploiting a reducing gas environment to mediate proper nucleation conditions, allowing size control of nanoparticles with robust motifs for particle sizes ~5-300 nm. However, due to rapid coalescence oxidation-free nanoparticles cannot be produced monodisperse for sizes larger than ~30 nm.[1]

---

[1] *G.H. ten Brink, G. Krishnan, B.J. Kooi, and G. Palasantzas, J. Appl. Phys. 116, 104302 (2014).*

4.2   Introduction

Nowadays nanoparticles (NPs) have emerged as key materials for important modern-day applications in plasmonics, catalysis, bio diagnostics, and nanomagnetics[1–7]. To produce NPs a number of techniques are available either as a top down or a bottom-up approach. Among all techniques magnetron sputtering has emerged as a mature and good candidate for clean NPs science[6,8–11]. Nevertheless, even under clear vacuum conditions a wide variety of studies have shown that impurities play an important role in the nucleation and subsequent growth of NPs, as well as in the structural motifs they may develop.

In fact, for copper (Cu) NPs an early *in-situ* transmission electron microscope (TEM) study has shed light on the effects of oxygen in the early stages of sintering, coalescence, and morphology. It was shown that NPs produced under clean conditions experience substantial sintering and grain growth upon contact, even at room temperature, while NPs exposed to traces amounts of oxygen remained distinct[12–16]. Therefore, if rapid sintering occurs, it can be difficult to form ultraclean metal nanophase materials[12–16].

Further studies for Cu NPs indicated that the NPs grow upon oxygen exposure, which slows sintering and alters the structure of the NPs, by Brownian coagulation to produce self-similar distributions[14–16].

This model confirmed the role of oxygen inhibiting surface diffusion processes, and the NP size distribution approached the common log-normal distribution[17–20]. It was concluded that oxygen impurities may be desirable to limit agglomeration and to permit dense NP compact formations. Furthermore, an interaction has been observed between Cu NPs and amorphous carbon which produces graphite shells[12]. The shell formation suggested a solid-state analog to that when NPs catalyze the growth of carbon fibers via decomposition in a hydrocarbon atmosphere[12].

Oxidation studies of Cu NPs with sizes less than 10 nm by Transmission Electron Microscopy (TEM) have revealed that beginning with multiply twinned particles as stable structures for NPs with diameters less than 5 nm, and of cube-octahedral for larger NPs, then in the transitional state between pure metal and oxide both states can coexist within the same particle[15,16,21].

The creation of sub-oxides with lower reactivity than the pure metal NPs could also lead to morphologies which are different from the pure metal[15,16,21,22]. However, it still remains obscure how the transition between an oxidizing environment to a carbon or hydrogen based reducing atmosphere can influence the nucleation and growth of oxidation sensitive metal NPs. Indeed, Cu NPs have not only been a subject of various oxidizing studies in the past but also, they have a small nucleation barrier making them suitable as a model nanomaterial[23].

Without any preventive measure Cu NPs formed during high pressure magnetron sputtering within a vacuum system (with base pressure ~10^{-9} mbar that is close to ultra-high vacuum) are highly oxidized because the experimental setup still contains enough oxygen and water[24].

In fact, it is known that carbon deposition on the Cu target surface can prevent surface oxidization[25]. The presence of carbon also plays a role in the NP formation process[26,27]. This is because C atoms can be adsorbed on the primary NP nucleus aiding the coalescence processes during high pressure magnetron sputtering of Cu, and in the final stages can diffuse out of the NPs forming a thin carbon layer, which helps to prevent rapid oxidization under atmospheric conditions[26-28].

As it will be shown in the following, a carbon or hydrogen based reducing gas environment can remove the strong effect of oxygen and enhance both the size control of NPs and quality of structural motifs in the size range 5-300 nm. This size range is unique for this type of high-pressure magnetron sputtering and to our knowledge has not been shown before due to the fact that oxidation is normally limiting the final NP-sizes.

4.3   Experimental methods

The initial Cu NPs produced with a high-pressure magnetron sputtering source had limited sizes in the range of about 1-30 nm.

The size of NPs could be altered e.g., by changing the aggregation length, the pressure and type of gas (argon and helium), and magnetron power[23,30–32]. The NPs were deposited on either (holey) carbon coated Cu grids or on 20 nm thick silicon nitride membranes. Careful TEM/EDX[33] analysis was performed to address the oxidation state and structure of the NPs. In fact, the NPs were characterized with a JEOL 2010F TEM or an FEI Tecnai C^2 both operating at 200 kV. The obtained TEM images were statistically processed by Image-Pro Plus v.7 software[34] to obtain the NP size distributions.

The latter were also fitted by the log-normal size distribution using MATLAB routines[35,36]

$$f_X(x; \mu, \sigma) = \frac{1}{x\sigma\sqrt{2\pi}} e^{-\frac{(\ln x - \mu)^2}{2\sigma^2}} \ (x>0) \ \textbf{(4.1)}$$

in order to verify that the typical NP growth process takes place during high pressure magnetron sputtering by condensation of a supersaturated vapor, where the growth rate is independent of size. In Eq.(1) the parameters μ and σ are, respectively, the mean and standard deviation of $\ln(x)$ with x the particle size.

The actual standard deviation of the particle sizes Ds as a function of μ and σ is given by:

$$\Delta\sigma = \sqrt{\exp(\sigma^2) - 1}\, \exp(\mu + \sigma^2/2)^{36} \quad \textbf{(4.2)}$$

4.4   Results and discussion

4.4.1   TEM images;

Figures 4-2 and 4-3 show a bright field TEM image of as-deposited Cu NPs without introduction of any other gas except Argon gas for sputtering into the deposition system. The size of the NPs was limited to ~10-30 nm, which appeared to be a common outcome for any achievable operating window of the deposition source.

The first impression is that the NPs appear to have normal shape and structure. However, closer inspection reveals that they are nearly spherical agglomerates, and they are largely oxidized with only a smaller crystalline inner cores in the primary NPs forming the agglomerate.
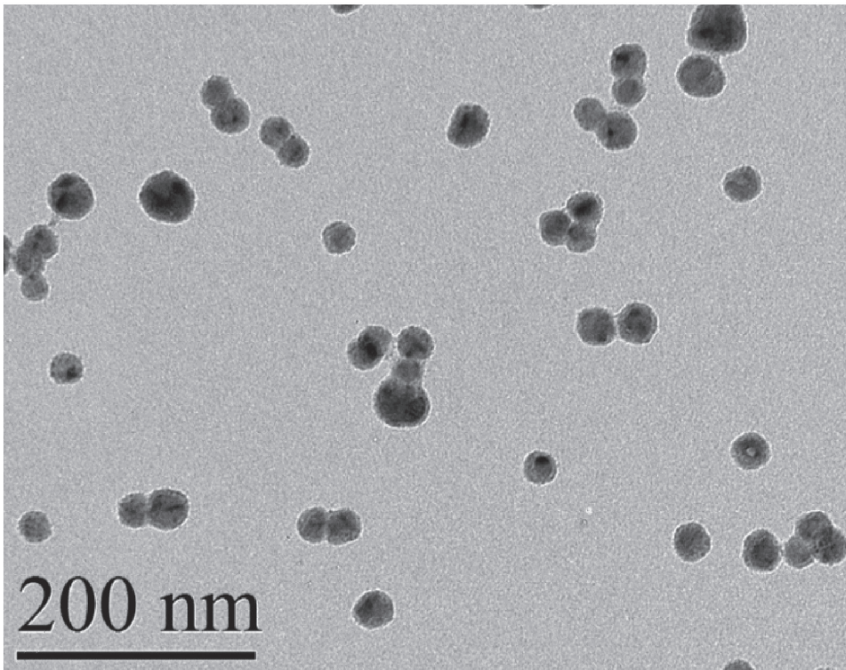
Figure 4-1 Bright Field TEM image of as-deposited Cu NPs without deliberate any other gas than Ar 5.0 present during the deposition. The image seems to indicate successful NP formation, but closer inspection reveals largely oxidized NPs forming agglomerates.as indicated by the EDX data
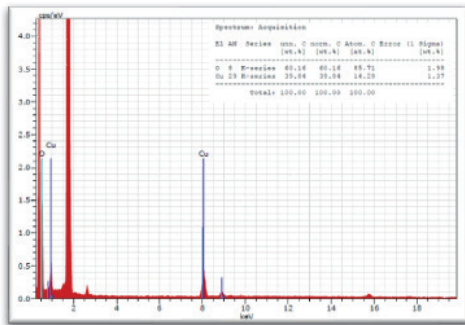
Figure 4-2-EDX analysis from the Cu NPs from TEM image Figure 4-2.
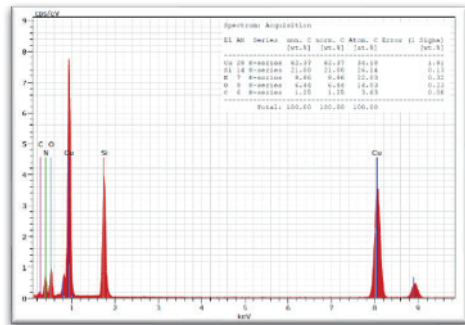
Figure 4-3-EDX analysis from the Cu NPs from TEM image Figure 4-3.
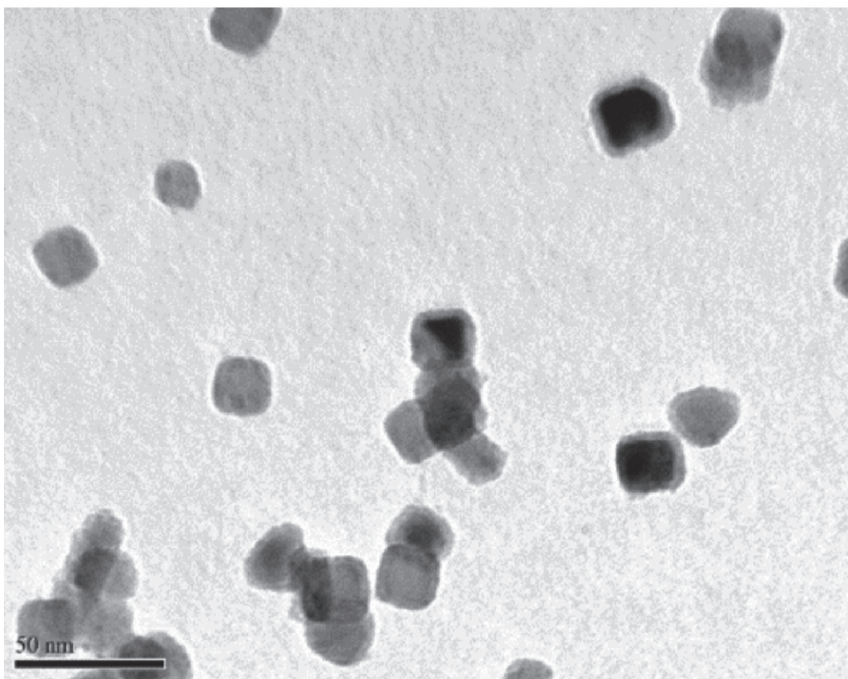
Figure 4-2 Bright Field TEM as-deposited Cu NPs with only Ar 5.0 present during the deposition

The BF TEM image show square/cube shape Cu NPs clearly demonstrating that they are affected by oxidation. This is also confirmed with Energy dispersive X–ray (EDX) analysis see Figs. 4-3 and 4-4 where, however, some variation has been documented for different depositions.

Although Cu (together with Ag and Au) is in group eleven of the periodic table, the high reactivity of NPs makes them sensitive to oxidization[27,28]. In addition, also NPs with cubic (square in projection) crystal habit were observed (see Fig. 4-3), which is indicative that the Cu is oxidized. The NPs are basically truncated octahedral structures and become cubic, square in projection, only when they are formed in the presence of oxygen. Indeed, oxygen exposure deepens the (100) and (111) cusps of the γ-plot (Wulff construction) for Cu[13,37,38]. Without oxygen interference Cu NPs would grow into icosahedral multiple twinned particles since it is energetically the most favorable state for fcc Cu with NP sizes ~5-30 nm[39]. Recent research has suggested that oxygen plays a crucial role for NP nucleation but it hinders NP growth[14,32]. Although in our former studies using a similar deposition system (an Oxford NC200B deposition source at a base pressure ~5.10^{-8} mbar) we have produced Cu crystalline NPs with an ultrathin (~1-2 nm thick) outer oxide shell[40–42], the oxidation situation in the present system remained unaltered even by excellent bake-out and introduction of higher grade sputtering gas. In practice only a few options remained to eliminate sources of water or oxygen inside a vacuum system and limit the oxidation of NPs[24]. However, small amounts of impurities aid NP formation[32].

Therefore, when we tried to remove all possible sources of oxygen and water contaminations within the deposition system, the nucleation of NPs was completely blocked under normal operating conditions (e.g., as in Fig. 4-1). To overcome this nucleation problem and form crystalline Cu NPs with controlled size, a reducing gas, e.g. methane or hydrogen, was used to remove or minimize any remnant oxidizing impurities from the system (but still allowed or aided NP nucleation). A small amount of methane or hydrogen into the magnetron plasma during sputtering would react in-situ with remnant water and oxygen and convert it into volatile species which could be pumped away[43]. Therefore, after system bake out to achieve ~5.10^{-9} mbar base pressure, a small amount of methane or hydrogen gas was introduced, by means of a high precision UHV-leak valve, in the aggregation chamber up to a pressure of ~ 2.10^{-5} mbar or less. Direct measurement of the methane or hydrogen partial pressure during sputtering was not possible because the magnetron is operated at a higher Ar pressure for sputtering (~0.5 mbar). The NP production took place within the normal operating window e.g. 20-40 sccm argon which equals 0.30-0.50 mbar; depending also on the size of the aperture used.

The direct partial oxidation of methane to synthesis gas proceeds exothermic and endothermic via the reactions[43]:

$$CH_4 \ + \ ½\,O_2 \rightarrow CO \ + \ 2H_2 \ (\Delta H = -22.1 kJ/mol\,)$$
$$CH_4 \ + \ H_2O \ \leftrightarrow \ CO \ + \ 3H_2 \ (\Delta H = \ 226 \ kJ/mol) \quad \textbf{(4.3)}$$
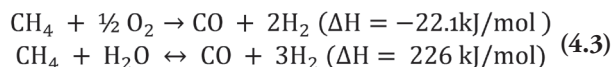
The high temperatures (~1000 K) needed for the endothermic conversion are easily achieved inside the magnetron plasma during sputtering[44–46].

Subsequent reactions with CO and H_2:

$$H_2 + \tfrac{1}{2} O_2 \rightarrow H_2O \ (\Delta H = -248 \ \text{kJ} / \text{mol})$$
$$CO + \tfrac{1}{2} O_2 \rightarrow CO_2 \ (\Delta H = -283 \ \text{kJ} / \text{mol})$$
$$(4.4)$$
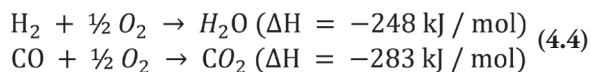
will form CO_2 and H_2O which can be pumped away. The byproduct of gas synthesis, i.e., carbon, aids the system in multiple ways. Carbon deposition as byproduct can in return prevent the sputtering target from corrosion

$$(CH_4 \leftrightarrow C + 2 H_2 \ (\Delta H = -89.9 \ \text{kJ} / \text{mol}))[25] \quad (4.5)$$
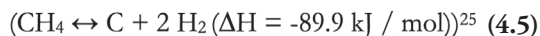
Carbon also plays a role in the formation process of NPs[27]. Indeed, C atoms can be adsorbed on the primary NP nucleus aiding in the coalescence process, and in the final stage diffuse out of the NP forming a thin carbon layer which prevents quick oxidization under atmospheric conditions[23,47]. In a similar way, hydrogen used as a reducing gas can also react with remnant oxygen. The resulting NPs (Fig.4-6) clearly show the effect of the reducing gas environment. Oxide containing aggregates are not formed and NPs now have a multiple twinned near-icosahedral structure as should be the case for clean NPs not influenced by oxidation.
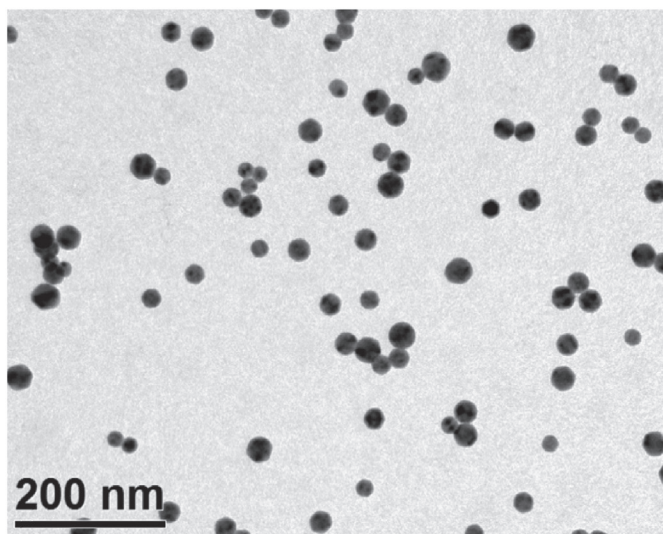
Figure 4-3 Bright Field TEM image of as-deposited Cu NPs with 2.10^{-5} mbar methane and Ar 6.0 present during the deposition. Metallic NPs are formed with a proper multiple twinned near-icosahedral structure.

Moreover, EDX analysis showed the apparent absence of oxygen
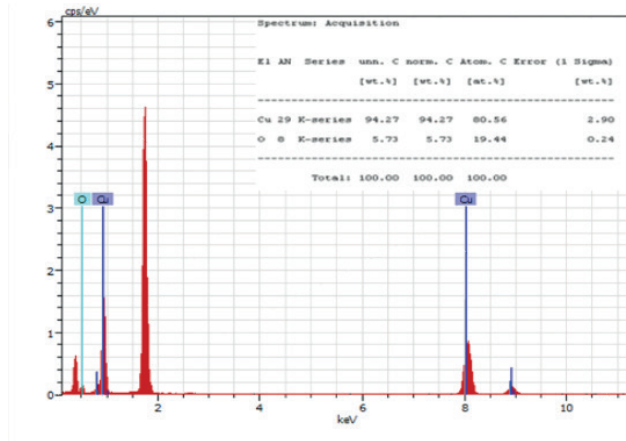
Figure 4-4 One representative Energy Dispersive X-ray (EDX) spectrum analysis from the Cu NPs from either Figure 4-4, 4-5, 4-6, 4-9 and 4-10
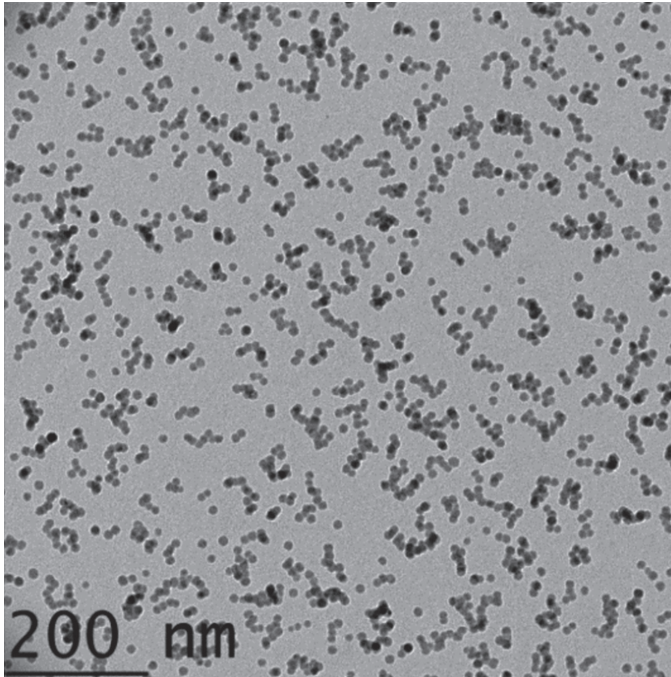
Figure 4-5 Bright Field TEM image of as-deposited Cu NPs with 2.10-5 mbar hydrogen and Ar 6.0 present during the deposition. Monodisperse metallic Cu NPs are formed with log-normal distribution peaked at 12 nm, and with a standard deviation below 3 nm.

4.4.2   NP size distributions

The NP size distributions were fitted using the log-normal distribution:

$$f_X(x; \mu, \sigma) = \frac{1}{x\sigma\sqrt{2\pi}} e^{-\frac{(\ln x - \mu)^2}{2\sigma^2}} \ (x > 0) \ (4.1)$$

where μ and σ can be called the location parameter and the scale parameter, respectively.
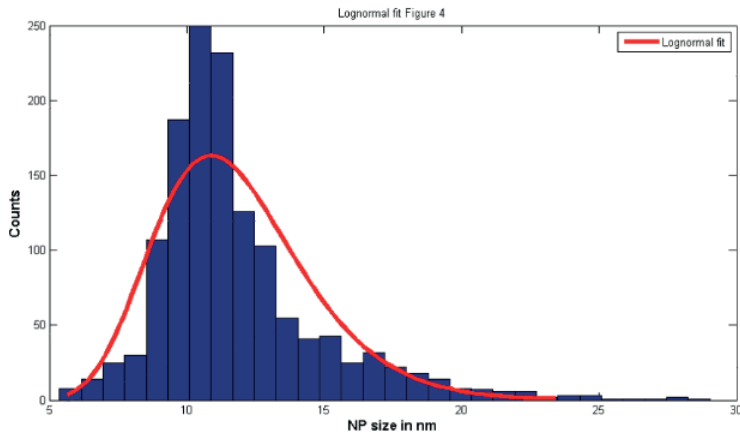
Figure 4-6 Lognormal distribution fit Cu NPs from Figure 4-6 with fitting parameters m= 19 and s = 3.
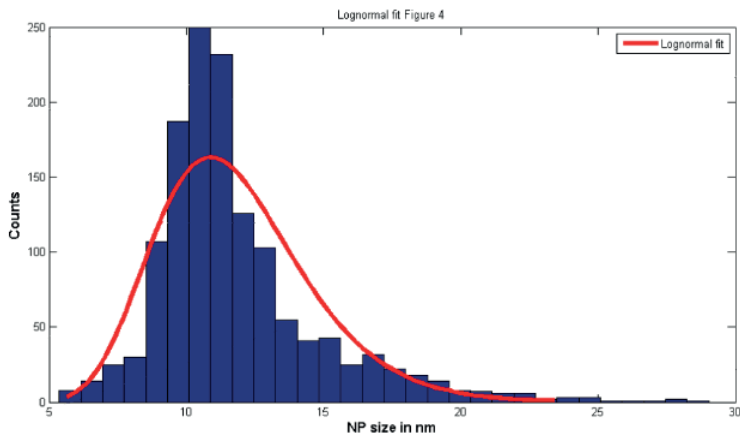
Figure 4-7 Lognormal distribution fit Cu NPs from Figure 4-8 with fitting parameters m= 12, and s = 3.

4.4.3 HR-TEM images;

In fact, lattice spacing measurements confirm the existence of a pure fcc Cu inner core surrounded by an ultra-thin ~2 nm thick Cu_2O shell. High resolution TEM (HRTEM) analysis revealed also the presence of an ultra-thin (~2 nm) layer of carbon.

This finding can be understood, because, according to the C-Cu phase diagram, C cannot be dissolved within bulk Cu (<<0.001 at%)[48] and when present during nucleation it is pushed outside during growth, where of course the situation might be different for NPs compared to bulk. Still, the use of methane reducing gas environment for production of metallic NPs in general is expected to be limited to metals showing a low carbon solubility and of course metals which are not too strong carbide formers although we have obtained good results with it for iron NPs as well.
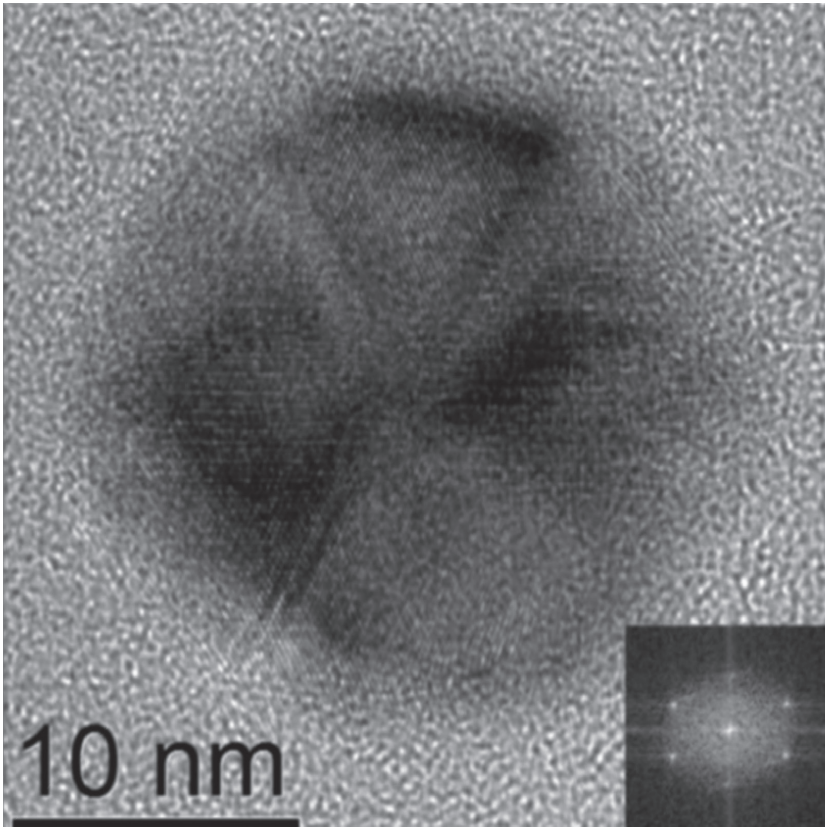
Figure 4-8 HRTEM image from one Cu NP in Fig 4-4 showing an icosahedron shaped multiple twinned particles, the insert FFT of part of the particle is showing lattice spacings d=0.18 and d=0.21 nm, which are the d_{200} and d_{111} of metallic Cu, respectively
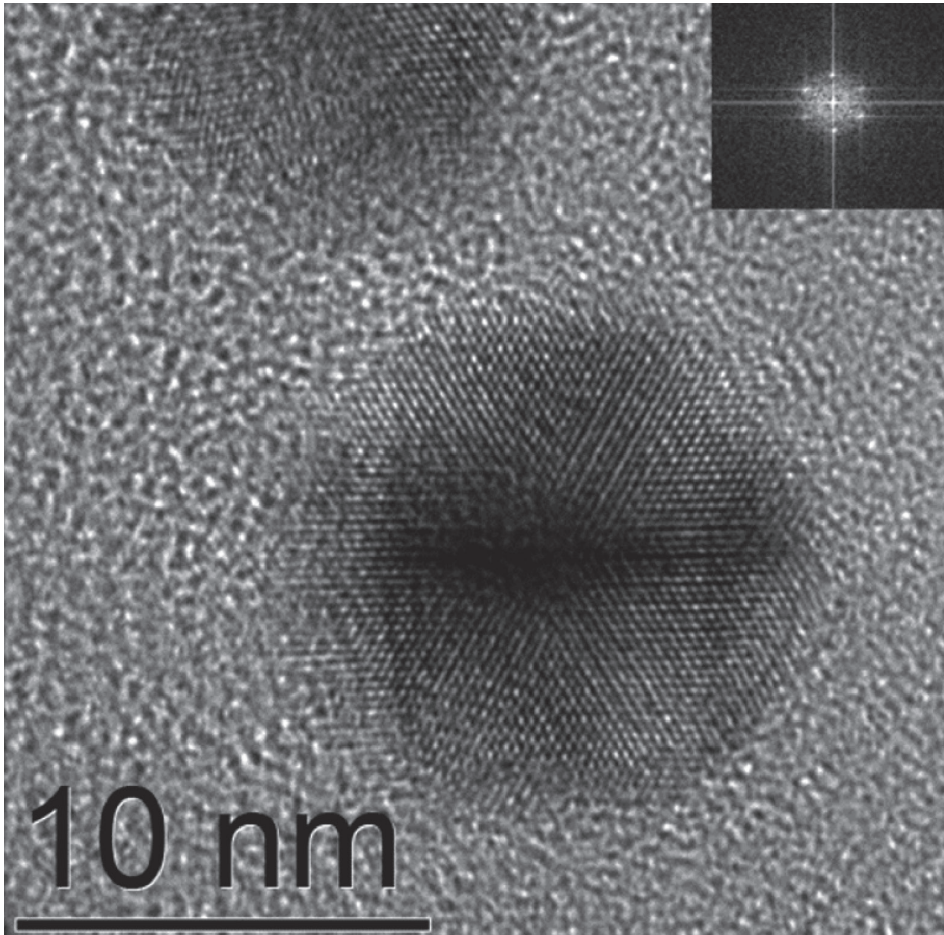
Figure 4-9 HRTEM image from one Cu NP in Fig 4-6 Showing an icosahedron shaped multiple twinned particles, the insert FFT of part of the particle is showing lattice spacings d=0.21 nm, which is the d_{111} of icosahedron, three-fold axis metallic Cu

Moreover, important generalized findings for the reducing environment are the following. A short aggregation length (5 cm) in the dedicated nanoparticle source leads to a particle size of ~10 nm with rather monodisperse size distribution. Smaller particles (<10 nm) can be made using helium (in addition to argon) to increase NP cooling. The maximum aggregation length (13 cm) gives a NP-size range up to ~300 nm (see Fig. 4-11)
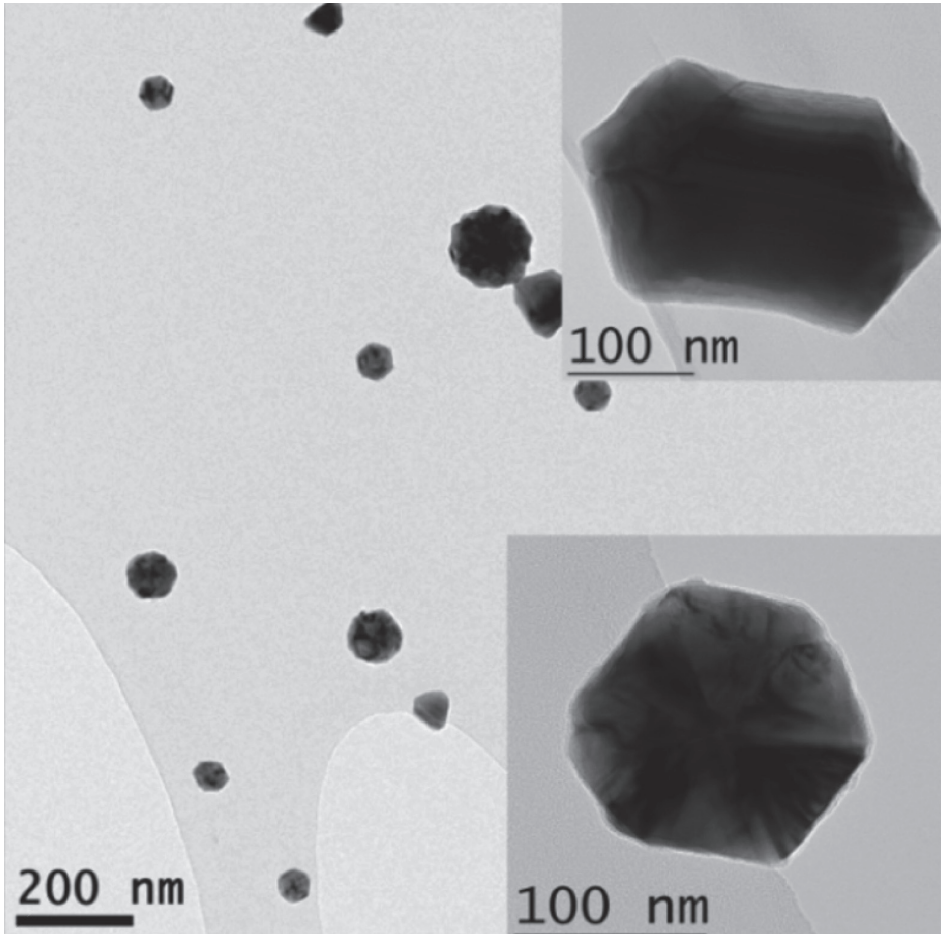
Figure 4-10 Bright Field TEM image of as-deposited Cu NPs with high purity Ar 6.0 for sputtering and 2.10^{-5} mbar CH_4 during the deposition using the longest aggregation length (13 cm). Cu NPs with sizes of over 300 nm are formed. with the remark that for the longer aggregation length the size distribution is not mono-disperse anymore. This can be expected, because the icosahedron-based pure Cu NPs can rapidly coalesce, because not interfered by oxygen shells of the primary NPs. Only by introducing excess methane the size limiting role of oxygen is taken over by carbon at the surface of the primary NPs preventing their rapid coalescence.

In any case, Figs 4-12 till 4-15 shows an overview of the different stages that can be identified during the NP formation[49].

First, nucleation takes place on a critical cluster size $r^* = 2\sigma_e m/kT\rho \ln(\varphi)$[49,50]. σ_e stands for the surface energy of a small droplet of atoms, ρ is its density, m is its atomic or molecular mass, and $\varphi = p_k/p_s$ is its condition for super saturation (p_k and p_s are the vapor and saturation vapor pressure, respectively). For larger radii accretion of atoms on the small cluster becomes thermodynamically favorable leading to rapid growth.
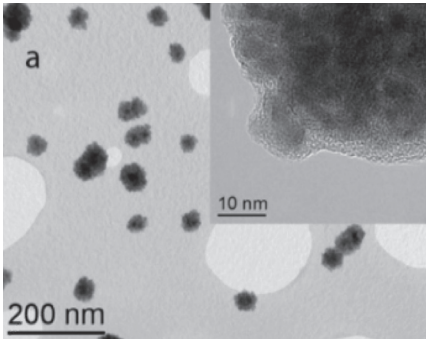
Figure 4-11
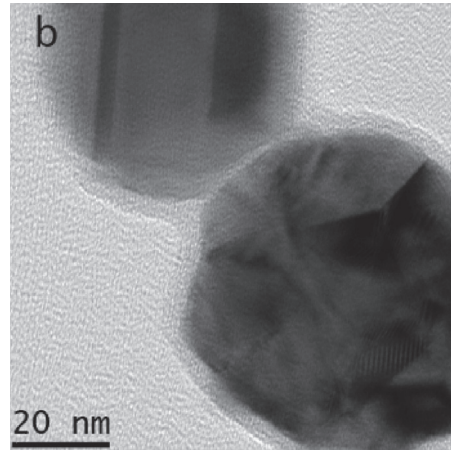
Figure 4-12
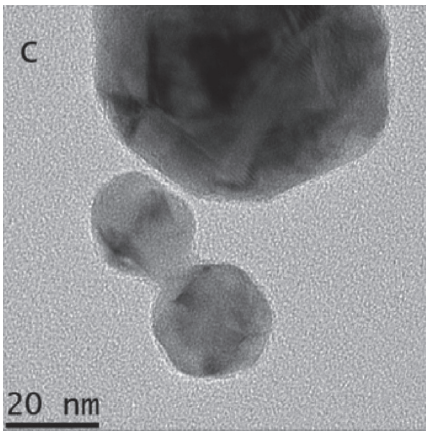
Figure 4-13
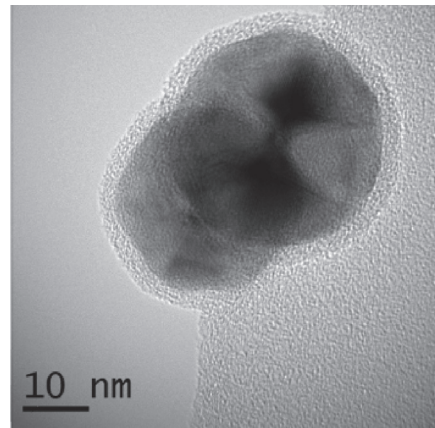
Figure 4-14

Figures 4-12-4-15 Bright Field TEM overview of the different stages in the coalescence and agglomeration process of deposited Cu NPs with increasing amounts of methane (from a→d)) during deposition.

Figure 4-12(a) NPs agglomerates are formed from primary Cu NPs with thin oxide shells as it is shown in the inset.

Figure 4-13(b) Higher methane content in the aggregation chamber: accretion and coalescence to form bigger particles. Remnant amounts of oxygen are still present and produce a thin oxide layer thereby hindering further coalescence.

Figure 4-14(c) An intermediate condition with a thinner oxide layer than in (b). Coalesce is taking place, while the necking is clearly visible without grain boundary formation. Figure 4-15(d) A Higher methane addition is leading to NP formation with excess of carbon, which limits effectively the NP size to grow further.

Depending on the amount of remnant oxygen and water in the system, NPs agglomerates are formed from primary particles, e.g., small particles, in which the primary particles remain identifiable being Cu NPs with a thin oxide shell (see Fig. 11 and HRTEM inset and also Fig.1). Then Figs. 4-12-4-15 show results of a gradual increasing methane addition to the aggregation chamber. Due to less surface oxidization, accretion and coalescence takes place and bigger particles are formed. However, there is still a thin oxide layer preventing further coalescence see Fig. 4-12. Figure 4-13 shows an even thinner oxide layer than that in Fig. 4-12, where coalesce is taking place. Here the necking is clearly visible but no grain boundary is yet formed. Under normal operating conditions e.g., ~0.3-0.5 mbar sputtering gas depending also on the exit aperture of the aggregation volume, see Fig. 2-9. Distinct facetted NP are formed with good size control as can be seen from the overview in Fig.4-6 and Fig. 4-8, 4,9 and 4-10 for more details of the NPs structure.

4.5   Conclusions

Cu nanoparticles can be synthesized with high pressure magnetron sputtering having tunable sizes and shapes as high-resolution transmission electron microscopy demonstrated. Although Cu NPs are used as a model material because of their small nucleation barrier, their oxidization sensitivity makes it difficult to control sizes of purely metallic NPs over large ranges. However, with the aid of a reducing gas environment to minimize NP oxidization (by removing oxygen and water) we can achieve a proper NP nucleation condition to form metallic NPs. Moreover, we can enhance the size control of these NPs leading to narrow size distributions and robust (near icosahedral) structural motifs for particle sizes up to ~30 nm. Metallic NPs with sizes as large as 300 nm can be readily produced because coalescence of primary NPs in the reducing atmosphere is not prevented by the presence of oxide shells. However, in the case of excess methane the high carbon content limits the NPs to grow further in size

4.6 References

[1] P.D.U. Kreibig and P.D.M. Vollmer, in Opt. Prop. Met. Clust. (Springer Berlin Heidelberg, 1995).

[2] E. Prodan and P. Nordlander, Nano Lett. 3, 543 (2003).

[3] J.P. Wilcoxon and B.L. Abrams, Chem. Soc. Rev. 35, 1162 (2006).

[4] A.S. Edelstein and R.C. Cammaratra, editors, Nanomaterials: Synthesis, Properties and Applications, Second Edition, 2nd ed. (Taylor & Francis, 1998).

[5] C. Binns, Surf. Sci. Rep. 44, 1 (2001).

[6] P. Jensen, Growth of Nanostructures by Cluster Deposition : A Review (1999).

[7] W.A. de Heer, Rev. Mod. Phys. 65, 611 (1993).

[8] C. Xirouchaki and R.E. Palmer, Philos. Trans. R. Soc. Lond. Ser. Math. Phys. Eng. Sci. 362, 117 (2004).

[9] P.J. Kelly and R.D. Arnell, Vacuum 56, 159 (2000).

[10] K. Wegner, P. Piseri, H.V. Tafreshi, and P. Milani, J. Phys. Appl. Phys. 39, R439 (2006).

[11] Jensen and N. Combe, Compuational Mater. Sci. 24, 78 (2002).

[12] D.L. Olynick, J.M. Gibson, and R.S. Averback, Mater. Sci. Eng. A 204, 54 (1995).

[13] D.L. Olynick, J.M. Gibson, and R.S. Averback, Appl. Phys. Lett. 68, 343 (1996).

[14] D.L. Olynick, J.M. Gibson, and R.S. Averback, Philos. Mag. A 77, 1205 (1998).

[15] J. Urban, H. Sack-Kongehl, and K. Weiss, Z. Für Phys. At. Mol. Clust. 36, 73 (1996).

[16] J. Urban, H. Sack-Kongehl, and K. Weiss, Catal. Lett. 49, 101 (1997).

[17] L.B. Kiss, J. Söderlund, G.A. Niklasson, and C.G. Granqvist, Nanotechnology 10, 25 (1999).

[18] L.B. Kiss, J. S\öderlund, G.A. Niklasson, and C.G. Granqvist, Nanostructured Mater. 12, 327 (1999).

[19] C.G. Granqvist and R.A. Buhrman, Solid State Commun. 18, 123 (1976).

[20] C.G. Granqvist and R.A. Buhrman, J. Appl. Phys. 47, 2200 (2009).

[21] I. Lisiecki, A. Filankembo, H. Sack-Kongehl, K. Weiss, M.-P. Pileni, and J. Urban, Phys. Rev. B 61, 4968 (2000).

[22] S. Giorgio and J. Urban, in Small Part. Inorg. Clust. (Springer, 1989), pp. 115–118.

[23] M. Gracia-Pinilla, E. Martínez, G.S. Vidaurri, and E. Pérez-Tijerina, Nanoscale Res. Lett. 5, 180 (2009).

[24] V.A. Vons, A. Schmidt-Ott, TU Delft: Applied Sciences: Chemical Engineering, and TU Delft, Delft University of Technology, (2010).

[25] A. Majumdar, J.F. Behnke, R. Hippler, K. Matyash, and R. Schneider, J. Phys. Chem. A 109, 9371 (2005).

[26] C. Hao, F. Xiao, and Z. Cui, J. Nanoparticle Res. 10, 47 (2008).

[27] S. Wang, X. Huang, Y. He, H. Huang, Y. Wu, L. Hou, X. Liu, T. Yang, J. Zou, and B. Huang, Carbon 50, 2119 (2012).

[28] G. Cheng and A.R. Hight Walker, Anal. Bioanal. Chem. 396, 1057 (2010).

[29] Gert H. ten Brink,†*, Gopi Krishnan,† Bart J. Kooi† and George Palasantzas, Supplemental material for Copper nanoparticle formation in a reducing gas environment: NP-deposition system, EDAX analysis, NP size distributions.

[30] A.N. Banerjee, R. Krishna, and B. Das, Appl. Phys. A 90, 299 (2007).

[31] A. Majumdar, D. Köpp, M. Ganeva, D. Datta, S. Bhattacharyya, and R. Hippler, Rev. Sci. Instrum. 80, 095103 (2009).

[32] A. Marek, J. Valter, S. Kadlec, and J. Vyskočil, Surf. Coat. Technol. 205, Supplement 2, S573 (2011).

[33] G.L. Hornyak, S. Peschel, T. Sawitowski, and G. Schmid, Micron 29, 183 (April).

[34] Computer Program Image-Pro Plus, http://www.mediacy.com/

[35] Computer Program MATLAB, http://www.mathworks.nl/products/matlab/

[36] S. Kotz, N. Balakrishnan, and N.L. Johnson, Continuous Univariate Distributions, 2nd ed. (Wiley, New York, 1994).

[37] B.E. Sundquist, Acta Metall. 12, 67 (1964).

[38] B.E. Sundquist, Acta Metall. 12, 585 (1964).

[39] S. Ino, J. Phys. Soc. Jpn. 27, 941 (1969).

[40] G. Krishnan, G. Palasantzas, and B.J. Kooi, Appl. Phys. Lett. 97, 131911 (2010).

[41] G. Palasantzas, S.A. Koch, and J.T.. De Hosson, Rev Adv Mater Sci 5, 57 (2003).

[42] G. Palasantzas, S.A. Koch, and J.T.M. De Hosson, Appl. Phys. Lett. 81, 1089 (2002).

[43] C.R.H. de Smet, Partial Oxidation of Methane to Synthesis Gas: Reaction Kinetics and Reactor Modelling (Technische Universiteit Eindhoven, 2000).

[44] E. Quesnel, E. Pauliac-Vaujour, and V. Muffato, J. Appl. Phys. 107, 054309 (2010).

[45] E. Pauliac-Vaujour, E. Quesnel, and V. Muffato, in Mater. Chall. Altern. Renew. Energy, edited by G. Wicks, J. Simon, R. Zidan, E. Lara-Curzio, T. Adams, J. Zayas, A. Karkamkar, R. Sindelar, and B. Garcia-Diaz (John Wiley & Sons, Inc., 2010), pp. 163–172.

[46] B. Chapman, Glow Discharge Process (s.n., 1980).

[47] C.-H. Chen, T. Yamaguchi, K. Sugawara, and K. Koga, J. Phys. Chem. B 109, 20669 (2005).

[48] G.A. López and E.J. Mittemeijer, Scr. Mater. 51, 1 (2004).

[49] R.C. Flagan and M.M. Lunden, Mater. Sci. Eng. A 204, 113 (1995).

[50] P. Feiden, J. Leygnier, P. Cahuzac, and C. Bréchignac, Eur. Phys. J. D 43, 49 (2007).
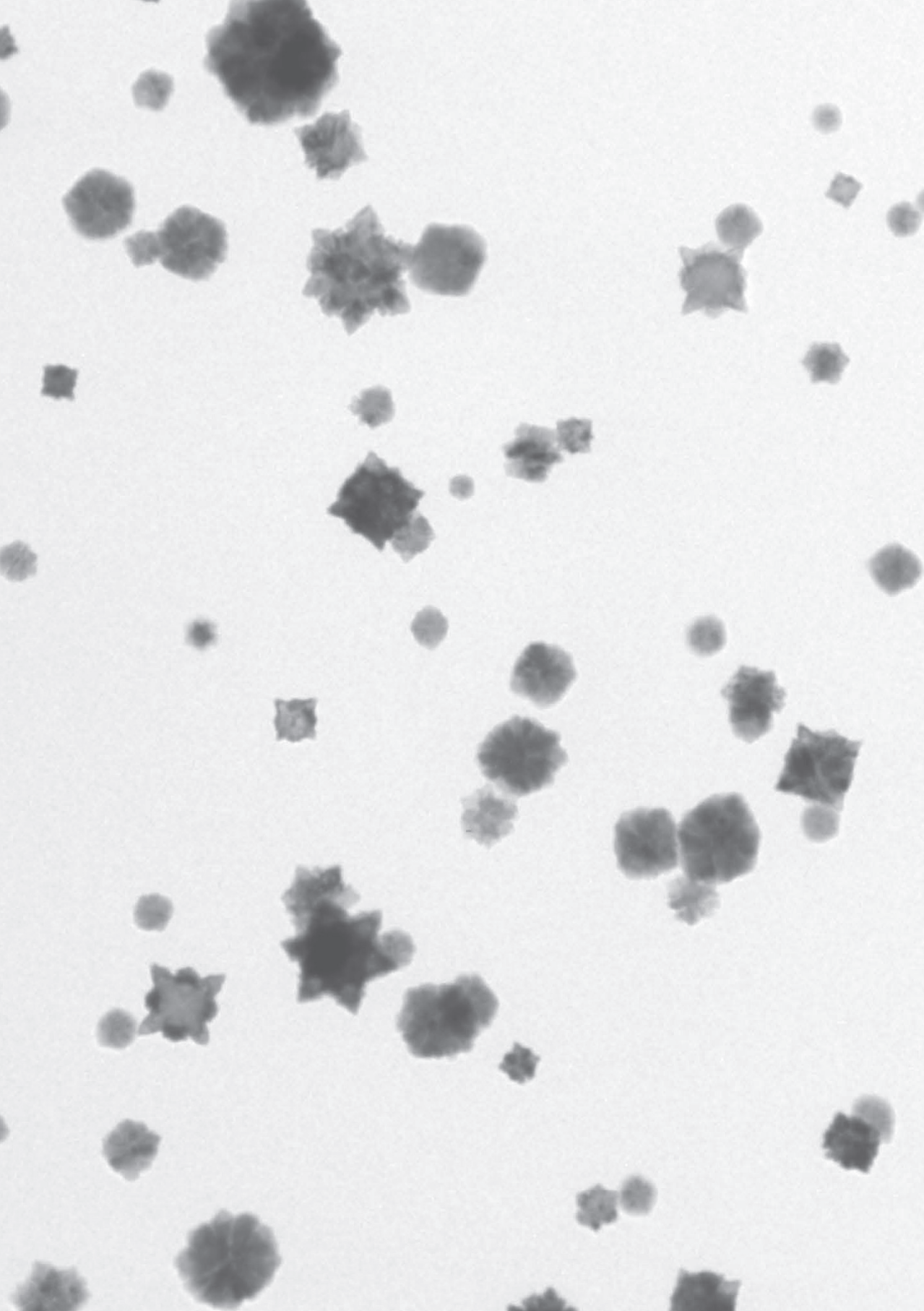
4

Chapter 5
Tuning structural motifs and alloying of bulk immiscible Mo–Cu bimetallic nanoparticles by gas-phase synthesis

5.1   Abstract

Nowadays bimetallic nanoparticles (NPs) have emerged as key materials for important modern applications in nanoplasmonics, catalysis, biodiagnostics, and nanomagnetics. Consequently the control of bimetallic structural motifs with specific shapes provides increasing functionality and selectivity for related applications. However, producing bimetallic NPs with well controlled structural motifs still remains a formidable challenge. Hence, we present here a general methodology for gas phase synthesis of bimetallic NPs with distinctively different structural motifs finally to a Janus/dumbbell, with the same overall particle composition. These concepts are illustrated for Mo–Cu NPs, where the precise control of the bimetallic NPs with various degrees of chemical ordering, including different shapes from spherical to cube, is achieved by tailoring the energy and thermal environment that the NPs experience during their production. The initial state of NP growth, either in the liquid or in the solid state phase, has important implications for the different structural motifs and shapes of synthesized NPs. Finally we demonstrate that we are able to tune the alloying regime, for the otherwise bulk immiscible Mo–Cu, by achieving an increase of the critical size, below which alloying occurs, closely up to an order of magnitude. It is discovered that the critical size of the NP alloy is not only affected by controlled tuning of the alloying temperature but also by the particle shape.[2]

[2] *G. Krishnan, M.A. Verheijen, G.H. ten Brink, G. Palasantzas, and B.J. Kooi, Nanoscale 5, 5375 (2013).*

5.2   Introduction

Today's advances in technology rely increasingly on multi- functional nanostructured materials. Within this class of materials bimetallic structured nanoparticles (NPs) have attracted strong interest, because their functionality can be tuned using the detailed interplay of the two elemental components, which can provide a variety of particle shapes, morphologies, and compositions. Hence enhanced performance can be facilitated for diverse applications in many fields such as catalysis, optics, biodiagonistics and magnetic systems.[1–20] In this respect nano-alloying of two elements, which are largely immiscible in bulk, has attracted strong attention due to the fact that new functional properties can be tailored that are quite unique and distinct from those of the corresponding bulk metals and alloys. Alloying of bulk immiscible elements is feasible in the nanoscale regime, because the enthalpy of mixing decreases with decreasing NP size and generally becomes negative below a certain size.[22–25] Besides the size effect, recent studies also suggest that the shape and the surface structure of NPs influence the alloying ability of immiscible materials.[21–24] Taking all these complex factors into consideration, the alloying ability of bulk immiscible compounds starts for NPs, depending on the composition selected, with size below 10 nm, while complete alloying (in the whole composition range) has been only observed for NPs with less than 2 nm size.[24]

Phase segregation/core–shell formation is one of the major problems affecting the stability of the alloyed NPs when the NP size is increased above 2 nm. Consequently, alloying of bulk immiscible NPs with sizes beyond 10 nm is a formidable challenge and so far has not been reported. Here, however, we report that alloying of Mo–Cu NPs, which are bulk immiscible, is possible up to sizes of 60 nm by tuning the thermal environment and the cooling rate during NP growth.

Bimetallic NPs can have various structural motifs: (a) nano- alloy: random or ordered alloys in a mixed state and (b) core– shell, onion structure (multishell), Janus structure (dumbbell) in a segregated or phase-separated state.[25–30] These bimetallic structural motifs can be synthesized by various techniques including electrochemistry, chemical reduction and gas phase synthesis.[25–33] Although gas phase synthesis of bimetallic NPs has recently received increased attention, because phase-separated NPs with clean high quality interfaces and surfaces can be produced,[31–33] the control of the various structures and shapes is still poorly understood. Nevertheless, the formation of various structural motifs for the same type of bimetallic NPs with mixed chemical composition (e.g. Mo–Cu) has not been reported so far because it is an extremely challenging task.

To address these challenges, we focus here on the Mo–Cu (bulk immiscible) NPs, because pure Mo NPs exhibit interesting self-organization phenomena to a decreasing surface energy of the system.[34–36] Indeed, Mo has a strong tendency to self-assemble into larger cubic particles from smaller structural sub- units of rhombic dodecahedrons or cubes.[34–36] It also has a size dependent

crystal structure transformation from body centered cubic (bcc) to face centered cubic (fcc) as the NP size decreases.[36] Hence, using gas phase synthesis, with addition of Cu we report on the synthesis of Mo–Cu NPs with distinctively different structural motifs: core–shell, onion (multishell NPs), and alloy NPs at the single particle level with the same composition. Not only we tune the various structural motifs but we can also produce them with well-defined shapes like cube or spherical. Simultaneously we illustrate the possibility to extend the alloying NP size from 6 up to 60 nm, closely up to an order of magnitude, by proper tuning of the thermal environment and the cooling rate of the NPs during their growth.

5.3   Experimental methods

The Mo–Cu nanoparticles with various structural motifs and shapes were produced by the nanoparticle system nanosys500 from Mantis Deposition Ltd. The sample chamber was evacuated to a base pressure of ~1 x 10^{-8} mbar with a partial oxygen pressure of ~10^{-9} mbar.
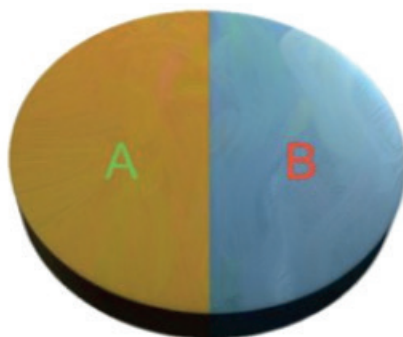
Figure 5-1 a 2 inch sputter target consisting of ½ Mo(B) and ½ Cu(A) (99.95% purity of the Mo and Cu as is was obtained from Alpha Aesar)

Super- saturated metal vapor is produced by magnetron sputtering of a sectioned target (Fig 5-1) in an inert argon atmosphere, pressures of ~0.25 to 1.5 mbar depending on the choice of the structural motifs that were synthesized.

The supersaturated metal vapor is then cooled by the Ar gas to form a nuclei which grow as nanoparticles. The nanoparticles formed in the aggregation volume are removed fast by the use of argon (Ar) which acts as a drift and sputter gas. The tuning of the thermal environment and energy was made by varying the discharge current and the pressure inside the aggregation volume (see Table 5-1). The nanoparticles transported from the aggregation volume were deposited onto 25 nm thick silicon-nitride membranes, which were used for Transmission Electron Microscopy (TEM) analysis in a JEOL 2010F TEM.

5.4   Results and discussion

Current (A)	GasFlow Rate(sccm)	shape	Structure	Aperture Size (mm)	Figures in the Manuscript
0.250	40	Cube	Alloy	3	Figure 5-2
0.250	70	Spherical	Alloy	3	Figure 5-2
0.350	40	Cube+Spherical	Core-Shell	3	Figure 5-3
0.550	40	Spherical	Onion/Multishell	3	Figure 5-7
0.550	100	Spherical	Core-Shell	3	Figure 5-11
0.550	150	Spherical +cube	Janus/ Dumbbell	5.5	Figure 5-12

Low gas flow	0-40 sccm
Medium gas flow	40-80 sccm
High gas flow	>80 sccm.

Tabel 5-1 The table (upper) shows the various parameters involved in the synthesis of various structural motifs of Mo-Cu bimetallic nanoparticles. (b) The table (bottom) shows the gas flow rates stated in the manuscript.

Figure 5-2 shows transmission electron microscopy (TEM) and Scanning TEM (STEM) results of Mo-Cu alloy NPs directly synthesized in the gas phase by maintaining a specific discharge current of 0.250 A. The principal difference in the synthesis conditions related to Figures 5-2(a-c) and Figures 5-2(d-f) was the Ar gas flow rate and thus the pressure in the aggregation volume of the nanoparticle source. This difference resulted in either cube or spherical shaped NPs as shown by the bright field TEM images in Figure 5-2(a) and Figure 5-2(d), respectively. The presence of Mo-Cu bcc based solid solutions (alloy) in both the shapes is confirmed by both Fourier transform analysis of HRTEM images and electron diffraction patterns shown in Figures 5-2(b), (c) and Figures 5-2(e), (f).

Moreover the measured interplanar distances in two orthogonal directions (110) and (1$\bar{1}$0) of Figure 5-2(b) is d110 =0.213±0.04 nm and deviates significantly from the one of pure Mo d110 =0.222 nm in both directions and it agrees with a lattice spacing corresponding to a bcc based solid solution of Mo-Cu. Also Figures 5-2(e) and (f) show that the NPs contain a bcc solid

solution of Mo-Cu.

Compositional analysis (EDS) in the TEM shows that the NPs consist of 86±1 at.% Mo and 14±1 at.% of Cu. The compositional analysis of randomly picked NPs with both cube and spherical shapes shows in all cases very similar compositions. So, the difference in shape is not a compositional effect.

The EDX mapping (STEM mode) of the cube Mo-Cu alloy NPs shown in Figure 5-2(g) also indicates that Cu and Mo are mixed within the NPs.
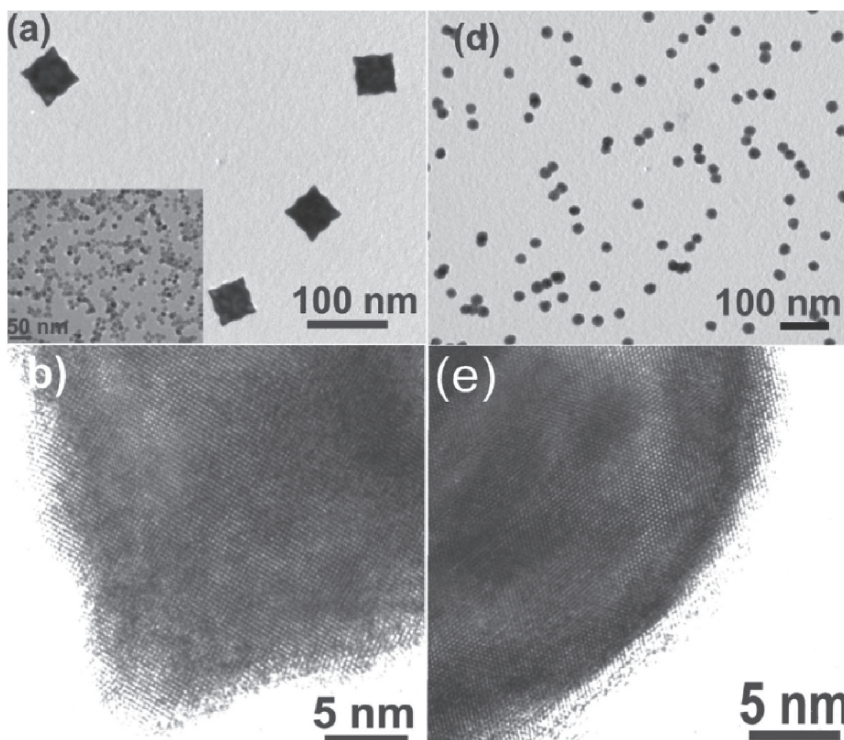
Figure 5-2 (a) Mo-Cu alloyed NPs synthesized in cube and spherical shapes with an average size of 59 ± 2 nm and 32 ± 3 nm, respectively. (a) Bright field TEM image of the Mo-Cu alloyed NPs with cube shape. (b) Corresponding HRTEM image of the Mo-Cu NPs. (d) Bright field image of the Mo-Cu alloyed NPs with spherical shape. (e) Corresponding HRTEM image of the alloyed NPs with spherical shape.
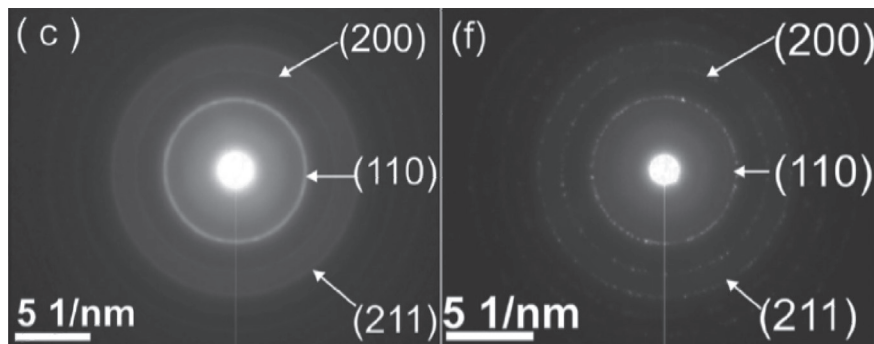
Figure 5-2(c) Electron Diffraction pattern of the cube Mo-Cu NPs with an alloyed structure. (f) Diffraction pattern of the alloyed NPs with spherical shape showing the presence of Mo-Cu alloyed structure

5
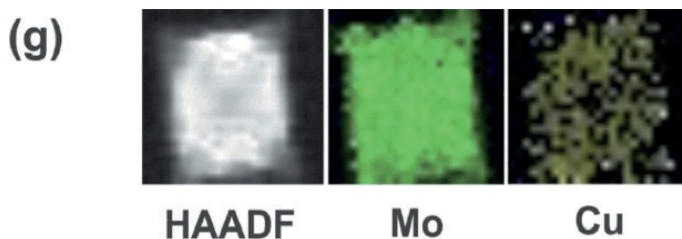
Figure 5-2 (g) Compositional (EDX) mapping of Mo and Cu in the cube shaped NPs.

Mo-Cu is an immiscible system in its bulk form and it has a positive enthalpy of formation of 28kJ/mol. It is well known that immiscible metals in bulk can be alloyed in the nano-size regime, because the enthalpy of formation decreases with decreasing particle size and can become negative below a critical particle size.[21-24] However, the critical size below which NPs can start to form an alloyed structure completely depends on its composition, shape and surface effects in the nano regime and is normally only observed below a size of about 10 nm.[22-25] In our case we show the alloying ability of Mo-Cu with sizes from 5 up to 60 nm in both cube and spherical shaped particles. In view of the previous work, it is not so surprising that we could produce alloyed Mo-Cu NPs with sizes 6±2 nm (see Fig 5-3 a,b,c).

However, the cube and spherical Mo-Cu NPs shown in Fig.5-2(which were produced without employing a mass filter) have an average diameter of 59±4 nm and 32±4 nm, respectively. Note the relatively monodisperse size distribution of the NPs present in the samples shown in Fig.5-2(d) In contrast to the earlier work[21-24], our results show that Mo and Cu are mixed in NPs having a size clearly larger than 10 nm. Of course this can be attributed to our synthesis method (based on dc magnetron

sputtering) which produces material far out of (thermodynamic) equilibrium, with temperatures in the plasma that can be beyond 3000 K ? and with the possibility of very high cooling rates of the material. One could expect that alloy NPs are formed in bulk immiscible systems, where mixing is still possible in the bulk liquid state. However, this mechanism cannot hold for bulk Mo-Cu, because even in the liquid state Mo-Cu is not miscible (only limited solubility of Cu in liquid Mo). Still, meta-stable alloy NPs can apparently be formed, because of their strongly reduced dimensions with a large surface to volume ratio. Recent work by S. Xiong et al. [25] with a surface-area difference model shows the increase of the critical size with increase in temperature and therefore the enthalpy of formation can become negative also for NPs larger than 10 nm in agreement with our current result.

Our results also indicate that the shape of the NPs (with the same composition) affects the critical size for alloying of immiscible systems and that a cube shape has a larger critical size than the spherical shape e.g. Fig 5-2. This is this also be explained based on the surface area difference model of Xiong et al.[24] In order to understand the effect of composition on the critical size for alloying Mo-Cu, we have also varied the composition of the Mo-Cu sputtering targets to increase the Cu at.%. We found that NPs with an average composition of 76±1 at.% Mo and 24±1 at% Cu (as determined by EDX) could only be alloyed with a size up to 20 nm. This means that the critical size for alloying decreases when the concentration of the two immiscible elements becomes more equivalent.[24]
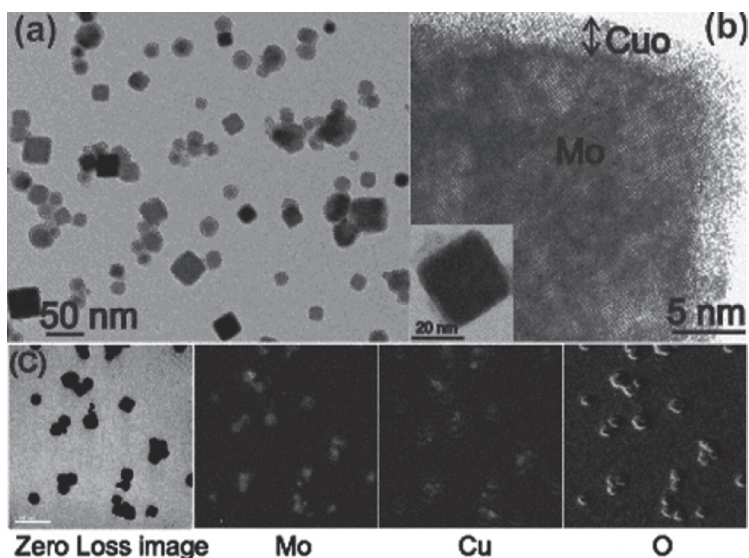
Figure 5-3 (a) Bright field TEM image of the Mo/Cu core/shell NPs with both spherical and cube shapes **(b)** HRTEM image of the Mo/Cu core/shell NPs showing d110 resolved lattice spacing of in the Mo core and an amorphous Cu-oxide shell (which develops out of Cu during the transfer to TEM). Inset shows the bright field TEM image of the same nanoparticles. **(c)** GIF mapping showing Mo, Cu and O elemental maps for the Mo/Cu core shell nanoparticles.

Fig. 5-3(a) shows a bright field TEM image of the Mo–Cu core–shell NPs with both spherical and cube shapes produced together within the same deposition. Compared to the process used in the case of Fig. 5-2 (a), the discharge current in the case of Fig. 5-3(a) was increased to 0.350 A (still using the same gas flow rate of 40 sccm).

In this case it was possible to make core–shell NPs with a size distribution of ≈19+/- 6 nm. However, core–shell N could also be produced with larger sizes than those shown for the alloy NPs in Fig. 5-2 and Fig.5-4.

Fig. 5-3(b) shows the HRTEM image of the atomically resolved lattice spacing of d(110) Mo core and the Cu-shell. Since Mo has a higher surface energy than Cu it is understood that particles with a Mo core and a Cu shell are produced. Comparing the Mo–Cu alloy and the Mo–Cu core–shell NPs we can infer that the energy supplied or energy gained by the NPs during their growth, and the thermal environment they experience, has significant influence on their structure.

Understanding how this behavior is related to the process conditions can provide the "know-how" to tune diffrent structures for a chosen bimetallic system. Therefore, we will try to obtain more insight into the NP formation process. Indeed, the process starts with the vaporization of the bi-metallic target with a bombardment of Ar ions. In the next step the evaporated energetic atoms collide with Ar molecules and/or drift gas (e.g. He) to lose their energy (thermalize) and form NP nuclei. Formation of the latter starts immediately after collision of the high energetic metal atoms with low energy Ar gas atoms, because there is a large drop in temperature and energy during collisions. Then the nuclei grow by a collision/aggregation process to form NPs. Normally at a high cooling rate (high Ar gas flow rate) the NPs are quenched very fast and remain in their high temperature state, which means that there is not suffcient time/energy for atomic diffusion to occur. Hence if we can cool the NPs slowly, suffcient atomic diffusion within the particles can occur resulting in large variations of the final NP structure.
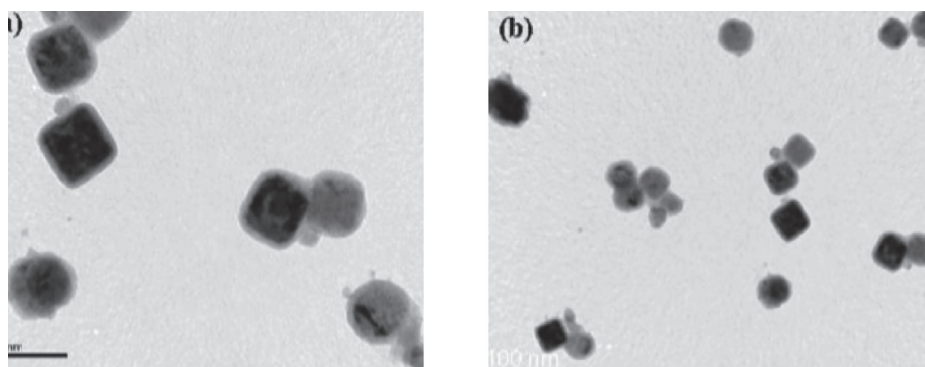
Figure 5-4 BF-TEM images showing Mo/Cu core/shell nanoparticles in two different magnifications with the same composition and size range of the Mo–Cu alloy nanoparticles shown in figure 5-2(b) of the manuscript.
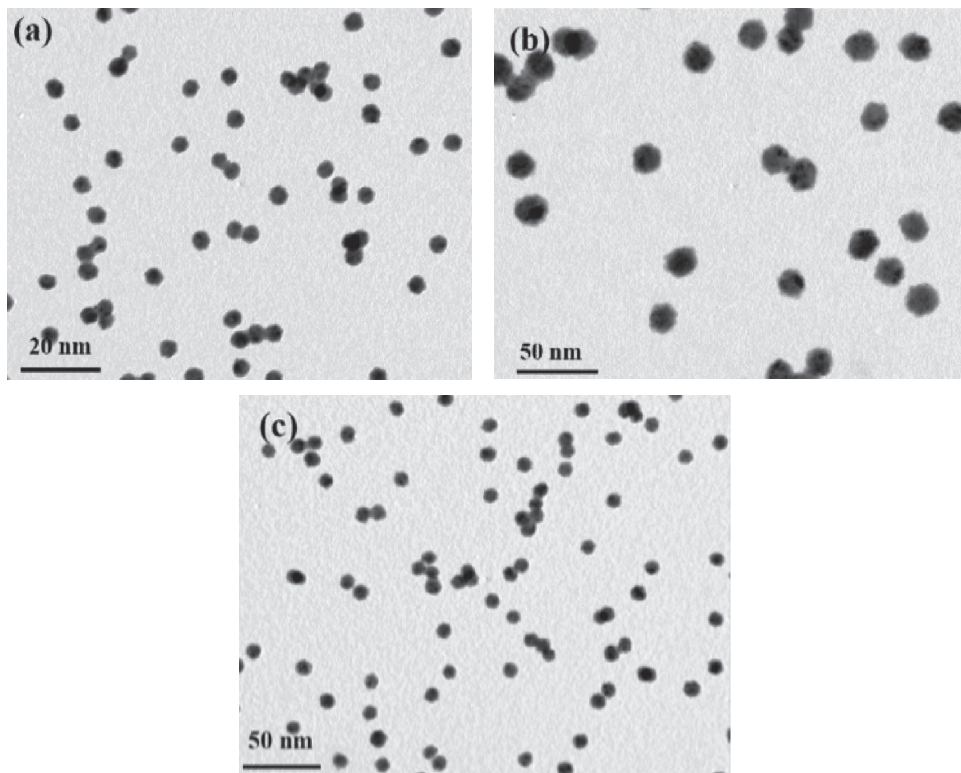
Figure 5-5 BF-TEM images of the Mo-Cu alloy NPs.

(a) Mo-Cu alloy NPs with a size distribution of 5±3 nm.

(b) Mo-Cu alloy nanoparticles produced with an average composition of Mo 75.6±1 at% and Cu 24.4±1 at% showing the NP size distribution of 20±2 nm.

(c) Mo-Cu alloy nanoparticles produced with an average composition of 70±1 at% Mo and 30±1 at% Cu showing nanoparticle size distribution of 16 ±2 nm.

Fig. 5-6(a) shows schematically relevant details of the bimetallic NP formation based on our gas phase synthesis process and the various chemical orderings that can be achieved within the NPs. Fig. 5-6(b) shows schematically the temperature drop/cooling rate of NPs with respect to the time of flight and for different Ar gas flow rates.

The sharp drop in the temperature after a certain time indicates that NPs are at the edge of the plasma region where the temperature drops very rapidly.

Thus, the thermal energy involved during the formation and growth of NP nuclei can be tuned opening the possibility to produce different structured NPs with the same composition.

During sputtering the energy that we can supply to the sputtered metal atoms through the Ar ions can be varied by using different discharge voltages and/or currents. Increasing the discharge current will increase the plasma density, which not only increases the energy of the growing species but also influences the temperature in the plasma and the cooling rate of NPs. This is because the energy dissipation rate between metal atoms and the more energetic Ar molecules (due to bombardment of highly energetic Ar ions) is reduced.
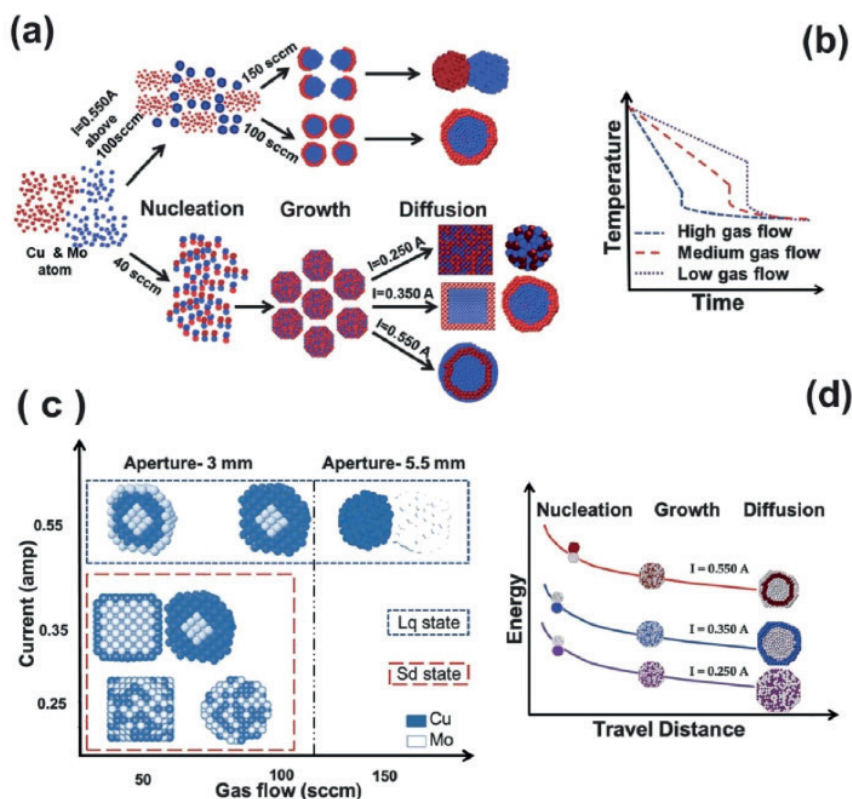
Figure 5-6 Schematic representation of the Mo–Cu NP formation including tuning of various structural motifs by controlling the thermal environment experienced by the NPs. (a) Formation mechanism of Mo–Cu NPs with various types of chemical ordering. (b) Effect of the gas flow rate (pressure) on the cooling rate experienced by the NPs. (c) The table shows the various structural motifs and shapes of Mo–Cu synthesized at various discharge currents and gas flow rates, Lq – Liquid state and Sd – Solid state indicate the NP formation state, the aperture size used for producing various structures is indicated as 3.0 and 5.5 mm. (d) Effect of the energy supplied (via discharge current) on various synthesized structures at a constant flow rate of Ar (e.g., 40 sccm in the present case).

Thus, varying the discharge current and Ar-gas flow (pressure) we can tune the temperature and the cooling rate along with the energy of the growing species.

Indeed, Fig. 5-6(c) shows a plausible overview of the different structural motifs of Mo–Cu that we could synthesize in a controlled and reproducible manner.

Fig. 5-6(d) gives an illustration of how the influence of thermal energy (different discharge current) can be utilized to prepare different motifs for a constant low gas flow rate.
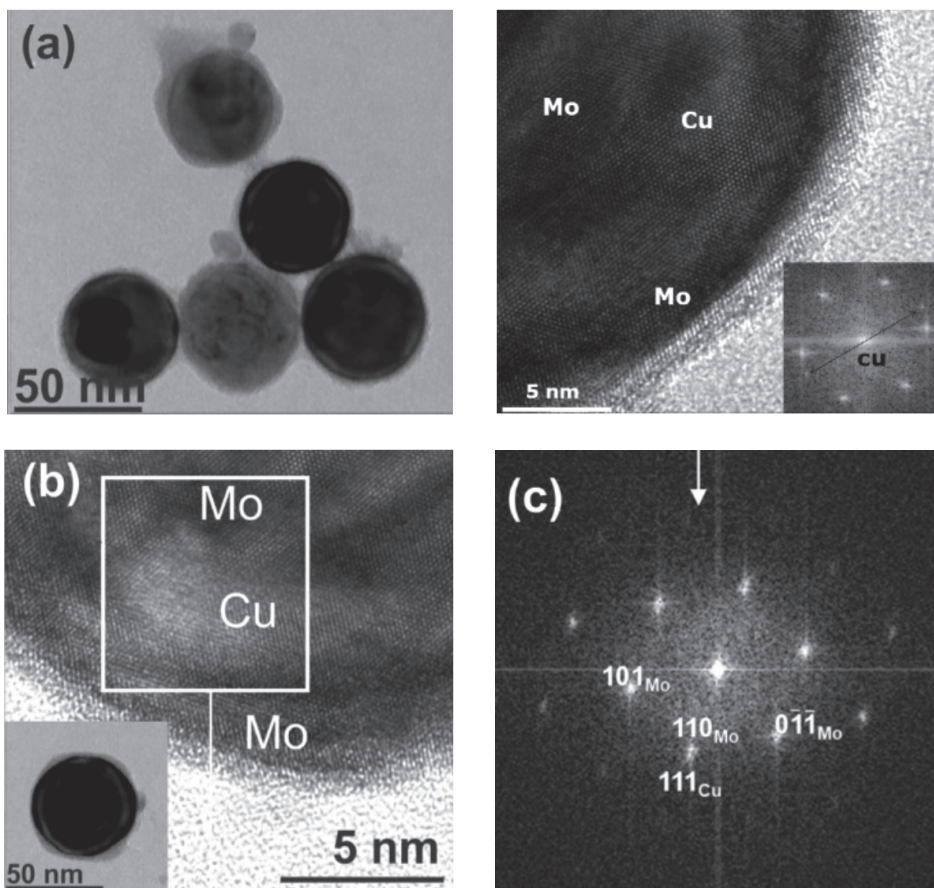
Figure 5-7 (a) Bright field TEM image of the Mo–Cu–Mo onion structured (multishell) NPs, I ¼ 0.55 A and Ar flow ¼ 40 sccm. (b) HRTEM image of the Mo–Cu–Mo showing the presence of Mo and Cu. The inset shows the bright field TEM image of the corresponding NP. (c) Fourier transform image of part of the HRTEM image in (b) indexed using a combination of a Mo{111} zone axis pattern and Cu(111) spots shows the presence of Mo(110) and Cu(111).

Having this background information, we will attempt to understand the reason behind the formation of Mo–Cu alloy and Mo–Cu core–shell structures, e.g., in Fig. 5-2 and 5-3. Initially, for the two flow rates (40 and 70 sccm) in Fig. 5-3 cube and spherical shaped alloy particles are formed.

However, with low gas flow rates reconstruction to cube shaped particles can occur during cooling, which is the expected morphology for pure Mo particles.[34–36] With higher gas flow rates there is insufficient time for the reconstruction and the particles remain spherical as observed. Although at the relatively low discharge current (≈0.250 A) the energy gained by Cu atoms in the plasma is just sufficient for mixing and formation of Mo–Cu solid solution, it is not sufficient to overcome the energy barrier leading to phase separation and Mo–Cu core–shell formation. The same result was also observed in the case of MoCu thin films, where only after annealing above 500°C phase separation and precipitation of Cu were observed.[37]Similarly, when we increase the discharge current or energy of the growing metal atoms it might be possible to form a core–shell structure for the same other settings. In fact, this was achieved in the case of Fig. 5-7 by increasing the discharge current to 0.350 A. As a result, the Cu atoms had sufficient energy to segregate to the surface and to enable phase separation.

Previous studies have shown oxidation driven de-alloying in Ag–Au alloy samples kept out of vacuum over an extensive period of time up to 2 years.[38] However, in our case the TEM analysis of the freshly prepared samples was completed in less than a week. Moreover, we examined the same Mo–Cu alloy NPs after six months and their structure remained unchanged, where the alloy was surrounded by an oxide shell. This confirms the fact that the Mo–Cu core–shell structure is formed during the production of NPs.

From the results depicted in Fig. 5-2, 5-3 and 5-4 we can understand that by further increasing the discharge current to 0.550 A at 40 sccm, one would expect a Janus shaped (dumbbell) or a core–shell structure to form.

Contrary to that Fig. 5-7 shows that these structures are not formed, but instead an onion structure Mo–Cu–Mo is formed.

Fig. 5-7(a) shows the bright field TEM image of the relatively monodisperse Mo–Cu–Mo NPs. The HRTEM image in Fig. 5-7(b) and the fast Fourier transform (FFT) image in Fig. 5-7(c) confirm that the onion structure is formed and consists of pure Mo and Cu shells. The FFT pattern displays double spots in the radial direction of the particle. This can be indexed using a combination of a Mo[111] zone axis pattern and Cu(111) spots. The alignment of the Mo(110) and Cu(111) spots implies an epitaxial relationship between two elements.

The HRTEM image also provides evidence for a hetero-epitaxy, as the crystal planes cross the alternating bright and dark contrast zones assigned to the different elements. This epitaxial

5

relationship was previously reported by Mundschau et al.[39] Both HRTEM images and diffraction patterns yielded lattice spacings that correspond to only pure Mo and Cu excluding Mo–Cu alloy formation. This holds for most of the NPs produced under these conditions. In Fig. 5-8 the contrast in the HRTEM image also shows the presence of the two different shells containing only Cu and Mo. The contrast originates from compositional variation and it is not related to the thickness effects, as observed previously by Ferrer et al. for multishell AuPd NPs.[39]

We observed the onion structure only for bigger NPs, which is similar to the other reported studies since phase segregation occurs for bigger NPs.[33,40] The principal reason for onion structure formation is likely related to the fact that with a higher discharge current the NPs nucleate and grow in the liquid state.

By contrast in the previous cases (e.g., Fig. 5-3 and 5-4) where the NPs were formed in the solid state.
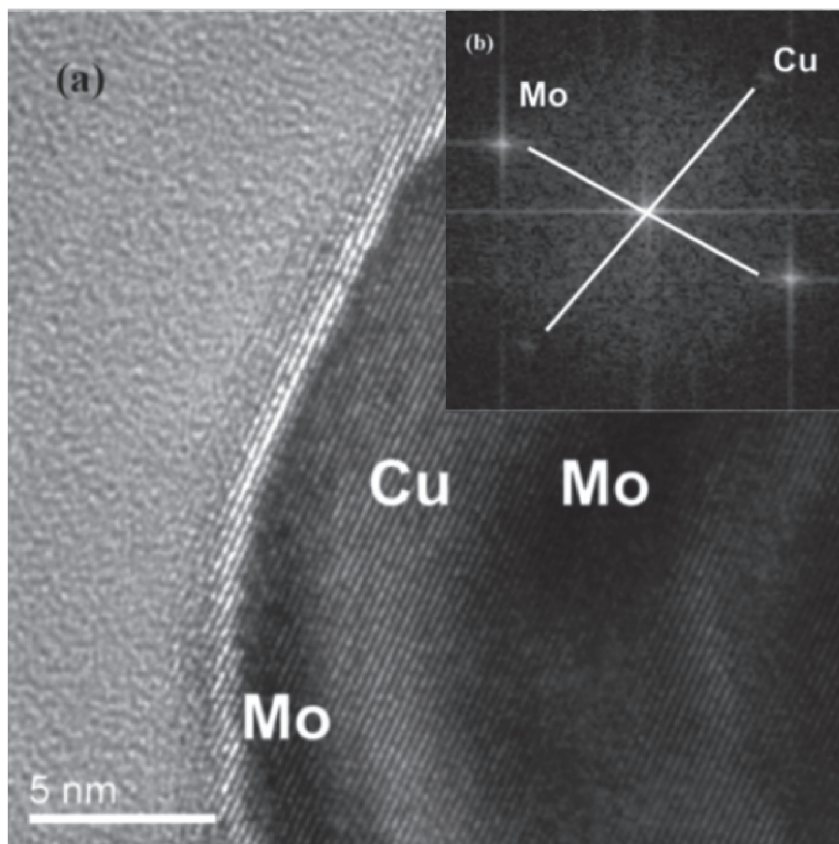
Figure 5-8. (a) HRTEM image of the Mo-Cu-Mo onion structure (b) FFT of the image showing the presence of pure Cu along with pure Mo.
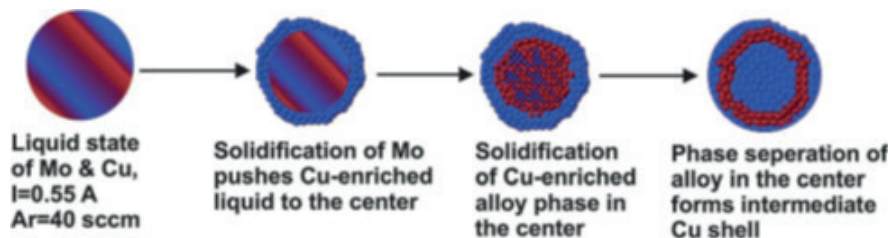
Figure 5-9 Schematic illustration of the formation mechanism of Mo–Cu–Mo onion structures.

Fig. 5-9 shows schematically the formation mechanism of the onion structures. The large size and spherical shape of the particles also reflect the liquid phase origin of the NPs. The excess kinetic energy has been used in the process of growth by collision of Mo and Cu nuclei and this in turn causes the melting of the NPs.

During solidification, Mo will tend to solidify first, because it has a higher melting point than Cu (T_{Mo} =2890.15 K and T_{cu}=1356.15 K). Solidification in a NP is a surface phenomenon (solidification occurs by collision with external species like Ar gas atoms) that leads to Mo solidification at the surface, while it drives Cu to the center of the NPs.[33]

Also from the literature it has been identified that the preferred sites for Cu growth inside the NPs are at the subsurface (just below the surface of the NPs) or at the center of the NPs.[30,41] Therefore Cu does not have sufficient energy or time to reach the surface, since the diffusion of Cu atoms starts from the interior of the NPs (in the liquid state Cu is pushed to the center of the NPs during slow solidification), and as a result it only gives rise to an intermediate layer of Cu in agreement with our observations.

Fig. 5-10(a) shows Mo–Cu core–shell NPs with a spherical shape having a size (distribution) of ≈16+/- 4 nm. To form these core–shell NPs with only one kind of morphology say spherical, we have used the highest discharge current of 0.550 A so that the NPs can grow in the liquid state. Note the difference between Fig. 5-3 and 5-11, where in Fig. 5-3 both spherical and cube shaped NPs are present, whereas in Fig. 5-11 only the spherical morphology is present. Compared to Fig. 5-7, which corresponds to the same discharge current, here a much higher gas flow rate was used (100 sccm; 40 sccm in Fig. 5-7).

Simultaneously as the cooling from high temperatures is rapid, the atoms lose their energy very rapidly during NP nucleation. Under these conditions only Mo is able to form stable nuclei. This is due to the fact that the kinetic energy of the sputtered Cu atoms is always higher than Mo due to its high energy transfer function and lower bond energy.[32,43,44] Simultaneously the high Ar gas flow rate (velocity of the NPs is proportional to the gas flow rate before the aperture of the aggregation volume is reached) will increase the velocity of the NPs forcing them to move

faster out of the plasma region. As a result Cu does not have sufficient time to lose efficiently its kinetic energy and form stable nuclei. Instead, Cu grows on Mo that is serving as the nuclei for the Cu shell, similar to the observation by Yin et al.[32,41,42] This conclusion is also based on the experimental fact that we do not observe any Cu NPs under these conditions.

Fig. 5-11(b) shows a HRTEM image of the Mo–Cu core–shell NPs (where the Cu-oxide shell is formed during ex situ transfer to the TEM). By increasing the Ar gas flow rate further to 150 sccm, we were able to achieve a very thin Cu-oxide shell as observed in TEM of only ≈1 to 2 nm thickness. The thinner Cu shell is the result of the high velocity of NPs leaving faster the plasma region. Therefore, this method (with variation of the gas flow rate) can be effectively employed to tune the Cu shell thickness around the Mo core.
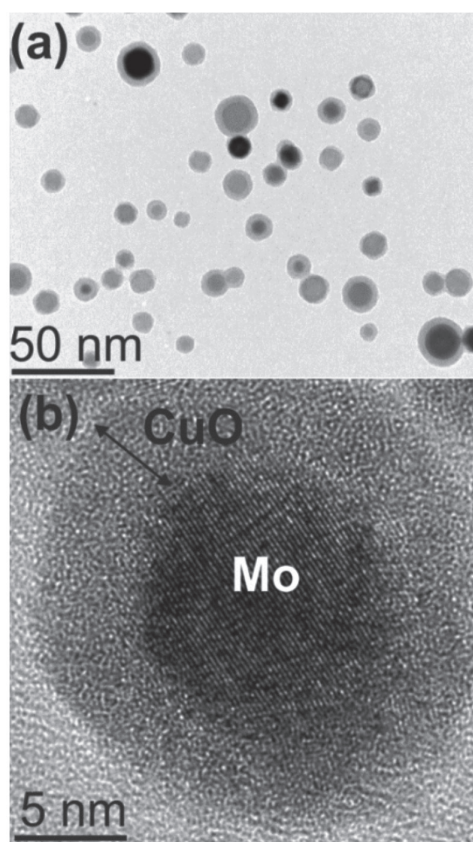
Figure 5-10 Mo–Cu core–shell NPs with only spherical shape, I=0.55 A and Ar flow =100 sccm. (a) Bright field TEM image of the Mo–Cu NPs with an average size of ≈16+/- 4 nm. (b) HRTEM image of the Mo core with {110} atomic planes resolved and with an amorphous Cu-oxide shell, which is possibly formed during ex situ transfer to the TEM.

By maintaining the same discharge current, but increasing the flow rate of Ar (150 sccm) further and increasing the aperture size (5.5 mm) at the end of the aggregation volume finally we were able to synthesize Mo–Cu NPs with a Janus/dumbbell structure. The principle for achieving this set of particles is the same as that described for the NPs shown in Fig. 5-11 The larger aperture (thus increasing the pumping rate of the aggregation volume through the aperture) increases the velocity of the emerging NP and in turn reduces the time for Cu to completely coat the Mo core. As a result a Janus type Mo–Cu structural motif emerges as is shown by the HRTEM image in Fig. 5-11

5
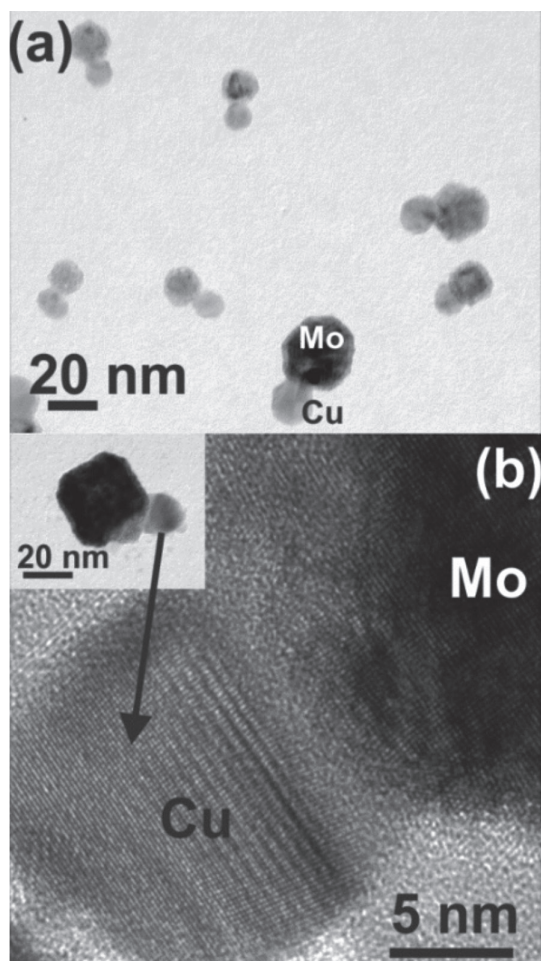
Figure 5-11 (a) Bright field TEM image of Mo–Cu Janus type NPs, I=0.55 A and Ar flow=150 sccm (aperture size =5.5 mm). (b) HRTEM image showing a phase separated Janus structure with the Cu{111} and Mo{110} lattice spacings resolved. The inset shows the corresponding NP at a lower magnification.

5.5   Conclusions

We have presented a gas phase method for tuning the structural motifs of otherwise bulk immiscible Mo–Cu NPs having both high quality and clean surfaces/interfaces. This method is feasible by tailoring the plasma energy, the cooling rate, and the diffusion process experienced by the NPs during their gas synthesis. The structural motifs range from completely alloyed particles with either cube or spherical shape, Mo–Cu core–shell particles with cube or spherical shape, spherical 'onion' Mo– Cu–Mo particles (intermediate Cu shell), and Janus/dumbbell type Mo–Cu NPs. The critical size for alloying Mo–Cu, e.g. for forming NPs in which Mo and Cu are completely mixed, is in our work considerably larger (closely to an order of magnitude) than has been reported before for bulk immiscible binary NPs. In this case also an effect of shape was observed, because alloyed cube particles were observed to be larger (having thus a larger critical size) than alloyed spherical particles. In principle, the method proposed in the present work can be extended to other bimetallic systems in order to tune NPs with different types of chemical ordering important for a wide range of research fields and applications in nanoplasmonics, catalysis, biodiagnostics, and nanomagnetics

5.6   References

[1]   J. P. Wilcoxon and B. L. Abrams, Chem. Soc. Rev., 2006, 35, 1162.

[2]   R. Fernando, J. Jellinek and R. Johnston, Chem. Rev., 2008,
108, 845.

[3]   A. E. Russell and A. Rose, Chem. Rev., 2004, 104, 4613.

[4]   V. R. Stamenkovic, B. Fowler, B. S. Mun, G. F. Wang,
P. N. Ross, C. A. Lucas and N. M. Markovic, Science, 2007,
315, 493.

[5]   E. Prodan and P. Nordlander, Nano Lett., 2003, 3, 543.

[6]   V. Skumryev, S. Stoyanov, Y. Zhang, G. Hadjipanayis,
D. Givord and J. Nogues, Nature, 2003, 423, 850.

[7]   C. Burda, X.-B. Chen, R. Narayanan and M. A. El-Sayed,
Chem. Rev., 2005, 105, 1025.

[8]   C. N. R. Rao, G. U. Kulkarni, P. J. Thomas and P. P. Edwards,
Chem. Soc. Rev., 2000, 29, 27.

[9]   Z. Y. Li, J. P. Wilcoxon, F. Yin, Y. Chen, R. E. Palmer and
R. L. Johnston, Faraday Discuss., 2008, 138, 363.

[10]   S. Alayoglu and B. Eichhorn, J. Am. Chem. Soc., 2008, 130, 17479.

[11]   F. Tao, M. E. Grass, Y. Zhang, D. R. Butcher, J. R. Renzas,
Z. Liu, J. Y. Chung, B. S. Mun, M. Salmeron and
G. A. Somorjai, Science, 2008, 322, 932.

[12]   S. E. Habas, H. Lee, V. Radmilovic, G. A. Somorjai and P. Yang, Nat. Mater., 2007, 6, 692.

[13]   S. Piccinin, S. Zafeiratos, C. Stamp, T. W. Hansen,
M. Havecker, D. Teschner, V. I. Bukhtiyarov, F. Girgsdies,
A. Knop-Gericke, R. SchlVogl and M. Scheffler, Phys. Rev. Lett., 2010, 104, 035503.

[14]   D. Zitoun, M. Respaud, M. C. Fromen, M. J. Casanove,
P. Lecante, C. Amiens and B. Chaudret, Phys. Rev. Lett., 2002, 89, 037203.

[15]   L. M. Liz-Marzan, Langmuir, 2006, 22, 32.

[16]   D. Alloyeau, C. Ricolleau, C. Mottet, T. Oikawa, C. Langlois,
Y. Le Bouar, N. Braidy and A. Loiseau, Nat. Mater., 2009, 8, 940.

[17]   W. H. Binder, Angew. Chem., Int. Ed., 2005, 44, 5172.

[18]   Z. M. Peng and H. Yang, J. Am. Chem. Soc., 2009, 131, 7542. 19 S. Kim, S. K. Kim and S. Park, J. Am.
Chem. Soc., 2009, 131, 8380.

[20]   Y. Vasquez, A. K. Sra and R. E. Schaak, J. Am. Chem. Soc., 2005, 127, 12504.

[21]   L. H. Liang, G. W. Yang and B. W. Li, J. Phys. Chem. B, 2005, 109, 16081.

[22]   S. Xiao, W. Hu, W. Luo, Y. Wu, X. Li and H. Deng, Eur. Phys. J. B, 2006, 54, 479.

[23]   J. M. Martinez De La Hoz, R. C. Tovar and P. B. Balbuena,
Mol. Simul., 2009, 35, 785.

[24]   S. Xiong, W. Qi, B. Huang and M. Wang, ChemPhysChem, 2011, 12, 1317.

25 S. Darby, T. V. Mortimer-Jones, R. L. Johnston and C. Roberts, J. Chem. Phys., 2002, 116, 1536.

26 F. Chen, B. C. Curley, G. Rossi and R. L. Johnston, J. Phys. Chem. C, 2007, 111, 9157.

27 M. Zhang and R. Fournier, THEOCHEM, 2006, 762, 49.

28 M. D. L. Hoz, J. M. Tovar, R. Callejas and P. Balbuena, Mol. Simul., 2009, 35, 785.

29 G. Rossi, A. Rapallo, C. Mottet, A. Fortunelli, F. Baletto and R. Ferrando, Phys. Rev. Lett., 2004, 93, 105503.

30 F. Baletto, C. Mottet and R. Ferrando, Phys. Rev. Lett., 2003, 90, 135504.

31 J.-M. Qiu and J. P. Wang, Adv. Mater., 2007, 19, 1703.

32 F. Yin, Z. W. Wang and R. E. Palmer, J. Am. Chem. Soc., 2011, 133, 10325.

33 Y.-H. Xu and J.-P. Wang, Adv. Mater., 2008, 20, 994.

34 A. S. Edelstein, G. M. Chow, E. I. Altman, R. J. Colton and D. M. Hwang, Science, 1991, 251, 1590.

35 F. H. Kaatz, G. M. Chow and A. S. Edelstein, J. Mater. Res., 1993, 8, 995.

36 T. Vystavel, S. A. Koch, G. Palasantzas and J. Th. M. De Hosson, Appl. Phys. Lett., 2005, 86, 113113.

37 G. Ramanath, H. Z. Xiao, L. C. Yang, A. Rockett and L. H. Allen, J. Appl. Phys., 1995, 78, 2435.

38 D. Beli´c, R. L. Chantry, Z. Y. Li and S. A. Brown, Appl. Phys. Lett., 2011, 99, 171914.

39 M. Mundschau, E. Bauer and W. ´Swiech, J. Appl. Phys., 1989, 65, 581.

40 D. Ferrer, A. Torres-Castro, X. Gao, S. Sepu´lveda-Guzm´an, U. Ortiz-M´endez and M. Jos´e-Yacam´an, Nano Lett., 2007, 7, 1705.

41 G. Krishnan, G. Palasantzas and B. J. Kooi, Appl. Phys. Lett., 2010, 97, 131911.

42 G. Krishnan, G. Palasantzas and B. J. Kooi, Appl. Phys. Lett., 2010, 97, 261912.

43 B. Chapman, Glow Discharge Processes, Wiley, New York, 1980.

44 T. J. Konno, S. Yamamuro and K. Sumiyama, J. Vac. Sci. Technol., B, 2002, 20, 834.

5

Chapter 6
Roughness controlled superhydrophobicity on a single nanometer length scale with metal nanoparticles

6.1   Abstract

Here we demonstrate high water pinning nanostructures and trapping of water droplets onto surfaces via control of roughness on a single nanometer length-scale generated by deposition of preformed gas phase distinct copper nanoparticles on hydrophilic and hydrophobic surfaces. It was found that the contact angles of the water droplets were increased to the superhydrophobic limit ~150º at high nanoparticle coverages (≥80 %) independent of the initial type of surface. The water droplets were trapped onto the surfaces by high adhesion forces similar like the rose petal effect. The droplets are in a Wenzel state at their outer part. Local nanocapilary can force liquid into crevices between nanoparticles and push trapped air within the center of the droplet forming a Cassie-Baxter metastable state. Hence our approach to alter the wetting state is extremely straightforward without involving special micro/nano structuring facilities, but instead using direct single nanoparticles deposition on any type of surfaces creating a rough surface on a single nanometer length-scale, allowing due to its peculiar high water pinning and nanoporous structure liquid trapping phenomena.[3]

---

[3]*G.H. ten Brink, N. Foley, D. Zwaan, B.J. Kooi, and G. Palasantzas, RSC Adv 5, 28696 (2015).*

6.2   Introduction

Wetting of liquids over material surfaces is a topic studied for the last 200 years both from the fundamental and application point of view.[1-20] Just to mention a few examples, wetting is important for self-cleaning, anti-icing, the adhesion of material surfaces, stiction issues in microelectromechanical systems (MEMS), Gecko's feet[21], capillarity phenomena, reduced fluid drug in micro/nanofluidic systems etc.. Moreover, trapping of water drops by modification of surface wettability can play important roles in the efficiency of drop condensation from vapor in heat exchangers and fog harvesters[22-25] and anti-fogging of windows and glasses.[26]

The surface wettability is measured by the contact angle θ between a water droplet and the surface to which itt is attached. A surface that gives a contact angle (CA) smaller than 90° is termed as hydrophilic, while one with larger than 90° is termed as hydrophobic. The creation also of superhydrophobic surfaces (q>150º) has attracted enormous attention[10-12], where examples in nature include the feathers of ducks, butterfly's wings or the leaves of the lotus plant.[16,27-30] It is believed that the origin of this bio inspired superhydrophobicity is only achieved by incorporating roughness on multiple length-scales.[21,31-35]
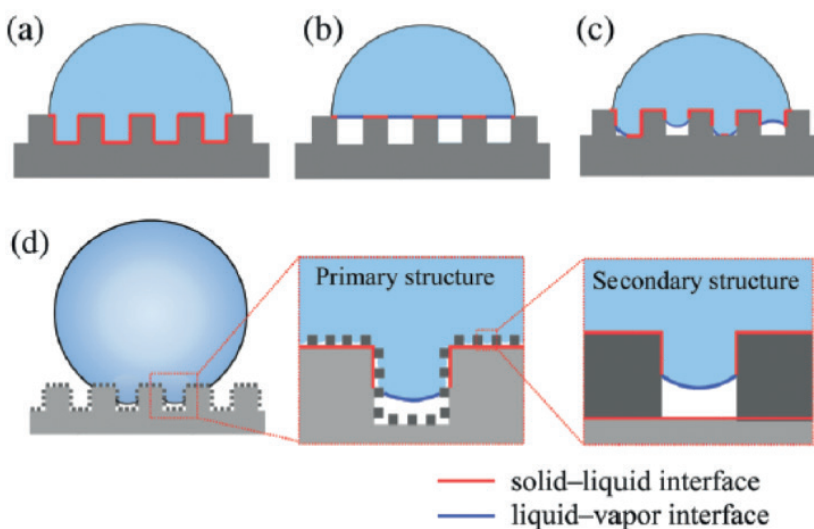
Figure 6-1 Schematic illustrations of a Wenzel and a Cassie-Baxter state for a liquid drop on top of a rough substrate: (a)Wenzel model, (b) Cassie–Baxter model, (c) partial wetting model for a one-scale structured surface and (d) partial wetting model for a dual-scale structured surface. The red and blue lines indicate the ratio of the solid–liquid interface and liquid–vapor interface, respectively. Adapted from Soft Matter, 2020,16, 3514[76]

Figure 6-1 illustrates the basic wetting surface states (hydrophilic/hydrophobic), where for flat surfaces, θ_Y is given by the Young's equation[1]:

$$\cos \theta_Y = (\gamma_{sg} - \gamma_{sl})/\gamma_{lg} \quad \textbf{(6.1)}$$

with g_{sg}, g_{sl} and g_{lg} the solid-gas, solid-liquid and liquid-gas interface energies, respectively. Surface chemistry and roughness play key roles in manipulating wetting phenomena in order to tame surface wettability by proper surface modification.[13–20,28–30,36–38]

For roughness effects, one may consider the Wenzel (W) model.[19] where the contact angle θ_w is given by:

$$\cos \theta_W = R_W{}^* \cos \theta_Y \quad \textbf{(6.2)}$$

with R* the ratio of the actual area of the solid/liquid interface to the normally projected area. This model suggests that a hydrophilic surface would be more hydrophilic with surface roughness, while a hydrophobic surface would be more hydrophobic. Moreover, it assumes complete contact of the liquid with the surface.

Figure 6-1(d)[76] implying that the droplet will not roll off the surface leading to large hysteresis between advancing and receding contact angles. However, liquid droplets on a rough surface are not expected to wet all surface crevices. In this composite or Cassie-Baxter (CB) state (Fig. 6-1), the droplet rests on surface protrusions and air pockets in between surface features[20] resulting in a higher contact angle.

Low hysteresis allows the droplets to roll off the surface easier, which is called the Lotus effect. In this model the contact angle θ_{CB} is given by:

$$\cos \theta_{CB} = f \cos \theta_Y - (1 - f) \textbf{(6.3)}$$

where f is the fraction of the solid surface area in contact with the liquid. This model allows for hydrophobicity on a rough surface, even if the flat surface is hydrophilic.

During the CB→W transition the air pockets are no longer thermodynamically stable and liquid nucleates within the crevices.[39]

Nowadays the major strategies to form hydrophobic and superhydrophobic surfaces combine roughening of a hydrophobic surface with additional alteration of the surface chemistry using low surface energy materials.[13–20,28–30,36–38,40] These endeavors aim to mimic the structure of the lotus leaf or butterfly wings that have strong water repellency and self-cleanliness.[16,28–30,41,42]

Another possibility is the rose petal effect where a superhydrophobic state exists with a high adhesive force towards water.

Other methods to create surfaces with adjusted wettability or hydrophobicity include micro scale roughness[21,28,33–35,41–43], where the roughness can be either random or structured. The structured micro scale roughness, which can take a form resembling a grid of pillars or nail heads sticking out of the surface, have attracted interest for making superhydrophobic and possibly omniphobic surfaces.[28,36–38,41,42.] Recently, it has also been shown that nanometer-size textures could facilitate more resilient coatings owing to geometry and confinement effects at the nanoscale.[40] It was revealed that the superhydrophobic state vanishes above critical pressures which depend on texture shape and size but this phenomenon was irreversible only for conical surface features.[40] A thermodynamic analysis of the possibility of making high-contact-angle rough surfaces from low-contact-angle materials has been also considered.[44] The high contact-angle state may not be stable and transition from the heterogeneous (CB) wetting regime to the homogeneous (Wenzel) regime with a lower contact angle may occur.[44] Theoretically it is possible to make a hydrophobic surface from a hydrophilic material if surface roughness is multivalued.[44]

Although micro- and nanoscale surface roughness can lead even to superhydrophobicity, the control of wettability via control of the nanostructure of surfaces is far from trivial.[31,33–35,43,45–47] Therefore, we propose here decorating surfaces with preformed single distinct metallic nanoparticles (NPs) as an attractive route to control surface wettability by varying the coverage and size of the deposited NPs, and subsequently only the single scale nanoscale surface roughness.

The challenge in forming hydrophobic surfaces from hydrophilic materials, as holds for metallic NPs oxidized at their outer surfaces, lies also in designing surface topographies that will lead to very high but stable contact angles. For this reason in order to avoid having different surface chemical compositions, samples were made with Cu NPs deposited onto flat copper surface (roughness much lower than the deposited NP sizes).
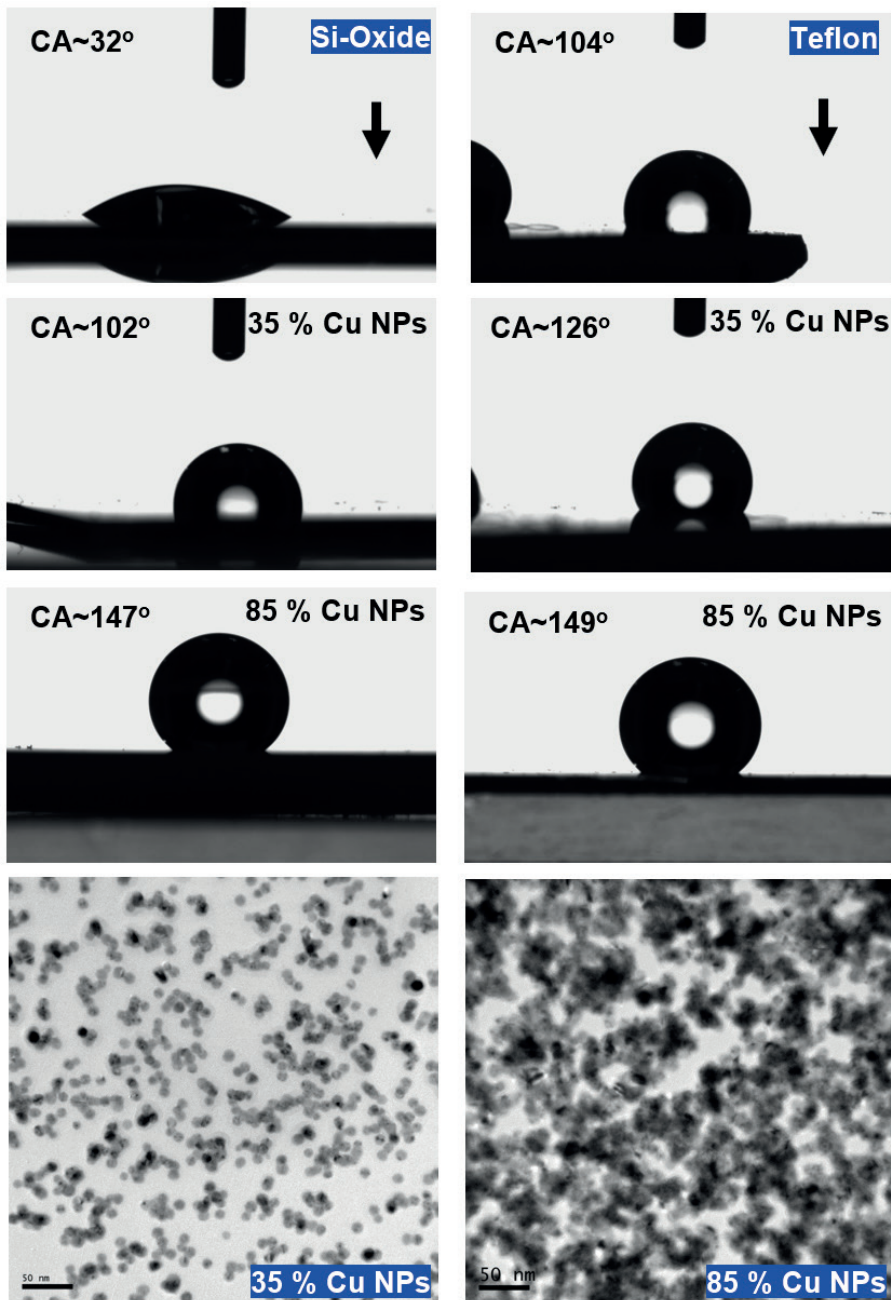
Figure 6-2 Contact angles between a water droplet and Si-oxide (left column) and Teflon (right column) surfaces (bare and with Cu NPs coverages as indicated). The bottom images are BF-TEM images to illustrate what the corresponding NP coverages mean

In addition, comparison is made with the same Cu NPs deposited on oxidized silicon wafers and on polished Teflon surfaces.

6.3   Experimental methods

The nanoparticles studied in this research were produced by using plasma sputtering in a home-modified Mantis Nanogen 50 unit. A 2-inch silicon wafer was prepared for samples by coating it with a homogeneous 20 nm thick layer of copper as a starting (relatively flat) substrate surface.

The homogeneity and roughness of the surface were assessed with a Veeco Nanoscope V atomic force microscope (AFM) in combination with Nanoscope Analysis v1.4 image analysis software.

The first set of samples were all made using the same settings to ensure the NPs were of the same size, and only the deposition time was varied between samples to get varying degrees of coverage on the surface.

For the second set of samples the deposition time was kept the same to keep the same degree of coverage, but other settings were varied in order to obtain varying size NPs. In addition, transmission electron microscope (BF-TEM) samples underwent deposition simultaneously as those for the contact angle measurements, and they were analyzed in an FEI Tecnai G2 20 TEM or a JEOL 2010 TEM to enable calculation of the surface coverage and measurement of the NP size (Fig. 6-2).

The images produced by the TEM were analyzed with Image-Pro Plus v4.5 image processing software.[48]

6.4   Results and discussion
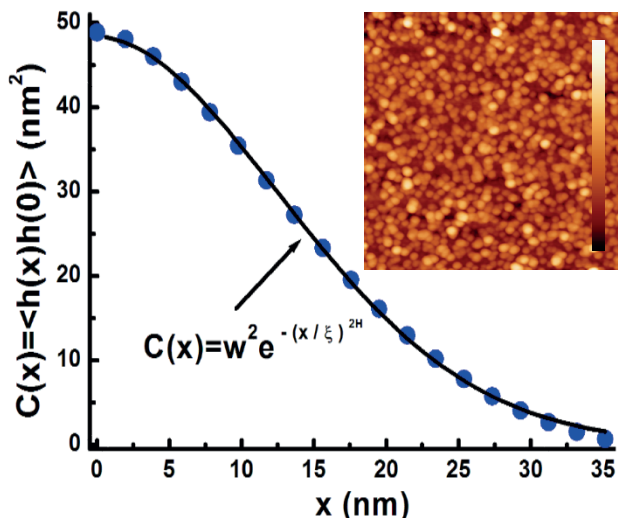
Figure 6-3 Height-height autocorrelation function (from the AFM image in the inset) C(x) =<h(x) h (0)> along the fast scan x-direction (and averaged along 512 lines in the slow scan y-direction) with the corresponding roughness parameters (w=6.9 nm, x=18.2 nm, and H=0.95 the roughness exponent) obtained from fitting a typical stretched-exponential form. The inset shows an AFM image with scan size 1x1 mm^2 of deposited Cu NPs with the indicated height scale from ~17 – 37 nm.

The AFM images of all the samples, e.g. see insert in Fig. 6-3, were taken over an area 2 μm2 to calculate the surface area difference (SAD) roughness and the root mean squared (RMS≡w) roughness.

The SAD roughness was calculated by the Nanoscope image Analysis v1.4 software using the formula:

$$SAD = (R_a / R_p - 1) \times 100\% \quad \text{(6.4)}$$

where Ra is the actual surface area and Rp the projected surface area. Correlation function analysis from the AFM topography data, as in Fig. 6-3, yielded all necessary roughness parameters (besides w, one obtains the roughness exponent H and the lateral roughness correlation x) to estimate the average local surface slope.[49]

The obtained average surface local slopes $\rho = tan(\phi) \approx w/\xi$ were significant (j~20°) indicating the formation of relatively steep local nanoscale topology.

The equation shown in the figure:

$$\theta_m = 71.2 + 9.8\Theta^{0.43}$$
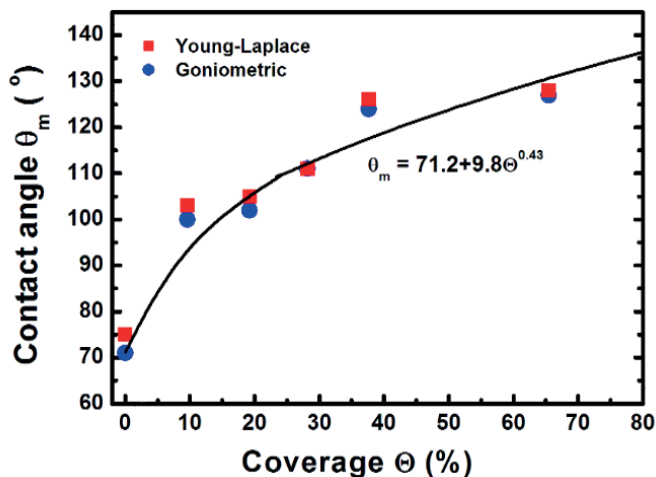
Figure 6-4 Dependence of contact angle on the coverage of Cu NPs, all having similar sizes of ~12 nm, on flat Cu surfaces.

6

Finally, the contact angle measurements (Figures 6-4,5,6) were performed using a Dataphysics OCA20 system. An automated syringe dropped ~2 μl droplets of pure water (MilliQ) on to the sample, where a high-speed camera recorded the pictures over a period of several seconds and fed them through to the Dataphysics SCA20 2, v4.1.17 build 1024 image processing software.

The values of the contact angle were obtained via a direct fit for the interface region only and a fit using the Young-Laplace (YL) equation based on shape analysis of a complete drop. (See Fig 6-4) for comparison of both methods.[50–52]

For every sample the CA measurements were repeated and averaged from seven drops of water.
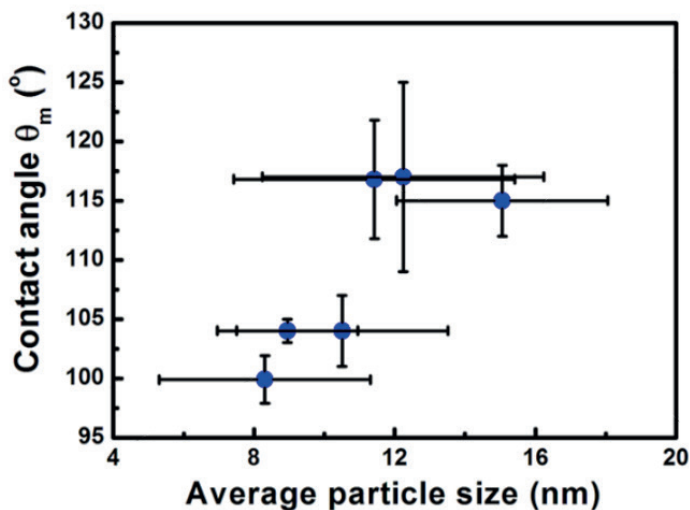
Figure 6-5 Dependence of contact angle on the particle size for similar NP coverages of ~40 % on flat Cu surfaces.

Figure 6-2 illustrates that deposition of a moderate NP coverage (~35 %) on a hydrophilic surface (e.g. Si-oxide) leads to fast transition to a hydrophobic surfaces, while if NPs are deposited on hydrophobic surfaces (e.g., as Teflon) the effect is less pronounced. However, at elevated NP coverages (> 80 %) then the surfaces become superhydrophobic (~150°) with the NP topology dominating the wetting state irrespective of the underlying substrate.

Moreover, the contact angle of a water droplet on the bare oxidized Cu substrate was measured to be ~75°, which is similar to the contact angle on flat lotus leave wax ~74°,[39] and increased by subsequent deposition of NPs (which are also surrounded by an oxide shell.[48] Figures 6-4,5,6 illustrates in more detail the relation between coverage, surface roughness (SAD and RMS), and contact angle.

The contact angles were measured after sufficient time for the droplet to adjust to its final shape. The error bars in the graphs represent twice the calculated standard deviation of the contact angles measured.
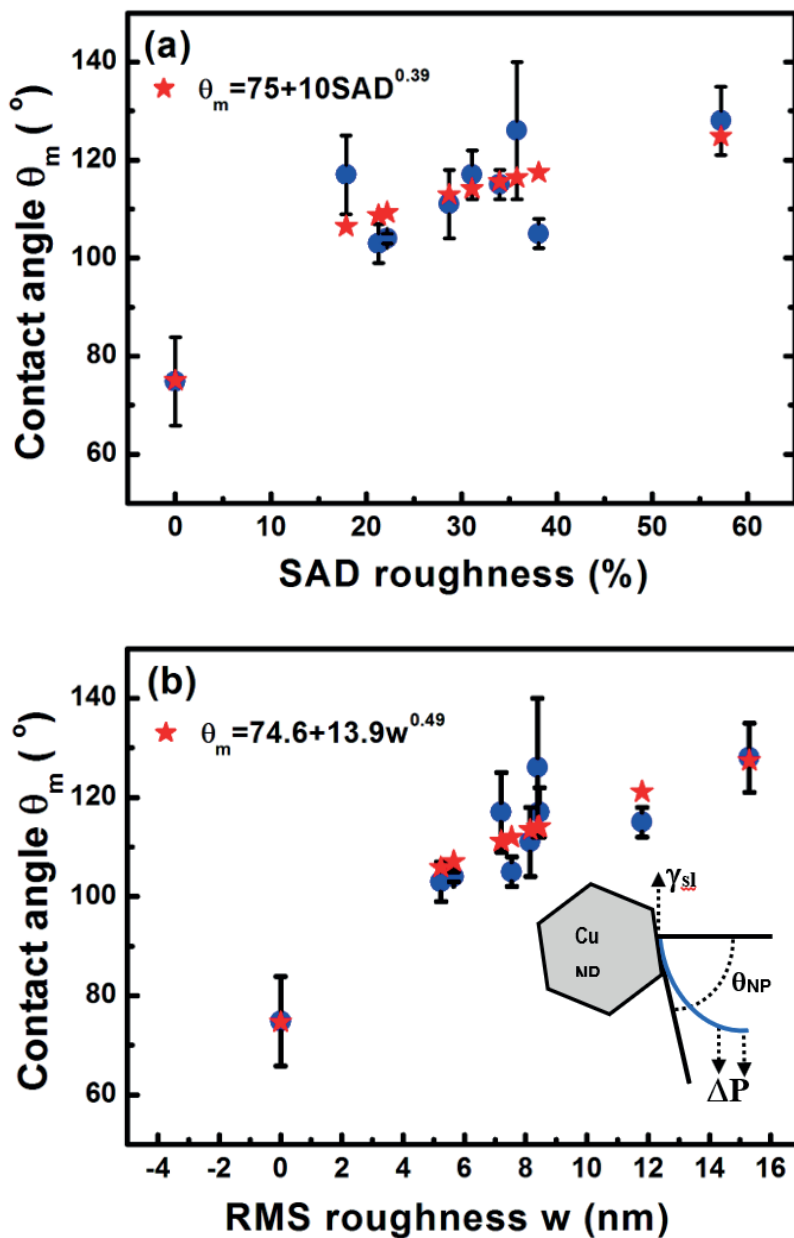
Figure 6-6(a) Dependence of contact angle on SAD roughness (%). (b) Dependence of contact angle on RMS roughness w (nm). The inset shows the simple geometry to estimate the maximum pressure for a transition from the Casie-Baxter to the Wenzel state.

The measured contact angle (q_{m}) in Fig.6-4 increases non-linearly with NP coverage (Q) above the value of bare surface following a power law behavior with coverage as $q_{\mathrm{m}} \sim Q^{0.43}$. The measured contact angle was ~130° at coverage of $Q \sim 65.5\%$, which is as expected below the superhydrophobic limit ~150°.

On the other hand in order to investigate the influence of particle size, the NP surface coverage (which is difficult to control precisely) was kept ~40%. The measurements in Fig. 6-5 imply that larger particles at the same coverage lead to a higher contact angle. If we investigate further the relation of the contact angle with SAD and RMS roughness, then, as shown in Fig. 6-6, similar power law dependences emerge $q_{\mathrm{m}} \sim SAD^{0.39}$ and $q_{\mathrm{m}} \sim w^{0.49}$, respectively. If we define the rough surface area as:

$$R_A = \int \sqrt{1 + (\vec{\nabla} h)^2} \, d^2 \vec{r} \quad \textbf{(6.5)}$$

where $h(\vec{r})$ is the local surface height at the lateral position $\vec{r} = (x, y)$, then for relatively weak local roughness ($\rho \approx w/\xi << 1$) we have after expansion: $R_A \approx R_P(1 + \rho^2/2 \dots)$

with $R_P = \int d^2 \vec{r}$.[49,53,54] Thus we obtain for the SAD roughness (to lowest order)

$$SAD \approx (\rho^2/2) \approx w^2/2\xi^2 \quad \textbf{(6.6)}$$

If we consider the power law dependence $q_{\mathrm{m}} \sim SAD^{0.39}$ from Fig. 6-6a, then we obtain $\theta_m \sim w^{0.78}$ in qualitative agreement with the power law obtained in Fig. 6-6b taking into account that in the expansion for SAD more terms $J(w/x)$ are in principle necessary, since w/x has significant values (~0.3) as shown for example by the AFM roughness analysis from Fig. 6-3.

Although one would think that a water drop on a rough surface is more likely to be in a Cassie-Baxter (CB-) state, the water droplets here appear to be in a Wenzel (W-) state. This conclusion is drawn empirically from the fact that as the water droplets were evaporating the area where they were making contact on the surface remained constant, meaning that the contact angle decreased with droplet evaporation time, as well as droplets remained pinned onto the surface independent of surface inclination and dynamic agitation.[32,45] However, more justification is necessary, because the weight of the liquid droplets used for the contact angle measurements causes only a pressure of at most several tens of Pascals (N/m²), which is insufficient to force liquid into surface nanocrevices.

The transition between the CB- and W-states is determined from the Laplace pressure: $\Delta P = P_{\mathrm{Liquid}} - P_{\mathrm{Air}}$ (assuming no drop impact as is the case here), which is the main contribution in terms of external forces.[38–45] It can induce the CB-W transition either via de-pinning from the

apex of surface features (if the contact angle formed by the liquid-air interface is greater than the maximum contact angle that can be sustained on the surface features), or via the sagging mechanism if liquid can reach the bottom of the surface. Even when a liquid-air interface can remain pinned at feature tops, the transition to the Wenzel state is possible.[61]

This is most likely to occur in our case taking into account the small groove depth of ~50 nm (e.g., see the scale bar of the AFM image in Fig. 6-3).

6
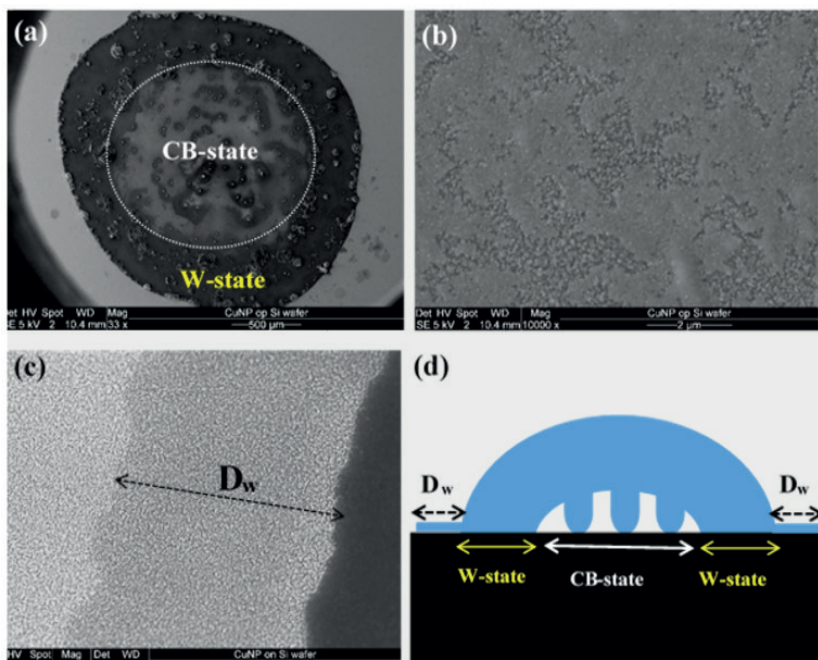
Figure 6-7 Signatures of droplet evaporation for Cu NP/Si surfaces with high (~85 %) NP coverage (see TEM image Fig.6-2) obtained with scanning electron microscopy (SEM): (a) Large overview with the CB-state indicated for clarity with a circle, and the W-state occurring within the dark area having lots of debris, (b) Higher resolution area of the NP topography within the CB-state area, (c) Completely wetted area of NPs in front of the W-state area, (d) Diagram explaining the W- and CB-state formation underneath the liquid drop.

Scanning electron microscopy investigation of the Si surfaces with high NP coverage (e.g., ~85 % in Fig. 6-12) after the liquid drops were evaporated, see Figure 6-7, showed that we deal with a rather complex structure where the outer part of the drop is in a W-like state, while air pockets still persist within the middle part of the drop which thus remains in a CB state (Fig. 6-7d). Moreover, in front of the drop circumference it appears that a fully wetted area with size D_w~5 μm (see Fig.6-7c) had been formed, while after water evaporation the area where a W-state persisted the surface features

strongly altered leading to complete removal of NPs or to their coalescence to larger structures.

However, within the central area, where a CB-state persisted, the surface NP structure is significantly less affected though alterations of the NP structures still occurs. See Fig. 6-12.

Since the NP surfaces are hydrophilic (at least an oxidized metal shell is present around the NP), they attract water forming nanocapillaries through the surface crevices and nanoporous NP assembly. As a result the pressure difference over the water–air interface increases driving the interface down more into the space between the NPs. Eventually the hydrophobic state collapses and water penetrates close to the bottom of the structures.[55–60,62,63] The vertical force due to pressure on the hanging air–water interface in a surface crevice is the Laplace pressure ΔP multiplied by the horizontal projection area A_{aw} of the air-water interface. This force in effect balances the vertical component of the surface tension,γ_{sl}, along the wetting line at the NPs top assuming an angle θ_{NP} that the vector tangent to the interface and normal to the boundary forms with the xy-plane (the contact angle is $\theta_{NP}+90°$, inset Fig. 6-6b.[55–57] Therefore we obtain $\Delta P = \gamma_{sl}\sin\theta_{NP}(S_{NPS}/A_{aw})$, with S_{NPS} the arc-length of the section of the boundary associated with the contact line between NPs.[55]

Thus the maximum Laplace pressure: ($\theta_{NP}=90°$) is:

$$\Delta P_{max} = \gamma_{sl}(S_{NPS}/A_{aw}) \quad \textbf{(6.7)}$$

For an estimation of ΔP_{max} we considered a surface consisting of a square array of cylindrical NPs of top diameter D at a separation that of the lateral correlation length x obtained by AFM analysis (see Fig. 6-3).

Thus we have:

$$\Delta P_{max} \approx \gamma_{sl}\pi D/(\xi^2 - \pi D^2/4),^{[56]} \quad \textbf{(6.8)}$$

where with D≈x≈18 nm (see Fig. 6-3) and γ_{sl}=72 mN/m[64] we obtain:

$$\Delta P_{max} \approx 5.7 \times 10^7 \text{ N/m}^2 \approx 5.7 \times 10^2 \text{ Atm.}$$

This pressure is much higher if we compare it with the internal Laplace pressure $\Delta P_d \approx 1.4 \times 102$ N/m2 of a spherical water drop of radius R~1 mm, which is used for the contact angle measurements.[64] Moreover, the Laplace pressure is high enough to push liquid into the crevices in agreement also with former studies on nanostructured surfaces.[31] Indeed, these pressures, if we compare with the SEM results in Fig. 6-7, can generate forces to cause NP rearrangement and fusion within the outer Wenzel area around the droplet (Fig. 6-7d) during the drying process. However, the central region of the droplet (after drying is completed, Fig. 6-7b) indicates less drastic NP rearrangement. Our

hypothesis is that the initial wetting and superhydrophobic state is not based on this rearrangement, because it occurs in a later stage during drying of the droplets. Finally, attempts were also made to investigate the influence of additional surface roughening on lateral length scales of the order of microns (having significant RMS roughness in the range of 200–800 nm, see Fig. 6-1 and table. 6-1 prior to NP deposition. The aim was to achieve a hierarchical surface roughness containing two distinct (micron and nanometer) length scales. These micron scale roughened Si oxide surfaces had prior to NP deposition contact angles≈40–45°, while after NPs deposition they were increased at most up to ≈108° for NP coverages in the range ≈20–40%, and comparable to intermediate coverages for the relatively flat surfaces. Thus, NPs increased again the contact angle and these results demonstrate that NPs continue to play a dominant role despite the underlying presence of rough surface features.
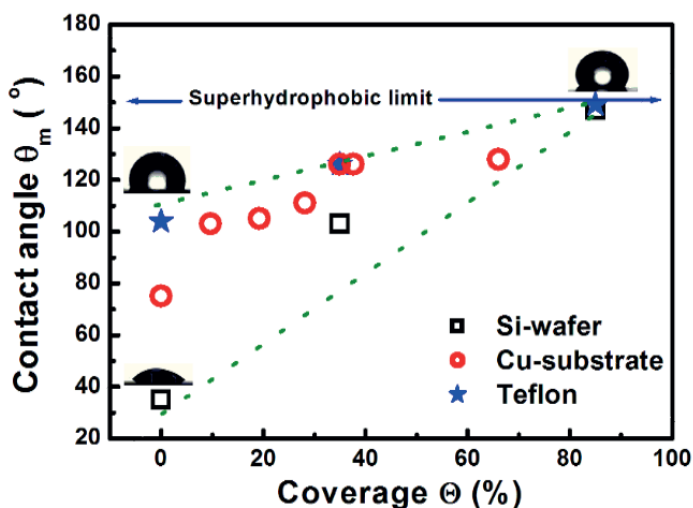
Figure 6-8 Overview of all contact angles for the different substrates showing the transition towards the superhydrophobic surface state at high NP coverages, irrespective of the initial type of surface.

Finally, attempts were also made to investigate the influence of additional surface roughening on lateral length scales of the order of microns (having significant RMS roughness in the range ∼200-800 nm, see Fig. 6-13 and Table 6-1

A 2-inch silicon wafer was prepared for samples by cutting them in square 1 cm^2 pieces. Another 2-inch silicon wafer was coated with a homogeneous 20 nm thick layer of copper as a starting (relatively flat) substrate surface and was also cut in 1 cm^2 pieces. Both these sample surface types were coated with copper NPs with various NP sizes and with various degrees of substrate surface coverage.

These final samples were used for CA measurements. The TEFLON samples were cut from a TEFLON plate grinded with P1000, P1200, P2400 and finally P4000 SiC paper (Struers) This

polished TEFLON plate was further treated analogously as the Si-wafer pieces. The aim was to achieve a hierarchical surface roughness containing two distinct (micron and nanometer) length scales. These micron scale roughened Si-oxide surfaces had prior to NP deposition contact angles ~ 40-45°, while after NP deposition they were increased at most up to ~108° for NP coverages in the range ~20-40 %, and comparable to intermediate coverages for the relatively flat surfaces. Thus, NPs increased again the contact angle and these results demonstrate that NPs continue to play a dominant role despite the underlying presence of rough surface features.

6.4.1 BF-TEM, SEM images and contact angle measurements of NPs assemblies

Below typical images from the transmission electron microscopy (TEM) measurements are shown to illustrate how the surfaces appear after deposition, and to determine the surface coverage with NPs. Even at the lowest coverage of the surface, there is a tendency that NPs stick on top of each other and cluster together where they land. Example TEM images have been paired with a photo of a drop on a Cu sample surface exposed to the corresponding NP deposition (as shown in the BF-TEM image) during the contact angle measurements.
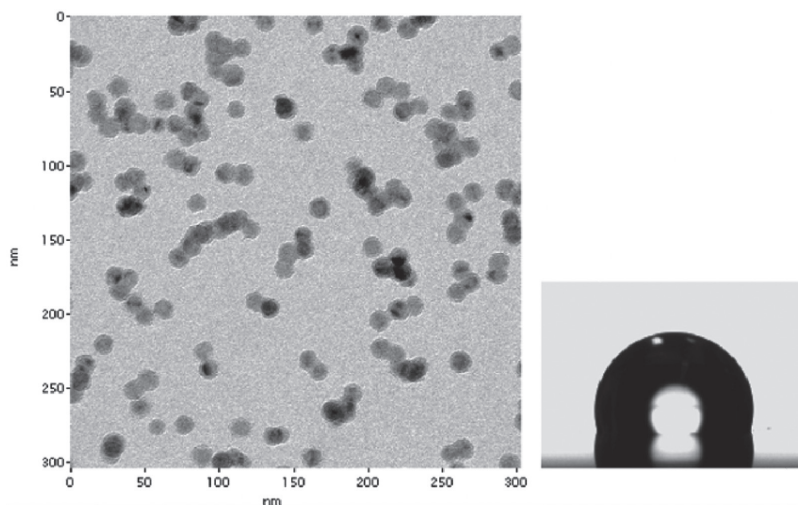
Figure 6-9 NP average size 14.2 ± 2.1 nm, surface coverage 19.2%, and contact angle 105°.
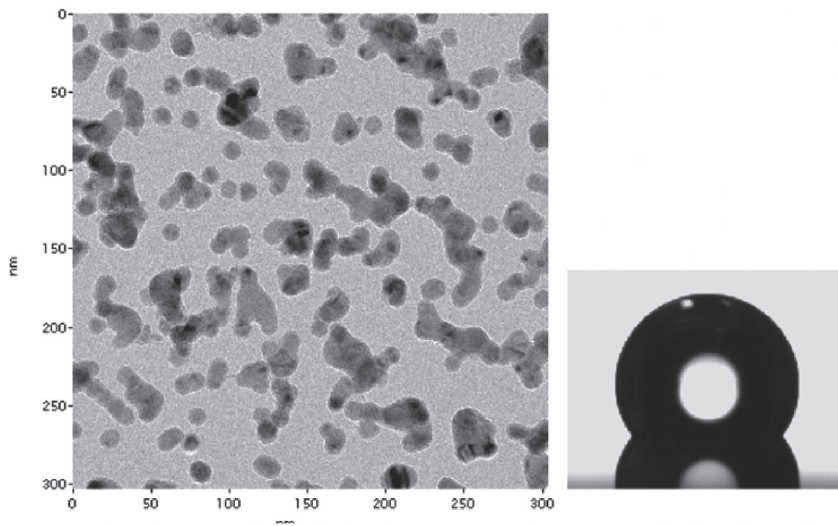
Figure 6-10 Particle size 12.5 ± 1.8 nm, surface coverage 37.6%, and contact angle 126°.
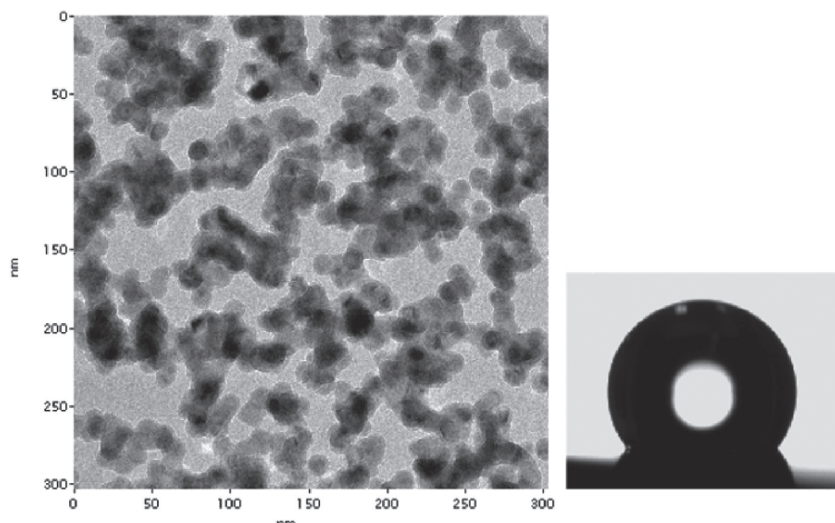
Figure 6-11 Particle size 13.5 ± 2.5 nm, surface coverage 65.5%, and contact angle 128°.
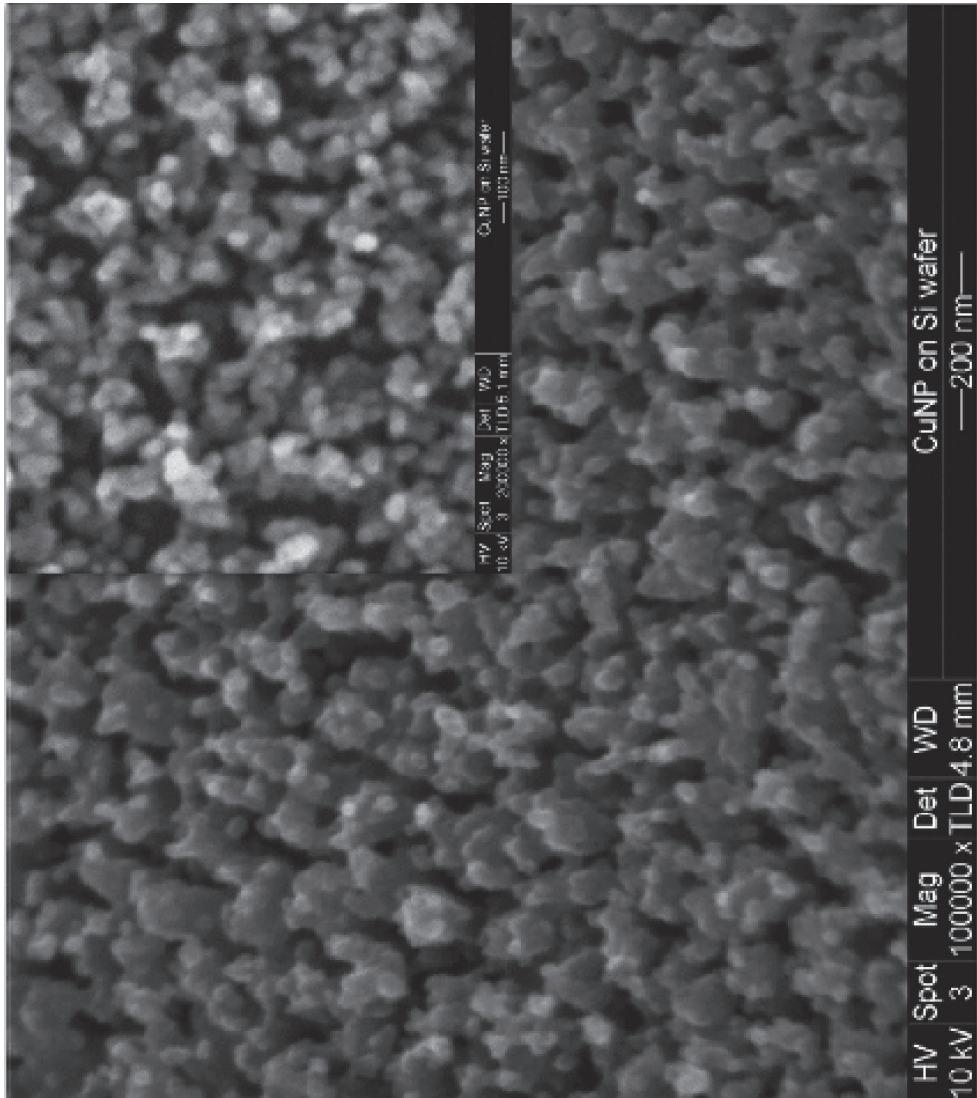
Figure 6-12 SEM image of NPs within the wetted area around the droplet (Fig. 6-7c) with the inset showing a similar image of NPs not exposed to water. The latter shows a higher degree of granular structure with more NPs visible.

6.4.2   SEM images and CA measurements on pre-roughened surfaces
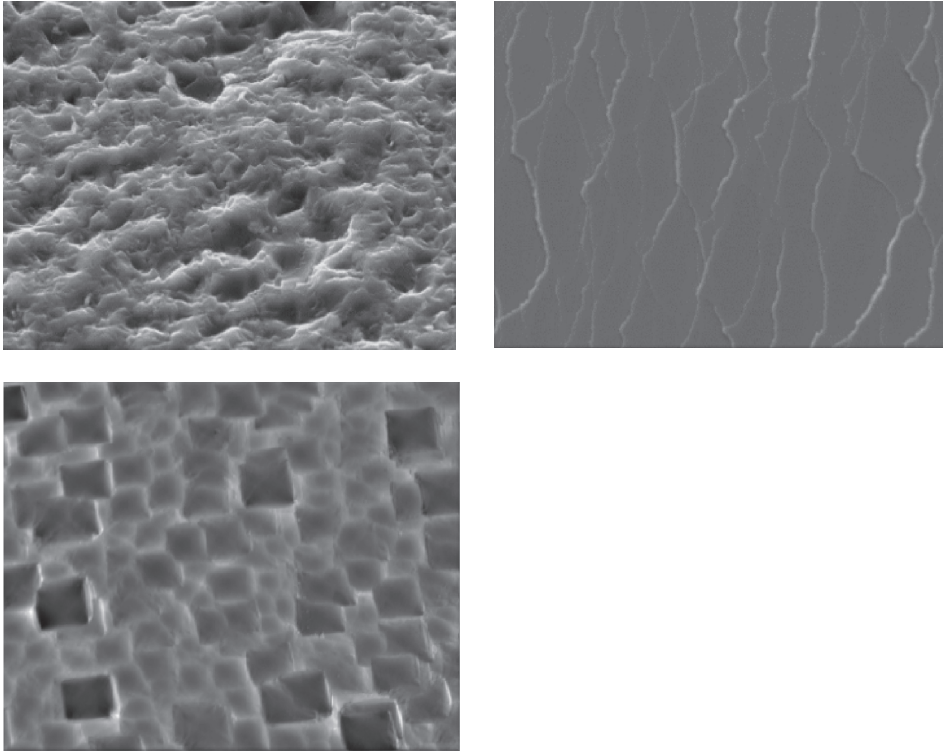
Figure 6-13 Indicative distinct Si oxide roughened samples prior to NP deposition (Top: Scanning Electron Microscope (SEM) image Solar cell*, Middle: SEM image of Roof tile surface, Bottom: Confocal Microscope image of Si(100) etched surface of 630x630 mm^2 in size). Detailed results of the contact angle measurements can be found in Table C1. The samples were kindly supplied by Hans Hauger from Advanced Wet Technologies GmbH.

Sample	RMS (μm)	NP size (nm)	NP coverage (%)	CA(°)
Flat SiO2	0	0	0	49±4
Nano100 (Etching 15min)	0.21	0	0	44±4
Nano100 (Etching 30min)	0.16	0	0	47±3
Rooftile (Etching 15min)	0.23	0	0	42±2
Rooftile (Etching 30min)	0.41	0	0	47±4
Solar cell template	0.79	0	0	41±3
Nano100 (Etching 15min)	0.21	13(±4)	37%	99±3
Nano100 (Etching 30min)	0.16	13(±4)	23%	99±1
NanoRooftile (Etching 15min)	0.23	13(±4)	37%	108±4
NanoRooftile (Etching 30min)	0.41	13(±4)	23%	98±4
NP solar cell template1	0.79	15(±5)	7%	49±7
NP solar cell template2	0.79	14(±4)	14%	81±2
NP solar cell template3	0.79	15(±6)	40%	85±3

Table 6-1 Results from the measured Si-oxide surfaces before and after NP deposition. The minutes refer to the etching time of the sample, and 100 refers to Si(100). All the samples were left at least one day after fabrication to allow for the oxide layer to reform completely and minimize surface chemical in homogeneities.

6.5   Conclusions

In conclusion, we demonstrated that superhydrophobicity can be induced by roughness on a single nanometer length scale with metal nanoparticles decorated surfaces. This roughness provides sufficient pinning of the contact line so that the superhydrophobic state is approached for elevated (hydrophilic) nanoparticle coverages independent of the initial type of surface (for an overview see Fig. 6-8) ensuring trapping of water droplets. Indeed, our studies indicate that the water droplets are in a Wenzel state at their outer part where locally nanocapillarity can force liquid into crevices between nanoparticles and push trapped air within the center of the droplet forming a Cassie-Baxter state (cf. Fig. 6-7c). In fact, the local Laplace pressures are high enough to favor the formation of a Wenzel state at least, as our estimates indicate, for a part of the water droplet. Independent of the exact details, our approach to alter the wetting state and induce droplet trapping is straightforward without involving special micro/nano (hierarchical) structuring facilities but instead using direct single distinct nanoparticle deposition onto any type of surface (hydrophilic or hydrophobic). Further studies are in progress to address issues related to oleophobic and omniphobic behavior.

6.6   References

1   G. Binnig, C. F. Quate and Ch. Gerber, *Phys. Rev. Lett.*, 1986, **56**, 930–933.

2   P. G. de Gennes, *Rev. Mod. Phys.*, 1985, **57**, 827–863.

3   Wettability :   John   C.   Berg :   9780824790462,   http://www.bookdepository.com/ Wettability/9780824790462?b=-3&t=-26#Bibliographicdata-26, (accessed October 24, 2014).

4   Rowlinson J S and Widom B - AbeBooks, http://www.abebooks.com/book-search/author/rowlinson-j-s-and-widom-b/, (accessed October 24, 2014).

5   *Modern Approaches to Wettability Theory and Applications.*, Springer Verlag, 2014.

6   Soft interfaces : the 1994 Dirac memorial lecture / P.G. de Gennes. - Version details - Trove, http://trove. nla.gov.au/work/15894919?q=+&versionId=18657496, (accessed October 24, 2014).

7   Y.-S. Ding, X.-F. Shen, S. Gomez, H. Luo, M. Aindow and S. L. Suib, *Adv. Funct. Mater.*, 2006, **16**, 549–555.

8   K. Ichimura, S.-K. Oh and M. Nakagawa, *Science*, 2000, **288**, 1624–1626.

9   H. Gau, S. Herminghaus, P. Lenz and R. Lipowsky, *Science*, 1999, **283**, 46–49.

10   J. D. J. S. Samuel, P. Ruther, H.-P. Frerichs, M. Lehmann, O. Paul and J. Rühe, *Sens. Actuators B Chem.*, 2005, **110**, 218–224.

11   H. Zhang, R. Lamb and J. Lewis, *Sci. Technol. Adv. Mater.*, 2005, **6**, 236–239.

12   W. Chen, A. Y. Fadeev, M. C. Hsieh, D. Öner, J. Youngblood and T. J. McCarthy, *Langmuir*, 1999, **15**, 3395–3399.

13   B. Roe and X. Zhang, *Text. Res. J.*, 2009, **79**, 1115–1122.

14   N. Gao and Y. Yan, *Nanoscale*, 2012, **4**, 2202–2218.

15   X.-M. Li, D. Reinhoudt and M. Crego-Calama, *Chem. Soc. Rev.*, 2007, **36**, 1350–1368.

16   C. R. Crick and I. P. Parkin, *J. Mater. Chem.*, 2009, **19**, 1074–1076.

17   C. Neinhuis and W. Barthlott, *Ann. Bot.*, 1997, **79**, 667–677.

18   R. G. Karunakaran, C.-H. Lu, Z. Zhang and S. Yang, *Langmuir*, 2011, **27**, 4594–4602.

19   N. Gao, Y. Y. Yan, X. Y. Chen and D. J. Mee, *Mater. Lett.*, 2011, **65**, 2902–2905.

20   R. N. Wenzel, *Ind. Eng. Chem.*, 1936, **28**, 988–994.

21   A. B. D. Cassie and S. Baxter, *Trans. Faraday Soc.*, 1944, **40**, 546–551.

22   M. Jin, X. Feng, L. Feng, T. Sun, J. Zhai, T. Li and L. Jiang, *Adv. Mater.*, 2005, **17**, 1977–1981.

23   S. Anand, A. T. Paxson, R. Dhiman, J. D. Smith and K. K. Varanasi, *ACS Nano*, 2012, **6**, 10122–10129.

24   X. Chen, J. Wu, R. Ma, M. Hua, N. Koratkar, S. Yao and Z. Wang, *Adv. Funct. Mater.*, 2011, **21**, 4617–4623.

25   C.-H. Chen, Q. Cai, C. Tsai, C.-L. Chen, G. Xiong, Y. Yu and Z. Ren, *Appl. Phys. Lett.*, 2007, **90**, 173108.

26   D. 't Mannetje, S. Ghosh, R. Lagraauw, S. Otten, A. Pit, C. Berendsen, J. Zeegers, D. van den Ende and F. Mugele, *Nat. Commun.*, , DOI:10.1038/ncomms4559.

27   A. Tricoli, M. Righettoni and S. E. Pratsinis, *Langmuir*, 2009, **25**, 12578–12584.

28   W. Barthlott and C. Neinhuis, *Planta*, 1997, **202**, 1–8.

29   M. Callies and D. Quéré, *Soft Matter*, 2005, **1**, 55–61.

30   D. Quéré, *Phys. Stat. Mech. Its Appl.*, 2002, **313**, 32–46.

6

[31] Handbook of Nanostructured Biomaterials and Their Applications in Nanobiotechnology, http://www.aspbs.com/nanobiomaterials.html, (accessed October 24, 2014).

[32] J. B. K. Law, A. M. H. Ng, A. Y. He and H. Y. Low, *Langmuir*, 2013, **30**, 325–331.

[33] H. Teisala, M. Tuominen, M. Aromaa, M. Stepien, J. M. Mäkelä, J. J. Saarinen, M. Toivakka and J. Kuusipalo, *Langmuir*, 2012, **28**, 3138–3145.

[34] B. Bhushan and M. Nosonovsky, *Philos. Trans. R. Soc. Lond. Math. Phys. Eng. Sci.*, 2010, **368**, 4713–4728.

[35] N. Michael and B. Bhushan, *Microelectron. Eng.*, 2007, **84**, 382–386.

[36] L. Feng, Y. Zhang, J. Xi, Y. Zhu, N. Wang, F. Xia and L. Jiang, *Langmuir*, 2008, **24**, 4114–4119.

[37] L. Cao, T. P. Price, M. Weiss and D. Gao, *Langmuir*, 2008, **24**, 1640–1643.

[38] A. Tuteja, W. Choi, J. M. Mabry, G. H. McKinley and R. E. Cohen, *Proc. Natl. Acad. Sci.*, 2008, **105**, 18200–18205.

[39] Z. He, M. Ma, X. Xu, J. Wang, F. Chen, H. Deng, K. Wang, Q. Zhang and Q. Fu, *Appl. Surf. Sci.*, 2012, **258**, 2544–2550.

[40] C. Ishino and K. Okumura, *Eur. Phys. J. E*, 2008, **25**, 415–424.

[41] A. Checco, B. M. Ocko, A. Rahman, C. T. Black, M. Tasinkevych, A. Giacomello and S. Dietrich, *Phys. Rev. Lett.*, 2014, **112**, 216101.

[42] L. Cao, H.-H. Hu and D. Gao, *Langmuir*, 2007, **23**, 4310–4314.

[43] Y.-T. Cheng and D. E. Rodak, *Appl. Phys. Lett.*, 2005, **86**, 144101.

[44] H. Huang and N. S. Zacharia, *Langmuir*, , DOI:10.1021/la504095k.

[45] A. Marmur, *Langmuir*, 2008, **24**, 7573–7579.

[46] S. Wang and L. Jiang, *Adv. Mater.*, 2007, **19**, 3423–3424.

[47] C. W. Extrand, *Langmuir*, 2006, **22**, 1711–1714.

[48] H.-X. Ren, X. Chen, X.-J. Huang, M. Im, D.-H. Kim, J.-H. Lee, J.-B. Yoon, N. Gu, J.-H. Liu and Y.-K. Choi, *Lab. Chip*, 2009, **9**, 2140.

[49] G. H. ten Brink, G. Krishnan, B. J. Kooi and G. Palasantzas, *J. Appl. Phys.*, 2014, **116**, 104302.

[50] J. Krim and G. Palasantzas, *Int. J. Mod. Phys. B*, 1995, **09**, 599–632.

[51] http://www.surface-tension.org/news/54.html Young-Laplace equation fitting method (ADSA-PTM): Using completedrop shape for measurement of static contact angle

[52] *Applied Surface Thermodynamics, Second Edition*. page 161

[53] Z. Xu, *IET Micro Nano Lett.*, 2014, **9**, 6–10.

[54] B. N. J. Persson, *J. Chem. Phys.*, 2001, **115**, 3840–3861.

[55] G. Palasantzas, *Phys. Rev. E*, 1997, **56**, 1254–1257.

[56] Q.-S. Zheng, Y. Yu and Z.-H. Zhao, *Langmuir*, 2005, **21**, 12207–12212.

[57] E. J. Lobaton and T. R. Salamon, *J. Colloid Interface Sci.*, 2007, **314**, 184–198.

[58] P. Forsberg, F. Nikolajeff and M. Karlsson, *Soft Matter*, 2010, **7**, 104–109.

[59] P. Papadopoulos, L. Mammen, X. Deng, D. Vollmer and H.-J. Butt, *Proc. Natl. Acad. Sci.*, 2013, **110**, 3254–3258.

[60] D. Murakami, H. Jinnai and A. Takahara, *Langmuir*, 2014, **30**, 2061–2067.

[61] E. Bormashenko, A. Musin, G. Whyman and M. Zinigrad, *Langmuir ACS J. Surf. Colloids*, 2012, **28**, 3460–3464.

[62] B. He, N. A. Patankar and J. Lee, *Langmuir*, 2003, **19**, 4999–5003.

[63] N. A. Patankar, Langmuir, 2010, 26, 8941–8945.

[64] A. Giacomello, M. Chinappi, S. Meloni and C. M. Casciola, Phys. Rev. Lett., 2012, 109, 226102.

[65]

[66] G. H. ten Brink, N. Foley, D. Zwaan, B. J. Kooi and G. Palasantzas, RSC Adv, 2015, 5, 28696–28702.

[67] G. Torricelli, P. J. van Zwol, O. Shpak, C. Binns, G. Palasantzas, B. J. Kooi, V. B. Svetovoy and M. Wuttig, Phys. Rev. A, 2010, 82, 010101.

[68] Bin Chen, .

[69] G. Palasantzas, Phys. Rev. E, 1997, 56, 1254–1257.

[70] Characterization of Amorphous and Crystalline Rough Surface -- Principles and Applications, 1st Edition | Yiping Zhao, Gwo-Ching Wang, Toh-Ming Lu | ISBN 9780080531380, http://store.elsevier.com/Characterization-of-Amorphous-and-Crystalline-Rough-Surface-Principles-and-Applications/isbn-9780080531380/, (accessed June 20, 2016).

[71] V. B. Svetovoy and G. Palasantzas, Adv. Colloid Interface Sci., , DOI:10.1016/j.cis.2014.11.001.

[72] M. Sedighi, V. B. Svetovoy, W. H. Broer and G. Palasantzas, Phys. Rev. B, 2014, 89, 195440.

[73] V. M. Starov, S. R. Kosvintsev and M. G. Velarde, J. Colloid Interface Sci., 2000, 227, 185–190.

[74] K. S. Lee, N. Ivanova, V. M. Starov, N. Hilal and V. Dutschk, Adv. Colloid Interface Sci., 2008, 144, 54–65.

[75] V. M. Starov, S. R. Kosvintsev and M. G. Velarde, J. Colloid Interface Sci., 2000, 227, 185–190.

[76] G. Nagayama and D. Zhang, Soft Matter 16, 3514 (2020).

6
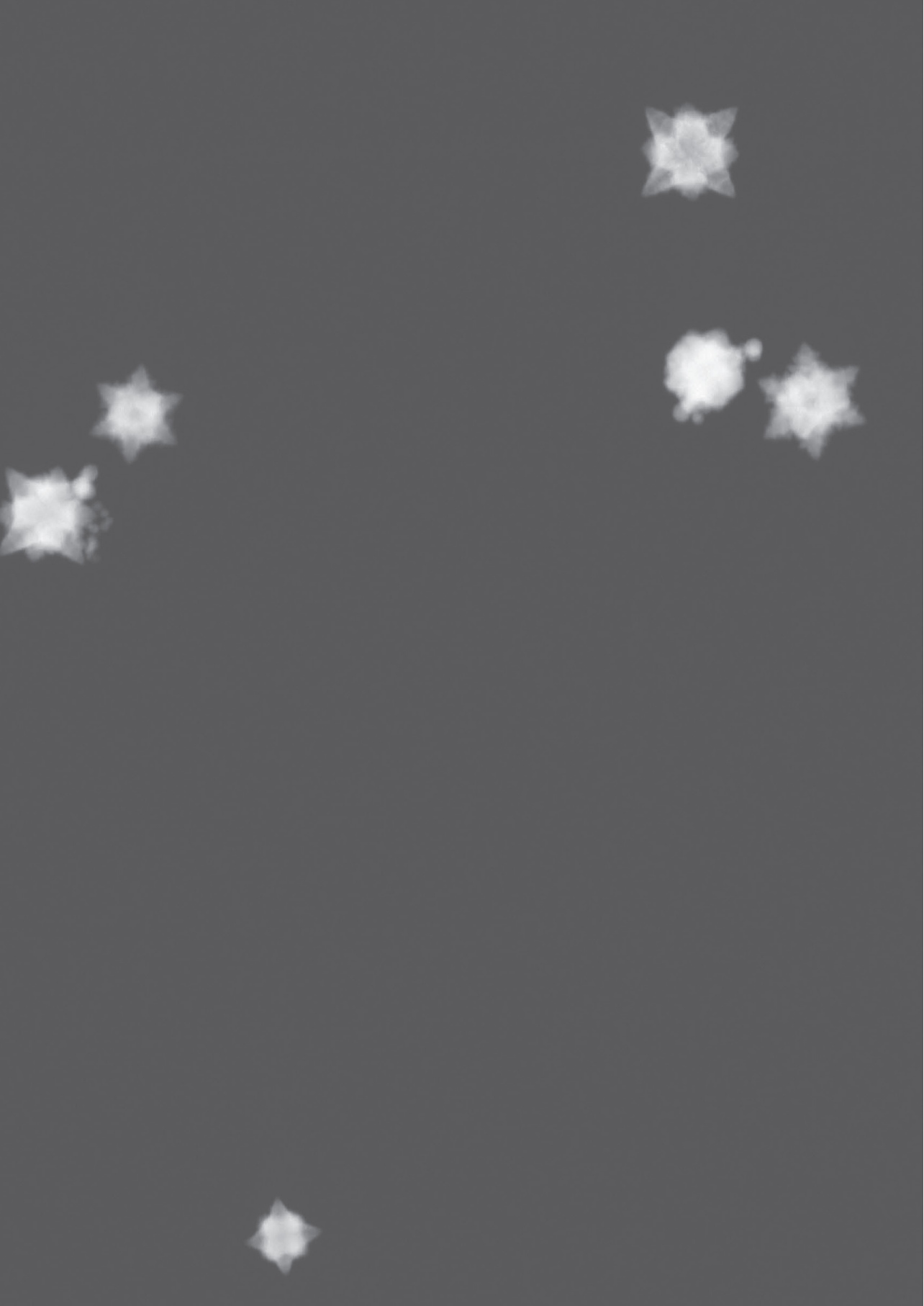
Chapter 7
Controlling surface wettability with nanoparticles from phase change materials

7.1 Abstract

The wetting state of surfaces can be controlled physically from the highly hydrophobic to hydrophilic states using the amorphous-to-crystalline phase transition of $Ge_2Sb_2Te_5$ (GST) nanoparticles as surfactant. Indeed, contact angle measurements show that by increasing the surface coverage of the amorphous nanoparticles the contact angle increases to high values ~140°, close to the superhydrophobic limit. However, for crystallized nanoparticle assemblies after thermal annealing, the contact angle decreases down to ~40° (significantly lower than that of the bare substrate) leading to an increased hydrophilicity. Moreover, the wettability changes are also manifested on the capillary adhesion forces by being stronger for the crystallized GST state.[4]

[4] G.H. ten Brink, P.J. van het Hof, B. Chen, M. Sedighi, B.J. Kooi, and G. Palasantzas, Appl. Phys. Lett. 109, 234102 (2016)

7.2 Introduction

Although a topic of more than 200 years old, wetting of liquids on solid surfaces attracts nowadays relentless attention from the fundamental and application point of view.[1-9] A few examples include self-cleaning, anti-icing, adhesion of material surfaces, stiction issues in micro-electromechanical systems (MEMS), capillarity, reduced fluid drug in micro / nanofluidic systems etc. Moreover, trapping of water drops by modification of surface wettability plays important role for the efficiency of drop condensation from vapor in heat exchangers and fog harvesters.[5-9] The surface wettability is measured by the contact angle (CA) between a water droplet and the supporting surface. A surface with CA<90° is termed as hydrophilic, while one with CA>90° is termed as hydrophobic.[1,2] Superhydrophobic surfaces with CA~150° have also attracted strong interest[1,2,] inspired by many examples in nature e.g. duck feathers, butterfly wings, lotus plant etc.[10-15] Controlling surface wettability by surface roughening and chemical modification is a topic of intense research area.[1-9]

The contact angle CA_f for a flat surface is given by the Young equation:

$$cos\, CA_f = (\gamma_{sg} - \gamma_{sl})/\gamma_{lg}\;^{1,2} \quad \textbf{(7.1)}$$

with $g$sg, $g$sl and $g$lg the solid-gas, solid-liquid and liquid-gas interface energies, respectively. For rough surfaces the Wenzel (W) model predicts that a hydrophilic/hydrophobic surface would be more hydrophilic/hydrophobic with surface roughening assuming complete contact of the liquid with the surface.[16] Nevertheless, droplets on a rough surface are not expected to wet deep surface crevices, leaving air pockets in between crevices and forming the Cassie-Baxter (CB) state.[17] During CB®W transitions thermodynamically unstable air pockets allow liquid to nucleate into crevices.[18] Processes to form hydrophobic surfaces involves combinations of surface roughening with alteration of surface chemistry using low surface energy materials to mimic the structure of the lotus leaf or butterfly wings that show strong hydrophobicity.[1-4] Other methods used random and deterministic structured microscale roughness.[2,19-22] The latter, resembling grid of pillars or nail heads, have attracted interest to create superhydrophobic and possibly omniphobic surfaces.[2,23-25] Nanometer-size textures could facilitate more resilient coatings due to nanoscale geometry and confinement effects.[22] Thermodynamically a hydrophobic rough surface can be formed from hydrophilic material if the roughness is multivalued.[26] Near superhydrophobicity and trapping of water droplets was also demonstrated for surfaces coated by Cu nanoparticles (NPs) produced by high pressure magnetron sputtering.[27]

Although micro/nanoscale surface roughness can lead to enhanced hydrophobicity, the physical change of surface wettability between hydrophilic to, even, superhydrophobic states by switching

the phase state of materials, without material composition changes and additional surface micro / nano-structuring, is highly nontrivial. It will be shown here, as a concept-of-proof, that this can achieved for surfaces covered by NPs derived from phase change materials (PCMs)[28,29] when they undergo reversible amorphous (A)-to-crystalline (C) phase transitions. In fact, PCMs are not only renowned for their use as active media in rewritable optical disks (i.e. CD, DVD and Blu-Ray Disks) using reversible A-C phase transitions[28,29], they are also are promising to provide the required reversible modification of the dielectric response leading to significant Casimir force contrast.[30,31]

7.3   Experimental methods

Here the $Ge_2Sb_2Te_5$ (GST) NPs[32, 33] were produced using high pressure plasma sputtering in a modified Mantis Nanogen 50 system.[33,34] The GST NPs were deposited on highly oriented pyrolytic graphite (HOPG) surfaces (approaching hydrophobic behavior) that have significant CA ~70° in order to illustrate more clearly the formation of distinct hydrophobic/hydrophilic states. Initially the NPs were deposited using a low discharge current ~0.1 A to ensure that they were in the amorphous state.[32] Furthermore, the amorphous NPs assemblies on HOPG were crystallized by ex-situ annealing for 10 min. on a hot plate at a temperature of ~120°C.[32]

The homogeneity and roughness of the surfaces were assessed with a Bruker atomic force microscope (AFM, Multimode 8; see Figure. 7-1) in combination with scanning electron microscopy (SEM; see Figs 7-2a,b)

The samples were all made using the same settings to ensure the NPs were of comparable size (~10 %), and only the deposition time was varied between samples to obtain varying degrees of NP coverages on the sample surfaces. Moreover, transmission electron microscope (BF-TEM) samples Figs 7-5a, b underwent deposition simultaneously as those for the contact angle measurements, and they were analyzed in an JEOL 2010 TEM to enable calculation of the surface coverage and measurement of the NP size distribution with the Image-Pro Plus v4.5 software.[33]

7.4   Results and discussion

The AFM images of the samples were taken over areas 3x3-5x5 μm^2 to calculate the root mean squared (RMS≡w) roughness. Height-height correlation difference function analysis, $g(x)=<[h(x)-h(0)]^2>$ vs. lateral scale x, with $<...>$ indicating statistical average, from the topography data (Fig. 7-1) yielded all necessary roughness parameters.

Besides w, one obtains from g(x) the lateral roughness correlation length x and the roughness exponent H (0<H<1), for which g(x)≈r^2x^{2H} for x<<x, to estimate the average local surface slope r(≈w/x^H)[35,36] for roughness exponents H significantly lower than 1 (see Fig. 7-1c) The obtained average surface local slope:

$$\phi = tan^{-1}\rho \ \ (\rho \approx w/\xi^H) \ ^{36} \ \textbf{(7.2)}$$

was rather significant indicating the formation of a steep nanoscale topology (e.g., ϕ ≈40°) for the amorphous GST NPs in Fig.7-1a). Although the AFM morphologies in Fig. 7-1 appear similar, the amorphous surface has particles more distinct and uniform in size (without any significant coalescence as TEM analysis indicated[32]) that is inherent to soft impact deposition of NPs leading to porous assemblies. However, for the crystalline surface some coalescence occurs during annealing leading to a larger variation of grain sizes and lower porosity but rougher than the amorphous surface (as also the z-scales indicate). Notably during the initial stages of NP deposition, we observed preferential decoration of surface step edges (inset Fig. 7-1a) due to stronger van der Waals forces on surface steps than on planar parts of the HOPG surface.[37, 38] To measure the wetting state of samples, the contact angle measurements were performed using a Dataphysics OCA20 system (see Fig. 7-3). An automated syringe dropped ~2 µl droplets of pure water (MilliQ) on to the sample, where a camera recorded the pictures over a period of several seconds. The drop shape is analyzed based on the shape of an ideal sessile drop, the surface curvature of which results only from the force equilibrium between surface tension weight. The values of the contact angle were obtained via a fit using the Young-Laplace (YL) equation based on shape analysis of a complete drop and compared also to results obtained from geometrical CA analysis.[39,40] For every sample the CA measurements were repeated for several drops on different sample areas.

Figures 7-3 and 7-4 show the temporal evolution of the CA on HOPG coated with amorphous and crystallized GST NPs of high coverage >80 % to obtain high CA values for the amorphous NPs as we have shown in our previous studies[27], respectively. For the as-deposited amorphous NPs in Fig.7-3a, the CA after a transient relaxation ~2 sec still preserves a large value CA>132° that indicates strong hydrophobicity.

7
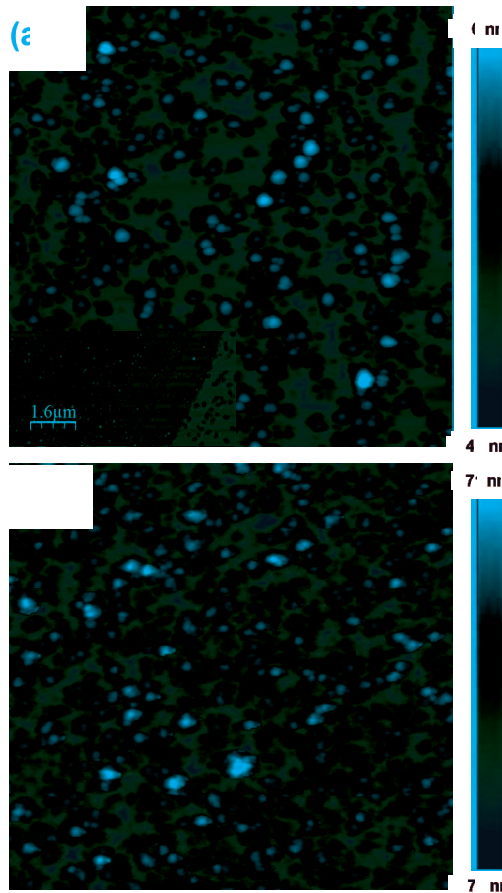
Figure 7-1 (a) AFM topography of amorphous NPs. The inset shows the preferential decoration of NPs at HOPG step edges during initial deposition stages. (b) AFM topography of crystallized NP assemblies. The topology indicates partial fusion of NPs yielding a more compact granular structure with reduced porosity. In both cases the scan area was 3x3 μm^2.

Indeed, the CA is almost twice that of the bare HOPG surface (CA~70°), and it is comparable to those measured for high coverage of Cu NPs.[27] However, for the crystallized GST (Fig.7-3b) after annealing, the CA after a rapid drop within ~2 sec approaches values less than that of the bare HOPG surface and dramatically reduces to a hydrophilic state with CA~40°, which is comparable to hydrophilic SiO$_x$ surfaces.[27]
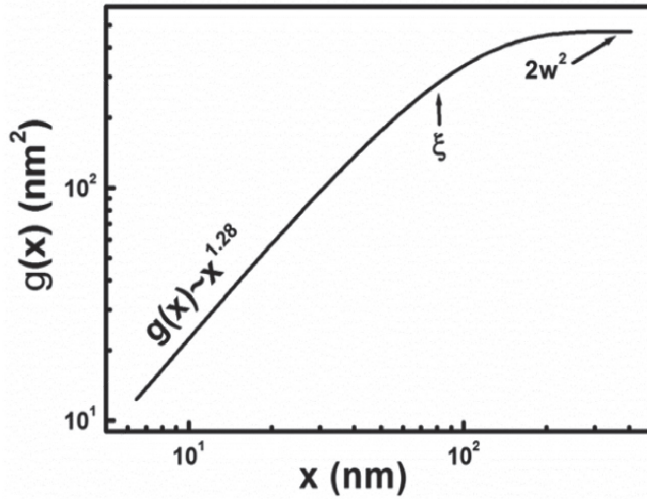
Figure 7-1(c) The roughness analysis of g(x) vs. x (from the AFM image in Fig.1a) gave w=15.3 nm, H=0.64, and x=85.9 nm. These parameters gave a local slope r≈0.18 that corresponds to average surface feature inclination $j≈46°$ (=tan^{-1}r).

Further analysis of the relaxation dynamics of CA for the crystalline GST was performed in Fig.7-4a using the averaged data of Fig.7-3a. Since in the past the kinetics of wetting and spreading have been described via a single exponential behavior:

$$\cos(CA) \sim [1 - \exp(-t/\tau)] \text{ [41,42] } \textbf{(7.3)}$$

we fitted our data for cos(CA) using the more general form:

$$\cos(CA) = \cos(CA|_{t=0}) + A[1 - \exp(-(t/\tau)^c)] \textbf{(7.4)}$$

In our case we obtained the exponent c=0.57, which is smaller than the single exponential case (c=1), indicating also a slower approach to final CA (though after some time evaporation takes place limiting the possibility to obtain an equilibrium CA). The stretched exponential form has been widely used in the past to describe complex relaxation where more mechanisms contribute to a phenomenon.[35]
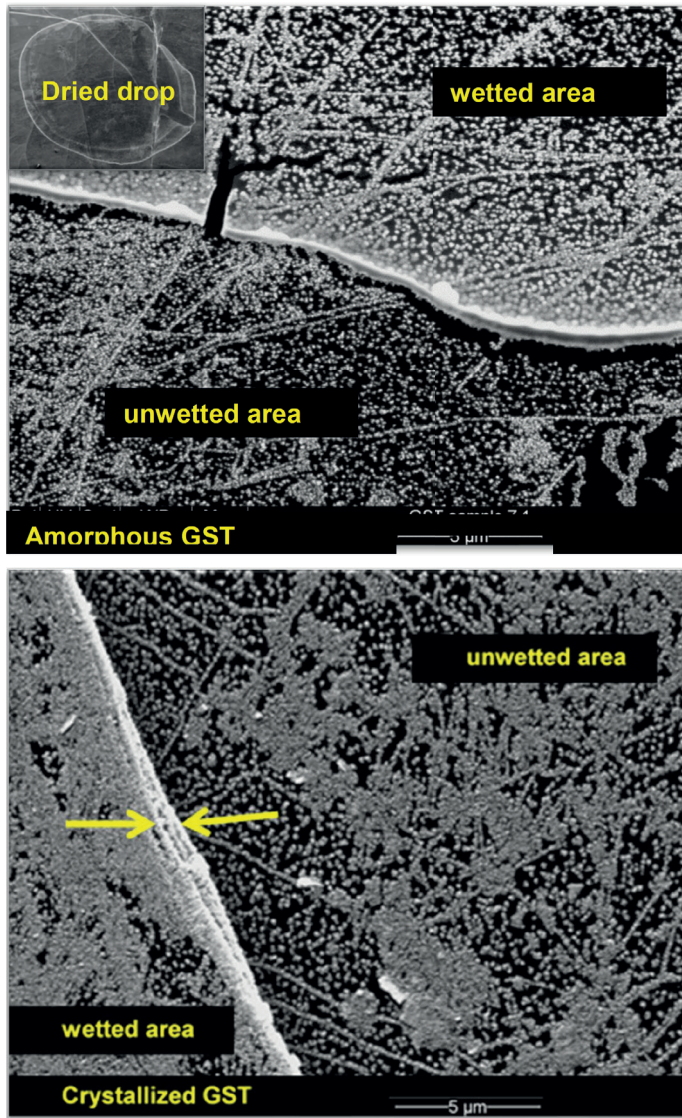
Figure 7-2 SEM images of the GST NPs with the boundary (indicated by arrow) of both the wetted and unwetted areas as obtained after the water drops were evaporated.

Top: amorphous GST NPs, Bottom: crystallized GST. The inset in the top shows a macroscopic shape of a dried drop of a radius ~1 mm.

By contrast, for the amorphous NPs we obtained an almost simple exponential increase c≈1 as the fit in Fig.7-4b indicates. This type of exponential for cos(CA) suggests that the NPs on the sample surface have a surfactant-like behaviour[41,42] that determines the droplet spreading towards a relaxed state. Using the measured CA we also obtained an estimation of the size of the drop, as the CA decreases to its final state, via the expression[41,42]

$$r_D = (6V/\pi)^{1/3}[\tan(CA/2)(3 + \tan^2(CA/2))]^{-1/3} \text{ (7.5)}$$

where r_D is the radius of the wetted spot, and V is the drop volume (prior to water evaporation) that is assumed to remain constant. The inset in Fig. 7-4a indicates that the size of the drop to its almost final hydrophilic state increases by almost ~100 %. The more rapid increase of r_D occurs within ~2-3 sec, while after this short transient it follows a slow increase as a power law with

$$r_D/(6V/\pi)^{1/3} \approx 0.7t^{0.1}. \text{ (7.6)}$$

In contrast, for the amorphous NPs (inset Fig.7-4b) we only observe a weak increment of r_D up to ~10 % in agreement with the strong droplet pinning on the surface. Moreover, if we introduce the dimensionless wetted area $S(t) = r_D^2/(6V/\pi)^{2/3}$ and substitute Y=cos(CA), we obtain[42]:

$$S(t) = (1 + Y)(1 - Y)^{-3}(4 + 2Y)^{-2/3} \text{ (7.7)}$$

S(t) shows also a stretched exponential temporal dependence $S(t)\sim[1 - \exp(-(bt)^c)]$ with an exponent c≈0.54 (see Fig.7-4a, 7-4b) that is close to that obtained for cos(CA) despite the more complex dependence on cos(CA).

In addition, the spreading rate is positive with $dS(t)/dt > 0$ but it decreases with time since $d^2S(t)/dt^2 < 0$ (see in Fig. 7-4b) corresponding to a behaviour also known as "low surfactant activity"[42], if we consider the effect of the crystallized GST as a type of surfactant.

Despite the strong differences in wetting behavior for the amorphous and crystalline states of the GST NPs, the water drops remain firmly attached on the surface (after tests we performed at 90° inclinations and fully inverted; as well as the receding/advancing CA were close to the static CA) indicating the formation of a rose petal or equivalently a Wenzel like state, where liquid is wetting surface crevices at least in the outer area of the droplets to yield strong sufficient surface pinning in a manner similar to Cu NPs.[27]
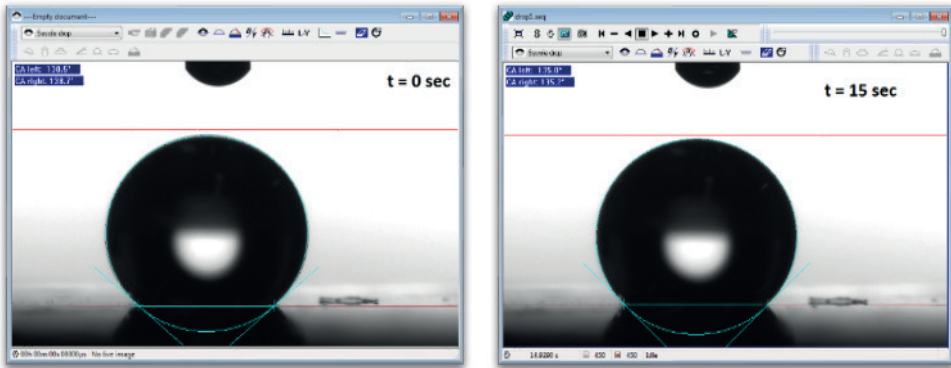
Figure7-3(a) Contact angle images of the initial (t= 0 sec) final state (t=15 sec) of the water droplets: Amorphous NPs. The contact angle images were taken from the software that is used for their measurement.
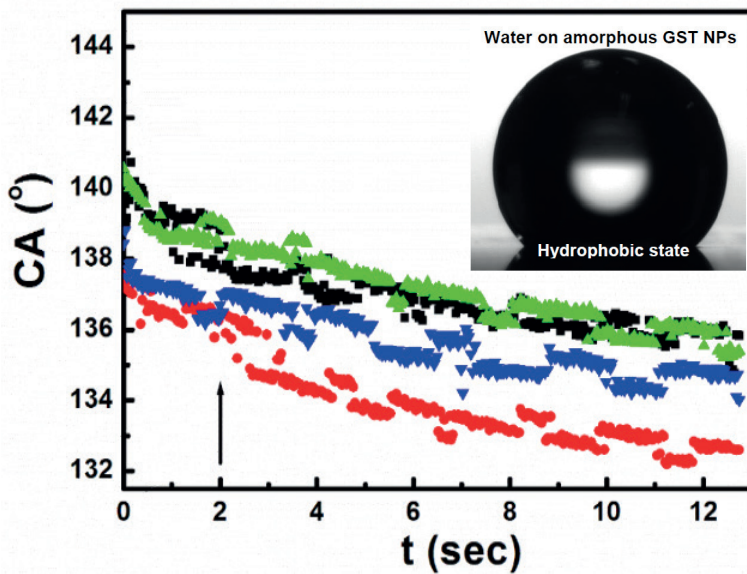
Figure 7-3(a) Contact angle (CA) vs. relaxation time (t) for amorphous GST NPs with data taken from different locations on the sample surface.
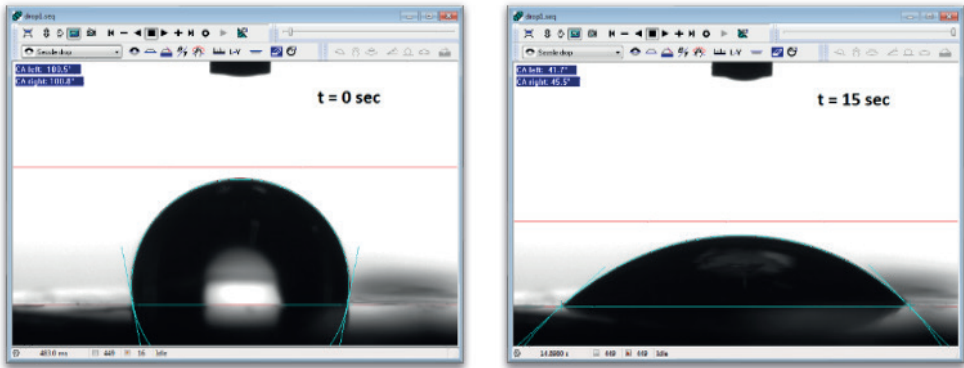
Table 7-3(b) Contact angle images of the initial (t= 0 sec) final state (t=15 sec) of the water droplets: Crystalline NPs. The contact angle images were taken from the software that is used for their measurement.
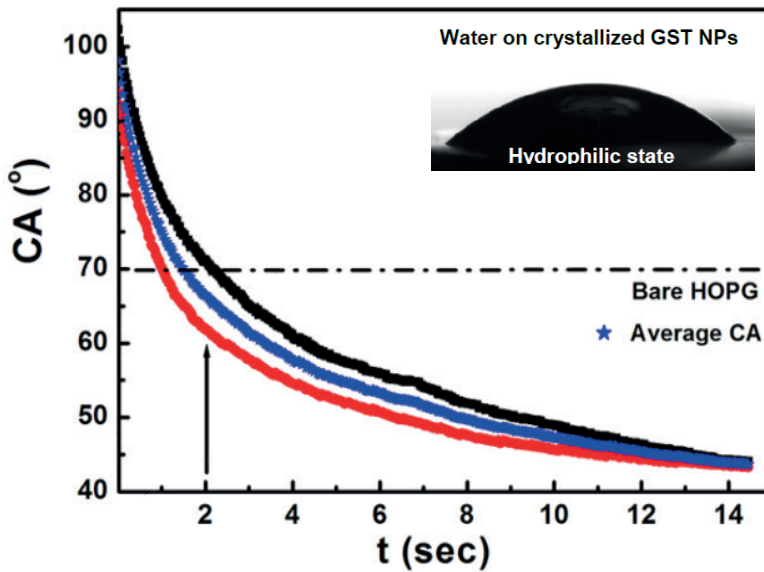
Figure 7-3(b) Contact angle (CA) vs. relaxation time (t) for crystalline GST NPs with data taken at two different locations on the sample surface (for illustration purposes). The insets show in both cases the final state of the water droplet.

This is also supported by the accumulation of more material along the periphery of the water drop, as the SEM images indicate (see Fig.7-2a,b) forming a boundary of height ~300 – 400 nm that is much larger than the average NP size ~20 nm.[32]

The accumulation of NPs at the boundary is more pronounced for the crystallized GST samples, where it appears that to some degree fusion of the NPs has taken place during thermal annealing.

The strong pinning of water droplets for the amorphous NPs is attributed to strong capillary forces within the nanoporous structure of the NP assemblies decorating the surfaces.[27]

However, for the crystallized GST the increased wettability of the PCM material and the partial reduction in porosity lead to increased hydrophilicity though the pinning of the triple line still remains significant to sustain a rose petal behavior. Note that the Wenzel model predicts that the roughness will enhance the hydrophilic/hydrophobic nature of surfaces.

Since the bare HOPG surface has a wetting angle < 90°, it is expected the addition of NPs, leading to surface roughness, to decrease CA or equivalently increase hydrophilicity that is clearly for the crystalline state, while it goes to other way for the amorphous NPs due to the higher porosity leading to stronger pinning and thus higher CA.
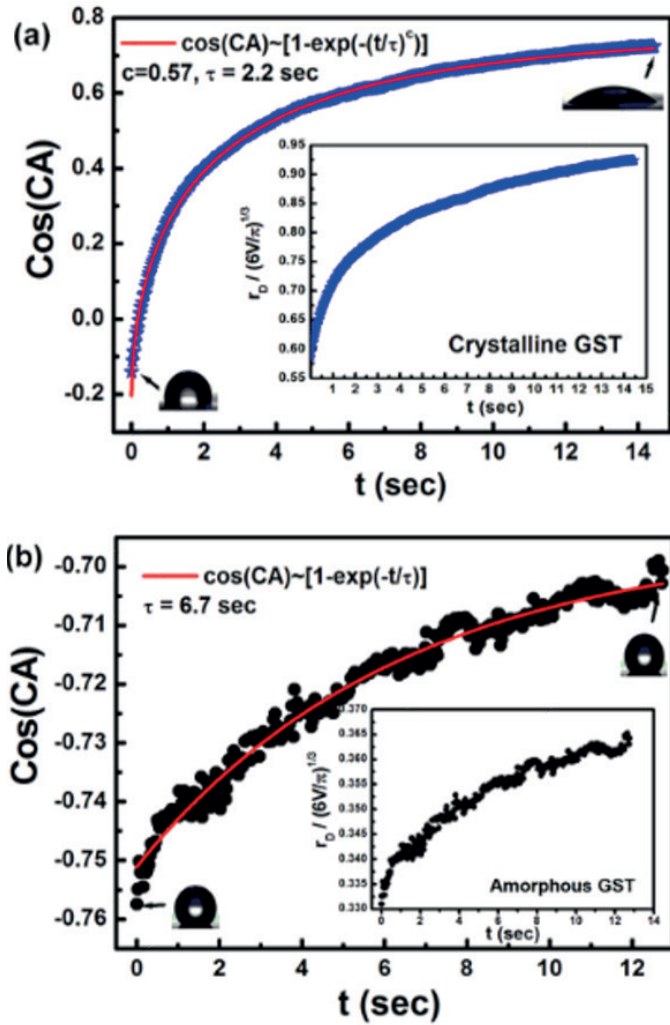
Figure 7-4 (a) cos(CA) vs. relaxation time t for crystalline GST NPs using the averaged data from Fig. 7-3 with the corresponding fit curve. The inset shows the temporal dependence of the droplet radius. (b) Similar plots as in (a) for crystallized GST NPs.
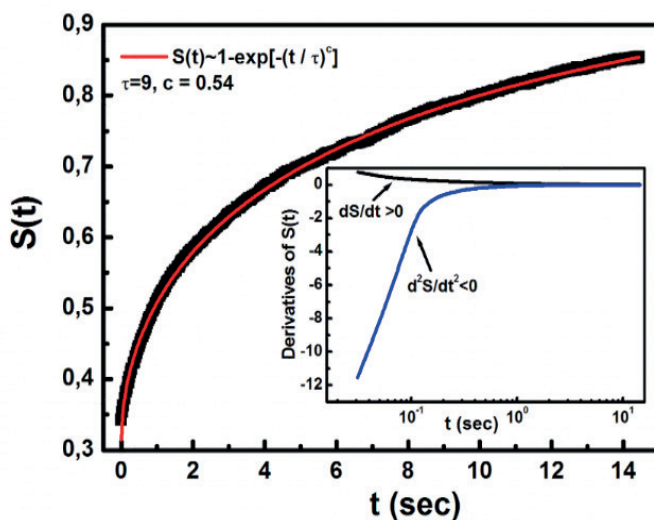
Figure 7-5 Wetted area S vs. relaxation time (t) for the crystalized GST. The fit yielded the analytic form $S(t) = 0.31 + 0.74[1 - \exp(-(t/9)^{0.54})]$, which it was used to calculate the first and second derivatives of S(t) that are shown in the inset.

Finally, we tested the wetting nature of the GST NPs surfaces by measurement of the capillary adhesion force due to water meniscus formation upon contact with another surface (at effective separations for spontaneous meniscus formation < 3 nm)[43-46]. The capillary force measurements were performed with the AFM using a micron size smooth borosilicate sphere (20 μm in diameter and hydrophilic)[46] attached on a tipless cantilever (sphere-plate geometry), and a softer tipless cantilever to compare the effect from different interaction geometries (and thus surface interaction areas) as it is shown in Fig. 7-4. For consistency we tested the sphere on a flat SiC surface yielding large adhesion forces in agreement with past studies.[45, 46]

The force measurements were averaged over 10 consecutive repetitions and the maximum measured force is shown for both the amorphous and crystalline GST surfaces. In both cases, the adhesion force is stronger for the crystallized GST surface in agreement with its increased hydrophilic nature. However, for the amorphous NPs the increased contact angle due to pinning (leading to increased hydrophobic behaviour) leads apparently to weaker capillary forces implying thinner water surface layer[45, 46], though by itself the surface of amorphous GST NPs is hydrophilic. Also with increasing GST surface roughness (if we compare in Figs 7-2 the samples HOPG-7 and 8) the capillary force strongly diminishes.

This is because only a few surface asperities contribute to the force[44, 45] or say even a single NP at the apex position leading to adhesion forces of the order of ~10 nN, with the amorphous / crystalline surfaces shown the same trend. Quantitative understanding of capillary forces on NP assemblies is also complicated by the fact that in many instances the surface probe (e.g., sphere, tipless cantilever etc.) picks up NPs leading to weak capillary forces.
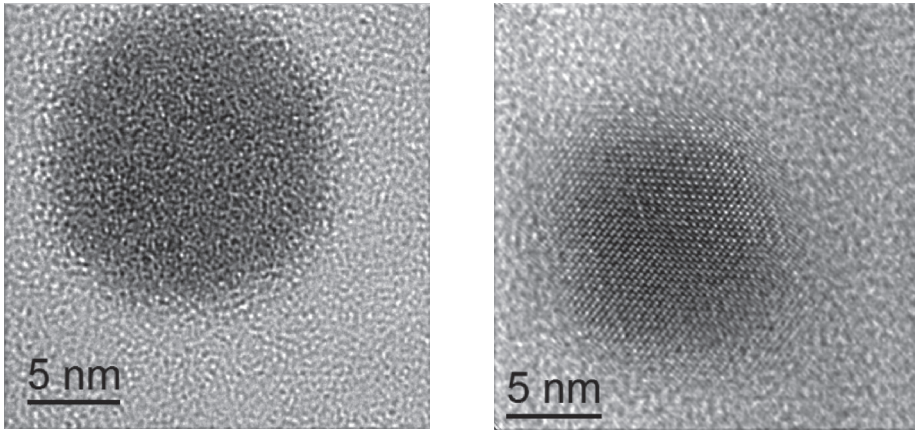
Figure 7-6(a,b) Example of high resolution transmission electron microscopy (BF-HRTEM) images of the amorphous (left) and crystalline (right) $Ge_2Sb_2Te_5$ nanoparticles (GST NPs)[32]

7
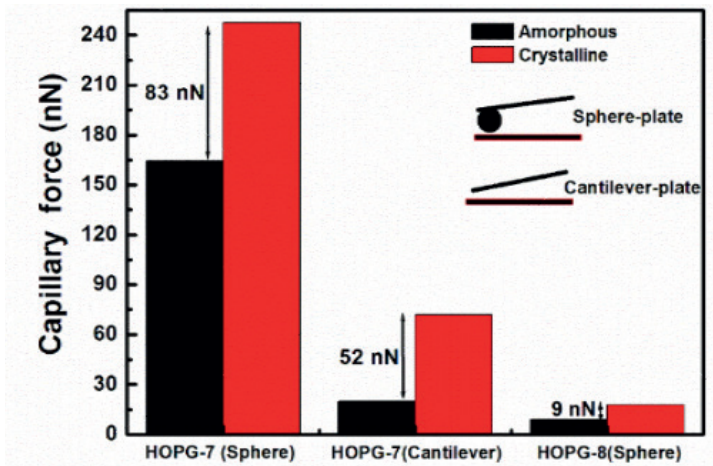
Figure 7-7 Capillary adhesion force measurements with an AFM using a 20 μm in diameter borosilicate sphere attached on a cantilever with spring constant k=2.25 N/m, and directly with a tipless cantilever of spring constant k=0.4 N/m. The latter was less stiff in order to increase the force sensitivity since in this case the interaction area, and formation of the capillary meniscus was smaller than that of the sphere. The HOPG 7 and 8 indices indicate different samples with the 8-series being rougher leading to weaker adhesion.

7.5   Conclusions

In conclusion, our study demonstrated, as a proof-of-concept, that surface wetting can be physically changed between highly hydrophobic - hydrophilic states using the amorphous-to-crystalline phase transitions of GST NPs acting as a kind of surfactant. CA measurements have shown that by increasing the coverage of amorphous NPs the contact angle increases to values close to the superhydrophobic limit (for NP coverages ≥ 80 %), while for crystalized the GST the CA decreased down to ~40° indicating significant hydrophilicity. Moreover, the GST phase also affects capillary adhesion due to water meniscus formation by being stronger for the more hydrophilic crystallized GST state. Therefore, PCM NPs offer a potent strategy to tune surface wetting depending on the desired application.

7.6   References

[1]   P. G. de Gennes, Rev. Mod. Phys. 57, 827 (1985)

[2]   D. Bonn, J. Eggers, J. Indekeu, J. Meunier, and E. Rolley, Rev. Mod. Phys. 81, 739 (2009)

[3]   G. I. Loeb and M. E. Schrader, Modern Approaches to Wettability: Theory and Applications (Springer 1992).

[4]   V. M. Starov, M. G. Velarde, and C. J. Radke, Wettability (CRC, Boca Raton, 2007).

[5]   S. Anand, A. T. Paxson, R. Dhiman, J. D. Smith and K. K. Varanasi, ACS Nano. 6, 10122 (2012)

[6]   X. Chen, J. Wu, R. Ma, M. Hua, N. Koratkar, S. Yao and Z. Wang, Adv. Funct. Mater. 21, 4617 (2011)

[7]   C.-H. Chen, Q. Cai, C. Tsai, C.-L. Chen, G. Xiong, Y. Yu and Z. Ren, Appl. Phys. Lett. 90, 173108 (2007)

[8]   D. 't Mannetje, S. Ghosh, R. Lagraauw, S. Otten, A. Pit, C. Berendsen, J. Zeegers, D. van den Ende and F. Mugele, Nat. Commun. 5, 3559 (2014)

[9]   A. Tricoli, M. Righettoni and S. E. Pratsinis, Langmuir 25, 12578 (2009)

[10] C. Neinhuis and W. Barthlott, Ann. Bot. 79, 667 (1997)

[11] Barthlott and C. Neinhuis, Planta 202, 1 (1997)

[12] M. Callies and D. Quere, Soft Matter 1, 55 (2005)

[13] D. Qu´er´e, Phys. A 313, 32 (2002)

[14] G. Palasantzas, J. Th. M. DeHosson, K. F. L. Michielsen, and D. G. Stavenga, Handbook of Nanostructured Biomaterials and their applications in Biotechnology 1, Biomaterials (2005).

[15] D.G. Stavenga, S. Foletti, G. Palasantzas, and K. Arikawa, Proc. R. Soc. B 273, 661 (2006).

[16] R. N. Wenzel, Ind. Eng. Chem. 28, 988 (1936)

[17] A. B. D. Cassie and S. Baxter, Trans. Faraday Soc. 40, 546 (1944)

[18] C. Ishino and K. Okumura, Eur. Phys. J. E 25, 415 (2008)

[19] D. Quere, Phys. Stat. Mech. Its Appl. 313, 32 (2002)

[20] L. Cao, H. -H. Hu, and D. Gao, Langmuir 23, 4310 (2007).

[21] Y. -T. Cheng and D. Rodak, Appl. Phys. Lett. 86, 144101 (2005)

[22] A. Checco, B. M. Ocko, A. Rahman, C. T. Black, M. Tasinkevych, A. Giacomello, and S. Dietrich, Phys. Rev. Lett. 112, 216101 (2014)

[23] L. Cao, T. P. Price, M. Weiss, and D. Gao, Langmuir 24, 1640 (2008)

[24] A. Tuteja, W. Choi, J. M. Mabry, G. H. McKinley, and R. Cohen, Proc. Natl. Acad. Sci. 105, 18200 (2008)

[25] Z. He, M. Ma, X. Xu, J. Wang, F. Chen, H. Deng, K. Wang, Q. Zhang, and Q. Fu, Appl. Surf. Sci. 258, 2544 (2012)

[26] A. Marmur, Langmuir 24, 7573 (2008)

[27] G. H. ten Brink, N. Foley, D. Zwaan, B. J. Kooi, and G. Palasantzas, RSC Adv 5, 28696 (2015)

[28] M. Wuttig and N. YaMada, Nature Materials 6, 824 (2007)

[29] E. R. Meinders, A. V. Mijritskii, L. van Pieterson, and M. A. Wuttig, Optical Data Storage: Phase Change Media and Recording (Springer, Berlin, 2006)

[30] G. Torricelli, P. J. van Zwol, O. Shpak, C. Binns, G. Palasantzas, B. J. Kooi, V. B. Svetovoy, and M. Wuttig, Phys. Rev. A 82, 010101(R) (2010)

[31] G. Torricelli, P. J. van Zwol, O. Shpak, G. Palasantzas, V. B. Svetovoy, C. Binns, B. J. Kooi, P. Jost and M. Wuttig, Advanced Functional Materials 22, 3729 (2012)

[32] B. Chen, G.H. ten Brink, G. Palasantzas, and B. J. Kooi, Submitted (2016)

[33] G. H. Brink, G. Krishnan, B. J. Kooi, and G. Palasantzas, Appl. Phys. 116, 104302 (2014)

[34] For the NP deposition system see also: www.mantisdeposition.com

[35] J. Krim and G. Palasantzas, Int. J. Mod. Phys. B 9, 599 (1995)

[36] G. Palasantzas, Phys. Rev. E 56, 1254 (1997)

[37] V. B. Svetovoy and G. Palasantzas, Adv. Colloid Interface Sci. 216, 1 (2015)

[38] M. Sedighi,V. B. Svetovoy, W. H. Broer, and G. Palasantzas, Phys. Rev. B 89, 195440 (2014)

[39] http://www.surface-tension.org/news/54.html, Young-Laplace equation fitting method (ADSA-PTM): Using the complete drop shape for measurement of static contact angle.

[40] Z. Xu, IET Micro Nano Lett. 9, 6 (2014)

[41] V. M. Starov, S. R. Kosvintsev, and M. G. J.Velarde, Colloid Interface Sci. 227, 185 (2000)

[42] K. S. Lee, N. Ivanova, V. M. Starov, N. Hilal, and V. Dutschk, Adv. Colloid Interface Sci. 144, 54 (2008)

[43] H. J. Butt, B. Cappella, M. Kappl, Surf. Sci. Rep. 59, 1 (2005)

[44] J. Israelachvili, Intermolecular and Surface Forces (Elsevier Science Publishing, 3rd Ed. 2011)

[45] P. J. van Zwol, G. Palasantzas, and J. Th. M. de Hosson, Phys. Rev. E 78, 031606 (2008)

[46] M. Sedighi, V. B. Svetovoy, and G. Palasantzas, Phys. Rev. E 93, 062803 (2016)
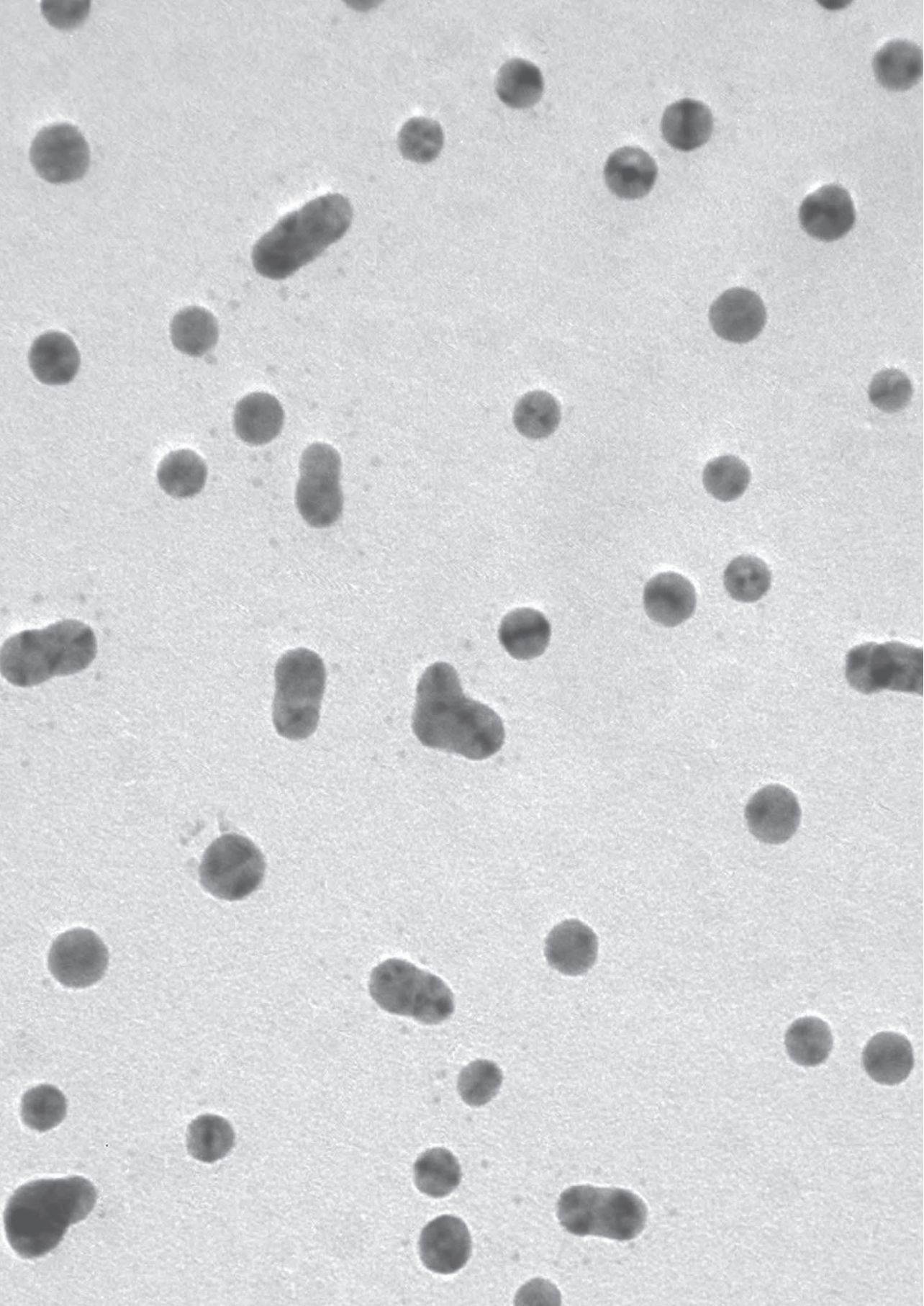
7

Chapter 8
Wetting of surfaces decorated by gas-phase synthesized silver nanoparticles: Effects of Ag adatoms, nanoparticle aging, and surface mobility

8.1 Abstract

The wetting state of surfaces can be rendered to a highly hydrophobic state by the deposition of hydrophilic gas phase synthesized Ag nanoparticles (NPs). The aging of Ag NPs leads to an increase in their size, which is also associated with the presence of Ag adatoms on the surface between the NPs that strongly affect the wetting processes. Furthermore, surface airborne hydrocarbons were removed by UV-Ozone treatment, providing deeper insight into the apparent mobility of the NPs on different surfaces and their subsequent ripening and aging. In addition, the UV-Ozone treatment revealed the presence of adatoms during the magnetron sputtering process. This surface treatment lowers the initial contact angle (CA) of the substrates and facilitates the mobility of Ag NPs and adatoms on the surface of substrates. Adatoms co-deposited on clean high surface energy substrates will nucleate on Ag NPs that will remain closely spherical in shape and preserve the pinning effect due to the water nano-meniscus. Their mobility is restricted if the adatoms are co-deposited on a UV-Ozone cleaned low surface energy substrate. They will nucleate in two-dimensional islands and/or nanoclusters on the surface instead of connecting to existing Ag NPs. This growth results in a rough surface without overhangs, where the wetting state is reversed from hydrophobic to hydrophilic. Finally, different material surfaces of transmission electron microscopy (TEM) grids revealed strong differences in the sticking coefficient for the Ag NPs, suggesting another factor that can strongly affect their wetting properties.[5]

8.2   Introduction

The wettability of nanostructured surfaces has generated relentless interest from both the fundamental and technological points of view to understand and control surface wetting[1–5]. Surface wetting is a heavily studied topic for more than 200 years dating back to T. Young in 1805[6], who showed the relationship between the contact angle (CA)θ, the surface tension of the liquid σ_{lg}, the interfacial tension σ_{sl} between the liquid and solid, and the surface free energy σ_{sg} of the solid. In 1936 Wenzel[2] and later Cassie and Baxter[3] showed the dependence of the water CA on real surfaces by incorporating the influence of surface roughness. The equation of Young in combination with the Wenzel and Cassie Baxter models suggests that the wetting of a surface is controlled by both its chemical nature and roughness. For rough surfaces, the Wenzel (W) model[2] gives the contact angle:

$$CA_W = \cos^{-1}[R^*\cos\theta] \quad \textbf{(8.1)}$$

with R* the ratio of the actual to the normal projected area of the solid/liquid interface. In this model, a hydrophilic/hydrophobic surface would be more hydrophilic/hydrophobic with surface roughening (assuming complete contact of the liquid with the surface).

Compared with the surface chemical composition, the surface roughness can then even play a more dominant role in the wettability[7].

Previous studies showed that one can alter the wetting behavior of an intrinsically hydrophilic material, e.g. Cu nanoparticles (NPs)[8,9] in combination with nanoscale roughness, leading to superhydrophobic surfaces[10]. On the other hand, it is known that wetting phenomena are determined by molecular interactions within the interfacial area between the liquid and the solid at the location of the triple line[4,5,1]. In fact, it has been argued that the wetting behavior on rough surfaces can be classified into four classes: Wenzel, Cassie-Baxter, Pinning, and Hemi-wicking state[11]. From theoretical calculations, two special microstructures have been proposed to produce super-hydrophobic states on hydrophilic substrates as is shown in Fig. 9(a,b) of the paper of J-L Liu et al.[12]. However, it is claimed that if the air beneath the water droplet on a sinusoidal substrate is open to the atmosphere, then the superhydrophobic state can exist only when the substrate is hydrophobic.

The NPs here represent a state of matter that is intermediate between atoms and the bulk solid-state, with properties that depend strongly on their size, shape, and material, as well as also on its environment[13] offering wider possibilities for wetting and other surface phenomena investigations (e.g. catalysis[14], antibacterial applications as is the case for Ag[15–18]). The general aim of using NP's is to modify the surface roughness and/or morphology and create surfaces with different

functionalities that are not present in bulk. Individual NPs and porous structures made with NPs of sizes smaller than 30 nm are rather difficult to image on a solid substrate[19]. To visualize the NP size distribution and surface coverage during sputtering, NPs can be deposited also on a TEM grid from the same particle beam[10,20]. The TEM grid can then be analyzed separately with high enough magnification for characterization. However, as it will be shown below this method does not always lead to the same NPs both in size and surface coverage. Moreover, the necessity for pre-cleaning both the substrates and TEM-grids will also be addressed.

Therefore, we will investigate here the wetting properties of various substrates that are covered up to various degrees with Ag NPs to demonstrate water pinning nanostructures leading to near super-hydrophobicity via control of roughness on a single nanometer length scale. The Ag NPs were deposited on flat surfaces using the Inert Gas Condensation (IGC) magnetron sputtering from Ag targets on both hydrophilic and hydrophobic surfaces. Moreover, we investigated the aging and ripening over time of the Ag NPs on various substrates taking into account their cleanness due to pollution by airborne hydrocarbons. In fact, it will be shown that NP decorated surfaces lead to a change of surface roughness by generating a nano-porous network forming many nano-capillaries upon contact with water during wetting studies. The change of the contact angle (CA) is the result of the pinning of the triple line leading to apparent super-hydrophobicity of a hydrophilic surface, which can be associated with high pinning force due to nano-capillaries formed around the NPs[20,21]. Moreover, we will demonstrate that the wetting state depends strongly on the choice of NPs, the substrate material, and cleaning, as well as on the NPs surface dynamics due to aging and ripening[21].

In the case of Ag NPs, which are made from high surface energy material, a substrate dependence is found in the sense that the NPs behave differently when deposited on a relatively low[22] (e.g., oxides, graphite/carbon) or a high surface energy material (clean metal surfaces). The aging results of the AgNPs are also of particular interest for their use in other applications, e.g., catalysis and medicine[23,24]. In addition, the mechanisms that are responsible for coarsening phenomena known as *Ostwald* and *Smoluchowski* ripening[25] act and age NPs differently depending on the NPs-substrate system.

8.3 Experimental methods: Wetting of various surfaces coated with various coverages of Ag NPs

To synthesize Ag NPs several techniques are available [26–30]. IGC with high-pressure magnetron sputtering is now recognized as a mature method to produce a beam of monodispersed clean metal NPs, which can be deposited on a variety of substrates to produce porous thin films with both controlled coverage and size of NPs[31–36]. The initial Ag NPs have been produced with a

home-modified high-pressure magnetron sputtering source based on a commercially available Mantis Nanogen-50© unit. The Ag NPs have a monodisperse size distribution (FWHM < 10%) with the operating window set for NP sizes in the range of ~10-40 nm. The size of the NPs could be altered e.g. by changing the aggregation length, the pressure, type of gas (argon and helium), and the magnetron power[35,37–39]. The Ag NPs were co-deposited on Silicon wafers, polished Graphite, and polished Ag targets.

To exclude the influence of substrate cleanness, all substrates received a UV-Ozone cleaning for 30 min before the deposition of the NPs. The deposition of NPs was progressed as quickly as possible on holey or continuous carbon-coated Cu grids "HC/CC" (300 mesh), 5nm thick High-Resolution Silicon TEM grid, 40nm thick Silicon Oxide TEM grid, and 20nm thick Silicon Nitride TEM grids (all from TEM windows©).

Careful TEM/EDX (Energy Dispersive X-ray) and diffraction analysis were performed to address the oxidation state and structure of the NPs (see Fig.8-1, 8-12(a) and 8-13(b)).

The NPs were characterized with a JEOL 2010 TEM operating at 200 kV and an FEI Helios G4 CX dual beam system in S(T)EM mode operating at 18kV. The High Resolution (S) TEM images were taken with a monochromated aberration-corrected Thermo Fisher Scientific ThemisZ (S)TEM operating at 300kV. The obtained (S)TEM images were statistically processed by the Image-Pro Plus v.7 software[40] to obtain the NP size distributions see Fig 8-7. The latter was fitted by the log-normal size distribution

$$f_X(x; \mu, \sigma) = \frac{1}{x\sigma\sqrt{2\pi}} e^{-\frac{(\ln x - \mu)^2}{2\sigma^2}} \quad (x > 0) \; \textbf{(8.2)}$$

using MATLAB and Origin routines[41]. This is performed to verify that the typical NP growth process takes place during high-pressure magnetron sputtering by condensation of a supersaturated vapor, where the growth rate is independent of size. In Eq.(8.2) the parameters μ and σ are the mean and standard deviation of ln(x), respectively with x the particle size. The actual standard deviation of the particle size *Ds* as a function of μ and σ is given by:

$$\Delta\sigma = \sqrt{\exp(\sigma^2) - 1} \, \exp\left(\mu + \frac{\sigma^2}{2}\right) \textbf{(8.3)}$$

The substrates were commercially available Si wafers 2 inches in diameter, and carefully polished Ag(5N) and Graphite(4N) substrates. The polishing procedure was Method B taken from the Struers Metalog Guide with the last polishing step using 0.25 μm size diamonds.

Finally, the contact angle measurements were performed using a Dataphysics OCA20 system. An automated syringe dropped ~2 μl droplets of pure water (MilliQ) on the sample, where a camera recorded the images for several seconds (10) and fed them through the Dataphysics[42] SCA202,

v4.1.17 build 1024 image processing software. The values of the contact angles were obtained via a direct fit to the interface region only, and a fit using the Young-Laplace (YL) equation based on the shape analysis of a complete drop[43].

8.4   Results and discussion: Wetting behavior on various substrates and different coverages of Ag NPs.

In the pursuit for further research of super-hydrophobicity on a single nanometer lenghtscale[10], a series of Ag NPs depositions were performed on native Si oxide surfaces from Si <100> substrates, and polished Teflon surfaces. The Ag NPs were sputtered for 30, 60, 120, and 360 minutes. Ag is less sensitive for oxide formation than Cu, as it is shown in Fig. 8-1 and 8-12 and 8-13, and it revealed a slightly higher Static Contact Angle (SCA) compared with Cu NPs with oxidized surfaces under the same experimental conditions[10]. The resulting coverages from analyzing the co-deposited TEM grids, as can be seen in Fig. 8-2, were 12, 28, 58, and 83 %. The corresponding SCAs are given in Figs. 8-3 and 8-4.

As shown in Fig. 8-4, the deposited Ag NPs transform the initial hydrophilic surface of Si oxide with an SCA of 52° degrees to a closely superhydrophobic (assigned to CA=150 degrees) with 143° degrees. Interestingly, a very similar SCA approaching 140° is found for the highest Ag NP coverage on Teflon substrates. So, although the bare surfaces can have clearly different CAs, the highly covered ones become all similar, close to super-hydrophobicity. The TEM images (see Figs. 8-1 and 8-2) and S(T)EM images (Figs 8-8 till 8-11) show individual NPs with monodisperse size distribution and coverage that scales in proportion with the deposition time (see Figs 8-14 a and d), though the NPs even at low coverages tend to also land on top of each other. See Fig. 8-13 and also Figs. 1-3 in ref.[44] The resulting SCA is due to the pinning of the triple line by the NPs, particularly by the water nanomeniscus in the apex between the NP and substrate, as was discussed in the previous studies[10,45,46].
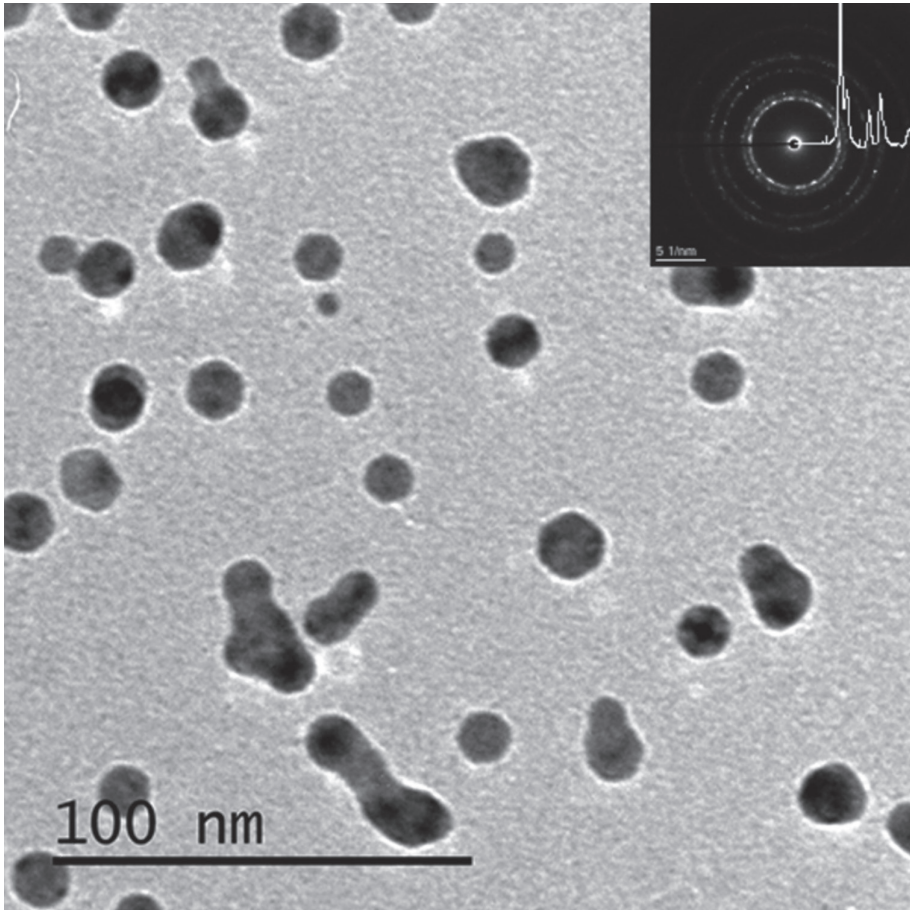
Figure 8-1 BF-TEM images for AG NPs. The Inset shows the electron diffraction pattern (SAD) and corresponding intensity profile of the diffraction spots consistent with fcc Ag;<111> plane; k[1/nm]=4.248 d=2.35 Å;<200> plane k[1/nm]=4.845, d=2.06 Å;<220> plane k[1/nm]=6.957,d=1.44 Å and the <311> plane k[1/nm]=8.219, d=1.22 Å

The same experiment was carried out on carefully polished Ag and Graphite substrates. The resulting surfaces and the effect of UV-Ozone cleaning[47] for the SCA of water are shown in Table 8-1. The high-resolution SEM images in Figs. 8-6(d,e) revealed two distinct surfaces. The graphite surface (a system with low surface energy comparable with the also carbon-based CC/HC TEM grids to be discussed below) showed individual Ag NPs merging into "fluffy" aggregates and forming bigger objects, but with most individual Ag NPs still visible. In contrast, the Ag substrate with deposited Ag NPs revealed that almost all of the Ag NPs coalesced into larger aggregates without preserving the individual character of the original Ag NPs. The resulting surface appeared very similar to thermally evaporated Ag thin films of 1, 5, and 15 nm thickness[29].

The rapid coalescence of NPs is one of the reasons why it is difficult to make nanoscale materials and to keep them distinct so that they maintain their individual character [39,48–50]. On the other hand, Cu NPs deposited on Teflon and Si substrates (as discussed earlier[10]) and the Ag NPs on polished graphite did not show (the same level of) coalescence.
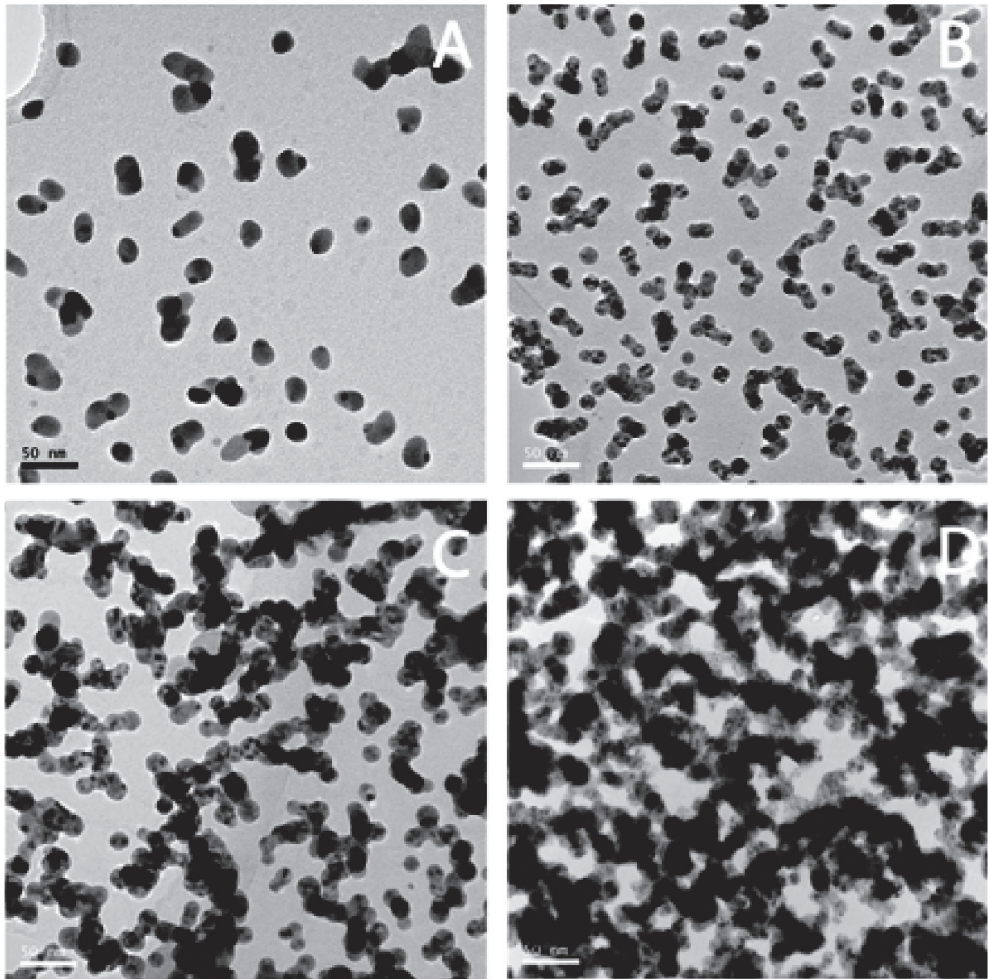
Figure 8-2 BF TEM images from deposited AgNPs on HC TEM grids: A,B,C,D =12, 28, 58, 83 % Coverage (30, 60, 120, 360 min deposition time).
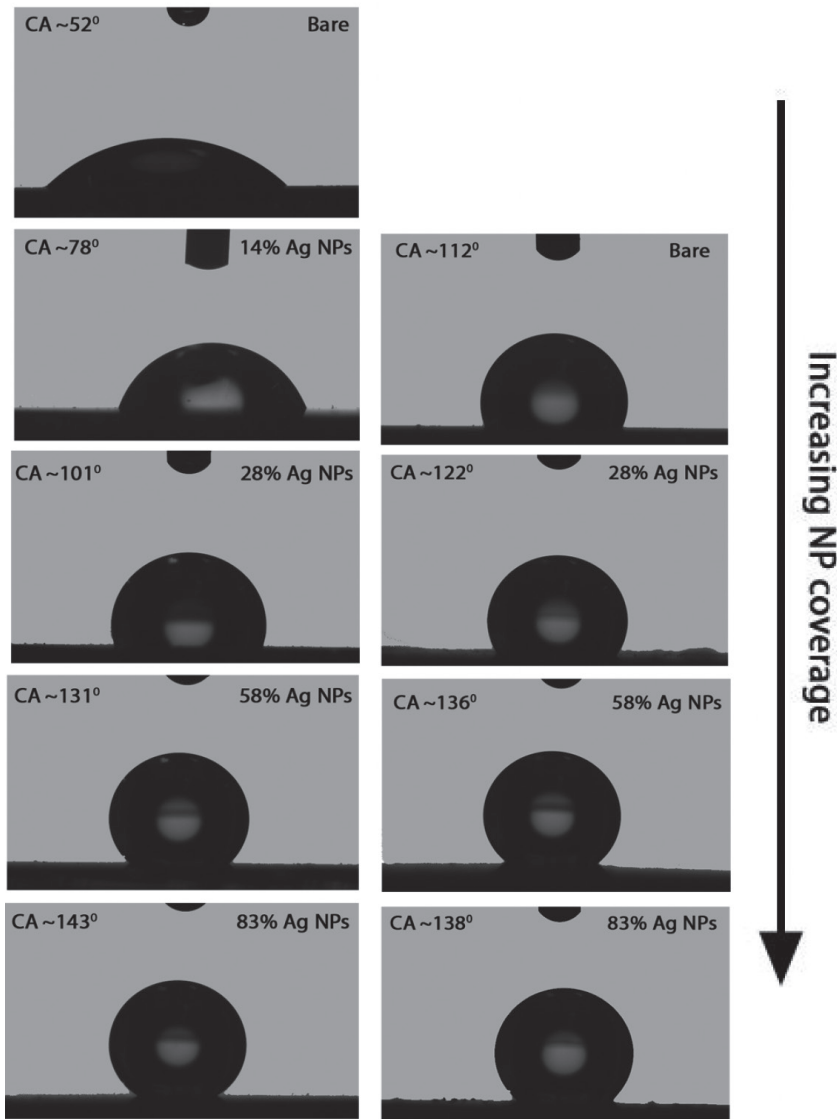
Figure 8-3 Static contact angles and side-view images of the water droplet for different coverages of AgNPs on a silicon wafer (left) and polished Teflon (right)

The obvious question that arises is why Ag NPs behave so differently on the four different substrates. From MD calculations and earlier experiments with Au NPs/clusters on different substrates, one derives relatively mixed conclusions. Some works claim that Au clusters are immobile on a surface[25,44,51–53], whereas others claim high mobility and state for the mobility/ cluster-diffusion speed to be as high as an individual (ad)atoms[51,54–56]. These conclusions were

made by experiments inside a Scanning Tunneling Microscope with an extremely clean substrate, and under ultra-high vacuum conditions. The main conclusion for the mobility of the Au NPs was the influence of the substrate.

On graphite, a low surface energy material (HOPG 60 mJ/m²), the mobility of the Au NPs was high. For a substrate of a crystalline high energy material (Ag[57] 1200 mJ/m², Cu[57] 1600 mJ/m², and Au[57] 1400 mJ/m²) the mobility was reduced, and upon reaching the upper limit of epitaxy the particles would stay fixed[52,58].

The data derived from MD calculations for clusters ≥ 200 atoms at 300 K indicate immobile NPs. In our case, the Ag NPs, soft-landing on an amorphous native Si oxide layer, are much larger than 200 atoms. In fact, a 30 nm in size Ag NP contains about $n = 738 \cdot 10^3$ atoms[59] ($n = (r_n/r_w)^3$ where r_n is the diameter in nm of the NP, and $r_w = 1.66$ Å is the Wigner-Seitz radius of Ag).

An amorphous substrate has no order, and therefore there is no driving force for the NPs to realign[52]. As a result, the force that remains is the van der Waals interaction, which is strong enough for the NPs to stick to the surface.

At higher coverages, the next layer of Ag NPs lands on top of other Ag NPs leading to rougher surfaces and creating even more water nano-capillaries[13,58]. The soft landing deposited Ag NPs can react with the substrate in different ways. They can stick on the surface and maintain their shape, and they can also (by aligning along with a crystallographic orientation of the substrate) sink totally or partly into the substrate wetting the total or only part of the surface[60].

If the Ag NPs upon mutual contact realign and coalesce into bigger *spherical* NPs, the result is an apparent hydrophobic CA due to pinning of the triple line as a consequence of the formation of the nanomeniscus (underneath the particles). If the same Ag NPs land on a clean Ag surface (UV-Ozone cleaned to remove airborne hydrocarbons) a situation different from non-cleaned surfaces arises. This polished Ag surface is crystalline and the d-spacing of the atoms in Ag NPs closely matches the bulk d-spacing from the substrate. The Ag NPs will align along the crystallographic orientation direction and wet the surface[61,62]. Similar explanations for the observed coalescence phenomena have been found by Grouchko et al.[61,62], which were to understand the mechanism of coalescence of Ag NPs a series of in-situ high-resolution TEM experiments were performed by imaging the contact of two individual NPs. They found that two Ag NPs particles with the same crystal structure result in a larger particle with the original crystal structure[61]. However, processes can be complex, because they also found that Ag NPs and Au NPs tend to stay distinct in contact with each other, whereas the Ag NPs in contact with a gold rod would "merge and sink" and lose their morphology[62].

In our case, it is evident that the Ag NPs on the clean polished Ag substrate coalesce (see Fig. 8-6(e). It is unfortunately unknown if the nanomeniscus with the substrate is removed if the Ag NPs coalesce and merge with the substrate. However, judging from the current SCA measurements and the obtained hydrophobic CA, the nanomeniscus must be present. In theory, with increasing roughness, the surface should become more hydrophilic based on the Wenzel model[8,9]. However, the SCA here evolves from 50° degrees for the clean polished Ag surface to 105° degrees for a surface with only 28% Ag NPs coverage. The latter means that part of the Ag NPs or the resulting surface still has a high degree of pinning due to the nanomeniscus formed between the NPs and the substrate surface.
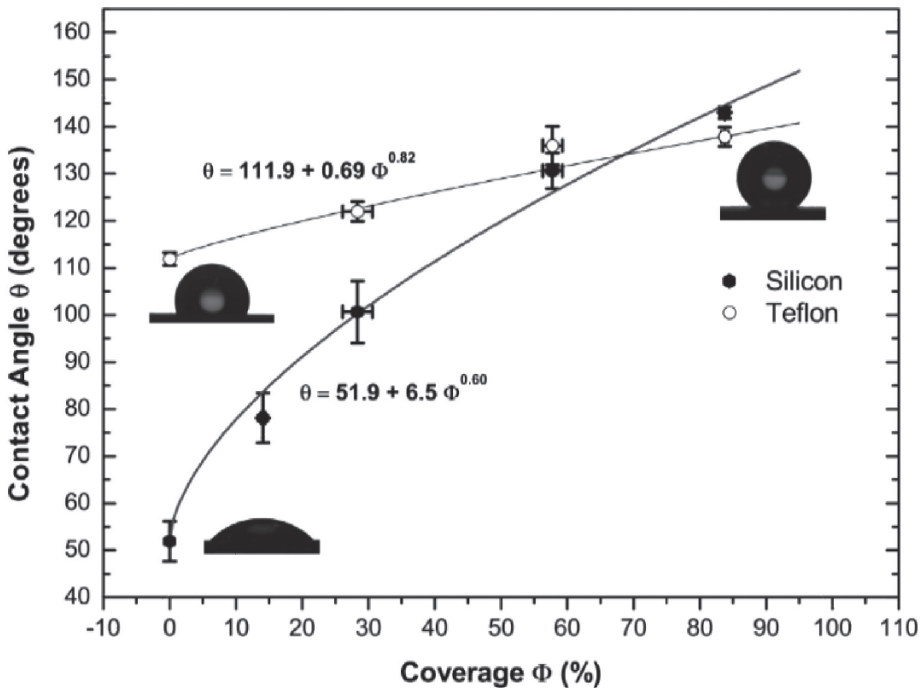
Figure 8-4 Dependence of the static contact angle on the coverage of Ag NPs on both Teflon and Silicon, which are initially hydrophobic and hydrophilic surfaces respectively. Power functions have been fitted through both the data sets. Although the effect of induced surface roughness is lower on silicon, the CA tends towards the same value indicating the predominant effect of the NP topology.

Moreover, a Si wafer surface with the same amount of Ag NPs gives an SCA of also roughly 105° degrees. These identical results for the Ag and Si-oxide surfaces are a clear indication that the Ag NPs and their shape determine the SCA of the surface. The HR-SEM image in Fig. 8-6(d) shows the altered state of the Ag NPs on the polished graphite surface as compared to the polished Ag surfaces (see Fig. 8-6(e)). The Ag NPs on the polished graphite surface show a different morphology despite deposition under identical conditions. On the polished graphite, the Ag NPs appear to be movable over the surface, because of the lower surface energy of the carbon in agreement with conclusions made by several authors[44,51,53,56]. However, regardless of the visible NP shapes that remain spherical, the SCA for the graphite surface is much lower than the SCAs for the Ag and Si-oxide surfaces. Judging from the SEM images, a thin coherent film is made on the graphite from individual Ag NPs (since coalesce into larger spheres is not observed). The resulting SCA of 36° degree (Fig. 8-6 and Table 8-1) for the NPs covered graphite surface suggests a slightly more hydrophilic state than the surface of the clean polished graphite target (CA=46° degrees). This is also smaller than the 50 degrees CA of a polished Ag target.

The Ag NPs layer on graphite, therefore, behaves hydrophilic in a Wenzel state as it happens for a rough Ag thin film. The latter can be seen in the HR-SEM images of Fig. 8-6(d). The rough surface appears to be constructed of Ag NPs, though judging from the SCA, it lacks the many nanomeniscus' between the particles and the substrate which leads to water pinning.
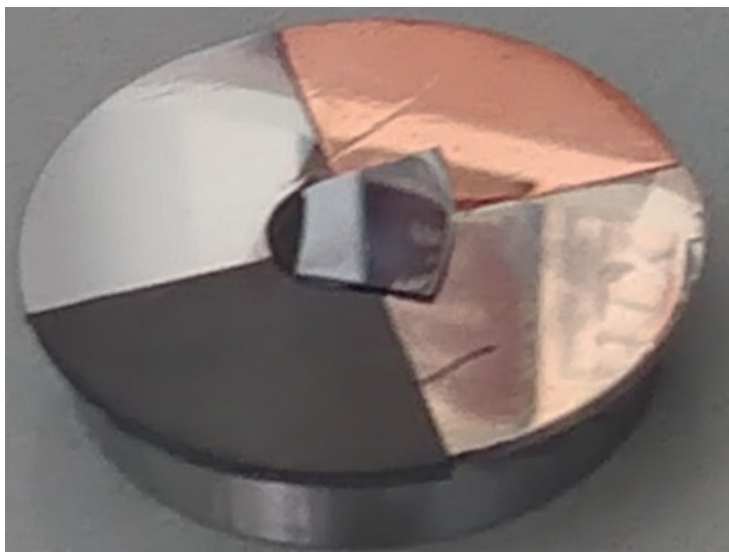
Figure 8-5 Four equally polished substrates (Ag, Mo, Cu,Graphite).

SCA in degrees°	Before UV-O$_3$	After UV- O$_3$	After 10 days
Polished Ag (P-Ag)	59 ± 3	50 ± 1	87 ± 5
Polished Graphite (P-C)	78 ± 1	46 ± 0.5	49 ± 2
P-Ag + 60 min AgNPs		105 ± 4	
P-C + 60 min AgNPs		36 ± 2	

Table 8-1 Static contact angles for two different substrates. The AgNPs coverage is approximately 28% after 60 min NP sputtering on polished Graphite and Ag surfaces. The effect of UV-Ozone cleaning on the CA is also shown.
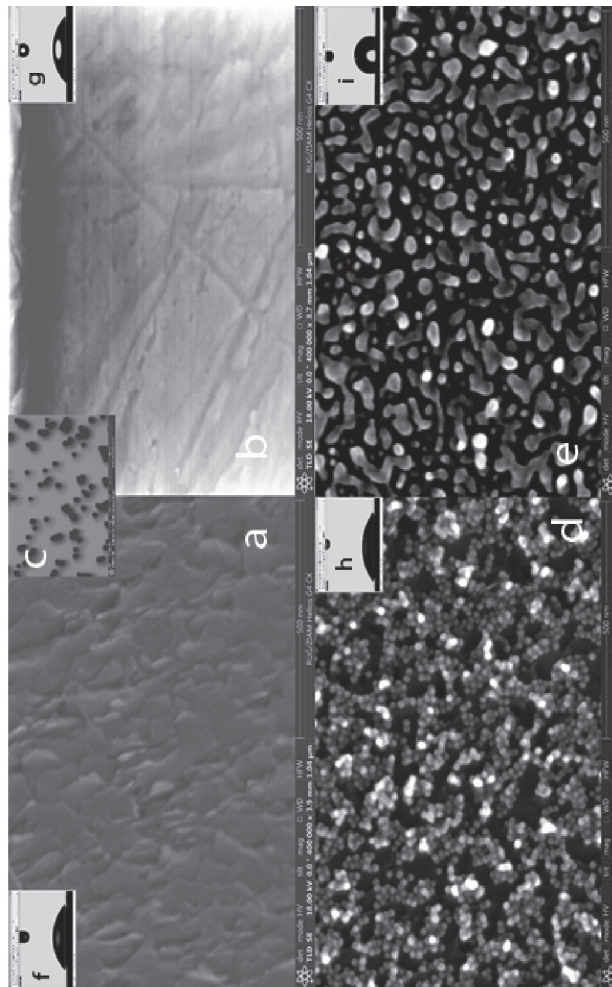
Figure 8-6 HR-SEM images taken before (a,b) and after the deposition (c,d) to illustrate the nanoscale rough surface at 400K X mag. Image (c) is the corresponding BF S(T)EM image scaled to size Images inserts (f,g,h, i) are the Static Water Contact Angles (SCA) from the corresponding surfaces

To check if the loss of the water nanomeniscus (transition from spheres into a rough layer) was the reason for this behavior, a series of Ag NPs depositions were performed (see Fig. 8-7). One of the conclusions of these experiments is that during the deposition besides NPs also adatoms are being deposited. This phenomenon appears to have been overlooked in other experiments/ explanations.[63,64] These adatoms are very mobile on a graphite surface (HOPG), and samples covered with airborne hydrocarbons[21]. The adatoms are co-deposited and diffuse leading to nucleation on the substrate and also under the deposited NPs[60] filling up the apex' underneath the NPs and therefore preventing water pinning by nanomeniscus'.

In the case of sintering or coalescence of contacting spheres of radius r, theoretical calculations[60] have shown that the sintering kinetics is described by $X^n/r^m = A(T)t$ where X is the neck radius, A(T) is a temperature-dependent constant that varies with the mass transport mechanism, n and m are constants, and t is the time. From the several mechanisms available for mass transport, the two most likely ones involve diffusion either through the bulk or via the surface of the contacting islands. For bulk diffusion we have n = 5 and m=2, whereas for surface diffusion n = 7 and m = 3, while calculations show that surface diffusion dominates sintering. Ostwald ripening, sintering and cluster migration are different phenomena taking place and interfering at the same time [60]. Surface nucleation of adatoms on a substrate has been described in great detail by Knauer[65] et al. based on Knudsen cell deposition, though the principles of surface nucleation of (ad)atoms are still valid here.

Although the Ag NPs on the Ag target are less mobile as compared to the graphite target[25,44,53–56,56,66–68], they appear to coalesce into bigger spherical NPs where a reason could be again the overlooked role of adatoms. The Ag NPs as a whole are too big to move around and coalesce on the crystalline substrate. However, the individual adatoms can migrate towards the bigger NPs and nucleate/sinter on them as can be seen in HR-(S)TEM images (Figs. 8-12(a,b) A process that normally takes place is Ostwald ripening, where traditionally larger NPs grow at the expense of the smaller ones. This process occurs because the barriers for atom diffusion are relatively low on a metal surface[25,69]. The next logical step would be that these atoms nucleate on the Ag NPs (achieving a lower energy state) along with the crystal orientation of the Ag NPs. The second ripening mechanism is the Smoluchowski ripening, where particle migration and coalescence lead to larger clusters.

That same nucleation mechanism would occur on the graphite surface, where, however, the graphite substrate does not aid the crystallization step. Consequently, the resulting surface consists of individual Ag NPs, where the apex under the particles is filled with adatoms resulting

in a rough Ag decorated substrate being in a Wenzel state. The resulting rough surface should be more hydrophilic than the flat surface as the experiment confirms. Moreover, it is also a clear indication that the high SCAs of NP covered Ag, Teflon and Si-oxide surfaces are caused by the shape of the Ag NPs in combination with a flat substrate that allows to create water nanomeniscus between NP and substrate. If this condition is not fulfilled then the SCA will decrease as it has also been confirmed by Guo et al.[20,21], where it is shown that there is a linear relationship with the apex under the Cu NPs and the measured SCA. Moreover, the findings are in agreement with recent observations supporting that the *asperity shape* is more important than the *asperity height*[4,70] in determining the wetting state.

8.5 Experimental methods: Aging of Ag NPs on CC-HC-TEM grids and the effect of ozone cleaning

To analyze in more detail the behavior of Ag NPs on different substrates and explain its influence on wetting, a series of experiments was performed on TEM grids and analyzed using high-resolution electron S(T)EM images. The Ag NPs coverage should be low enough to analyze the individual NPs but sufficiently high for coalescence to take place. Furthermore, the effect of cleaning of the substrate, in our case UV-Ozone cleaning, should be addressed. Since the TEM grids should be electron transparent and amorphous, only a limited number of different TEM grids are available, which in our case are Continues Carbon (CC) grids, Holey Carbon (HC) grids, and Silicon Nitride/Oxide TEM grids.

For each deposition condition, there was always a comparison between deposition on a grid without and one with UV-Ozone treatment for 30 min. Experimental setup/methods
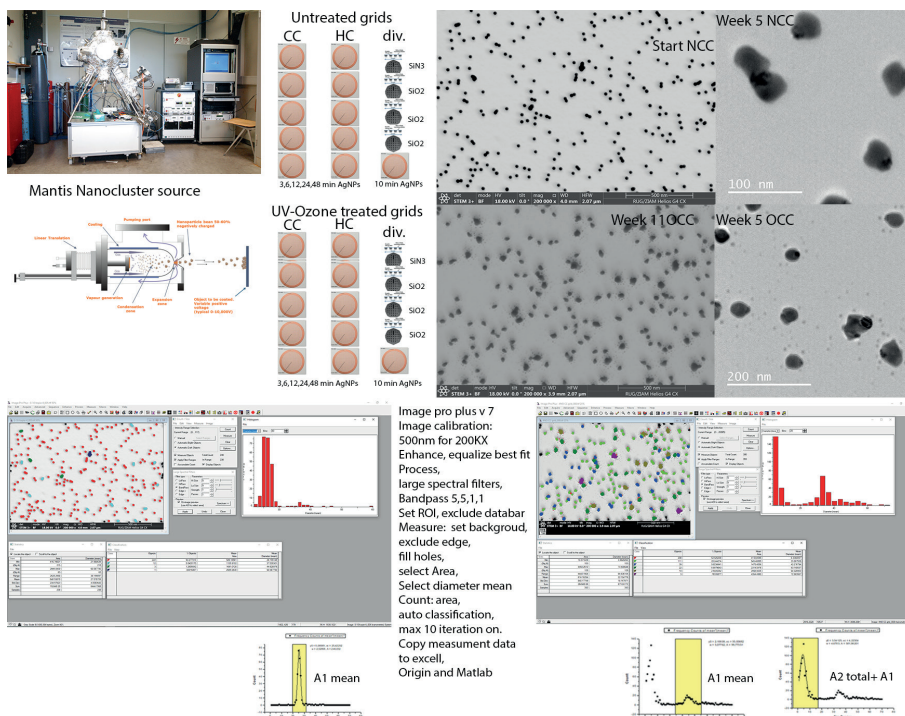
Figure 8-7: Image analysis routine used in Image-Pro Plus 7. The tabulated data output was used to create frequency counts of the size distributions and FWHM derived by using Origin and Matlab. The tabulated data were used to construct Tables. 8-1, 8-2 and 8-3 and Fig. 8-14

In total, three sets of experiments were conducted (see above Fig. 8-7). Each set was performed without interrupting the vacuum.

The TEM grids were labeled as follows:

i) 10 CC grid (as is = N; Ozone cleaned=O) samples: 1-5NCC,1-5OCC;

ii) 10 HC grid samples: 1-5NHC, 1-5OHC,

iii) 8 Silicon Nitride/Oxide TEM grids and 2 HC TEM Grids

Insets (i) and (ii) the CC and HC TEM grids were exposed to Ag NPs deposition for 3, 6, 12, 24, and 48 min, respectively, and therefore the sample numbers 1-5 appeared.

After the depositions, S(T)EM images were obtained as fast as possible in less than two days. The S(T) EM images in the Figs. 8-8 and 8-9 were analyzed with the image analysis protocol as explained in Fig. 8-7. The data in tables 8-14 are also shown graphically in Figs. 8-2 and 8-3. The cluster-source was set to a fixed current of 0.15 Amp, and a Quartz Crystal Microbalance (QCM) recorded a linear mass uptake during all depositions. (as an example for just 1 typical deposition see Fig 8-0)
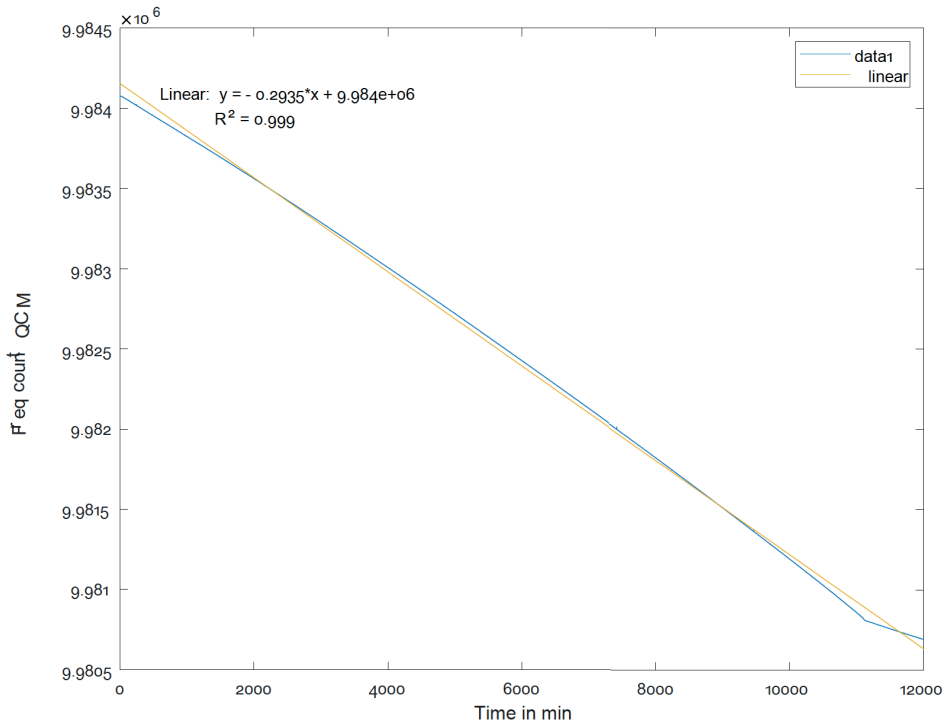
Figure 8-0 Raw QCM data plotted in Mathlab to record yield and time during the AgNPs deposition of experiment 8-2c (120 min AgNPs deposition)

The average size of the Ag NPs deposited on the NCC and OCC grids was 27.6 nm and 28.2 nm, respectively, and the FWHM after fitting the log-normal size distributions, was found to be 3 nm. The NHC and OHC grids showed NP sizes of 28.0 nm and 28.5 nm, respectively, Taking the FWHM of 3 nm into account, the cluster-source thus produces, according to the S(T)EM images, Ag NPs with a consistent size of 28 nm for the time period of 186 min (93 min for each of the two sets).

The coverage (by counting all pixels from the Ag NPs covering the area in the S(T)EM images) scales linearly with time (see Fig. 8-14), though judging from the S(T)EM images some NPs are landing on top of each other (see Fig. 8-13)

8.6 Results and discussion: Aging of Ag NPs on HC-CC TEM grids and the effect of ozone cleaning

The average size of the Ag NPs after 11 weeks of aging (see the S(T)EM images in the Fig 8-14 and table 8-1 increased (from 27.6) to 42.4 nm for the NCC grids, while for the UV-ozone cleaned grid OCC it was increased (from 28.2) to 37.4 nm.

The FWHM increased to 4.2 nm for the CC grids, and to 5.9 nm for the UV-ozone cleaned grids. This is an increase in NP diameter of 54 % for the uncleaned grids, and 33 % for the UV-Ozone cleaned grids. All data is summarized in Table 8-1 and Fig 8-14.

The untreated HC grids showed an increase of 40% in size after 11 weeks of aging, while the UV-Ozone-treated HC grids showed an increase of 34 % in size. From these numbers, it becomes evident that Ag NPs ripen/age more on untreated CC-TEM grids than on UV-Ozone treated CC-TEM grids.

One explanation for the increased growth of the NPs on samples that were not UV-Ozone treated can be attributed to the higher mobility of atoms due to airborne hydrocarbons on these samples. In contrast, on the UV-Ozone cleaned surfaces many new ultra-small circular Ag nuclei are formed (see HR-S(T)EM in Figs 8-12 and 8-13.

The overall growth of the NPs can be explained by Ostwald ripening[70] or NP coalescence. Then, the NP number density must decrease though this is not observed. A plausible explanation for the observed phenomena here is the presence of many adatoms, which are co-deposited during the sputtering process as a remnant from the plasma in the cluster source and after aging contribute to the NP growth.

Judging from the HR-S(T)EM images in Figs. 8-12 and 8-13, it is inconclusive if the adatoms nucleate in 2D or 3D islands and diffuse over the grid or coalesce into bigger spheres. The adatoms after deposition on the substrate start to nucleate to minimize their surface free energy[60]. The nucleation in the form of 2D islands is more likely to take place because of the large increase in the covered area upon aging. Such a large increase due to adatoms is possible in 2D islands, but spherical Ag NPs would require an unrealistically high number of adatoms during aging. The FFT measurements from the (S)TEM data, see e.g. Fig. 8-13, show d-spacing's consistent with fcc Ag. No other phase is observed, also after aging, but a major effect that interferes with the observations is the continuous contamination/redeposition of hydrocarbons.

Amorphous carbon is deposited during image acquisition, and it results in a carbon blanket obscuring everything underneath it[70]. After 1.5 weeks the effect of the airborne hydrocarbon contamination and influence on the CA is at its maximum, and when it reaches a plateau[20,21,70](see Fig. 8-6b).
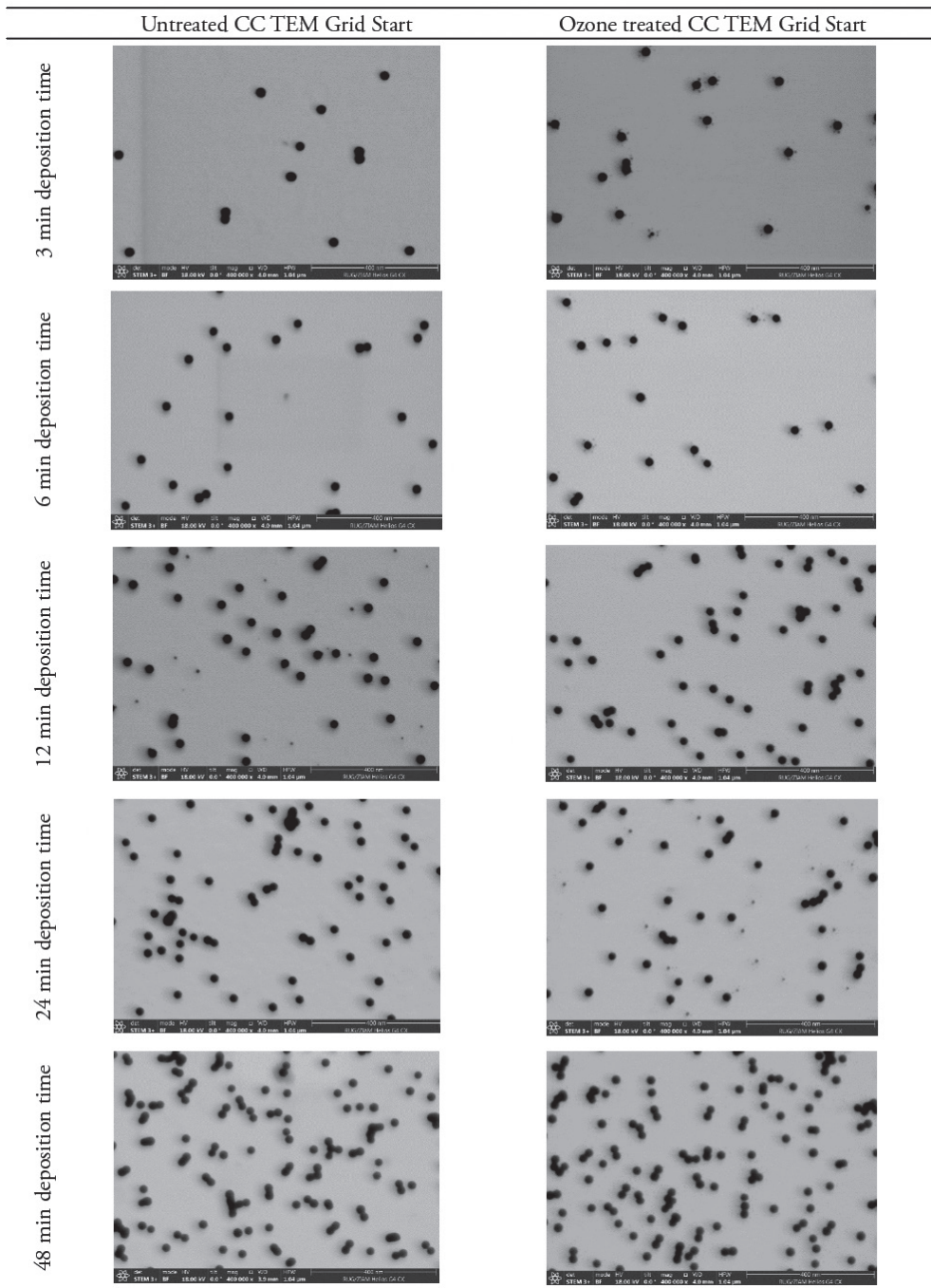
Figure 8-8 400KX BF S(T)EM images showing the starting condition for studying ripening and aging of different coverages Ag NPs on untreated Continues Carbon (CC) grids and UV-Ozone treated (OCC) grids.

Untreated CC TEM Grid Week 11	Ozone treated CC TEM Grid Week 11

3 min deposition time

6 min deposition time

12 min deposition time

24 min deposition time

48 min deposition time
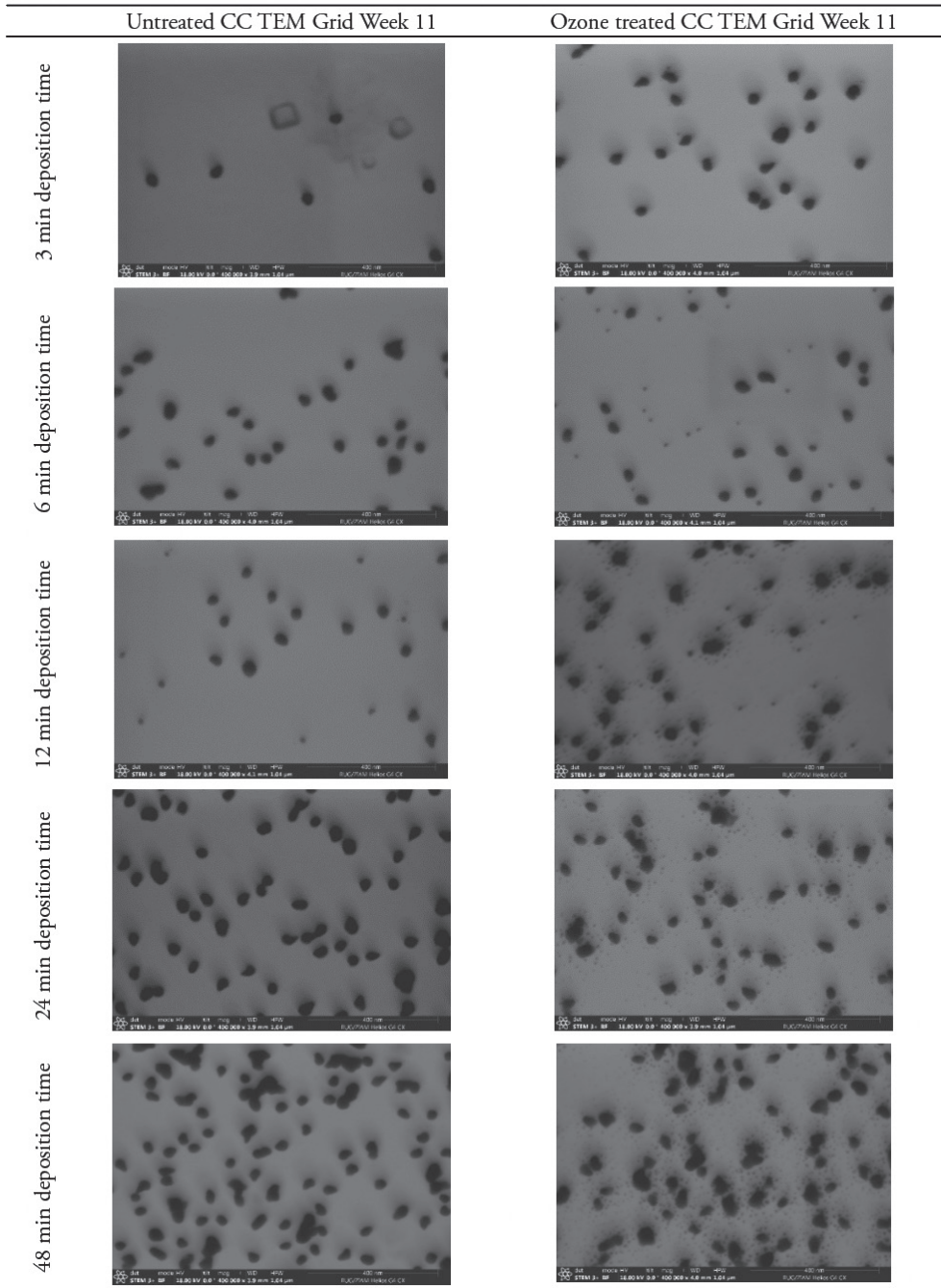
Figure 8-9 400KX BF S(T)EM images showing the ripening and aging of different coverages Ag NPs on untreated Continues Carbon (CC) grids and UV-Ozone treated (OCC) grids after 11 weeks of aging at room conditions.
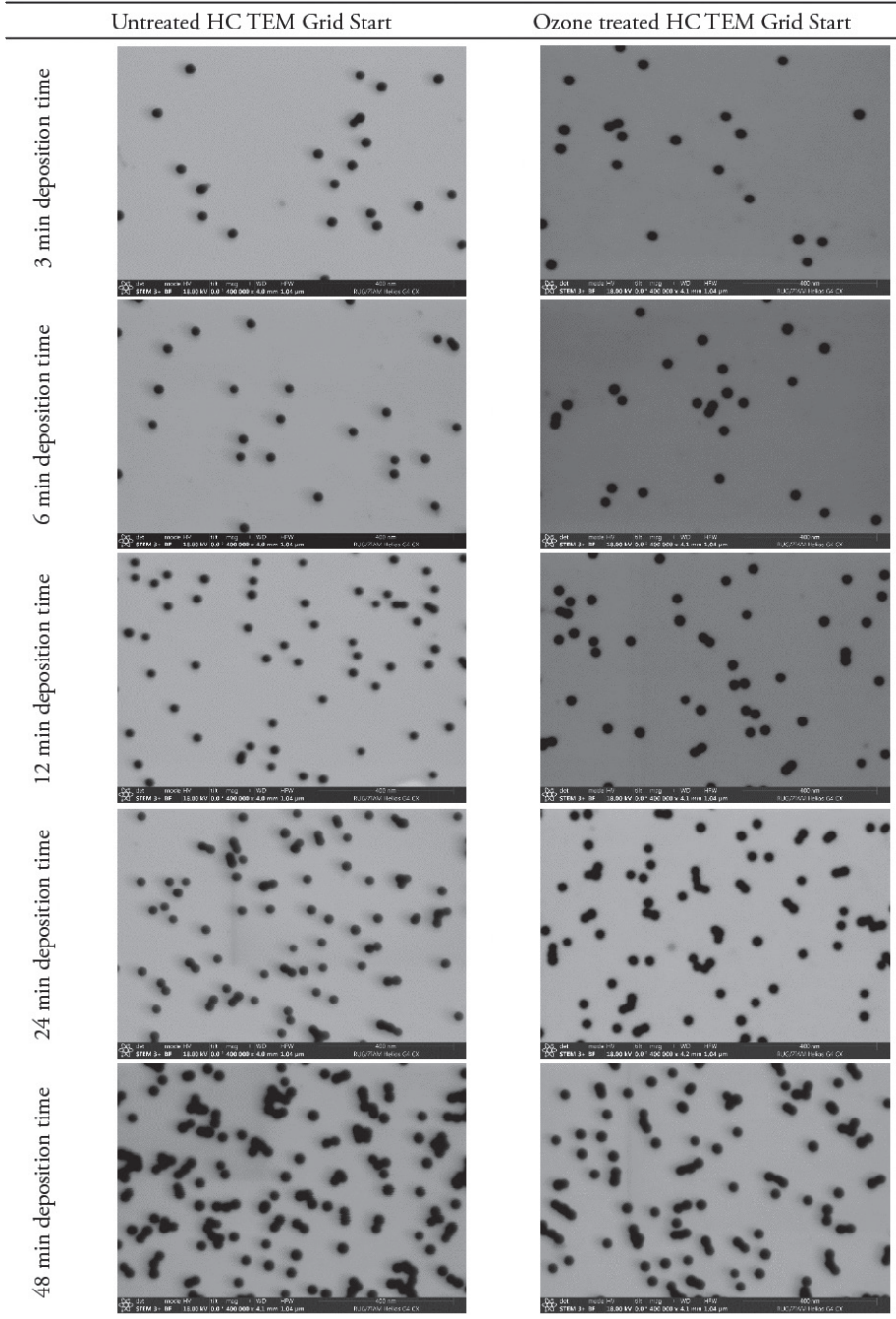
Figure 8-10 400KX BF S(T)EM images showing the initial starting condition for studying ripening and aging of different coverages Ag NPs on untreated Holey Carbon(HC) grids and UV-Ozone treated (OHC) grids.
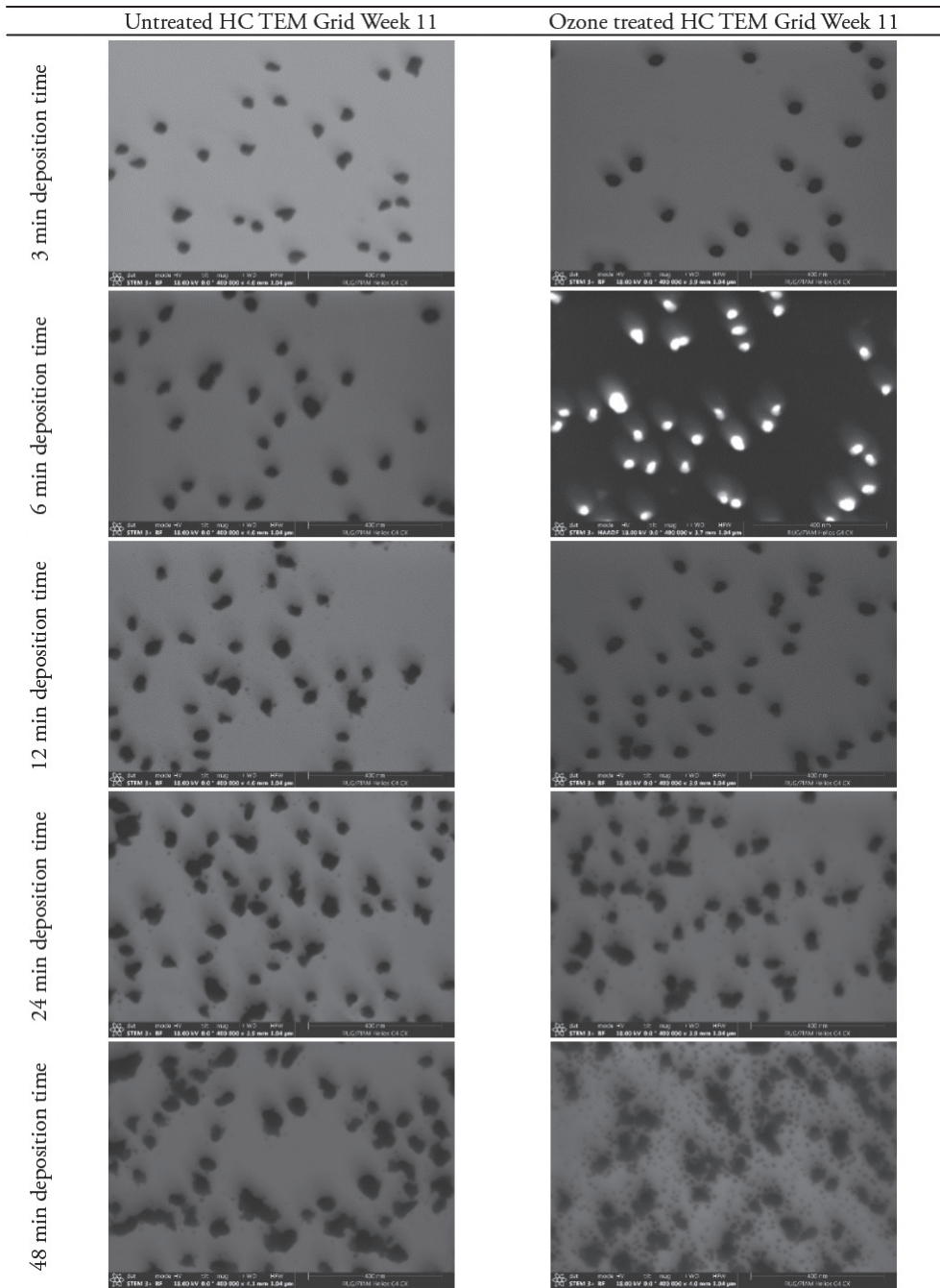
Figure 8-11 400KX BF S(T)EM images showing the ripening and aging of different coverages Ag NPs on untreated Holey Carbon(HC) grids and UV-Ozone treated (OHC) grids after 11 weeks of aging at room conditions.

Increase (%) in Ø diameter (nm)

	Ø diam nm	Increase (%
CC TEM grid	Ø diam nm	
Avg NCC W11	42,4	53,6%
Avg NCC Start	27,6	
Avg OCC W11	37,4	32,6%
Avg OCC Start	28,2	
HC TEM grid	Ø diam nm	
Avg NHC W11	39,2	40,0%
Avg NHC Start	28	
Avg OHC W11	38,2	34,0%
Avg OHC Start	28,5	
Si_3N_4 TEM grid	Ø diam nm	
avg N W11	38	19,5%
Avg N start	31,8	
Avg O W11	37	27,6%
Avg O Start	29	
5 nm SiO_2 TEM grid	Ø diam nm	
Avg N W11	35,2	21,0%
Avg N start	29,1	
Avg O W11	36,8	29,6%
Avg O Start	28,4	
5 nm SiO2 TEM grid	Ø diam nm	
Avg N W11	42,7	47,8%
Avg N start	28,9	
Avg O W11	50,3	77,7%
Avg O Start	28,3	
40 nm SiO_2 TEM grid	Ø diam nm	
Avg N W11	86,1	112,6%
Avg N start	40,5	
Avg O W11	41,6	34,2%
Avg O Start	31	
HC TEM grid	Ø diam nm	
Avg N W11	44,7	68,7%
Avg N start	26,5	
Avg O W11	39,1	47,0%
Avg O Start	26,6	

Tabel 8-1 Tabulated data showing the average increase in NP diameter Ø in nm and % between UV-Ozone treated and untreated TEM grid.
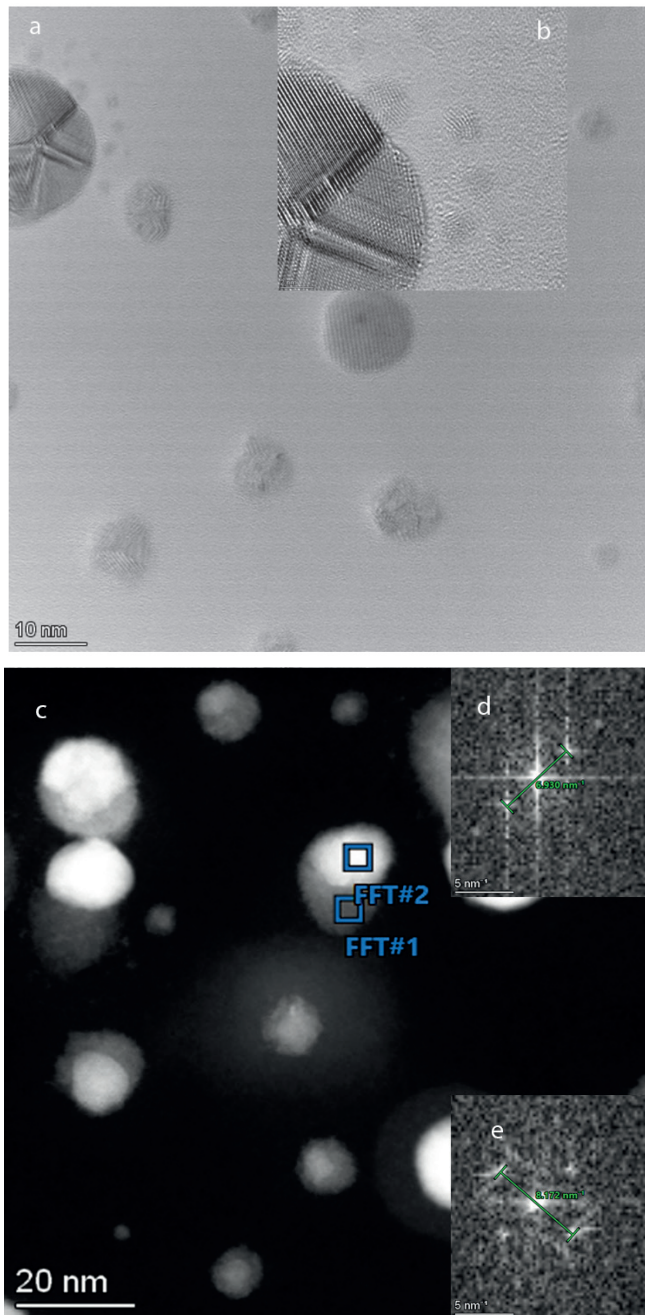
Figure 8-12(a) HR BF TEM Image (taken with a Fei ThemisZ) after aging, (b)Zoomed in HR BF TEM (c)STEM HAADF image of the same area zoomed in on a single AgNP (d)FFT#2 of 2 different areas of the same aged AgNP showing the <311> plane and (e)FFT #1 showing the <220> plane

Any surface (and high-surface energy materials are even more susceptible to this effect) attract airborne hydrocarbons, which subsequently are adsorbed on the surface and "shield" the polar surface sites leading to a decrease of the overall surface energy. Therefore, the TEM grids were analyzed both directly after deposition and after 11 weeks. The images show a dynamic process, down to atomic resolution, in which NP covered surfaces can change rather dramatically over time due to NP growth, where adatoms probably play a major role, and due to airborne hydrocarbon contamination. Both processes have a major effect on the wetting properties of the NPs covered surfaces as was already shown in section 8.5

For aged Ag NPs, the average NP size on the N-SiO$_2$ grids is 9% taller than it is on the NHC grids. The Ag NPs coverage on NHC is 3.2% again comparable to the previous deposition, but it is only 0.5% on the 40 nm SiO$_2$ TEM grid. One possible reason could be the effect of electrostatic repulsion[75–77]. After aging, the NP coverage on the SiO$_2$ TEM grid increases up to 1.5% due to the large size increase (growth) of a few Ag NPs. Moreover, another striking effect is the absence of the ultra-small Ag ('2D') nuclei on the nitride and oxide surface, which is in sharp contrast to the UV-Ozone treated CC and HC grids. Therefore, it can be argued that, due to the lack of mobility on the CC and HC, the adatoms nucleate on the substrate instead of migrating towards and nucleating on the Ag NPs as is the case for the nitride and oxide surfaces. Then, we have to explain why the Si$_3$N$_4$/SiO$_2$ substrates are different from the CC/HC.

To explain this it is first instrumental to analyze the role of the surface hydrocarbons and their removal by the UV-Ozone treatment. as Fig.8-6b shows, this process lowers the initial SCA of the substrates by making them more hydrophilic. However, the absolute change in SCA differs for the different substrates shown in Fig. 8-6. Unfortunately, the SCA change on the TEM grids cannot be measured since the grids are too small in diameter to allow macroscopic water drops for wetting measurements. During atmospheric exposure, the airborne hydrocarbons re-contaminate the substrate surface, and saturation is achieved after approximately 1.5 weeks, which is a reversible process[21].

8
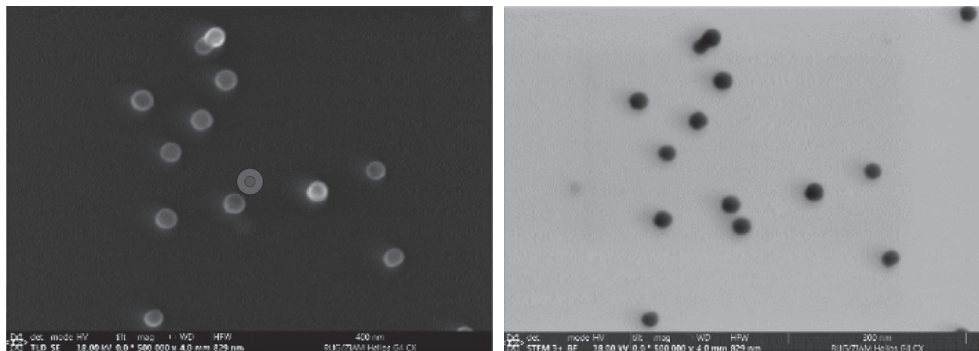
Figure 8-13(a) HR-SEM image in SE-TLD mode from the surface of an HC TEM grid showing 12 individual AgNPs. And (b)HR-BF S(T)EM image from the same area showing 14(5) (12+3) individual AgNPs; ergo 2 AgNPs have ended up on the other side of the TEM grid and 2 on top of each other.

Starting point

Depo time	Sample	CC TEM grids		
		Size	FWHM	% cov
3 min	1N CC	29,5	2,1	1,1%
3 min	1O CC	31,7	2,6	1,3%
6 min	2N CC	26,9	2,5	1,7%
6 min	2O CC	33,5	7,9	2,3%
12 min	3N CC	30,6	2,2	3,7%
12 min	3O CC	25,6	2,5	4,1%
24 min	4N CC	25,4	2,5	4,6%
24 min	4O CC	25,6	2,8	2,9%
48 min	5N CC	25,4	2,3	8,6%
48 min	5O CC	24,5	2,3	7,9%
	avg N+O CC	27,9	3,0	
	avg N	27,6	2,3	
	avg O	28,2	3,6	

Depo time	Sample	HC TEM grids		
		Size	FWHM	% cov
3 min	1N HC	30,5	2,9	1,7%
3 min	1O HC	29,4	4,5	1,8%
6 min	2N HC	27,3	3,0	2,1%
6 min	2O HC	28,9	3,1	2,4%
12 min	3N HC	26,2	2,9	3,5%
12 min	3O HC	27,7	3,5	6,0%
24 min	4N HC	26,9	3,2	6,4%
24 min	4O HC	27,6	2,9	6,3%
48 min	5N HC	29,2	4,5	12,3%
48 min	5O HC	29,1	4,6	9,3%
	avg N+O HC	28,3	3,5	
	avg N	28,0	3,3	
	avg O	28,5	3,7	

Depo time	Sample		Div grids	
		Size	FWHM	% cov
10 min	1N Si$_3$N$_4$	31,8	5,7	5,0%
10 min	1O Si$_3$N$_4$	29,0	6,9	4,2%
10 min	2N 5nm SiO$_2$	29,1	4,6	3,4%
10 min	2O 5nm SiO$_2$	28,4	4,7	4,2%
10 min	3N 5nm SiO$_2$	28,9	4,5	4,5%
10 min	3O 5nm SiO$_2$	28,3	4,3	4,3%
10 min	4N 20nm SiO$_2$	40,5	2,2	0,5%
10 min	4O 20nm SiO$_2$	31,0	5,9	2,8%
10 min	5N HC	26,5	5,1	3,2%
10 min	5O HC	26,6	4,7	4,7%
	avg N+O All	30,0	4,9	
	avg N	31,3	4,4	
	avg O	28,7	5,3	

Table 8-2: Tabulated data derived using the procedure illustrated in Fig.8-7, from the starting condition of the TEM grids covered with various degrees of AgNPs; Size in nm and FWHM (nm) of the Ag NPs and the total area covered by the Ag NPs (%).

After 11 weeks of aging

Depo time	Sample	CC TEM grids		
		Size	FWHM	% cove
3 min	1N CC	41,5	4,5	1,5%
3 min	1O CC	38,6	5,4	2,8%
6 min	2N CC	36,1	4,2	3,1%
6 min	2O CC	34,5	3,5	4,1%
12 min	3N CC	55,9	1,5	4,7%
12 min	3O CC	43,3	8,2	9,5%
24 min	4N CC	44,6	6,2	12,5%
24 min	4O CC	35,0	5,0	8,7%
48 min	5N CC	34,0	4,6	13,5%
48 min	5O CC	35,7	7,1	16,5%
	avg N+O CC	39,9	5,0	
	avg N	42,4	4,2	
	avg O	37,4	5,9	

Depo time	Sample	HC TEM grids		
		Size	FWHM	% cove
3 min	1N HC	39,0	6,9	3,0%
3 min	1O HC	41,9	6,5	3,0%
6 min	2N HC	39,3	6,2	4,9%
6 min	2O HC	33,8	5,7	3,8%
12 min	3N HC	38,5	5,8	7,2%
12 min	3O HC	37,0	5,1	6,7%
24 min	4N HC	37,5	9,6	12,9%
24 min	4O HC	39,4	7,0	12,2%
48 min	5N HC	41,9	11,7	19,0%
48 min	5O HC	46,4	16,0	27,3%
	avg N+O HC	39,5	8,1	
	avg N	39,2	8,1	
	avg O	39,7	8,1	

Depo time	Sample		Div grids	
			Size	FWHM	% cove
10 min	1N Si_3N_4		38,0	9,7	4,7%
10 min	1O Si_3N_4		37,0	10,3	5,5%
10 min	2N 5nm SiO_2		35,2	8,2	3,9%
10 min	2O 5nm SiO_2		36,8	9,1	7,5%
10 min	3N 5nm SiO_2		42,7	7,4	8,8%
10 min	3O 5nm SiO_2		50,3	16,3	14,2%
10 min	4N 20nm SiO_2		86,1	10,2	1,5%
10 min	4O 20nm SiO_2		41,6	10,2	4,7%
10 min	5N HC		44,7	9,0	8,6%
10 min	5O HC		39,1	10,6	10,9%
	avg N+O All		45,1	10,1	
	avg N		49,3	8,9	
	avg O		30,9	8,1	

Table 8-3: Tabulated data derived using the procedure illustrated in Fig. 8-7, after 11 weeks of aging of the TEM grids (at RT conditions) covered with various degrees of AgNPs coverage, Size in nm and FWHM (in nm) of the size distribution, and the total area covered by the Ag NPs (%).

The hydrocarbons enhance the mobility of both the Ag NPs(?) and adatoms on the substrate, in the same way as the difference in surface energy between the Holey/Continuous Carbon TEM grids and the Silicon Nitride/ Oxide TEM grids. If the surface hydrocarbons are removed from the CC/ HC TEM grid/substrates, then the surface diffusion of adatoms is restricted to smaller distances, and they nucleate to form ultra-small ('2D') nuclei that grow in size and number density over time. In contrast, on the Silicon Nitride/ Oxide TEM grids the adatoms always remain more mobile and they diffuse to the already existing NPs and do not nucleate in the ultra-small nanoclusters.

The above process is in contrast to the traditional Ostwald and Smoluchowski ripening[78]. The Ostwald ripening process itself does not stop since the average size of the original Ag NPs has increased by 30-100% in observed diameter. However, the overall coverage of the surface with (smaller) NPs continues to grow without any new atoms being added to the surface except for the airborne hydrocarbons and oxygen. So, we do not have here a case where the bigger NPs grow at the expense of the smaller ones, but we have growth due to nucleation of adatoms in islands on the surface or due to their migration towards existing NPs.

Upon careful inspection of the SiO_2 and Si_3N_4 TEM grids, there is even a large difference in the coverage of the TEM windows in comparison to the support frame as can be seen in the Fig 8-17(a) and Fig 8-18(b) and tables 8-2 and 8-3. For the Si_3N_4 grids, the ratio was 44/12, which is a factor of four higher on the windows. The 5 nm non-porous SiO_2 grids have a ratio of 35/9, which is also close to a factor four higher on the windows. For the 40 nm SiO_2 TEM grid we

have a factor of 10/5, which is a factor of two though it has a factor of four lesser Ag NPs overall. A similar observation of the difference in the sticking coefficient from NPs on supported and suspended graphene has been found, and some explanation has been proposed in the work by Chen et al.[79] Although further research is necessary, the fact is that in all cases of the investigated TEM grids the average size of the Ag NPs increased over time, where the aging, ripening, and/or coarsening process is a continuous process.

8.7   Results and discussion: Apparent mobility dynamics of silver nanoparticles and adatoms on various substrates

A final series consisting of 5 untreated and 5 UV-Ozone cleaned TEM grids were prepared: Duplo series of 5 nm thick Silicon High-Resolution TEM grids, 40 nm Silicon oxide TEM grids, 20 nm Silicon Nitride TEM grids (all from TEM windows©), and one HC grid.

For comparison, all TEM grids received an identical 10 min Ag NPs deposition. The S(T)EM images in Figs 8-14 and 8-15 have been analyzed with the same image analysis protocol as explained in Fig. 8-7.

The tabulated data in the Table 8-2 and 8-3 is graphically displayed in Fig. 8-14, where the data points are connected as a guide for the eye.

The 10 min Ag NPs deposition should show the same size and coverage (ignoring the influence of the deepening of the Ag target racetrack during sputter deposition[73,74]) on the different TEM grids. Then, the four lines in the two graphs should be horizontal lines on top of each other. This is clearly not the case.

The experiment shows that there is a clear difference in the sticking coefficient (and coverage) of the Ag NPs on the different TEM grids, and the effect is more pronounced after aging.

For an equal amount of time in the cluster beam of the Ag NPs, the NHC TEM grid gave a 3-4 % coverage with an NP size of 26.5 nm, which is comparable with the previous depositions. The 20 nm Si_3N_4 and 5 nm SiO_2 grids showed an increased Ag NPs average size up to 30 nm. The 40 nm SiO_2 TEM grid after S(T)EM imaging gave Ag NPs with an average size of 40 nm, indicating a size increase of about 50% compared to the NHC grid. Moreover, the difference in size and coverage becomes more pronounced after aging (compared with the observations of the CC and HC TEM grids) as is shown in the Table 8-1.

Finally, a surprising observation is thus the difference in the sticking coefficient for Ag NPs on different TEM grids. For the same flux of Ag NPs, the HC TEM grids compared to the CC TEM

show a higher number of NPs in the S(T)EM Bright field (BF) image (see in Fig. 8-13) due to the additional Ag NPs redeposited on the backside. These NPs are imaged in BF S(T)EM mode, and they are counted as well in the BF TEM image. Since most TEMs do not have SE-TLD imaging, they are overlooked. Thus calculating the yield using an HC-TEM grid and imaged in BF-TEM mode, the actual yield is overestimated,(see in Figs 8-10, 8-11 and 8-14, 8-15 only HC TEM grids).

a

b

c

d

8

e

f
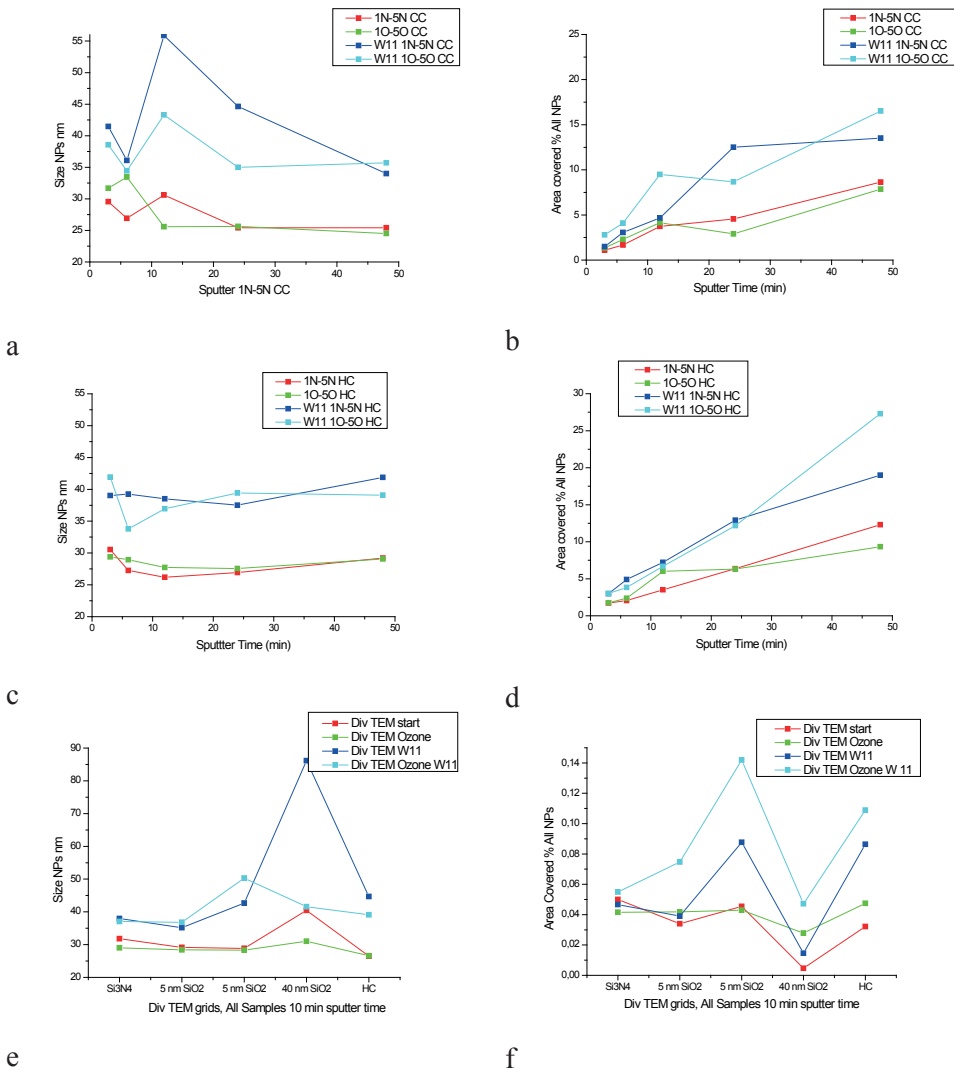
Figure 8-14 Graphical display of the size of NPs and coverage(sticking coefficient) for a fixed sputter time (10 min) on different TEM grids, Si_3N_4, 5nm SiO_2, 40nm SiO_2, and HC and the effect of aging/ripening. on the size (in nm) and covered area (in %)

	Untreated Div TEM Grid Start	Ozone treated Div TEM Grid Start
10 min depo time Si_3N_4		
10 min depo time 5 nmSiO_2		
10 min depo time 5nm SiO_2		
10 min depo time 40 nm SiO_2		
10 min depo time HC		
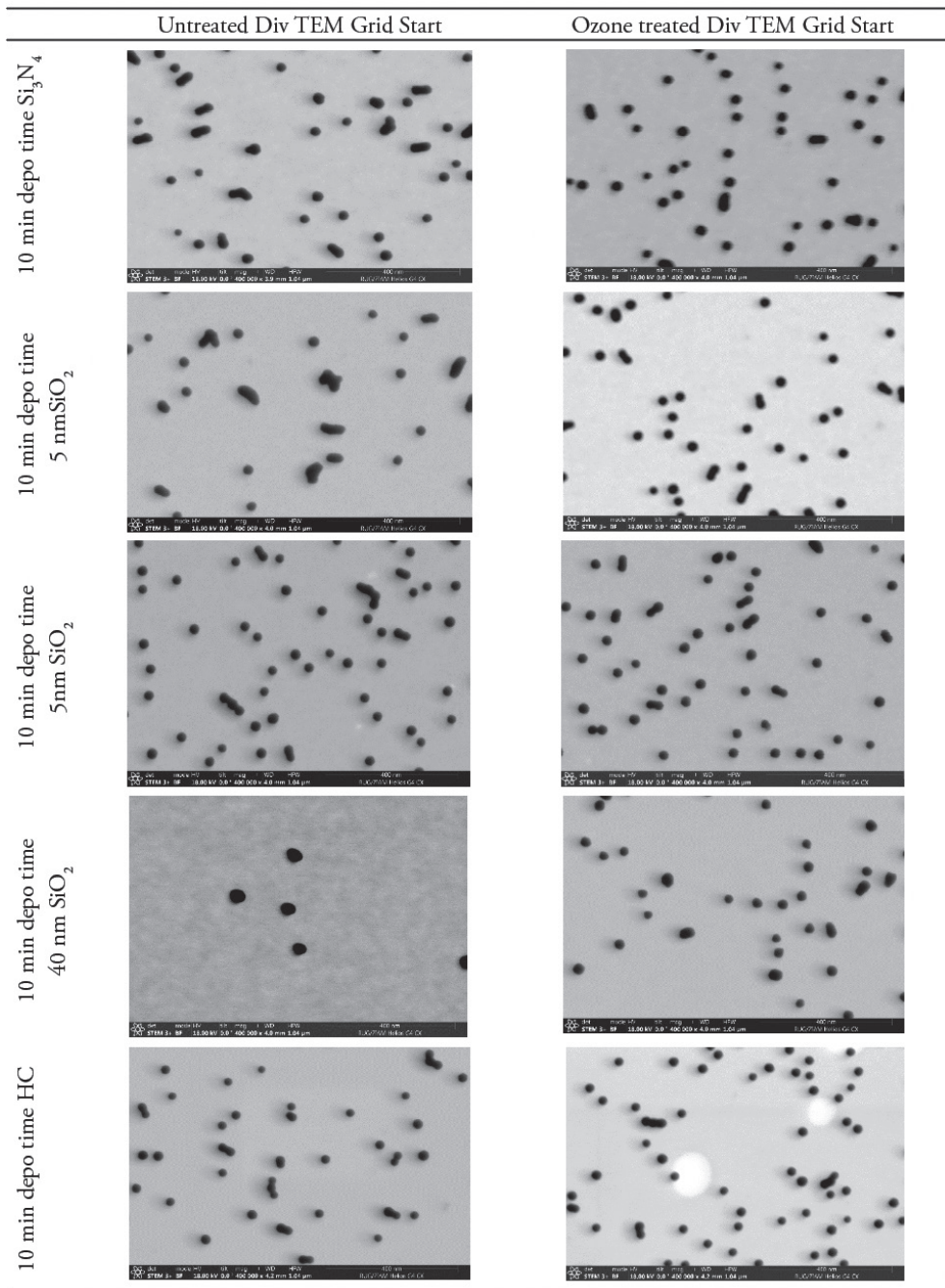
Figure 8-15 400KX BF S(T)EM images showing the initial starting condition for studying ripening and aging of the same (10 min) coverage Ag NPs on untreated 20nm Si_3N_4, 5nmSiO_2, 5nm SiO_2, 40nm SiO_2, and Holey Carbon(HC) TEM grids and in same order UV-Ozone treated (OHC) grids.

	Untreated Div TEM Grid week 11	Ozone treated Div TEM Grid week 11
10 min depo time Si_3N_4		
10 min depo time 5 nm SiO_2		
10 min depo time 5nm SiO_2		
10 min depo time 40 nm SiO_2		
10 min depo time HC		

8
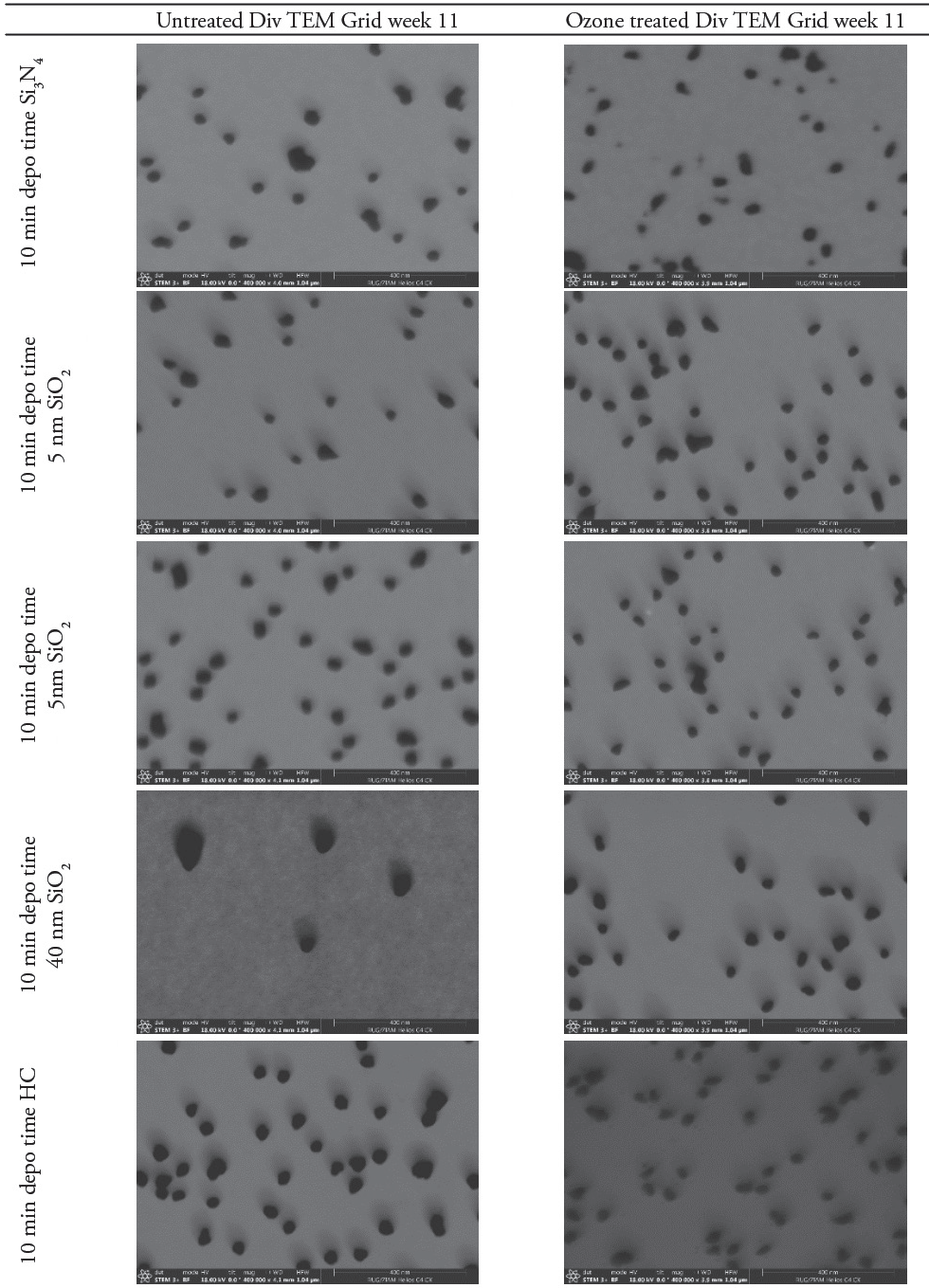
Figure 8-16 BF S(T)EM images showing the ripening and aging of the same (10 min) coverage Ag NPs on untreated 20nm Si_3N_4, 5nm SiO_2, 5nm SiO_2, 40nm SiO_2 and Holey Carbon(HC) TEM grids and in same order UV-Ozone treated (OHC) grids. After 11 weeks of aging at room conditions
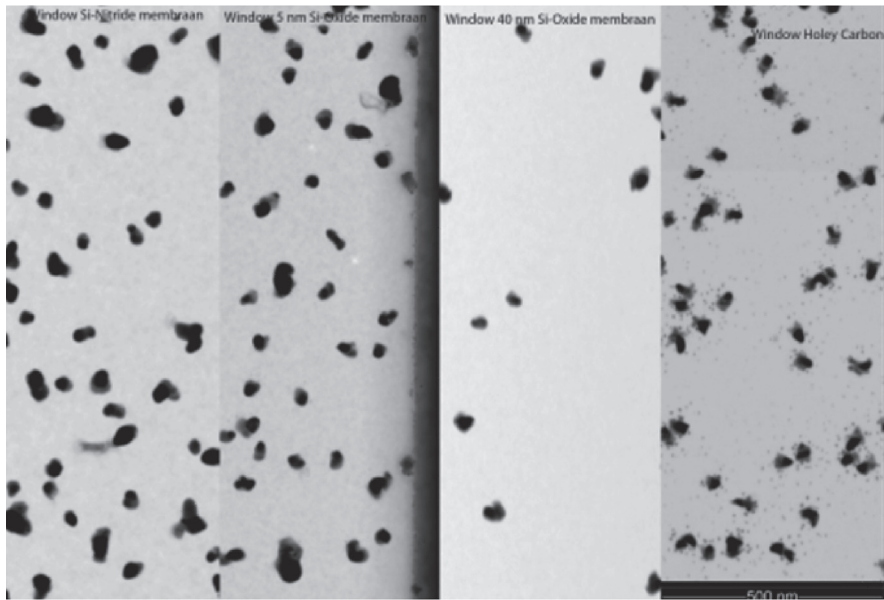
Figure 8-17(a) BF HR S(T)EM images taken from the window of a Si$_3$N$_4$ grid, 5nm SiO$_2$ grid a 40nm SiO$_2$ grid, and a Holey Carbon grid. All grids received the same (10 min) Ag NPs deposition.
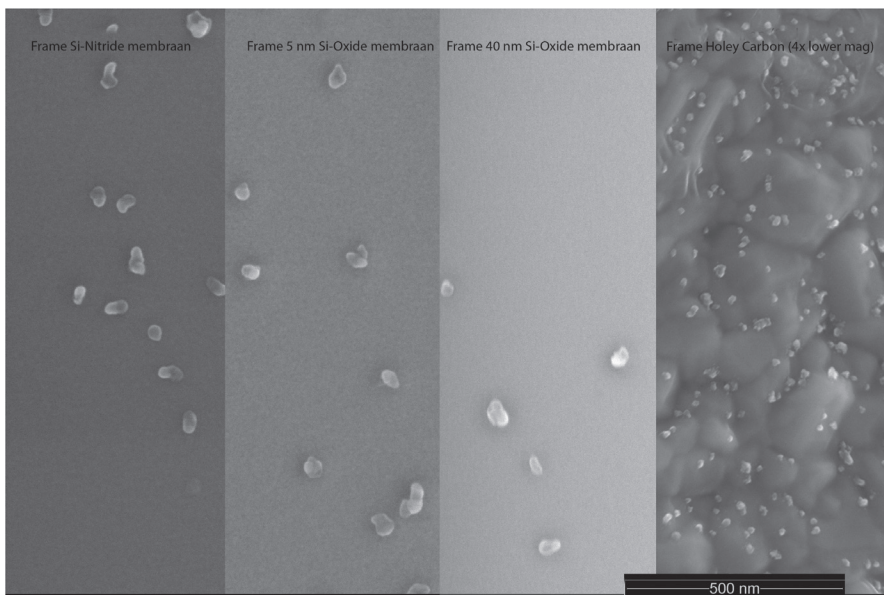
Figure 8-18(b) HR SEM (TLD mode) images taken from the support frame of the TEM grids, a Si$_3$N$_4$ grid, 5nm SiO$_2$ grid a 40nm SiO$_2$ grid, and a Holey Carbon grid. All grids received the same (10 min) Ag NPs deposition

No of NPs	Si_3N_4-grid	5nm SiO_2-grid	40 nm SiO_2 grid	HC grid
Window	44	35	10	45
Frame	12	9	5	NC
Ratio	4	4	2	NC

Tabel 8-2 AgNPs counted (fig. 8-17a and 8-18(b)) on the support frame and window of the different TEM grids; a Si_3N_4 grid, 5nm SiO_2 grid a 40nm SiO_2 grid, and a Holey Carbon grid. And the calculated ratio

The Ag NPs on the Si_3N_4 TEM grid show the same coverage and size as the NPs on the CC TEM grid. In sharp contrast, the Ag NPs deposition on the 40 nm SiO_2 grid shows by far the lowest sticking coefficient but the highest increase in size and volume gain after aging. There is a big difference after the UV-Ozone treatment of the CC and HC TEM grids, though the UV-Ozone treatment has a lesser influence on the oxide and nitride TEM grids except for the 40 nm SiO_2 grid. After UV-Ozone treatment the sticking coefficient of the Ag NPs increased to a comparable number as for the 5 nm SiO_2 TEM grids. Finally, the coalesce process appears different on different substrates (SiO_2, Si_3N_4 vs HC, CC TEM grids), and a large difference of approximately a factor of 4 exists in the coverage between the transparent window and the supporting frame. These extensive results demonstrate that the sticking coefficient of NPs on different substrates, even when the top layer is identical, can largely differ. Therefore, an NP coverage measured on a CC or HC TEM grid cannot be used to determine the NP coverage on an oxide-covered silicon wafer. Such detailed knowledge is indispensable when performing accurate wetting experiments on NPs covered surfaces.

8.8   Conclusions

The wetting state of surfaces can be rendered to a highly hydrophobic state by the deposition of gas-phase synthesized Ag NPs that have intrinsic hydrophilic nature. The aging of the Ag NPs leads to an increase in their size, which is also associated with the presence of Ag adatoms during the sputtering process that has a strong effect on the wetting processes of surfaces decorated by NPs. Therefore, this research can serve as a model system for the wetting of nanostructured surfaces in an attempt to explain the relationship between the shape of the NPs, their curvature at the point of contact with the substrate, and the influence of the adatoms. Furthermore, since surface chemistry plays a crucial role in the wetting state, surface airborne hydrocarbons were removed by UV-Ozone treatment providing deeper insight into the apparent mobility of the NPs on different surfaces, and their subsequent ripening and aging. In addition, the UV-Ozone treatment in combination with aging revealed the presence of adatoms during the magnetron sputtering process.

8

The UV-Ozone surface treatment lowers the initial contact angle (CA) of the substrates and facilitates the mobility of Ag NPs and adatoms on the surface of the substrates. Adatoms co-deposited on clean high surface energy substrates will nucleate on the Ag NPs, which will remain closely spherical in shape and preserve the pinning effect due to the water nanomeniscus. If the adatoms are co-deposited on a UV-Ozone cleaned low surface energy substrate, their mobility is restricted and they will nucleate in two-dimensional islands and/or nanoclusters on the surface instead of on the existing Ag NPs. This growth results in a rough surface, where the nanomeniscus is filled and/or removed and the wetting state is reversed from hydrophobic to hydrophilic. Finally, extensive measurements on different material surfaces of transmission electron microscopy (TEM) grids revealed strong differences in the sticking coefficient for the Ag NPs suggesting another factor that can strongly affect the wetting properties of NP decorated surfaces.

8.9 References

[1] P.G. de Gennes, Rev. Mod. Phys. **57**, 827 (1985).

[2] R.N. Wenzel, Ind. Eng. Chem. **28**, 988 (1936).

[3] A.B.D. Cassie and S. Baxter, Trans. Faraday Soc. **40**, 546 (1944).

[4] C.W. Extrand, Langmuir **32**, 7697 (2016).

[5] H. Wang, Langmuir **35**, 10233 (2019).

[6] T. Young, Philos. Trans. R. Soc. Lond. **95**, 65 (1805).

[7] Q. Wang, M. Safdar, X. Zhan, and J. He, CrystEngComm **15**, 8475 (n.d.).

[8] M.E. Schrader, J. Colloid Interface Sci. **100**, 372 (1984).

[9] K.W. Bewig and W.A. Zisman, J. Phys. Chem. **69**, 4238 (1965).

[10] G.H. ten Brink, N. Foley, D. Zwaan, B.J. Kooi, and G. Palasantzas, RSC Adv **5**, 28696 (2015).

[11] Y. Katasho, Y. Liang, S. Murata, Y. Fukunaka, T. Matsuoka, and S. Takahashi, Sci. Rep. **5**, (2015).

[12] J.-L. Liu, X.-Q. Feng, G. Wang, and S.-W. Yu, J. Phys. Condens. Matter **19**, 356002 (n.d.).

[13] C. Binns, Surf. Sci. Rep. **44**, 1 (2001).

[14] S. Zhang, X. Zhang, G. Jiang, H. Zhu, S. Guo, D. Su, G. Lu, and S. Sun, J. Am. Chem. Soc. **136**, 7734 (2014).

[15] H. Barani, M. Montazer, A. Calvimontes, and V. Dutschk, Text. Res. J. **83**, 1310 (2013).

[16] K. Nomiya, A. Yoshizawa, K. Tsukagoshi, N.C. Kasuga, S. Hirakawa, and J. Watanabe, J. Inorg. Biochem. **98**, 46 (2004).

[17] A. Gupta and S. Silver, Nat. Biotechnol. **16**, 888 (1998).

[18] S.Y. Liau, D.C. Read, W.J. Pugh, J.R. Furr, and A.D. Russell, Lett. Appl. Microbiol. **25**, 279 (1997).

[19] G.L. Hornyak, St. Peschel, Th. Sawitowski, and G. Schmid, Micron **29**, 183 (April) 1988.

[20] W. Guo, C. Ye, G.H. ten Brink, K. Loos, V.B. Svetovoy, and G. Palasantzas, Phys. Rev. Mater. **5**, 015604 (2021).

[21] W. Guo, B. Chen, V.L. Do, G.H. ten Brink, B.J. Kooi, V.B. Svetovoy, and G. Palasantzas, ACS Nano (2019).

[22] C.H.F. Peden, K.B. Kidd, and N.D. Shinn, J. Vac. Sci. Technol. A **9**, 1518 (1991).

[23] I. De Leersnyder, L. De Gelder, I. Van Driessche, and P. Vermeir, Nanomaterials **9**, 1684 (2019).

[24] https://en.wikipedia.org/wiki/Homogeneous_catalysis

[25] Y. Fukamori, M. König, B. Yoon, B. Wang, F. Esch, U. Heiz, and U. Landman, ChemCatChem **5**, 3330 (2013).

[26] A.Kuzminova, J. Beranová, O. Polonskyi, A. Shelemin, O. Kylián, A. Choukourov, D. Slavínská, and H. Biederman, Surf. Coat. Technol. **294**, 225 (2016).

[27] S. Yan, D. Sun, Y. Gong, Y. Tan, X. Xing, G. Mo, Z. Chen, Q. Cai, Z. Li, H. Yu, and Z. Wu, J. Synchrotron Radiat. **23**, 718 (2016).

[28] I. Shyjumon, M. Gopinadhan, O. Ivanova, M. Quaas, H. Wulff, C.A. Helm, and R. Hippler, Eur. Phys. J. - At. Mol. Opt. Plasma Phys. **37**, 409 (2006).

[29] P.L. Redmond, A.J. Hallock, and L.E. Brus, Nano Lett. **5**, 131 (2005).

[30] D. Paramelle, A. Sadovoy, S. Gorelik, P. Free, J. Hobley, and D.G. Fernig, Analyst **139**, 4855 (2014).

[31] Dr. Yves Huttel, Gas-Phase Synthesis of Nanoparticles. Wiley-VCH. ISBN: 978-3-527-34060-6

8

[32] A.S. Edelstein and R.C. Cammaratra, editors , *Nanomaterials: Synthesis, Properties and Applications, Second Edition*, 2nd ed. (Taylor & Francis, 1998).

[33] H. Haberland, J. Vac. Sci. Technol. Vac. Surf. Films **10**, 3266 (1992).

[34] P. Grammatikopoulos, S. Steinhauer, J. Vernieres, V. Singh, and M. Sowwan, Adv. Phys. X **0**, 1 (2016).

[35] L. Martínez, M. Díaz, E. Román, M. Ruano, D. Llamosa P., and Y. Huttel, Langmuir **28**, 11241 (2012).

[36] In *Gas-Phase Synth. Nanoparticles* (John Wiley & Sons, Ltd, 2017), pp. i–xx.

[37] A. Marek, J. Valter, and J. Vyskočil, North. Irel. 4 (2011).

[38] A. Marek, J. Valter, S. Kadlec, and J. Vyskočil, Surf. Coat. Technol. **205, Supplement 2**, S573 (2011).

[39] G.H. ten Brink, G. Krishnan, B.J. Kooi, and G. Palasantzas, J. Appl. Phys. **116**, 104302 (2014).

[40] Image pro plus v 7.0 https://www.mediacy.com/imageproplus

[41] Originlab 8.1 https://www.originlab.com/

[42] OCA Software V. 5.0.24 build 5024 https://www.dataphysics-instruments.com/products/oca/

[43] D. Li, P. Cheng, and A.W. Neumann, Adv. Colloid Interface Sci. **39**, 347 (1992).

[44] L. Bardotti, B. Prével, P. Mélinon, A. Perez, Q. Hou, and M. Hou, Phys. Rev. B **62**, 2835 (2000).

[45] E. Bormashenko, A. Musin, G. Whyman, and M. Zinigrad, Langmuir ACS J. Surf. Colloids **28**, 3460 (2012).

[46] E. Bormashenko, O. Gendelman, and G. Whyman, Langmuir **28**, 14992 (n.d.).

[47] J.R. Vig, J. Vac. Sci. Technol. A **3**, 1027 (1985).

[48] D.L. Olynick, J.M. Gibson, and R.S. Averback, Appl. Phys. Lett. **68**, 343 (1996).

[49] D.L. Olynick, J.M. Gibson, and R.S. Averback, Philos. Mag. A **77**, 1205 (1998).

[50] D.L. Olynick, J.M. Gibson, and R.S. Averback, Mater. Sci. Eng. A **204**, 54 (1995).

[51] L. Bardotti, P. Jensen, A. Hoareau, M. Treilleux, B. Cabaud, A. Perez, and F.C.S. Aires, Surf. Sci. **367**, 276 (1996).

[52] K. Meinander, J. Frantz, K. Nordlund, and J. Keinonen, Thin Solid Films **425**, 297 (2003).

[53] L. Bardotti, B. Prével, P. Jensen, M. Treilleux, P. Mélinon, A. Perez, J. Gierak, G. Faini, and D. Mailly, Appl. Surf. Sci. **191**, 205 (2002).

[54] L.J. Lewis, P. Jensen, N. Combe, and J.-L. Barrat, Phys. Rev. B **61**, 16084 (2000).

[55] P. Jensen, A. Clément, and L.J. Lewis, Comput. Mater. Sci. **30**, 137 (2004).

[56] L. Bardotti, P. Jensen, A. Hoareau, M. Treilleux, and B. Cabaud, Phys. Rev. Lett. **74**, 4694 (1995).

[57] W.R. Tyson, Can. Metall. Q. **14**, 307 (1975).

[58] K. Meinander, K. Nordlund, and J. Keinonen, Nucl. Instrum. Methods Phys. Res. Sect. B Beam Interact. Mater. At. **228**, 69 (2005).

[59] B.M. Smirnov, in *Clust. Small Part.* (Springer New York, 2000), pp. 144–185.

[60] M. Ohring, in *Mater. Sci. Thin Films* (Elsevier, 2002), pp. 357–415.

[61] M. Grouchko, I. Popov, V. Uvarov, S. Magdassi, and A. Kamyshny, Langmuir **25**, 2501 (2009).

[62] M. Grouchko, P. Roitman, X. Zhu, I. Popov, A. Kamyshny, H. Su, and S. Magdassi, Nat. Commun. **5**, 2994 (2014).

[63] S. Marom, M. Plesser, R. Modi, N. Manini, and M.D. Vece, J. Phys. Appl. Phys. **52**, 095301 (2018).

[64] R.D. Glover, J.M. Miller, and J.E. Hutchison, ACS Nano **5**, 8950 (2011).

[65] W. Knauer, J. Appl. Phys. **62**, 841 (1987).

[66] Jensen and N. Combe, Computational Mater. Sci. **24**, 78 (2002).

[67] P. Jensen, ArXivcond-Mat9903141 (1999).

[68] P. Jensen, Rev. Mod. Phys. **71**, 1695 (1999).

[70] https://en.wikipedia.org/wiki/Gibbs-Thomson_equation

[70] C.W. Extrand, Langmuir **18**, 7991 (2002).

[71] A.J.V. Griffiths and T. Walther, J. Phys. Conf. Ser. **241**, 012017 (2010).

[72] W. Guo, C. Ye, G.H. ten Brink, K. Loos, V.B. Svetovoy, and G. Palasantzas, ArXiv210105052 Phys. (2021).

[73] M. Ganeva, A.V. Pipa, and R. Hippler, Surf. Coat. Technol. **213**, 41 (2012).

[74] L. Xing, G.H. ten Brink, B.J. Kooi, and G. Palasantzas, J. Appl. Phys. **121**, 024305 (2017).

[75] M. Oćwieja, M. Morga, and Z. Adamczyk, J. Nanoparticle Res. **15**, 1460 (2013).

[76] M. Arbab, Thin Solid Films **381**, 15 (2001).

[77] Y. Yan, S.-Z. Kang, and J. Mu, Appl. Surf. Sci. **253**, 4677 (2007).

[74] https://eng.thesaurus.rusnano.com/wiki/article5246

[79] B. Chen, G.H. ten Brink, G. Palasantzas, P. Rudolf, and B.J. Kooi, Nanotechnology **29**, 505706 (2018).

8
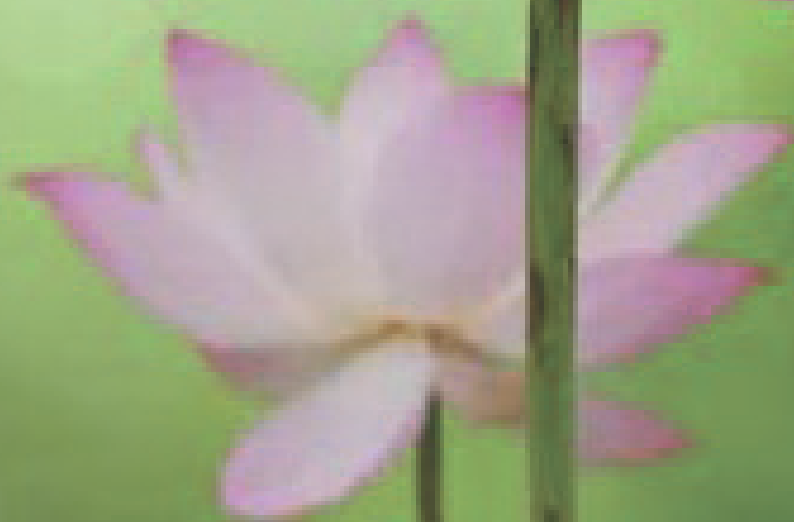
Chapter 9
Summary en Samenvatting

9.1 Summary: Connecting the Dots

Surface wetting is an extensively studied research field because it is a fascinating topic with many examples in nature (e.g., on many different plants' leaves). Wetting also has large implications for technology. To name a few: self-cleaning, anti-icing, antifogging (of windows), surface adhesion, stiction, and capillarity phenomena.

It was the seminal work performed by T Young in 1805 which showed the relationship between the contact angle (CA) θ, the surface tension of the liquid σ_{lg}, the interfacial tension σ_{sl} between the liquid and solid, and the surface free energy σ_{sg} of the solid. Surprisingly this famous equation is not actually given in the seminal manuscript. Unfortunately, it only holds for flat surfaces but breaks down for rough surfaces. Wentzel and Cassie-Baxter extended the wetting research to more realistic surfaces by developing equations that also include the influence of roughness. Yet, many cases exist where both models do not agree with the observations. Therefore, more in-depth wetting research is required to arrive at a more comprehensive understanding of the wetting of real surfaces.

The lotus leaf effect is arguably the most famous case, where wetting is strongly controlled by roughness. The exceptionally low roll-off angle and the associated self-cleaning of the lotus leaf have been attributed to hierarchical surface roughness, with roughness at both micrometer length scales (laterally and in height) and at nanometer length scale. A bottom-up approach has been used in the work presented in this PhD thesis to directly deposit nanoscale material, i.e. nanoparticles (NPs), on real (rough) surfaces. Such depositions create a roughness that increases when more material is deposited. Still, the desired nanoscale roughness is only achieved when these NPs stay distinct and intact after deposition. The nanocluster source used in the present work can fulfill this requirement, as shown in chapter 4. Then upon continued deposition of these individual NPs, they form a porous network/aggregates that also shows additional roughness at longer length scales in the same way as the lotus leave.

The NPs deposition system is described and explained in great detail in chapters 3 and 4. In particular, how to produce/synthesize a high-quality monodisperse conical beam with precise size and motive control of NPs. Chapter 4 explains the boundary conditions for proper NPs formation and how to achieve/create these conditions. One major obstacle in achieving proper NPs formation is the rapid oxidation of these very reactive NPs in the first place, and this is

addressed and solved. To produce a proper NPs cluster beam, working in a clean and reducing gas environment is essential. However, these extreme clean conditions stop all seed formation and, consequently, the NPs formation. By redesigning the cluster source and introducing trace levels of impurity gas, we can achieve proper NPs nucleation conditions to form metallic NPs. Moreover, this includes good size control with narrow size distributions and robust (in the case of copper near icosahedral) structural motifs for particle sizes ranging from ~30 nm to 300 nm.

Chapter 5 is a good example of the state-of-the-art synthesis possibilities with the modified/redesigned cluster source. Two bulk immiscible metals become miscible at a nanometer length scale. In a traditional chemical way this intermixing of the atoms cannot be achieved. Moreover, we can tune the structural motifs of Mo–Cu NPs by having good control over the plasma energy, the cooling rate, and the diffusion process. The structural motifs range from completely alloyed particles with either cube or spherical shape, Mo–Cu core-shell particles with a cube or spherical shape, spherical 'onion' Mo– Cu–Mo particles (intermediate Cu shell), and Janus/dumbbell type Mo–Cu NPs. The critical size for alloying Mo–Cu, e.g., for forming NPs in which Mo and Cu are completely mixed, is considerably larger (closely to an order of magnitude) than has been reported before for bulk immiscible binary NPs. Needless to say that the cluster source can be extended to produce other binary and ternary alloy systems to tune NPs with different types of chemical ordering important for a wide range of research fields, which is a very promising possibility.

Chapter 6 is yet another demonstration of different behavior shown by nanoparticles than its bulk counterpart. Wetting research, a heavily studied area, is known by two mainstream theories (the Wenzel and Cassie Baxter model) explaining the physics behind wetting, including surface roughness. However, both Wenzel and Cassie Baxter's model cannot explain the wetting behavior when silver or copper NPs are deposited on various types of substrates. The observed superhydrophobic behavior is achieved by hydrophilic metal nanoparticles' roughness on a single nanometer length scale due to the (close to spherical) shape of the NPs and the resulting apex between particle and substrate. This roughness provides sufficient contact line pinning. The nanocapillary can force liquid into crevices between nanoparticles and push trapped air within the center of the droplet, forming a Cassie-Baxter state. Yet, it is the pinning of the triple line's that leads to a rose petal state.

Chapter 7 is a follow-up of this wetting anomaly and an attempt to address the chance in physical nature of the NPs and their influence on their wetting behavior. As a proof-of-concept, surface wetting can be changed between highly hydrophobic - hydrophilic states using the amorphous-to-crystalline phase transitions of GeSbTe NPs (with a composition close to $Ge_2Sb_2Te_5$). Contact angle (CA) measurements show that by increasing the coverage of amorphous NPs, the contact

9

angle increases to values close to the superhydrophobic limit (for NP coverages ≥ 80 %), while for crystalized GeSbTe NPs, the CA decreased to ~40°, which is clearly hydrophilic. The GeSbTe phase also affects capillary adhesion due to water meniscus formation by being stronger for the more hydrophilic crystallized GST state.

The research presented in chapter 8 combines the results of the previous chapters' wetting topics and connects all the dots. It shows the rich and complex behavior of NPs deposited surfaces and their effect on wetting. Adding new in-depth knowledge and understanding to this fascinating field

It reconfirms the superhydrophobic behavior of surfaces covered with intrinsic hydrophilic Ag NPs, similar to the behavior of surfaces decorated with Cu NPs described in chapter 6. This behavior cannot be explained based on the Wenzel or Cassie Baxter models. A logical explanation for this wetting anomaly is that the pinning effect of the NPs on a surface at the triple line is not considered in both these models. This pinning effect of the NPs at the triple line can be a good explanation for the observed rose petal effect. Contrary to the low role-off angle on the lotus leaf, in the rose petal state the water droplets stay attached to the surface even when flipped upside down.

In chapter 8 also the aging of the Ag NPs has been investigated. It is shown that aging of NPs leads to an increase in the size of the NPs, which has an effect on the wetting properties. This NPs size increase due to aging is also associated with the presence of (initially invisible) Ag adatoms produced during the sputtering process, which again strongly affect the wetting processes of surfaces decorated by NPs.

In the wetting of surfaces, surface chemistry plays a crucial role. Clean surfaces are necessary to understand the intrinsic behavior of a (clean) surface and the subsequent role of surface contamination. Therefore airborne hydrocarbons need to be removed by UV-Ozone treatment. This treatment needs to be performed before the wetting measurements. This cleaning method provided more insight into the apparent mobility of the NPs on different surfaces and their subsequent ripening and aging. This UV-Ozone treatment also revealed the presence of adatoms during the magnetron sputtering process which start to cluster into very tiny particles (just visible with the current state-of-the-art STEM). One last conclusion: STEM measurements

on different material surfaces of transmission electron microscopy grids revealed surprisingly strong differences in the sticking coefficient of the Ag NPs, which is an unexpected observation requiring more in-depth research.

9.2 Samenvatting: Connecting the Dots

Oppervlaktebevochtiging is een uitgebreid bestudeerd onderzoeksgebied omdat het een fascinerend onderwerp is met veel voorbeelden in de natuur (bijvoorbeeld op de bladeren van veel verschillende planten). Bevochtiging heeft ook grote gevolgen voor de technologie. Om er een paar te noemen: zelfreinigend, anti-ijsvorming, anticondens (van ramen), oppervlaktehechting, stictie en capillariteitsverschijnselen.

Het was het baanbrekende werk uitgevoerd door T Young in 1805 dat de relatie aantoonde tussen de contacthoek (CA) θ, de oppervlaktespanning van de vloeistof σ_{lg}, de grensvlakspanning σ_{sl} tussen de vloeistof en de vaste stof, en de oppervlaktevrije energie σ_{sg} van de solide. Verrassend genoeg wordt deze beroemde vergelijking niet eens vermeld in dit baanbrekende manuscript. Desalniettemin geldt de formule alleen voor vlakke oppervlakken, maar breekt het af voor ruwe oppervlakken. Wentzel en Cassie-Baxter breidden het bevochtigingsonderzoek uit naar meer realistische oppervlakken door vergelijkingen te ontwikkelen die ook de invloed van ruwheid omvatten. Toch zijn er veel gevallen waarin beide modellen het niet eens zijn met de waarnemingen. Daarom is meer diepgaand bevochtigingsonderzoek nodig om tot een beter begrip te komen van de bevochtiging van echte oppervlakken.

Het lotusbladeffect is misschien wel het meest bekende geval, waarbij bevochtiging sterk wordt beheerst door ruwheid. De uitzonderlijk lage afrolhoek en de daarmee gepaard gaande zelfreiniging van het lotusblad zijn toegeschreven aan hiërarchische oppervlakteruwheid, met ruwheid op zowel micrometer lengteschalen (lateraal en in hoogte) als op nanometer lengteschaal. In het werk gepresenteerd in dit proefschrift is een bottom-up benadering gebruikt om materiaal op nanoschaal, d.w.z. nanodeeltjes (NPs), direct op echte (ruwe) oppervlakken te deponeren. Dergelijke afzettingen creëren een ruwheid die toeneemt naarmate er meer materiaal wordt afgezet. Toch wordt de gewenste ruwheid op nanoschaal alleen bereikt wanneer deze NP's na afzetting duidelijk en intact blijven. De

nanoclusterbron die in het huidige werk wordt gebruikt, kan aan deze vereiste voldoen, zoals getoond in hoofdstuk 4. Bij voortzetting van de afzetting van deze individuele NP's vormen ze vervolgens een poreus netwerk/aggregaten dat ook extra ruwheid vertoont op langere lengteschalen op dezelfde manier als de lotus vertrekt..

Het depositiesysteem van de NP's wordt in detail beschreven en uitgelegd in de hoofdstukken 3 en 4. In het bijzonder hoe een monodisperse conische bundel van hoge kwaliteit geproduceerd/ gesynthetiseerd kan worden met precieze grootte en motiefcontrole van NP's. Hoofdstuk 4 legt de randvoorwaarden uit voor een goede vorming van NP's en hoe deze voorwaarden te bereiken zijn. Een belangrijk obstakel bij het bereiken van de juiste vorming van NP's is in de eerste plaats de snelle oxidatie van deze zeer reactieve NP's, en dit wordt aangepakt en opgelost. Om een goede mono disperse NP's clusterbundel te produceren, is werken in een schone en reducerende gasomgeving essentieel. Deze extreem schone omstandigheden stoppen echter alle zaadvorming en bijgevolg de vorming van NP's. Door de clusterbron opnieuw te ontwerpen en sporenniveaus van onzuiverheidsgas te introduceren, kunnen we de juiste NP's-kiemvormingsomstandigheden bereiken om metallische NP's te vormen. Bovendien omvat dit een goede groottecontrole met smalle grootteverdelingen en robuuste (in het geval van koper in de buurt van icosaëdrische) structurele motieven voor deeltjesgroottes variërend van ~ 30 nm tot 300 nm.

Hoofdstuk 5 is een goed voorbeeld van de state-of-the-art synthesemogelijkheden met de gewijzigde/herontworpen clusterbron. Twee niet-mengbare metalen in bulk worden mengbaar op een nanometer-lengteschaal. Op een traditionele chemische manier kan deze vermenging van de atomen niet worden bereikt. Bovendien kunnen we de structurele motieven van Mo-Cu NP's afstemmen door goede controle te hebben over de plasma-energie, de afkoelsnelheid en het diffusieproces. De structurele motieven variëren van volledig gelegeerde deeltjes met een kubus- of bolvorm, Mo-Cu kern-schaaldeeltjes met een kubus- of bolvorm, bolvormige 'ui' Mo-Cu-Mo-deeltjes (tussenliggende Cu-schaal) en Janus/haltertype Mo-Cu NP's. De kritische grootte voor het legeren van Mo-Cu, bijvoorbeeld voor het vormen van NP's waarin Mo en Cu volledig zijn gemengd, is aanzienlijk groter (dicht bij een orde van grootte) dan eerder is gemeld voor niet-mengbare binaire NP's in bulk. Onnodig te zeggen dat de clusterbron kan worden uitgebreid om andere binaire en ternaire legeringssystemen te produceren om NP's af te stemmen met verschillende soorten chemische ordening die belangrijk zijn voor een breed scala aan onderzoeksgebieden, wat een veelbelovende mogelijkheid is.

Hoofdstuk 6 is weer een demonstratie van ander gedrag van nanodeeltjes dan zijn tegenhanger in bulk. Onderzoek naar bevochtiging, een zwaar bestudeerd gebied, is bekend door twee gangbare theorieën (het Wenzel- en Cassie Baxter-model) die de fysica achter bevochtiging verklaren, inclusief oppervlakteruwheid. Zowel het model van Wenzel als Cassie Baxter kan het

bevochtigingsgedrag echter niet verklaren wanneer zilveren of koperen NP's worden afgezet op verschillende soorten substraten. Het waargenomen superhydrofobe gedrag wordt bereikt door de ruwheid van hydrofiele metalen nanodeeltjes op een enkele nanometer lengteschaal vanwege de (bijna bolvormige) vorm van de NP's en de resulterende top tussen deeltje en substraat. Deze ruwheid zorgt voor voldoende contactlijn pinning. Het nanocapillair kan vloeistof in spleten tussen nanodeeltjes dwingen en ingesloten lucht in het midden van de druppel duwen, waardoor een Cassie-Baxter-toestand ontstaat. Toch is het het vastzetten van de drievoudige lijnen die tot een rozenblaadjesstaat leiden.

Hoofdstuk 7 is een vervolg op deze bevochtigingsafwijking en een poging om de kans in fysieke aard van de NP's en hun invloed op hun bevochtigingsgedrag aan te pakken. Als proof-of-concept kan oppervlaktebevochtiging worden veranderd tussen zeer hydrofobe - hydrofiele toestanden met behulp van de amorfe-naar-kristallijne faseovergangen van GeSbTe NP's (met een samenstelling die dicht bij $Ge_2Sb_2Te_5$) ligt. Contacthoekmetingen (CA) laten zien dat door de dekking van amorfe NP's te vergroten, de contacthoek toeneemt tot waarden dichtbij de superhydrofobe limiet (voor NP-dekkingen $\geq 80\ \%$), terwijl voor gekristalliseerde GeSbTe NP's de CA daalde tot ~40°, die duidelijk hydrofiel is. De GeSbTe-fase beïnvloedt ook de capillaire adhesie als gevolg van de vorming van watermeniscus door sterker te zijn voor de meer hydrofiele gekristalliseerde GST-toestand.

Het onderzoek gepresenteerd in hoofdstuk 8 combineert de resultaten van de bevochtigingsonderwerpen van de vorige hoofdstukken en verbindt alle punten. Het toont het rijke en complexe gedrag van door NP's afgezette oppervlakken en hun effect op bevochtiging. Nieuwe diepgaande kennis en begrip toevoegen aan dit fascinerende veld

9

Het onderzoek gepresenteerd in hoofdstuk 8 combineert de resultaten van de bevochtigingsonderwerpen van de vorige hoofdstukken en verbindt alle punten. Het toont het rijke en complexe gedrag van door NP's afgezette oppervlakken en hun effect op bevochtiging. Nieuwe diepgaande kennis en begrip toevoegen aan dit fascinerende veldHet (her)bevestigt het superhydrofobe gedrag van oppervlakken bedekt met intrinsieke hydrofiele Ag NP's, vergelijkbaar met het gedrag van oppervlakken versierd met Cu NP's beschreven in hoofdstuk 6. Dit gedrag kan niet verklaard worden op basis van de Wenzel of Cassie Baxter modellen. Een

logische verklaring voor deze bevochtigingsafwijking is dat het pinning-effect van de NP's op een oppervlak op de drievoudige lijn in beide modellen niet wordt beschouwd. Dit pinning-effect van de NP's op de drievoudige lijn kan een goede verklaring zijn voor het waargenomen rozenblaadjeseffect. In tegenstelling tot de lage afrolhoek op het lotusblad, blijven de waterdruppels in de staat van het rozenblaadje aan het oppervlak vastzitten, zelfs als ze ondersteboven worden gehouden.

In hoofdstuk 8 is ook de veroudering van de Ag NPs onderzocht. Het is aangetoond dat veroudering van NP's leidt tot een toename van de grootte van de NP's, wat een effect heeft op de bevochtigingseigenschappen. Deze toename van de NP's als gevolg van veroudering houdt ook verband met de aanwezigheid van (aanvankelijk onzichtbare) Ag-adatomen geproduceerd tijdens het sputterproces, die opnieuw een sterke invloed hebben op de bevochtigingsprocessen van oppervlakken die zijn versierd met NP's.

Bij het bevochtigen van oppervlakken speelt oppervlaktechemie een cruciale rol. Schone oppervlakken zijn nodig om het intrinsieke gedrag van een (schoon) oppervlak en de daaruit voortvloeiende rol van oppervlakteverontreiniging te begrijpen. Daarom moeten in de lucht aanwezige koolwaterstoffen worden verwijderd door middel van een UV-ozonbehandeling. Deze behandeling moet worden uitgevoerd vóór de bevochtigingsmetingen. Deze reinigingsmethode gaf meer inzicht in de schijnbare mobiliteit van de NP's op verschillende oppervlakken en hun daaropvolgende rijping en veroudering. Deze UV-ozonbehandeling onthulde ook de aanwezigheid van adatomen tijdens het magnetron sputterproces die beginnen te clusteren tot zeer kleine deeltjes (net zichtbaar met de huidige state-of-the-art STEM). Een laatste conclusie: STEM-metingen op verschillende materiaaloppervlakken van transmissie-elektronenmicroscopieroosters onthulden verrassend sterke verschillen in de kleefcoëfficiënt van de Ag NP's, wat een onverwachte observatie is die meer diepgaand onderzoek vereist.die opnieuw een sterke invloed hebben op de bevochtigingsprocessen van oppervlakken die zijn versierd met NP's.

9
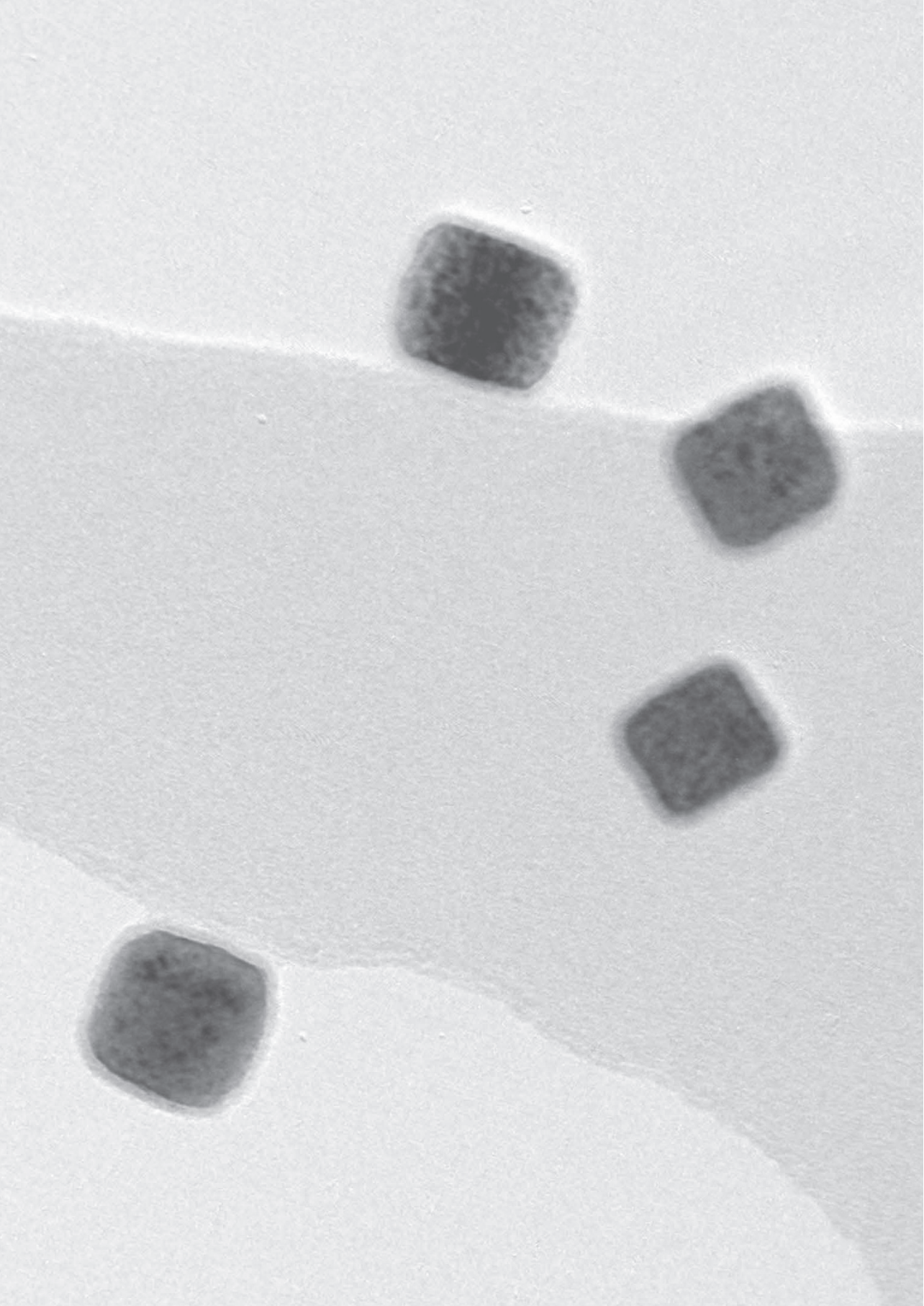
Chapter 10
List of publications

10.1 In this thesis

Chapter 4: G.H. ten Brink, G. Krishnan, B.J. Kooi, and G. Palasantzas, J. Appl. Phys. 116, 104302 (2014).

Chapter 5: G. Krishnan, M.A. Verheijen, G.H. ten Brink, G. Palasantzas, and B.J. Kooi, Nanoscale 5, 5375 (2013).

Chapter 6: G.H. ten Brink, N. Foley, D. Zwaan, B.J. Kooi, and G. Palasantzas, RSC Adv 5, 28696 (2015).

Chapter 7: G.H. ten Brink, P.J. van het Hof, B. Chen, M. Sedighi, B.J. Kooi, and G. Palasantzas, Appl. Phys. Lett. 109, 234102 (2016).

Chapter 8: G.H. ten.Brink, Wetting of surfaces decorated by gas-phase synthesized silver nanoparticles: Effects of Ag adatoms, nanoparticle aging, and surface mobility, J. Chem. Phys. 155, 214701 (2021).

10.2 As co-author

1. Adjokatse, S. et al. Effect of the Device Architecture on the Performance of FA(0.85) MA(0.15)PbBr(0.45)I(2.55) Planar Perovskite Solar Cells. ADVANCED MATERIALS INTERFACES 6, (2019).

2. Bagnato, G. et al. Hydrogenation of Biobased Aldehydes to Monoalcohols Using Bimetallic Catalysts. ACS SUSTAINABLE CHEMISTRY & ENGINEERING 8, 11994–12004 (2020).

3. Balazs, D. et al. Counterion-mediated ligand exchange for PbS colloidal quantum dot superlattices. ABSTRACTS OF PAPERS OF THE AMERICAN CHEMICAL SOCIETY 251, (2016).

4. Balazs, D. M. et al. Counterion-Mediated Ligand Exchange for PbS Colloidal Quantum Dot Super lattices. ACS NANO 9, 11951–11959 (2015).

5. Chen, B., de Wal, D., ten Brink, G. H., Palasantzas, G. & Kooi, B. J. Resolving Crystallization Kinetics of GeTe Phase-Change Nanoparticles by Ultrafast Calorimetry. CRYSTAL GROWTH & DESIGN 18, 1041–1046 (2018).

6. Chen, B. et al. Dynamics of GeSbTe phase-change nanoparticles deposited on graphene. NANOTECHNOLOGY 29, (2018).

7. Chen, B., ten Brink, G. H., Palasantzas, G. & Kooi, B. J. Size-dependent and tunable crystallization of GeSbTe phase-change nanoparticles. SCIENTIFIC REPORTS 6, (2016).

8. Chen, B., ten Brink, G. H., Palasantzas, G. & Kooi, B. J. Crystallization Kinetics of GeSbTe Phase-Change Nanoparticles Resolved by Ultrafast Calorimetry. JOURNAL OF PHYSICAL CHEMISTRY C 121, 8569–8578 (2017).

9. Dong, J. et al. Mechanism of Crystal Formation in Ruddlesden-Popper Sn-Based Perovskites. ADVANCED FUNCTIONAL MATERIALS 30, (2020).

10. Duim, H., Adjokatse, S., Kahmann, S., ten Brink, G. H. & Loi, M. A. The Impact of Stoichiometry on the Photophysical Properties of Ruddlesden-Popper Perovskites. ADVANCED FUNCTIONAL MATERIALS 30, (2020).

11. Duim, H. et al. Mechanism of surface passivation of methylammonium lead tribromide single crystals by benzylamine. APPLIED PHYSICS REVIEWS 6, (2019).

12. Foadi, F., ten Brink, G. H., Mohammadizadeh, M. R. & Palasantzas, G. Roughness dependent wettability of sputtered copper thin films: The effect of the local surface slope. JOURNAL OF APPLIED PHYSICS 125, (2019).

13. Groeneveld, B. G. H. M. et al. Stable Cesium Formamidinium Lead Halide Perovskites: A Comparison of Photophysics and Phase Purity in Thin Films and Single Crystals. ENERGY TECHNOLOGY 8, (2020).

14. Groeneveld, B. G. H. M. et al. Improved efficiency of NiOx-based p-i-n perovskite solar cells by using PTEG-1 as electron transport layer. APL MATERIALS 5, (2017).

15. Guo, W. et al. Effect of Airborne Hydrocarbons on the Wettability of Phase Change Nanoparticle Decorated Surfaces. ACS NANO 13, 13430–13438 (2019).

16. Guo, W. et al. Tunable wettability of polymer films by partial engulfment of nanoparticles. PHYSICAL REVIEW MATERIALS 5, (2021).

17. Kamminga, M. E. et al. Micropatterned 2D Hybrid Perovskite Thin Films with Enhanced Photoluminescence Lifetimes. ACS APPLIED MATERIALS & INTERFACES 10, 12878–12885 (2018).

18. Krishnan, G. et al. Strategies to initiate and control the nucleation behavior of bimetallic nanoparticles. NANOSCALE 9, 8149–8156 (2017).

19. Krishnan, G. et al. Shape and structural motifs control of MgTi bimetallic nanoparticles using hydrogen and methane as trace impurities. NANOSCALE 10, 1297–1307 (2018).

20. Krishnan, G. et al. Synthesis and exceptional thermal stability of Mg-based bimetallic nanoparticles during hydrogenation. NANOSCALE 6, 11963–11970 (2014).

21. Krishnan, G., Verheijen, M. A., ten Brink, G. H., Palasantzas, G. & Kooi, B. J. Tuning structural motifs and alloying of bulk immiscible Mo-Cu bimetallic nanoparticles by gas-phase synthesis. NANOSCALE 5, 5375–5383 (2013).

22. Kroezen, H. J. et al. Schottky barrier formation at amorphous-crystalline interfaces of GeSb phase change materials. APPLIED PHYSICS LETTERS 100, (2012).

23. Lalpoor, M., Eskin, D. G., ten Brink, G. & Katgerman, L. Microstructural features of intergranular brittle fracture and cold cracking in high strength aluminum alloys. MATERIALS SCIENCE AND ENGINEERING A-STRUCTURAL MATERIALS PROPERTIES MICROSTRUCTURE AND PROCESSING 527, 1828–1834 (2010).

10

24. Liu, J. et al. N-Type Organic Thermoelectrics: Improved Power Factor by Tailoring Host-Dopant Miscibility. ADVANCED MATERIALS 29, (2017).

25. Mahfud, F. H., Bussemaker, S., Kooi, B. J., Ten Brink, G. H. & Heeres, H. J. The application of water-soluble ruthenium catalysts for the hydrogenation of the dichloromethane soluble fraction of fast pyrolysis oil and related model compounds in a two phase aqueous-organic system. JOURNAL OF MOLECULAR CATALYSIS A-CHEMICAL 277, 127–136 (2007).

26. Oosthoek, J. L. M., Schuitema, R. W., ten Brink, G. H., Gravesteijn, D. J. & Kooi, B. J. Charge collection microscopy of in-situ switchable PRAM line cells in a scanning electron microscope: Technique development and unique observations. REVIEW OF SCIENTIFIC INSTRUMENTS 86, (2015).

27. Perez, L. L. et al. Stabilization of Self-Assembled Alumina Mesophases. CHEMISTRY OF MATERIALS 25, 848–855 (2013).

28. Shao, S. et al. N-type polymers as electron extraction layers in hybrid perovskite solar cells with improved ambient stability. JOURNAL OF MATERIALS CHEMISTRY A 4, 2419–2426 (2016).

29. Shao, S. et al. Elimination of the light soaking effect and performance enhancement in perovskite solar cells using a fullerene derivative. ENERGY & ENVIRONMENTAL SCIENCE 9, 2444–2452 (2016).

30. Shao, S. et al. The Effect of the Microstructure on Trap-Assisted Recombination and Light Soaking Phenomenon in Hybrid Perovskite Solar Cells. ADVANCED FUNCTIONAL MATERIALS 26, 8094–8102 (2016).

31. Shao, S. et al. Enhancing the Performance of the Half Tin and Half Lead Perovskite Solar Cells by Suppression of the Bulk and Interfacial Charge Recombination. ADVANCED MATERIALS 30, (2018).

32. Shao, S. et al. Enhancing the crystallinity and perfecting the orientation of formamidinium tin iodide for highly efficient Sn-based perovskite solar cells. NANO ENERGY 60, 810–816 (2019).

33. Shao, S. et al. Efficient Perovskite Solar Cells over a Broad Temperature Window: The Role of the Charge Carrier Extraction. ADVANCED ENERGY MATERIALS 7, (2017).

34. Shao, S. et al. Highly Reproducible Sn-Based Hybrid Perovskite Solar Cells with 9% Efficiency. ADVANCED ENERGY MATERIALS 8, (2018).

35. Shao, S. et al. Influence of the stoichiometry of tin-based 2D/3D perovskite active layers on solar cell performance. JOURNAL OF MATERIALS CHEMISTRY A 9, 10095–10103 (2021).

36. ten Brink, G. H. et al. Control surface wettability with nanoparticles from phase-change materials. APPLIED PHYSICS LETTERS 109, (2016).

37. ten Brink, G. H., Foley, N., Zwaan, D., Kooi, B. J. & Palasantzas, G. Roughness controlled superhydrophobicity on single nanometer length scale with metal nanoparticles. RSC ADVANCES 5, 28696–28702 (2015).

38. ten Brink, G. H., Krishnan, G., Kooi, B. J. & Palasantzas, G. Copper nanoparticle formation in a reducing gas environment. JOURNAL OF APPLIED PHYSICS 116, (2014).

39. Vagias, A. et al. Investigation of the Nanoscale Morphology in Industrially Relevant Clearcoats of Waterborne Polymer Colloids by Means of Variable-Angle-Grazing Incidence Small-Angle X-ray Scattering. ACS APPLIED POLYMER MATERIALS 1, 2482–2494 (2019).

40. Vermeulen, P. A., Calon, J., ten Brink, G. H. & Kooi, B. J. Combining Ultrafast Calorimetry and Electron Microscopy: Reversible Phase Transformations in SeTeAs Alloys. CRYSTAL GROWTH & DESIGN 18, 3668–3673 (2018).

41. Vermeulen, P. A., Kumar, A., ten Brink, G. H., Blake, G. R. & Kooi, B. J. Unravelling the Domain Structures in GeTe and LaAlO3. CRYSTAL GROWTH & DESIGN 16, 5915–5922 (2016).

42. Westerwaal, R. J. et al. Optical, structural, and electrical properties of Mg2NiH4 thin films in situ grown by activated reactive evaporation. JOURNAL OF APPLIED PHYSICS 100, (2006).

43. Xi, X.-Y. et al. Catalyst Performance Studies on the Guerbet Reaction in a Continuous Flow Reactor Using Mono- and Bi-Metallic Cu-Ni Porous Metal Oxides. CATALYSTS 10, (2020).

44. Xing, L. et al. Synthesis and morphology of iron-iron oxide core-shell nanoparticles produced by high pressure gas condensation. NANOTECHNOLOGY 27, (2016).

45. Xing, L., ten Brink, G. H., Kooi, B. J. & Palasantzas, G. Preparation of tunable-sized iron nanoparticles based on magnetic manipulation in inert gas condensation (IGC). JOURNAL OF APPLIED PHYSICS 121, (2017).

46. Zhang, H. et al. Nanostructure and thermal power of highly-textured and single-crystal-like Bi2Te3 thin films. NANO RESEARCH doi:10.1007/s12274-021-3743-y.

47. Zhang, X. et al. Microstructure, precipitate and property evolution in cold-rolled Ti-V high strength low alloy steel. MATERIALS & DESIGN 192, (2020).

48. Zhang, Z. et al. On the drug adsorption capacity of SBA-15 obtained from various detemplation protocols. MATERIALS LETTERS 131, 186–189 (2014).

49. Zhu, X., ten Brink, G. H., de Graaf, S., Kooi, B. J. & Palasantzas, G. Gas-Phase Synthesis of Tunable-Size Germanium Nanocrystals by Inert Gas Condensation. CHEMISTRY OF MATERIALS 32, 1627–1635 (2020).

50. Zhu, X., Xing, L., ten Brink, G. H., Kooi, B. J. & Palasantzas, G. Tailoring Growth Kinetics toward a Size-Dependent Work Function of Ge Nanocrystals Synthesized by Inert Gas Condensation. JOURNAL OF PHYSICAL CHEMISTRY C 125, 12870–12879 (2021).

10
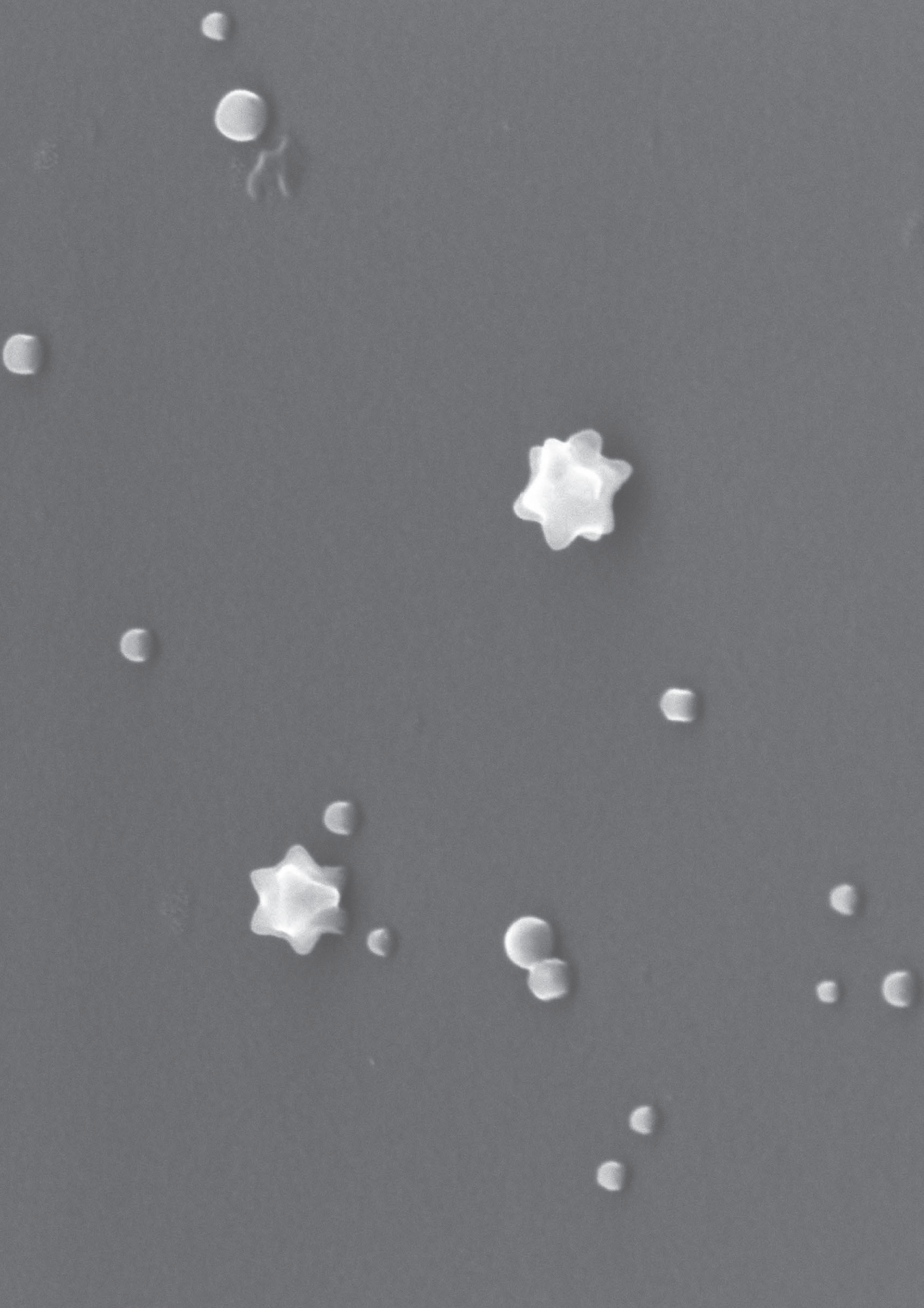
Chapter 11
Acknowledgments/Dankwoord

11.1   Acknowledgments

At the end of LOTR (Lord of the Rings), there was some space left for Sam (Samwise Gamgee) to complete the last sentences of the long story about their journey together (Just Google It). That is how it feels to write these "Acknowledgments and words of thank you" in this thesis. Not least because completing more than ten years of research is now neatly described, but my work is never finished. For most Ph.D. students, the Ph.D. thesis is the conclusion of what is mainly a pleasant period of 4 years. My Ph.D. research and the publications in this thesis continue my daily work. And so, now is the time and place to highlight the people who have contributed to my Ph.D. thesis and the daily work over the past decade. To promote is a verb and that work you cannot do alone. But to list all the people who have helped me over the years are numerous, and I'm afraid by forgetting even one person would do them shortly. because there were many. Many colleagues whom I often worked with in good friendship or continue to work with. I think back at my early period at the RUG. Dating back to 2002, I owe the NIMR (Dutch Institute for Metals Research) a lot. Back in 2002 when dealing with the forced closure of the Philips Semiconductor factory where I was stationed and with our youngest daughter being just 3 months old, it was an intense period in our life. Still, the transition from Philips to the NIMR was a pleasant transition. The NIMR was renamed M2i in 2008. Due to a reorganization in 2010 where the M2i was forced to fire all the technicians. I again was fortunate enough that, my current supervisors give me a technician position @ the RUG/ZIAM without any problems. Physically nothing in my workplace changed at that time, but the status quo did change Both institutes (the NIMR/M2I and the RUG) are inspiring working environments, where it is a pleasure to work for me as a microscopist. Normally you express your gratitude first to your promotor and second to the co-promoter, but not in my case. I consider them much more than highly learned opponents and consider them far more as valued colleagues, trusted persons, sources of information (Russian intelligence), and friends. To be named only as Supervisors would not do them justice. From 2009 till the present, we as the Nano Materials and Interface group (NMI) have grown as a close group, not soggy, with short communication lines and with a clear goal in mind.

If it has to be George Palasantzas, who was assigned as my first promotor and to be mentioned as first. Then I would like to thank him for the great (mental) support and stimuli. His always heartfelt encouragement "now who wants to get a doctorate degree, as for I already have one ?" and to finish the end of the (many) discussions, We can Agree To Disagree. Then certainly a big heartfelt thank you to Bart for all the help and support during the last 20+ years. The tedious TEM training and the never-ending urge to search for perfection in almost everything. It forced me to become better at almost everything. The advice was usually given during the daily debriefings on our quick bike rides through the inner city of Groningen, back a2n02d forth between the Zernike complex and

train station. Nothing but a ton of respect for your difficult choices in life and having to live so far away, yet always keep the door open for other people's problems. They may not know that it was Prof. Doekele Stavinga who (graciously) urged me to write the first article (chapter 4) now more than 12 years ago. After the first paper, I picked up the thread repeatedly at different intervals. It took a long time for the Mantis 50 nanocluster-source research to get underway, just ask Gopi. I will attempt to list in chronological order the many people that I would like to mention or thank (if not mentioned, my sincere apologies in advance).

During my NIMR/M2i period, already enjoyed the support of Bart and George as a source of information and for the training on the Jeol Auger and Jeol TEM, the Philips SEM's were already part of my expertise. Obviously, Sibbe Hoekstra, Annelies Swanenburg, Oscar Ruigrok and all the people of the M2i office.in Delft need to be mentioned together with my direct colleagues at the RUG during that period: Paul Bronsveld ✝, Henk Bron ✝, Jan Harkema, Uko Nieborg ✝, Klaas Post ✝, James Kuipers, Pim van den Dool, David Vaihnstein, Vasek Ocelik, Maarten Hilgenga, and the Koffietafel people: Alie Nanning, Henk Hanson along with the people from theW "ateruitje group". During this period, I supervised and trained many Ph.D. students on the many SEMs and other microscopic techniques that the RUG possesses: Damiano Galvan, David Matthews, Emiel Amsterdam, Henk Haarsma, Nuno Carvalho, Ramanathaswamy Pandian, Ronald Popma, Sasha Fedorov, Toni Chezan, Uzi de Oliveira, Vašek Ocelík, Willem-Pier Vellinga, Yutao Pei, and Yueling Qin. Zhuengo Chen, Tony Kazanthis I wish them every success in the future and maybe to see you again.

During this NIMR/M2i period, I supervised and trained many Ph.D. students and research fellows on the many SEMs and other microscopic techniques that the RUG possesses: Damiano Galvan, David Matthews, Emiel Amsterdam, Henk Haarsma, Nuno Carvalho, Ramanathaswamy Pandian, Ronald Popma, Sasha Fedorov, Toni Chezan, Uzi de Oliveira, Vašek Ocelik, Willem-Pier Vellinga, Yutao Pei, and Yueling Qin. Zhuengo Chen, Tony Kazanthis I wish them every success in the future and maybe to see you again.At the beginning of the NMI group (2009-2010), the group consisted of a few Ph.D. students. I have had a lot of interaction and collaboration with: Peter van Zwol, Jasper Oosthoek, Gert Eissing, Orcun Ergingan, Zwammy and Gopi Krishnan. The many photos taken during our first group outing in Katwijk aan Zee are still etched in my memory. My special thanks go to Gopi Krishnan, who was when we met first a Ph.D.candidate and later a postdoc in our group. I have much appreciation for the many pleasant hours working together (a trip to Leuven). Gopi started to work on the Mantis Nano Clusters source and I helped him with the technical support. I am gratefully granted the use of his RSC-advance paper in chapter 6 of this Ph.D thesis. Also many thanks to the people from the workshop who helped fix the nano-cluster source aka. Sputnik in the early days. They all deserve an honorable mention;

11

Bert van Dammen, Harry van Driel, Koos Duim, and last but not least, Jacob Baas and Henk Bonder. Helpful as always in solving the many technical problems.Many students have carried out their bachelor's and master's research under my watchful and critical eyes. Their research contribution is recognized by mentioning them as co-authors in the five papers that make up this thesis: Arjan Bijlsma, Nolan Foley, Darin Zwaan, Peter Jan van het Hof, Bin Chen, Liuan Xing, Mehdi Sedig2h0i3, Xiaotian Zhu, Weiteng Guo, Koen Blauw, Luuc Assing and last but not least Vitaly Svetovoy.for the smart comments, sharp observations and many useful discussions. I need to appreciate Jamo Momand for making the QCM (currently the George 1.0 design) The design and construction are explained in great detail in chapter 2.9

Furthermore, the current NMI group members receive my appreciation. One a big thank you to all for being pleasant and humorful roommates, for the good working environment, and for maintaining (most of the time) the plants and flower jungle in my room; Daniel Yilman, Razi Bakhshandehseraji, Hadisch Hassanzadeh, Masoud Ahmadi, Hui Wang, Atul Atul, Nana Gavhane, Laura Dillingh, and Sytze de Graaf. thanks.

A special word of appreciation goes to my two Para nymphs. Majid Ahmadi and Julien van der Ree many thanks for taking on this task (I am honored). Referring to proposition number 2 "Mens sana in corpore sano", my boot camp buddies also want an honorable mention. Ditto, I also greatly thank my mental coach and tireless training buddy, Martin Veenhuizen. I have to give him my superior recognition in many sports, but I know how to fix a bike and I can windsurf!

I am indebted to professors Maria Loi, Katja Loos, and Harold Zandvliet for participating in the reading committee, for assessing the draft thesis, and for making suggestions for improvements.

The last sentences are reserved for my family, my always faithful rock in the surf together with the two small storm breakers; My dear Liesbeth, Anna and Eva, you are the happy thoughts in Peter Pan's ability to fly (Just Google It) I think of my dear parents and in melancholy of both my parents-in-law. Unfortunately, my mother, mother, and father-in-law have passed away too early to attend and experience my promotion. My two lovely daughters are who they are, thanks to their good care and for being always there for us and them. Thanks also to my older and younger sister, and my younger brother, always in miniature form, but certainly already adults, who time and time again inquired about the progress sometimes with interest and teasingly noted when finally the party is coming, hereby at last, and you are all invited!

Gert ten Brink
June 2022.

11.2 Dankwoord

Aan het einde van Lords Of The Ring was er nog wat ruimte voor Sam (Samwise Gamgee) overgelaten om de laatste zinnen van het lange verhaal over hun lange reis tezamen op te schrijven (Just Google It). Eenzelfde gevoel bekruipt mij om dit "dankjewel" in dit proefschrift te schrijven. Niet in de laatste plaats, omdat het afronden van meer dan tien jaar onderzoek nu netjes is beschreven. Echter mijn werk is nooit af. Voor de meeste Ph.D. studenten, is de Ph.D. scriptie een afsluiting van wat vooral een plezierige periode van 4 jaar is. Mijn doctoraal onderzoek en de publicaties in dit proefschrift zijn nu afgerond en op schrift, maar mijn dagelijkse werk gaat gewoon door. Als onderdeel van deze afronding is het nu tijd om de mensen die hebben bijgedragen aan mijn Ph.D. proefschrift, en aan mijn dagelijkse werkzaamheden, te bedanken. Promoveren is een werkwoord, en dat werk doe je niet alleen. Om nu alle mensen te benoemen die me door de jaren heen hebben geholpen te bedanken, en dit zijn er velen, is dit welhaast een onmogelijke taak. Ik ben bang dat zelfs als ik er één vergeet ik ze te kort doe, juist omdat het er veel waren. Velen met wie ik vaak in goede vriendschap heb samengewerkt en nog steeds mee samenwerk. Ik denk terug aan mijn beginperiode aan de RUG. Ik ben het (toenmalige) Netherlands Institute of Metals Research, het NIMR uit Delft veel dank verschuldigd. In 2002 was de economische situatie van mijn toenmalige werkgever (Philips Semiconductor) niet echt rooskleurig en onze jongste dochter was net 3 maanden oud, een intense periode in ons leven. Toch kon ik vrijwel naadloos integreren in het NIMR met vergelijkbare werkzaamheden als bij Philips. Ik heb de tijd bij het NIMR altijd als plezierige ervaren. Het NIMR is in 2008 omgedoopt in naam tot het M2i. en heeft noodgedwongen tijdens een reorganisatie in 2010 alle vaste technici moeten ontslaan. Mede dankzij mijn supervisors kon ik gelukkig mijn technicus positie bij de RUG behouden. Fysiek veranderde er toen niets aan mijn werkplek, maar wel de status quo Beide instituten (het NIMR/M2I en de RUG) zijn inspirerende werkomgevingen, waar het een plezier was, en is om als microscopist te werken. Normaal bedank je eerst je promotor en daarna de copromotor, maar in dit geval kan (en wil) ik dit niet. Ik beschouw mijn beide supervisors veel meer dan hooggeleerde opponenten. Meer als zeer gewaardeerde collega's, vertrouwenspersonen, informatiebronnen (Russische inlichtingendienst) en als vrienden. Door ze alleen te noemen als Supervisors zou ik hun geen recht doen. Vanaf 2009-2010 (de oprichting van de NMI groep) tot heden zijn wij als Nano Materials and Interface group (NMI) gegroeid tot een hechte groep met korte communicatielijnen en een duidelijk doel voor ogen. Als het al George Palasantzas moet zijn, die als mijn promotor is aangewezen, dan wil ik hem hartelijk bedanken voor de geweldige steun en zijn altijd oprechte aanmoediging "wie wil er nu promoveren want ik heb mijn papieren al". En om het einde van de (vele) discussies af te ronden met: "kunnen we het eens zijn om het oneens te zijn". Dan zeker een welgemeende dankjewel aan Bart voor alle hulp en steun gedurende de laatste 20+ jaar. De minutieuze TEM-trainingen en de nooit aflatende drang om

in bijna alles naar perfectie te streven. Het heeft mij gedwongen om ook in veel dingen beter te worden. Het advies werd meestal gegeven tijdens de dagelijkse nabespreking, op onze snelle fietstochten door de binnenstad van Groningen, tussen het Zernikecomplex en het treinstation. Niets meer dan diep respect voor je moeilijke keuzes in het leven en het feit dat je zo ver weg woont, maar toch altijd de deur openhoudt voor andermans problemen.

Ze weten wellicht niet dat het Prof. Doekele Stavinga was die me (vriendelijk) aanspoorde om het eerste artikel (hoofdstuk 4), nu meer dan 12 jaar geleden, te schrijven. Na het eerste manuscript pakte ik de draad herhaaldelijk weer opnieuw op met verschillende tussenpozen. Het heeft lang geduurd voordat het onderzoek met de Mantis 50 nanocluster-source goed op gang kwam, vraag het Gopi. Ik zal in chronologische volgorde de vele mensen opnoemen die ik zou willen bedanken (en als ik ze niet vermeld, dan bij deze alvast bij voorbaat mijn excuses) Tijdens de NMIR/M2i periode genoot ik al de steun van Bart en George, als bronnen voor informatie en in het trainen op de JEOL-Auger en de JEOL-TEM, de Philips SEM was al mijn expertise. Uiteraard Sibbe Hoekstra, Annelies Swanenburg, Oscar Ruigrok en alle mensen van de M2i in Delft. Daarnaast wil op deze plek mijn directe collega's tijdens deze periode bedanken postuum: Paul Bronsveld ✝, Henk Bron ✝, Jan Harkema, Uko Nieborg ✝, Klaas Post ✝, James Kuipers, Pim van den Dool, David Vaihnstein, Vasek Ocelik, Maarten Hilgenga , de de fijne collega's van de Koffietafel, in het bijzonder: Alie Nanning, Henk Hanson en (met overlap) de collega's van het "wateruitje groep"

Tijdens deze periode heb ik vele Ph.D. studenten, de vele SEM's en andere microscopische technieken, die de RUG bezit, training gegeven: Damiano Galvan, David Matthews, Emiel Amsterdam, Henk Haarsma, Nuno Carvalho, Ramanathaswamy Pandian, Ronald Popma, Sasha Fedorov, Toni Chezan, Uzi de Oliveira, Vašek Ocelík, Willem- Pier Vellinga, Yutao Pei en Yueling Qin. Zhuengo Chen, Tony Kazanthis. Ik wens ze veel succes in de toekomst en misschien tot ziens.

Bij de start van de NMI-groep (2009-2010) bestond de groep uit enkele Ph.D. studenten. Ik heb veel interactie gehad met: Peter van Zwol, Jasper Oosthoek, Gert Eissing, Orcun Ergingan, Zwammy en Gopi Krishnan. De vele foto's gemaakt tijdens ons eerste groepsuitje in Katwijk aan Zee staan nog in mijn geheugen gegrift. Mijn speciale dank gaat uit naar Gopi Krishnan, eerst als Ph.D. kandidaat en later postdoc in onze groep. Gopi is begonnen te werken aan de Mantis Nano Clusters-source en ik heb hem geholpen met de technische ondersteuning. Ik maak dankbaar gebruik van zijn RSC-advance paper in hoofdstuk 6 van deze thesis Ook ben ik veel dank verschuldigd aan de techneuten van de technische werkplaatst die hebben geholpen bij het ontwikkelen van de nano-clustersource aka. Spoetnik Ze verdienen allemaal een eervolle vermelding; Bert van Dammen, Harry van Driel, Koos

Duim en last but not least Jacob Baas en Henk Bonder. Zoals altijd behulpzaam bij het oplossen van de vele technische problemen. Naast de samenwerking met promovendi post-docs en fellow researchers zijn er veel studenten die onder mijn toeziend en kritisch oog hun bachelor- en masteronderzoek hebben gedaan. Hun onderzoeksbijdrage is terug te vinden als co-auteurs in de vijf artikelen, die deel uitmaken van dit proefschrift: Arjan Bijlsma, Nolan Foley, Darin Zwaan, Peter Jan van het Hof, Bin Chen, Liuan Xing, Mehdi Sedighi, Xiaotian Zhu, Ceri Richards, Weiteng Guo, Koen Blauw, Luuc Assing en last but not least Vitaly Svetovoy, voor zijn immer slimme opmerkingen, zijn scherpe observaties.

en de vele nuttige discussies. Ik vind het een gemis dat hij door geopolitieke omstandigheden geen deel kan uitmaken van de defense comité. Ik wil Jamo Momand hartelijk bedanken voor het maken van de QCM (momenteel het George 1.0 ontwerp) tijdens zijn FIT stage. Het ontwerp en de constructie zijn de basis voor hoofdstuk 2.9.

Verder krijgen de huidige NMI-groepsleden mijn volle waardering. Een welgemeende dankjewel aan iedereen voor het zijn van, plezierige en humoristische kamergenoten, voor de goede werkomgeving en voor het onderhouden van (soms) de planten- en bloemenjungle in mijn kamer, Daniel Yilman, Razi Bakhshandehseraji, Hadisch Hassanzadeh, Masoud Ahmadi, Hui Wang, Atul Atul, Nana Gavhane, Laura Dillingh, Jesse Luchtenveld, en Sytze de Graaf. Hartelijk bedankt voor het zijn van fijne kamergenoten. Een speciaal woord van waardering gaat uit naar mijn twee Paranimfen. Majid Ahmadi en Julien van der Ree. Mijn hartelijke dank voor het op zich nemen van deze taak (ik voel me vereerd).

Onder verwijzing naar propositie nummer 2 "Mens sana in corpore sano" willen mijn bootcampmaatjes ook een eervolle vermelding. Idem, ook mijn mental coach en onvermoeibaar trainingsmaatje, Martin Veenhuizen, enorm bedankt voor alle coaching sessies. Ik moet in hem mijn meerdere erkennen in (te) veel sporten, maar ik weet wel hoe ik een fiets moet repareren en kan (beter) windsurfen!

11

Ik ben de professoren Maria Loi, Katja Loos en Harold Zandvliet veel dank verschuldigd voor hun deelname aan de leescommissie, het beoordelen van de conceptscriptie en het doen van suggesties voor verbeteringen.

De laatste zinnen zijn voorbehouden aan mijn familie, mijn altijd trouwe rots in de branding samen met de twee kleine stormbrekers; Mijn lieve Liesbeth, Anna en Eva, jullie zijn de gelukkige gedachten in Peter Pan's vermogen om te vliegen (JGI) Ik denk aan mijn lieve ouders en in melancholie aan mijn beide schoonouders. Helaas zijn mijn moeder, schoonmoeder en schoonvader te vroeg overleden om deze promotie mee te kunnen maken. Mijn twee lieve

dochters zijn wie ze zijn, mede dankzij hun goede zorgen en dat ze er altijd voor ons waren. Dank ook aan mijn oudere zus en jonger zusje en mijn jonger broertje, altijd in de verkleinvorm, maar nu zeker al als volwassenen. Telkens, keer op keer met belangstelling naar de vorderingen informeerden en al plagend opmerkten wanneer er nu eindelijk een feest aan komt, bij deze nu eindelijk en jullie zijn allemaal uitgenodigd!

Gert ten Brink
Juni 2022.

11

Chapter 12
About the Author

About the author

Talking about myself in the third person seems odd but since I followed not the average Ph.D. candidate route, explaining a bit about my background and education would make some sense.

Scientific career:

Gert ten Brink (b. 1967) earned a bachelor's degree in chemistry in 1993. After teaching chemistry and computational physics at the RUG Pharmacy department he returned back to paint research for AKZO Nobel coatings in Sassenheim. Having received the ing (bachelor's). degree at DSM coatings it was apparently a bad match. The two paint types don't mix The professional career continued as a physics analyst at the Innovative Engineering Group for Philips Semiconductor in Stadskanaal where the first hands-on experience operating an Scanning Electron Microscope took place. Having gained traction in this very inspiring academic environment, it was very unfortunate to be forced to find another position due to economic reasons. A position at the NIMR(located in Delft), was a perfect match since the available technician position was available at the RUG in Groningen, and it turned out to be a good switch. Even more SEM's to play with 😊 Due to the nature of the technician job, many new skills and techniques had to be mastered including the training and assistance of many bachelor and master students as well as numerous Ph.D. Candidates in the broad field of microscopy. As such, you can characterize him by his middle name, perfectly explained in the image. After a tumultuous period in 2008-2009, the materialkunde (Physics) group was traded for a newly formed group, Nanostructured Materials, and Interface group, under the supervision of two PI's. Bart.j. Kooi and George Palasantzas

PrivatLife:

In his private life, besides spending his time as a dedicated father and husband, he also tries to enjoy listening to symphonic rock music, piano playing and practice (to) many sports, including skating, skiing, bootcamp, triathlon, mountain biking. windsurfing, and kiting. Needless to say that 24 hours in a day is never enough, and life is way too short.

Gert